ABSTRACT

Title of dissertation: INVESTIGATION INTO THE UNSTEADY RESPONSE OF AIRFOILS DUE TO SMALL-SCALE MOTION

Matthew Ryan Catlett, Doctor of Philosophy, 2020

Dissertation directed by: Dr. James D. Baeder, Professor
Department of Aerospace Engineering

Unsteady pressures, forces, and pitching moments generated by foils experiencing vibratory motion in an incompressible, attached flow configuration are studied within this work. Specifically, two-dimensional, unsteady potential flow calculations and analysis are developed and performed on various numerically thin and Joukowski foils undergoing variable amplitude, small-scale heaving and pitching motions over a range of reduced frequencies between approximately 0.01 to 100. While the calculations and analysis are performed in the context of potential flow, the wide range of reduced frequencies are intended in order to be as widely applicable as possible, for either aerodynamic of hydrodynamic configurations. Given that substantially large reduced frequencies are being considered, a set of criteria are established based on the product of the reduced frequency and freestream Mach number in order to help ensure the applicability of potential flow to either experimental results or higher fidelity numerical results.

Calculated results are compared directly to predictions from implementing the Theodorsen model, which treats foils as infinitely thin, flat plates that shed a planar sheet of vorticity. The effects of relaxing these seemingly strict conditions are explored, and the particular terms which control the unsteady responses are identified and discussed. This involves the consideration of Joukowski foils of varying finite thickness and allowing for the wake of shed vorticity to convect according to the specifics of the unsteady velocity field. For sinusoidal disturbance motion of increasing heaving and pitching amplitude and

increasing reduced frequencies the shed wake is seen to become quite non-planar and to form coherent vortex structures. Despite this wake behavior, the normalized foil responses at the disturbance reduced frequency are seen to be largely unaffected. However, non-negligible responses are generated across a wide range of other frequencies which are separate from the specific reduced frequency of the disturbance motion.

Potential flow calculations for symmetric Joukowski foils of varying thickness show that there is marginal effect of foil thickness on the unsteady foil responses at reduced frequencies less than one for both heaving and pitching disturbance motions. For higher reduced frequency conditions however, the unsteady foil responses are seen to vary relative to the Theodorsen model in specific instances. For high reduced frequency heaving motion of Joukowski foil profiles with varying thickness, the unsteady pitching moment response, and not the unsteady lift, is seen to vary substantially in both its magnitude and phase properties relative to that of the flat foil. A specific augmenting expression is developed for this behavior through analysis within the potential flow framework. In a very similar manner and approach it is found for pitching disturbance motion about the foil mid-chord, that for variable thickness foils the unsteady lift response, and not the pitching moment, also varies in its magnitude and phase properties relative to the flat foil. A specific augmenting expression is also developed for this configuration, which leverages the fact that the unsteady flow field is defined by explicitly known expressions.

Lastly, unsteady potential flow calculations and analysis are also presented which specifically concentrate on the unsteady streamwise force response. While the unsteady properties of the response of this force component is often not a focus, it does exhibit interesting properties and is closely connected to the mean streamwise force response, as well as the unsteady lift response. A predictive expression is developed for the magnitude of the streamwise force response. This expression compares very favorably to the unsteady potential flow calculations performed within these efforts, and is also used successfully to assess the published results from several distinct references.

INVESTIGATION INTO THE UNSTEADY RESPONSE OF AIRFOILS DUE TO SMALL-SCALE MOTION

by

Matthew Ryan Catlett

Dissertation submitted to the Faculty of the Graduate School of the
University of Maryland, College Park in partial fulfillment
of the requirements for the degree of
Doctor of Philosophy
2020

Advisory Committee:
Professor James Baeder, Chair/Advisor
Associate Professor Pino Martin
Professor Kenneth Yu
Professor Konstantina Trivisa
Professor Amr Baz, Dean's Representative

Dedication

To my family.

Acknowledgements

I must start with acknowledging my family for supporting me throughout my educational endeavors, and for their unwavering encouragement.

I am very thankful for my advisor Dr. James Baeder, for all of the support and guidance he has provided me in pursuit of this degree. My path has not been typical, and yet he has guided and cultivated my academic pursuit with understanding and keen insight.

I am immensely thankful for the mentorship that I have received, both technically and professionally, by Dr. Jason Anderson. He has greatly influenced my career and development over the past ten years, and I am very indebted and grateful for the time and energy that he has invested in me.

Lastly, I am grateful to the Naval Surface Warfare Center, Carderock Division for support of this work by its Extended Term Training Program; and am specifically thankful for the persistent support provided to me by my immediate management, Marylou McNamara, Douglas Noll, and Mohammad Kapacee. Partial funding also came from the In-house Laboratory Independent Research (ILIR) program, managed by the NSWC Carderock Director of Research for the Office of Naval Research.

Table of Contents

List of Tables

List of Figures

Nomenclature

a	foil pitch axis
a_c	circle trailing edge location
a_∞	freestream speed of sound
b	foil half-chord
c	foil chord
$C(k)$	Theodorsen function
C_D	drag coefficient
C_L	lift coefficient
C_M	pitching moment coefficient
C_P	pressure coefficient
$C_{\Delta P}$	differential pressure coefficient
C_T	thrust coefficient
D	drag force
$f(z,t)$	complex-valued flow potential in the circle plane
$F(Z,t)$	complex-valued flow potential in the foil plane
F_x	force in the streamwise direction (i.e. thrust and/or drag)
F_y	force in the vertical direction (i.e. lift)
Δf	frequency resolution
$h, \dot{h}, \ddot{h}$	heaving position, velocity, and acceleration
k	reduced frequency
L	lift force
M_y	pitching moment
M_∞	freestream Mach number
$\hat{n}$	normal vector of the foil surface

P	pressure
ΔP	differential pressure
r	radial coordinate in the complex circle plane
r_c	circle radius
Re_c	Reynolds number based on foil chord
t	time
Δt	time step
t/c	foil maximum thickness-to-chord ratio
u, v	orthogonal velocity components in the complex circle plane
U, V	orthogonal velocity components in the complex foil plane
U_o	unsteady freestream velocity due to disturbance motion
U_∞	freestream flow velocity
$\vec{V}$	velocity vector
$w(z,t)$	complex-valued velocity in the circle plane
$W(Z,t)$	complex-valued velocity in the foil plane
x, y	Cartesian coordinates in the complex circle plane
X, Y	Cartesian coordinates in the complex foil plane
z	spatial dimension in the complex circle plane
Z	spatial dimension in the complex foil plane
z_γ	point vortex location in the circle plane
α_o	unsteady angle of attack due to disturbance motion
α_∞	freestream angle of attack
$\alpha, \dot{\alpha}, \ddot{\alpha}$	pitching position, velocity, and acceleration
δ_x, δ_y	offsets in the complex circle plane

Δ_x offset in the complex foil plane

γ point vortex strength

θ angle in the complex plane

ν kinematic viscosity

ξ foil surface normal vector angle

ρ fluid density

ϕ flow potential

ϕ phase angle, when used with a sinusoidal signal (should be clear from context)

ψ stream function

ω radial frequency

Φ_{C_D} auto-spectral density of the unsteady streamwise force coefficient; $C_D(k)C_D^*(k) \,/\, \Delta f$

Φ_{C_L} auto-spectral density of the unsteady lift coefficient; $C_L(k)C_L^*(k) \,/\, \Delta f$

Φ_α auto-spectral density of the unsteady pitch position; $\alpha(k)\alpha^*(k) \,/\, \Delta f$

$[\ \ ]^*$ complex conjugate

1. Introduction

1.1 Motivation and Approach

Lifting and non-lifting surfaces are routinely designed to operate in complex, turbulent velocity fields where significant unsteady forces and pressures are often generated. When a foil structure is subjected to a mean turbulent inflow velocity field, for example, this can result in small-scale vibratory foil motion which itself induces additional unsteady forces and pressures due to the foil's motion within the fluid stream. This fluid-structure interaction of small-scale foil motion and the unsteady pressures, forces, and pitching moment responses that subsequently act on a foil at high Reynolds numbers and low Mach numbers is the topic of interest of these efforts and study. A critical distinction at the onset of the description of this work is that any foil motion is assumed to be sufficiently small, such that no significant augmentation to the mean operating condition occurs due to this vibratory motion for a given foil configuration with attached flow. Phenomena such as large-scale flapping foils, dynamic stall, or flutter divergence are not currently under consideration, and while these are related, they are outside of the present scope.

Further, this work looks to study high Reynolds number, two-dimensional, incompressible, attached flows about aerodynamically efficient foils of variable profile. As such, a mixed analytical and numerical approach which utilizes Unsteady Potential Flow (UPF) calculations and analysis has been developed. The concept of this calculation approach is a numerical implementation of the unsteady potential flow framework posited by the Theodorsen model (Theodorsen (1935), Bisplinghoff et al. (1955)). The approach directly utilizes potential flow formulations and expressions, such that corroborating analysis and analytical development can occur in conjunction with numerical results.

For a subset of these results, there is also direct comparison to unsteady Reynolds-Averaged Navier-Stokes (RANS) calculations for equivalent operating conditions. These results were performed and intended to provide an independent check on the UPF results. They will be presented and the necessary

background will be described; however, they were performed separately from the UPF development and calculations, and are not the primary focus of the subsequent efforts and analysis.

An important note on the motivation and conditions of this work is the desire to remain within the confines of small disturbance motion and the applicability of potential flow. The operating conditions and foil configurations are intentionally general (i.e. not specific to a particular design, application, or configuration), and are intended to be representative of vibratory motion of a foil structure in a freestream. As such, the present efforts focus on the unsteady foil responses from two-dimensional slices of the foil profile for these representative types of structures. Disturbances of heaving (i.e. along the chord-normal direction) and pitching (i.e. rotation of the chord) motions are considered, while surging motion (i.e. in the streamwise direction) is not considered. Figure 1.1 provides an illustration of how these motions could manifest for a representative, large aspect ratio, cantilevered wing structure. Again, while not specific to a given configuration, this work is equally pertinent to fixed wings of aircraft, rotary blades of turbomachines and vehicles, biomimetic configurations, and others, which remain within the limits of the assumptions and conditions stated earlier.

Further, Figure 1.2 presents the characteristic regimes of reduced frequency and chord-based Reynolds number that result from typical incompressible, unsteady foil conditions where the fluid medium is taken to be either air or water (again, attempting to retain broad applicability). In addition to generally larger Reynolds numbers, hydrodynamic configurations can easily involve reduced frequencies which have historically received less attention than aerodynamic configurations. It is the intention of the present work to span a wide range of reduced frequencies which include several orders of magnitude in order to be as widely applicable as possible to either aerodynamic or hydrodynamic conditions. As the work is based in potential flow, the implication is that Reynolds numbers are exceedingly large and Mach numbers are low. This can be appropriate for either aerodynamic or hydrodynamic conditions, both of which can be modeled by potential flow under suitable conditions.

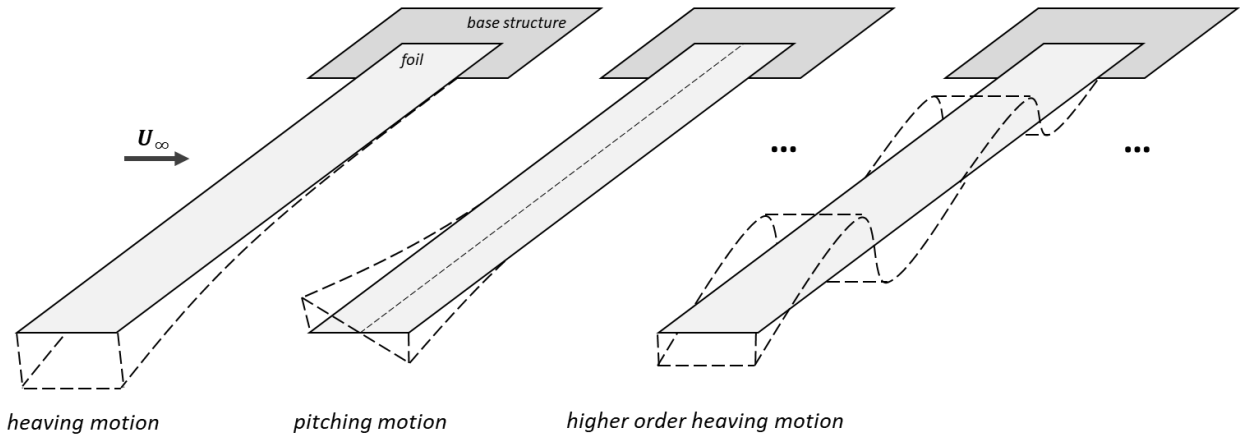

Figure 1.1. Illustration of heaving and pitching motions of a cantilevered structure

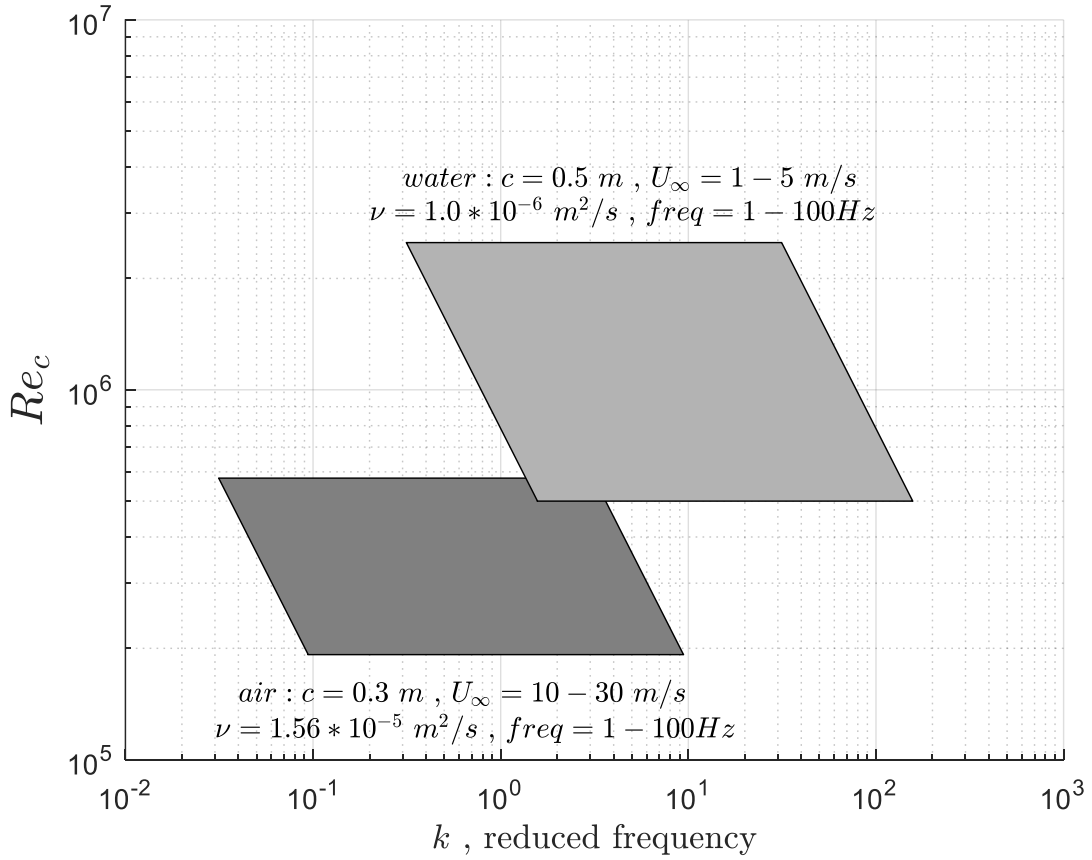

Figure 1.2. Characteristic reduced frequency and chord-based Reynolds number regimes

The primary motivation of the present work is to assess the unsteady pressures, forces, and pitching moment that result from vibratory motion, which is known, for real foils in high Reynolds number, incompressible, attached flow configurations. Therefore, an unsteady potential flow calculation approach

has been implemented where numerically flat and symmetric Joukowski foils with varying maximum thickness are subjected to unsteady, variable amplitude, heaving and pitching motion. The unsteady potential flow results are then compared directly to theoretical predictions from the Theodorsen model, as well as complementary unsteady RANS calculations, when available. These results are assessed and compared in both the time and frequency domains for unsteady conditions that span a wide range of reduced frequencies, as well as a wide range of amplitudes for small-scale disturbance motions.

The central premise of the work is the comparison of numerical results against the analytical Theodorsen model in order to identify for what conditions and considerations that differences from the model occur; then to understand the causes for any differences, and advance modeling capabilities as appropriate. As such, the following is a concise summary of major assumptions of the Theodorsen model, where correspondingly, areas which receive attention in the present work are denoted by an asterisk:

- two-dimensional, potential flow *
- foil is treated as an infinitely thin flat plate *
- no consideration for mean angle of attack
- disturbance motion is sufficiently small *
- motion and subsequent responses are harmonic
- shed vorticity travels along a planar, constant trajectory *
- unsteady responses scale linearly with disturbance motion *
- no unsteady streamwise force is available *

Consideration of mean angle of attack conditions are certainly amenable to the present UPF approach, however are not a part of the current work. Transient disturbance motions which are not harmonic can also be equally implemented with the UPF calculations, however should be assessed in the context of predictive expressions from the appropriate modeling approaches given the applicability of the disturbance motion, for which there are various possibilities (examples being the models of Küssner (1929), Wagner (1925), and comprehensive discussion found in Bisplinghoff et al. (1955) or Leishman (2006)).

1.2 Literature Survey

This form of fluid-structure interaction problem, where a foil structure undergoes motion within a fluid stream, has been widely studied given the various engineering applications where it can be an important, or primary, consideration. The works presently referenced are only a sample of the considerable number of relevant investigations, texts, and approaches that are available within the technical literature. As previously stated, the core premise of the present work is centered on the modeling framework offered by the Theodorsen model. Developed in the framework of potential flow, direct expressions for the unsteady pressure, force, and pitching moment due to heaving and pitching motions are achieved. Historically, the comparison between the results of utilizing this model to those of separate experimental and numerical work is very agreeable. Critically however, this agreement occurs both when the assumptions of the model are adhered to, and in situations where it would seem that these assumptions are not being adhered to. Additionally, it has been a more recent development that thorough experimental and numerical results are available to link the unsteady foil responses with the character of the unsteady flow field.

Separate from the available analytical efforts and models, there is an extensive history of experimental and numerical references in this fluid-structure interaction area of consideration. However, it is often the case that the conditions being investigated and concentrated on by these available references are not congruent with those of the present work. The following are critical differences with the present work which are often found: foil disturbance motions being considered are not small (ex. flapping wings), Reynolds numbers are low such that viscous effects are especially important, reduced frequencies are low (often a result of foil actuation or experimental conditions), or that analysis of results is in terms of mean performance parameters (ex. mean thrust generated due to defined foil motion). While peripherally relevant, this substantial body of potential references are often not directly applicable to the concentration on the unsteady responses of foils to small-scale motion. Configurations where foils shed considerable leading edge vortices, experience substantial three-dimensional effects, or undergo significant deformation of the foil profile (to cite some examples) occupy a different regime of unsteady foil problems than that of small-

scale disturbance motion with fully attached flow. Accordingly, these prior situations are not discussed within the present work.

The foundational beginning of the present study is considered to be the analytical framework of the Theodorsen model, which is described and reviewed by Bisplinghoff et al. (amongst others). As alluded to earlier however, this topic and configuration, in general, has certainly elicited attention even prior to these references. The reference of Platzer et al. (2008) provides a concise review of this history which reaches back to seminal works in the early $1900's$; these are not reviewed at present. The following is a succinct review of a select number of references that share common aspects with the narrower scope and motivations of the present work; however, it should be acknowledged that the entirety of Chapter 3 is dedicated to a detailed analysis of the relevant results from many of these references. Accordingly, brief descriptions of these references are presented here, and the more detailed reviews are found later. As is essentially unavoidable, some relevant references are surely, and unfortunately, not included.

Halfman (1952) documents a set of NACA-era subsonic wind tunnel tests where direct measurements of unsteady forces and moments are made on airfoils undergoing modest, sinusoidal, heaving and pitching motion up to a reduced frequency of approximately 0.4. These results generally align with the theory of Theodorsen, though some deviations are identified. Similarly, Rainy (1957) documents experimental work on an un-cambered airfoil which is pitching at both subsonic and transonic freestream conditions. An additional variable provided by this reference is that the foil is placed at several mean angles of attack, which are seen to induce differences in the unsteady foil response for angle of attack conditions approaching stall on the mean lift curve. Leishman (1993) provides a consolidated reference for three experimental configurations (Liiva et al. (1968), Wood (1979), and Davis and Malcolm (1980)) presenting unsteady lift as a result of foil pitching motion at subsonic conditions and reduced frequencies below 1.0, along with associated analytical work. Leishman (2006) is also a noteworthy text which presents and discusses many germane topics in this area. The work of Münch et al. (2010) presents analysis of CFD and experimental results for forced and free motion of a pitching foil over a wide range of reduced frequencies,

$0.02 - 100$, at a chord-based Reynolds number of approximately 10^6. Behavior of the foil response is discussed and modeled, which includes analysis of the dynamic system parameters of added moment of inertia, fluidic damping, and stiffness, as well as varying properties of the wake of shed vorticity.

Giesing (1968) describes a potential flow panel method approach for a pitching airfoil (as well as for the response from a gust and a foil starting from rest) and provides a modest amount of comparison of the numerical results to theory and experimental work. Complementary CFD, experimental results, and analysis of theory is provided by Strangfeld et al. (2015) for a pitching airfoil (as well as for surging motion) at distinct reduced frequencies and chord-based Reynolds numbers on the order of 10^5. The disturbance pitching motion conditions were reasonably small though viscous and hysteretic effects were still seen to be important in their work. The work of Ashraf et al. (2011) present a systematic study of unsteady RANS calculations for both heaving and pitching foils over a wide range of chord-based Reynolds numbers between approximately $10^2 - 10^6$, foil thickness-to-chord ratios between 6 and 50%, at a distinct reduced frequency of 2.0. The amplitude of the motion being considered is generally large, highlighting the importance of viscosity and the role of shedding vorticity from the foil leading edge.

The following experimental references of Bratt (1953), and Ohashi and Ishikawa (1972) provide wind tunnel flow visualization of the shed vorticity wake (from the trailing edge) at high reduced frequencies, which exhibit strong evidence of the non-planar and non-linear shed wake of vorticity at operating conditions where the reduced frequency is greater than 1.0. Finally, the separate reviews of McCroskey (1982) and Crighton (1985) provide particularly enlightening discussion and analysis of numerous additional references with respect to unsteady airfoil flows, effects of the trailing edge and the shed wake, and specifically the application of the Kutta condition.

The detailed review and analysis of references found in Chapter 3 includes additional works not listed here, and more importantly culminates with a subsection that provides a summary of the findings as they pertain to the motivations of this study. Additionally, several more references are leveraged within the results presented in Chapter 4. As stated earlier, this general topic area of unsteady foil motion has yielded

a prolific number of references, both historically and ones of more recent vintage; Tijdeman and Seebass (1980), Koochesfahani (1989), Heathcote and Gursal (2007), Boutet and Dimitriadis (2018), and Chao et al. (2019), being but a select number of additional works. However, not all are specifically applicable to the narrower scope of the present work.

1.3 Dissertation Organization

The topic and concentration on the unsteady responses of foils to small-scale motion within a freestream have been introduced. The motivations for the work and the implemented numerical and analytical approaches have also been discussed. Additionally, a succinct review of the numerous technical references in this area has just been presented. Beyond this opening chapter, this dissertation is organized into the following four chapters, with additional appendices.

Chapter 2 provides a detailed presentation of the background material and methodology for the analytical and numerical work developed and pursued. Specifically, the development of the Unsteady Potential Flow calculations is discussed, which includes the various considerations needed for implementation. Additionally, as utilization of the Theodorsen model is a central theme throughout this work, specific analysis and development of how the predictive expressions from this model are implemented is provided.

Chapter 3 offers an extended and in-depth review of the specifically pertinent results from fifteen distinct references. For these references, various results are either digitally extracted or copied and recreated from the reference documents, subsequently analyzed, and directly compared to in terms of the Theodorsen model. In addition to attempting to provide a consolidated compilation of analysis for this topic, the purpose of these exercises are: 1) to establish and present the general robustness and acceptability of the Theodorsen

model relative to varied experimental and numerical results, 2) to present this analysis in the common format which will be utilized throughout the present work, and 3) to attempt to identify where the model does not perform well, where its underlying assumptions appear to be not applicable, or conditions at which it has not been as extensively implemented.

Chapter 4 is the Results section, and presents the various Unsteady Potential Flow calculated results, in addition to the new analytical developments. As can be seen, there are several specific topics under consideration, however the general approach involves presentation and analysis of calculated results relative to the associated Theodorsen model expressions. Results from supplemental unsteady Reynolds-Averaged Navier-Stokes calculations are also presented when available. The results from this work include the development of new analytical expressions for foil responses and their subsequent comparison to calculated results.

Chapter 5 provides the conclusions and summarizing discussion for this body of work. The new contributions of this work are reiterated, and the outlook and proposals for future work are offered. Lastly, the document includes several appendices which is where much of the detailed analysis progressions for various considerations have been deferred in order to keep the presentation of the results to a concise and managed scope. The culminating expressions are highlighted in the subsequent results sections, while the appendices provide the complete detailed development.

2. Theoretical Background and Methodology

The core premise of this work is numerical implementation of the potential flow framework posited by the Theodorsen model, followed by efforts to identify primary flow conditions and foil properties that yield varied results relative to this predictive model. Accordingly, the following sections present the necessary background material for the analytical and numerical development of the Unsteady Potential Flow calculations, as well as the approach for how the Theodorsen model expressions are implemented throughout this work. For more thorough and detailed development specifically of the Theodorsen model, the reader is referred to several references, one being Bisplinghoff et al.

2.1 Unsteady Potential Flow Framework

The present work implements an unsteady potential flow analysis and calculation approach which yields the unsteady pressures and subsequent forces and pitching moment generated on a two-dimensional foil due to small-scale, unsteady heaving and pitching motions. The disturbances are restricted to be small, rigid-body motion of the profile sections. The concept of the approach is a direct numerical application of the model posited by Theodorsen, for which a brief partial summary is provided, prior to the more detailed description of the potential flow framework.

The approach leverages conformal mapping between complex planes describing a circle and foil flow field. In the Theodorsen model, the circle is centered at the origin, which yields a numerically thin foil (i.e. a line) using Joukowski mapping. No consideration is provided for finite profile thickness, camber, or mean angle of attack. The critical advantage being leveraged however, is that the flow over the circle, and therefore the foil, is known explicitly through the straightforward freestream and doublet potential flow terms. Disturbance motion is then introduced as either heaving (normal-to-chord) or pitching (with a variable pitch axis) motions. These disturbances are absorbed into the potential flow terms, such that

explicit expressions are still available. An essential assumption on the motion is that it is of a sufficiently small amplitude that the flow remains attached (i.e. maintaining the applicability of potential flow).

The disturbance motion however, leads to the critical component of the approach, which is the need to enforce the Kutta condition of flow smoothly leaving the sharp foil trailing edge. Unaccounted for, the disturbance motion yields flow character that is non-physical. Enforcement of the Kutta condition is performed by the shedding of vorticity into the flow field, in this circumstance, specifically from the foil trailing edge only. The amplitude of the shed vorticity is determined by the combined influence of the instantaneous disturbance motion and any previous shed vorticity which is convected with the flow field, and thus establishes an evolutionary problem in time. Under further assumptions of harmonic motion, that the vorticity may be discretized into point vortices, and that they convect in a planar trajectory at the freestream velocity, the unsteady differential pressure, lift, and pitching moment expressions of the Theodorsen model are yielded. These are the basic components of the approach which are emulated.

As this work is based in potential flow, the entire effort begins humbly in the context of solutions to Laplace's equation,

$$\nabla f^2 = 0 \tag{2.1}$$

The flow field of interest is constructed through superposition of explicitly known potential flow components, specifically a freestream, doublet, point vortices, and considerations for rotational velocity of the foil. These are expressed in the complex plane of the circle, $z = x + iy = r\, e^{i\theta}$. The freestream velocity and flow potential are defined in the complex circle plane as the following,

$$w(z) = U_\infty e^{-i\alpha_\infty} \quad ; \quad f(z) = U_\infty\, z\, e^{-i\alpha_\infty} \tag{2.2}$$

where U_∞ is the freestream velocity, and α_∞ is the mean freestream angle of attack. The velocity and flow potential for the doublet is,

$$w(z) = -U_\infty \frac{a_c^2 e^{i\alpha_\infty}}{(z - z_o)^2} \quad ; \quad f(z) = U_\infty \frac{a_c^2 e^{i\alpha_\infty}}{z - z_o} \tag{2.3}$$

where a_c is the trailing edge location of the circle (more thoroughly described in Section 2.3), and z_o is a possible offset of the circle from the origin. When the doublet is combined with the freestream, this defines the potential flow about a circle. Lastly, a point vortex is defined as,

$$w(z) = i\frac{-\gamma}{2\pi(z - z_\gamma)} \quad ; \quad f(z) = i\frac{-\gamma}{2\pi}\log(z - z_\gamma) \tag{2.4}$$

where γ is the vortex strength, and z_γ is the location of the point vortex in space. It is well established that for a foil at a mean angle attack, that mean circulation is necessary for enforcement of the Kutta condition in this steady configuration, and that this is provided by a constant-strength point vortex located at the circle center. While a readily implementable condition within the present framework, the consideration of mean angles of attack is not something which is specifically explored in the present work.

The potential in the complex plane is defined as,

$$f(z) = \phi(z) + i\psi(z) \tag{2.5}$$

where ϕ is the flow potential, and ψ is the stream function. The velocity in the complex plane is defined as the derivative of the potential,

$$w = \frac{\partial f}{\partial z} \tag{2.6}$$

such that,

$$\frac{\partial f}{\partial z} = \frac{\partial f}{\partial x} = \frac{\partial f}{\partial (iy)} = -i\frac{\partial f}{\partial y} \tag{2.7}$$

Substituting the potential and equating real and imaginary terms provides the Cauchy-Riemann equations,

$$\frac{\partial(\phi + i\psi)}{\partial x} = -i\frac{\partial(\phi + i\psi)}{\partial y} \quad \rightarrow \quad \frac{\partial \phi}{\partial x} = \frac{\partial \psi}{\partial y} \quad ; \quad \frac{\partial \psi}{\partial x} = -\frac{\partial \phi}{\partial y} \tag{2.8}$$

This results in the following definition for the velocity,

$$\frac{\partial f}{\partial z} = \frac{\partial f}{\partial x} = \frac{\partial(\phi + i\psi)}{\partial x} = \frac{\partial \phi}{\partial x} + i\frac{\partial \psi}{\partial x} = \frac{\partial \phi}{\partial x} - i\frac{\partial \phi}{\partial y} \quad \rightarrow \quad w(z) = u(z) - iv(z) \tag{2.9}$$

where the derivative in the first portion of the expression above is independent of direction and could have also been implemented along iy to yield the same definition.

An essential aspect of this approach is that the circle (and therefore the foil) remain impenetrable to the flow. For the freestream and doublet, this is what defines the circle. Therefore, as the considered flow fields are to be constructed by a superposition of an array of point vortices, it is necessary to include an equivalent set of image vortices. These are defined by introducing vortices of equal but opposite strengths at appropriate locations inside of the circle, such that the circle surface remains a streamline (i.e. ψ is a constant). For a circle of radius r_c centered at the origin and a vortex located at z_γ, the associated image vortex is located at,

$$z_{\gamma,image} = \frac{r_c^2}{z_\gamma^*} \tag{2.10}$$

where $[\quad]^*$ denotes the complex conjugate. Appendix F provides additional discussion on this point and shows how this is handled for circles not centered at the origin.

The conditions and calculations of the present effort concentrate on pitching motion of the subsequent foils, and accordingly, the induced velocity on the foil surface due to the angular pitch rate, $\dot{\alpha}(t)$, is introduced as a solid body rotation in the foil plane. Populating this term utilizes the subsequent moment arm from the pitch axis in the foil plane, which is known. For finite thickness foils, this occurs at a slight offset from the coordinate system origin so that the finite thickness Joukowksi foils can pitch about their respective mid-chords. This velocity contribution was not inherently assumed to be an acceptable potential flow term, therefore, the following were confirmed: 1) Laplace's equation is satisfied, 2) the circle is maintained as a streamline, and 3) a corresponding flow potential expression is achievable. The definition and development of this term is deferred to Appendix D for conciseness of the present discussion.

Lastly, while the specific handling of the unsteady heaving and pitching motion is addressed in the next subsection, these motions result in unsteady freestream and unsteady angle of attack conditions

such that $U_\infty \to U_o(t)$ and $\alpha_\infty \to \alpha_o(t)$. Combining all of these components, the entire velocity flow field in the circle plane can be constructed as,

$$w(z,t) = U_o(t)e^{-i\alpha_o(t)} - U_o(t)\frac{a_c^2 e^{i\alpha_o(t)}}{\left(z-\left(\delta_x + i\delta_y\right)\right)^2} + w_{rot.\ vel.} \cdots$$

$$+\sum_{n=1}^{N} -\frac{i\gamma_n}{2\pi\left(z - z_{\gamma_n}(t_n)\right)} + \frac{i\gamma_n}{2\pi\left(z - \frac{a_c^2}{z^*_{\gamma_n}(t_n)}\right)} \tag{2.11}$$

and evaluated at any desired location z. Similarly the flow potential is expressed as,

$$f(z,t) = U_o(t)\, z\, e^{-i\alpha_o(t)} + U_o(t)\frac{a_c^2 e^{i\alpha_o(t)}}{z-\left(\delta_x + i\delta_y\right)} + f_{rot.\ vel.} \cdots$$

$$+\sum_{n=1}^{N} -\frac{i\gamma_n}{2\pi}\log\left(z - z_{\gamma_n}(t_n)\right) + \frac{i\gamma_n}{2\pi}\log\left(z - \frac{a_c^2}{z^*_{\gamma_n}(t_n)}\right) \tag{2.12}$$

Several of these terms require clarification at this point in the description. The terms δ_x and δ_y are possible offsets of the circle from the origin. It is well established that non-zero values for these terms yield foil thickness and camber when implemented with Joukowski conformal mapping; this is not implemented in the Theodorsen model, but foil thickness is considered in the UPF calculations. The first term under the summation represents the point vortices that are shed into the flow field which are located at z_{γ_n}. The second term under the summation represents the necessary image vortices which are needed within the interior of the circle in order to maintain the impenetrability of the circle surface.

Figure 2.1 provides a sample view of the velocity field for the flow over a circle generated as an example of combining these potential flow sources. A normalized freestream encounters a circle with a discrete number of downstream point vortices of arbitrary strength. These are the basic building blocks of both the analytical development and the discretized numerical approach which is presently implemented.

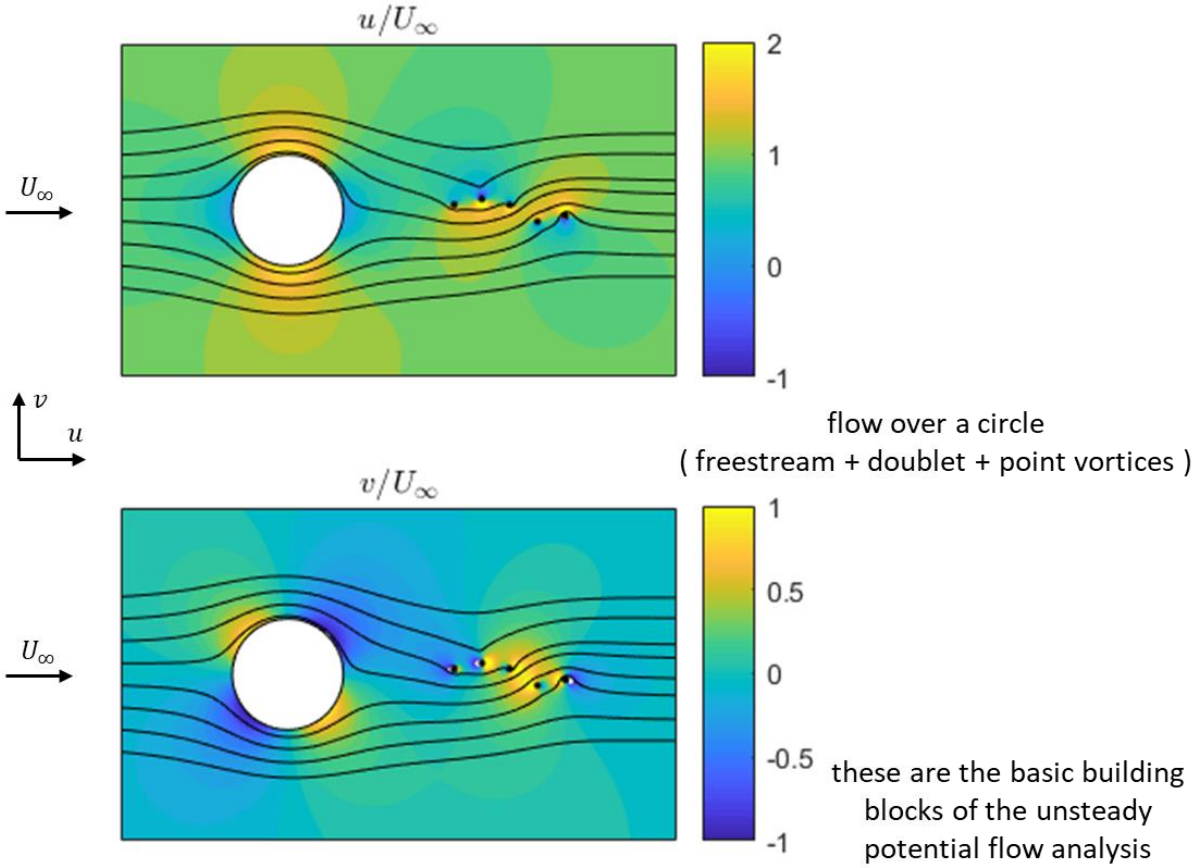

Figure 2.1. Example of the primary components of the potential flow field

2.2 Unsteady Heave and Pitch Motion

Both unsteady heaving and pitching motion are considered throughout this work. For clarity, Figure 2.2 provides a visual of these definitions. As discussed earlier, there are two critical assumptions imposed on these disturbance motions: 1) that they are small in amplitude, and 2) that they exhibit harmonic, statically stationary character. These are direct assumptions with the Theodorsen model, and also conditions adhered to within the UPF calculations. The first assumption maintains that the disturbance conditions are such that the flow across the foil remains attached. This is imposed primarily to minimize viscous effects and to retain the applicability of potential flow. The second assumption provides the ability for analytic closure of the Theodorsen model (i.e. it leads to the form of the Theodorsen function based on the shed vorticity) and for the direct unsteady foil responses expressions to be achieved.

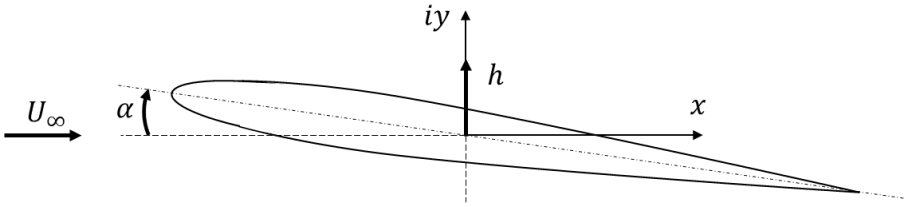

Figure 2.2. Illustration of heaving and pitching motions

For analyses which utilize the Theodorsen model, it is very often taken that this second assumption requires (or at least implies) sinusoidal disturbance motion. Through use of the Fourier transform to describe signals in the frequency domain, however, more generalized motion can equally be considered. The critical condition is that the motion is statistically stationary, providing the same statistical properties across time. Within the development of the UPF calculation approach, various motions were explored, such as ramps, swept sines, impulses, and broadband signals. Results for these types of motion are largely not considered in the present work, as the focus is on analysis based on the applicability of the Theodorsen model. However, a subset of results are presented in this document for broadband disturbance motion, as this statistically stationary motion can be equivalently analyzed in the frequency domain relative to the Theodorsen model.

Harmonic heaving and pitching motion provides the following well established properties for the expressions of position, velocity, and acceleration,

$$h = h_o e^{i\omega t} \;;\; \dot{h} = i\omega h_o e^{i\omega t} \;;\; \ddot{h} = -\omega^2 h_o e^{i\omega t} \quad ; \quad h \rightarrow \text{known} \;;\; \dot{h} = i\omega h \;;\; \ddot{h} = -\omega^2 h \tag{2.13}$$

$$\alpha = \alpha_o e^{i\omega t} \;;\; \dot{\alpha} = i\omega \alpha_o e^{i\omega t} \;;\; \ddot{\alpha} = -\omega^2 \alpha_o e^{i\omega t} \quad ; \quad \alpha \rightarrow \text{known} \;;\; \dot{\alpha} = i\omega \alpha \;;\; \ddot{\alpha} = -\omega^2 \alpha \tag{2.14}$$

such that for specified heaving and pitching conditions, all derivative terms are also equally known.

Within the UPF calculations, the necessary heaving and pitching sinusoidal motions are specified explicitly and implemented directly within the time domain. For the pitching motions, a maximum amplitude is specified for these signals. For the heaving motions, the necessary amplitude of the heaving position is determined in order to maintain a common $\dot{h}/U_\infty$ ratio between varying reduced frequency conditions. This condition maintains the same effective unsteady angle of attack between variable freestream conditions. As will be shown in the subsequent development and results, this is understood to provide the appropriate normalizing parameter for the unsteady responses due to heaving motion. Presently, these two motions are always considered separately in order to isolate their respective results, however there is no inherent limitation to the UPF approach for these needing to be separate. Many works consider combined heaving and pitching motions, especially when the primary focus is the production of mean forces (i.e. thrust). Further, as can be seen in the Theodorsen model (and therefore subject to the necessary assumptions), the influence of these disturbance motions is additive within the non-circulatory and circulatory portions of the expressions.

These small-scale heaving and pitching disturbance motions alter the definitions of the freestream velocity and angle of attack in the following ways by providing perturbations such that an unsteady angle of attack, $\alpha_o(t)$, and freestream, $U_o(t)$, must be considered,

$$\alpha_o(t) = \alpha'(t) + \tan^{-1}\left(\frac{\dot{h}(t)}{U_\infty}\right) \quad ; \quad U_o(t) = \left(U_\infty^2 + \dot{h}^2(t)\right)^{\frac{1}{2}} \tag{2.15}$$

where $\dot{h}$ is the unsteady heaving velocity and α' is the unsteady pitching position.

2.3 Conformal Mapping

As has been mentioned earlier, the development of the UPF calculations aims to emulate the approach posited by the Theodorsen model, by numerically implementing the various potential flow components. A critical aspect of this work is the utilization of conformal mapping to relate the complex plane for the flow over a circle to an associated plane for the flow over a foil profile. This is traditionally implemented in the spatial dimensions for a circle of radius, r_c, centered at the origin, that is mapped to a flat foil (i.e. a line) with the following conformal mapping function,

$$Z = z + \frac{a_c^2}{z} \quad ; \quad z = r_c e^{i\theta} + \delta_x + i\delta_y \tag{2.16}$$

where z is the spatial dimension in the circle plane, $z = x + iy$, Z is the spatial dimension in the foil plane, $Z = X + iY$, δ_x and δ_y are possible offsets of the circle from the origin, and a_c is the point at which the circle crosses the positive real axis. When δ_x takes a non-zero, negative value the resulting profile is a symmetric foil which exhibits a round leading edge and cusped trailing edge. When δ_y is non-zero, camber is introduced to the foil profile. When either δ_x or δ_y are non-zero, then $r_c \neq a_c$. This implementation is quite standard, and in the context and precedent of aerodynamics, this specific conformal mapping and resulting foil profiles are denoted as Joukowski mapping and profiles. Representative views of this implementation are provided in Figure 2.3. Within the present UPF calculations and unsteady potential flow analysis, numerically flat foils and symmetric Joukowski foils of variable finite thickness are implemented; therefore δ_y is always zero, and δ_x takes either zero or negative values. Consideration of foil camber is not made; though it is understood that the primary ramification on the UPF calculation framework would be the necessary adjusted handling of the shed vorticity.

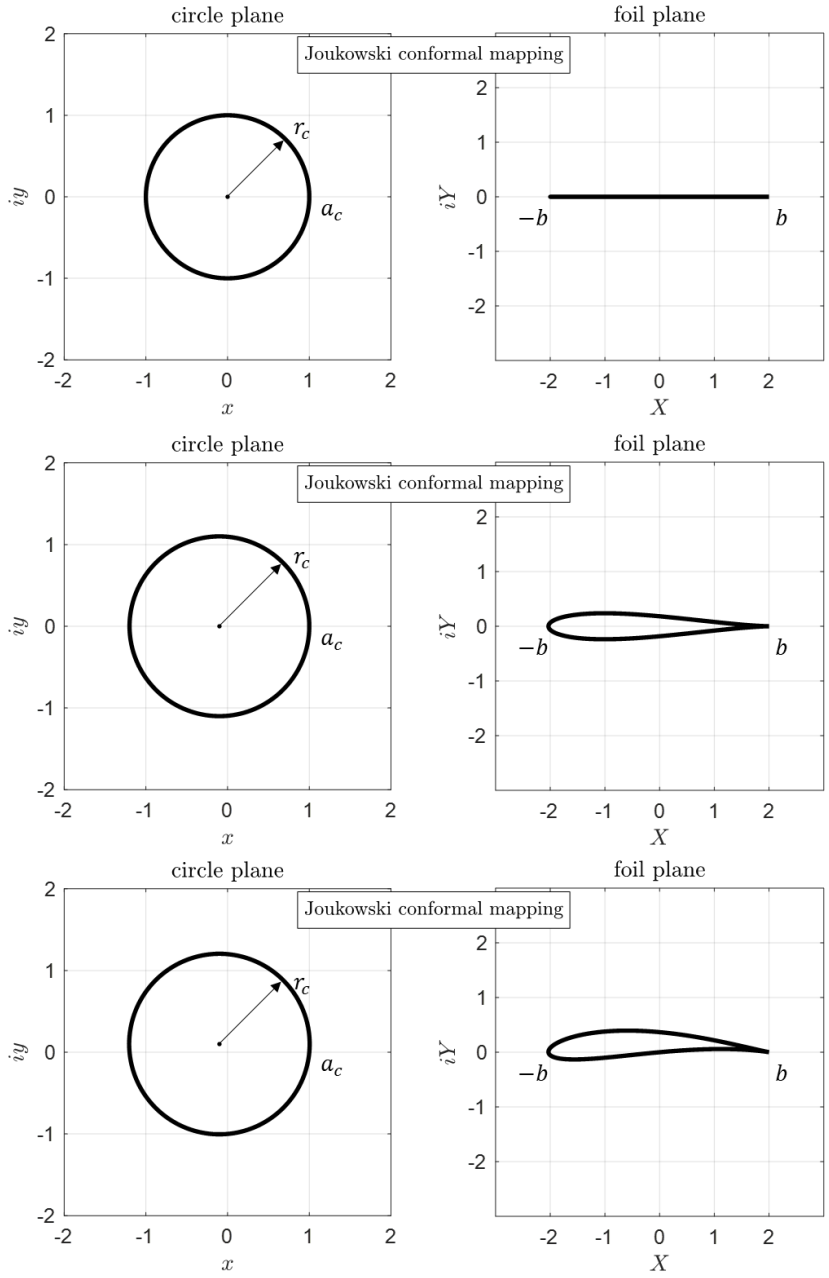

Figure 2.3. Representative views of the circle and foil planes for Joukowski conformal mapping

There are several advantages to implementing this conformal mapping approach, the primary and most notable one being that the unsteady flow fields in both the circle and foil planes are known explicitly by directly populated expressions. In relation to a vortex panel method, for example, there is no solving for the vortex panel strengths necessary to maintain impenetrability of the foil surface. Given that the flow field is defined by the superposition of known potential flow contributions, calculations can be performed very

rapidly, with the only necessary time-stepping occurring for the shedding and tracking of vorticity. Comparison and optimization of this advantage is not explored in the present work.

The main disadvantage of this approach however, is that the implemented foil profiles are completely dependent upon the mapping function used to define them. This could be seen as a serious constraint on the general applicability of the approach, however as demonstrated by Anderson and DiPerna (2017), variable conformal mapping can be generated for essentially any desired foil profile. This however, is not an aspect of work which is presently utilized. Further, while the implemented approach maintains a fairly specific scope, the references of Michelin and Smith (2009), Wang and Eldredge (2013), and Xia and Mohseni (2017) are a few additional references that could be sought for conformal mapping and potential flow methods which can have wider applicability and considerations of more general conditions.

As described in the potential flow section above, the velocity and potential flow are specified in the circle plane, and these are subsequently defined in the foil plane based on the implemented Joukowski mapping. The flow potential is invariant between the planes, such that,

$$f(z) = \phi(z) + i\psi(z) \; = \; F(Z) \tag{2.17}$$

where ϕ is the flow potential, ψ is the stream function, and lower and upper case variables correspond to the circle and foils planes, respectively. The velocities in the two planes are defined by the corresponding spatial derivative in the respective planes. As the velocity in the circle plane, $w(z)$, is explicitly defined, the velocity in the foil plane, $W(Z)$, is determined by the implemented mapping. This implementation is again standard, and leads to the following expressions,

$$W = \frac{\partial F}{\partial Z} \quad ; \quad w = \frac{\partial f}{\partial z} \quad ; \quad F = f \tag{2.18}$$

$$\frac{\partial F}{\partial Z} = \frac{\partial f}{\partial Z} \tag{2.19}$$

$$W = \frac{\partial f}{\partial z}\frac{\partial z}{\partial Z} = w\frac{\partial z}{\partial Z} \tag{2.20}$$

where for Joukowski mapping,

$$\frac{\partial Z}{\partial z} = 1 - \frac{a_c^2}{z^2} \tag{2.21}$$

This yields the following concise expression for defining the velocity field in the foil plane, based on the velocity and circle geometry defined in the circle pane,

$$W(Z) = \frac{w(z)}{1 - \frac{a_c^2}{z^2}} \tag{2.22}$$

The components of the velocity in the complex foil plane are defined as,

$$W(Z) = U(Z) - i\,V(z) \tag{2.23}$$

A particular utility of the this approach and the relative simplicity of the Joukowski mapping, is that transforming back and forth between the circle and foil planes for either the spatial or velocity fields is a simple step. A final set of points are necessary to acknowledge about the mathematical implementation of the conformal mapping approach. First, a singularity exists if attempting to map the circle origin into the foil plane; this however, is a location that is never needed for velocity and flow potential defined along the foil surface (i.e. properties are never needed to be determined at the origin in the circle plane).

The second consideration for this conformal mapping implementation is that the mapping of the velocity fields for flat foil conditions introduces two additional singularities that do need to be contended with; one at the foil leading edge and one at the foil trailing edge (i.e. when $z = a_c$ and $z = -a_c$ for a flat foil). These are potentially problematic, as the velocity and flow potential along the foil surface is needed to determine the corresponding pressure. The approach for dealing with these singularities is simply to avoid evaluation at these specific spatial locations. Evaluations of the velocity and flow potential at these specific locations are not utilized, and sufficient spatial discretization in their immediate vicinity is limited and checked as to not exhibit any clear numerical aberrations. It is believed that acceptability of this pragmatic approach is born out in the results of the numerical UPF calculations.

2.4 Application of the Kutta Condition

The application and enforcement of the Kutta condition is a central consideration within the UPF calculations. In the context of potential flow, this is an imposed condition based on the behavior of real fluids, and has received extensive attention throughout the technical literature (this rich history is not recounted at present). In terms of a verbal description, the behavior that the Kutta condition imposes is that the flow must leave the sharp trailing edge of the foil (cusped in this instance) smoothly. While the present work considers a wide range of reduced frequencies, the motion is generally small, and the Kutta condition is enforced for all configurations.

The pivotal step within these UPF calculations is the application of the Kutta condition as this defines the strengths of the shed and image vortices in relation to the history of the shed wake and the instantaneous disturbance motion. The Kutta condition is enforced by ensuring that contributions to the tangential velocity at $x = a_c$ on the circle (which is the trailing edge of the foil) from the non-circulatory and circulatory portions of the unsteady flow are equal but opposite, such that the flow leaves the foil smoothly. As the UPF calculations are intended to emulate the framework provided by the Theodorsen model, the critical expression for enforcing the Kutta condition is implemented by following the development of the Theodorsen model as provided by Bisplinghoff et al. (Eq. 5-297). The Kutta condition is implemented as an integral expression which balances the history of shed vorticity with the instantaneous disturbance motion for a flat foil condition,

$$\frac{2}{\pi}\int_0^{\pi}\frac{w_a \sin^2(\theta)}{\cos(\theta)-1}d\theta + \frac{1}{\pi b}\int_b^{\infty}\sqrt{\frac{X+b}{X-b}}\,\gamma_w(X,t)\,dX = 0 \qquad (2.24)$$

where w_a is defined as $w_a = -\dot{h} - U_\infty \alpha - \dot{\alpha}(X - ba)$, and γ_w is circulation per unit length of the wake. This integral equation is applicable for flat foils (i.e. circles centered at the origin), and needs to be augmented in order to account for circles displaced from the origin. Appendix E and Appendix F provide

the supplemental steps and description of how this is handled for circles displaced along the negative real axis (i.e. symmetric Joukowski foils).

Remaining with the expression of Eq. 2.24, the first integral term above is evaluated directly, however the disturbance velocity, w_a, cannot be completely pulled out of its integral due to the $\dot{\alpha}X$ term. The handling of this first integral is presented in Appendix E, which provides for a new term, $\widetilde{w}_a$. The resulting integral equation (still for flat foils) which defines the shed vorticity wake is,

$$\int_b^{\infty} \sqrt{\frac{X+b}{X-b}}\, \gamma_w(X,t)\, dX = -2\widetilde{w}_a \pi b \tag{2.25}$$

This expression is subsequently discretized in order to solve for the newly shed vortices at each time step,

$$\sum_{n=1}^{N} \sqrt{\frac{X_n+b}{X_n-b}}\, \gamma_w(X_n,t_n)\, \Delta X_n = -2\widetilde{w}_a \pi b \tag{2.26}$$

The summation is split in order to isolate the $n = N$ term, which is the newly created portion of the shed vorticity which is to be solved for,

$$\sqrt{\frac{X_N+b}{X_N-b}}\, \gamma_w(X_N,t_N)\, \Delta X_N = -2\widetilde{w}_a \pi b - \sum_{n=1}^{N-1} \sqrt{\frac{X_n+b}{X_n-b}}\, \gamma_w(X_n,t_n)\, \Delta X_n \tag{2.27}$$

$$\gamma_w(X_N,t_N)\, \Delta X_N = \left(\sqrt{\frac{X_N+b}{X_N-b}}\right)^{-1} \left(-2\widetilde{w}_a \pi b - \sum_{n=1}^{N-1} \sqrt{\frac{X_n+b}{X_n-b}}\, \gamma_w(X_n,t_n)\, \Delta X_n\right) \tag{2.28}$$

In this way the newly created portion of the vorticity wake can be solved for at every time step. The vorticity wake is then approximated by point vortices located at X_n at any time step t_n by the following,

$$\gamma_n\big(X_n(t_n)\big) = -\gamma_w(X_n,t_n)\, \Delta X_n \tag{2.29}$$

where γ_n defines the vortex strengths of the array of point vortices. This yields,

$$\gamma_N\left(X_N(t_N)\right) = \left(\sqrt{\frac{X_N + b}{X_N - b}}\right)^{-1} \left(2\tilde{w}_a \pi b - \sum_{n=1}^{N-1} \sqrt{\frac{X_n + b}{X_n - b}}\, \gamma_n\left(X_n(t_n)\right)\right) \tag{2.30}$$

It should be noted that within this work all point vortices retain a constant strength from their moment of creation.

Finally, it is acknowledged that as written, the expression above pertains to circles centered at the origin (or equivalently, flat foils), and that the shed vorticity is still assumed to exist only along the real axis. An augmentation is therefore necessary for conditions which consider symmetric Joukowski foils, and for the consideration of point vortices which do not have restrictions on their displacement within the flow field. Appendix F provides the subsequent detailed development, but the overall outcome is that the vortex weighting expressed by the square root term is adjusted. The resulting expression for the shed vorticity takes the same form, though is slightly more general,

$$\gamma_n\left(Z_N(t_N)\right) = G(z_N)^{-1} \left(2\tilde{w}_a \pi b - \sum_{n=1}^{N-1} G(z_n)\, \gamma_n\left(Z_n(t_n)\right)\right) \tag{2.31}$$

with the function $G(z)$ being provided in Appendix F. It is acknowledged that this weighting function is defined in the circle plane, however, this is acceptable because of the properties of the implemented conformal mapping; see Appendix F.

2.5 Handling of the Shed Vorticity from the Trailing Edge

The prior section highlights the determination of the necessary strength of the newly shed vorticity, while this section describes how the convection of this vorticity is handled in the downstream wake of the foil. As implemented within the Theodorsen model, the vorticity is enforced to convect downstream at the freestream velocity along an enforced planar trajectory (i.e. chord-line extended). Figure 2.4 provides a simple illustration of this for the thin foil configuration. While this is a necessary condition of the shed vorticity for the determination and definition of the frequency-dependent Theodorsen function, $C(k)$, it also appears quite reasonable based on the accompanying assumptions of the model. For the potential flow over a stationary, numerically thin foil, there is no wake deficit of the velocity field. Further, small disturbance motion implies that any cross-stream spatial variation should be minimal, and vorticity strengths should be small. For increased reduced frequencies and amplitude disturbance conditions, however, these conditions and assumptions should begin to breakdown. Larger disturbances (of non-descript value at present) would imply the need for stronger shed vorticity to enforce the Kutta condition, and that relative motion between the foil and shed vorticity may not be negligible. Elevated reduced frequencies (again, of un-specified value at present) also would imply stronger vorticity, in addition to shorter wavelengths of the distribution of the shed vorticity. Figure 2.5 provides illustration of this concept.

Figure 2.4. Illustration of the assumed vorticity convection in the Theodorsen model

Within the UPF calculations, the locations of the distribution of shed point vortices are known explicitly. Further, an expression for the entire unsteady velocity field is known. Therefore, the availability of this information is utilized in the determination of the convection of the shed point vortices. At the initial

instance of disturbance motion, the necessary shed vorticity is determined. At the next instance of time, this initial vortex is convected downstream, and the necessary new vortex is created. This process then simply repeats for all subsequent time steps, and Figure 2.6 provides another illustration of this concept.

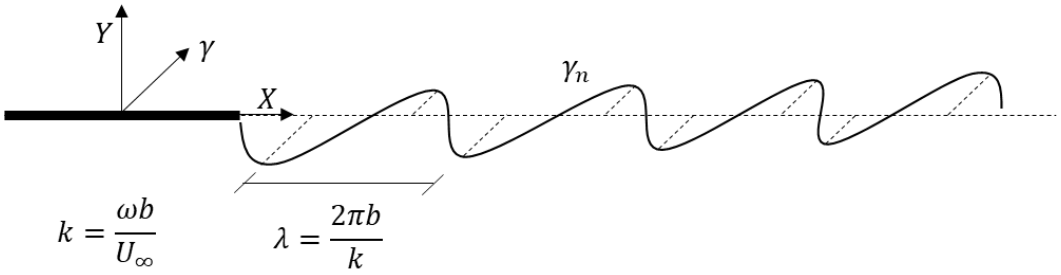

Figure 2.5. Illustration of the vorticity distribution as a function of reduced frequency

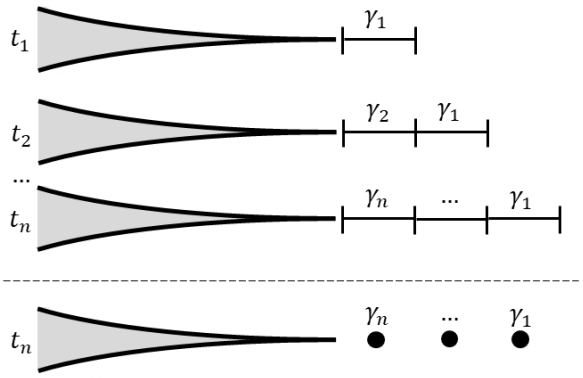

Figure 2.6. Illustration of the evolution of the shed vorticity

In the UPF calculations, the motion for all of the shed point vortices is determined through a predictor-corrector scheme such that each vortex is treated as a particle in space influenced by all other contributions, except itself. This motion of the point vortices is implemented in the foil plane such that consideration of a Routh correction is not warranted; though mapping back and forth between the circle and foil planes is needed. As potential flow is the framework for these calculations, and are subsequently elliptic PDE's, no particular numerical stability considerations need to be met (as in a CFL number), other than the desire to sufficiently sample and advance the unsteady problem in time and space. As just stated, the motion of the vortices is determined through a standard predictor-corrector numerical scheme, which takes the following form,

$$Z_{pred} = Z(t_n) + \Delta t\, W\big(Z(t_n)\big) \quad ; \quad Z_{corr}(t_{n+1}) = Z(t_n) + \frac{\Delta t}{2}\big[W\big(Z(t_n)\big) + W\big(Z_{pred}\big)\big] \qquad (2.32)$$

for discretized time, t_n, and time steps, Δt.

Figure 2.7 provides a visualization of the shed point vortices in both the circle and foil planes. Given the selected sinusoidal disturbance motions, the vortices predominantly travel along the chordline-extended, however, for distributions with strong and closely spaced vortices, they begin to interact and form counter-rotating vortex structures. Figure 2.8 provides another visualization of this behavior, where it can additionally be inferred that the mean velocity deficit as a result of the finite foil thickness yields a slightly slower convection of the wake.

A final comment is offered on the convection of the shed vortices. As can be seen earlier, the implemented vortices are not de-singularized with a viscous approximation (ex. as a Rankine vortex). This can conceivably result in a numerical singularity if while evaluating the flow field, two vortices are ever to collocate the same space (or be close enough). However, the present results do not exhibit any characteristics or numerical aberrations to this effect. A mitigating factor for this is believed to be the relatively fine temporal sampling (and therefore spatial sampling) for the high reduced frequency conditions at which the vortex clustering is seen to occur. This provides closely spaced or approaching vortices numerous time steps with which to interact and graze, in order to not induce unrealistic velocities.

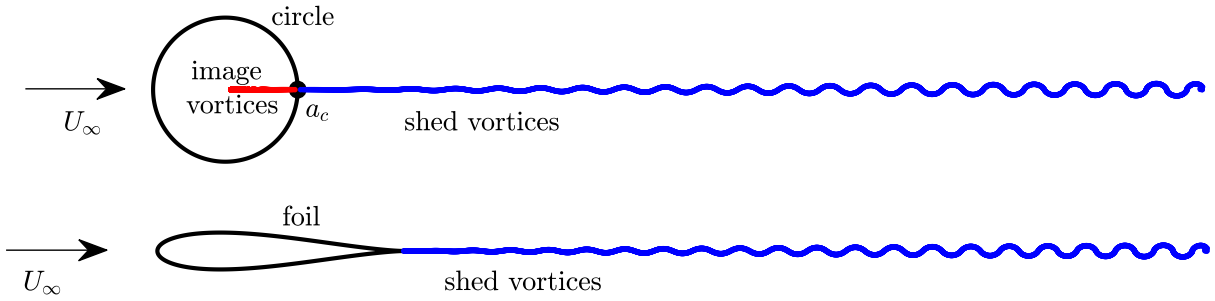

Figure 2.7. Visualization of the evolution of the shed point vortices in the circle and foil planes

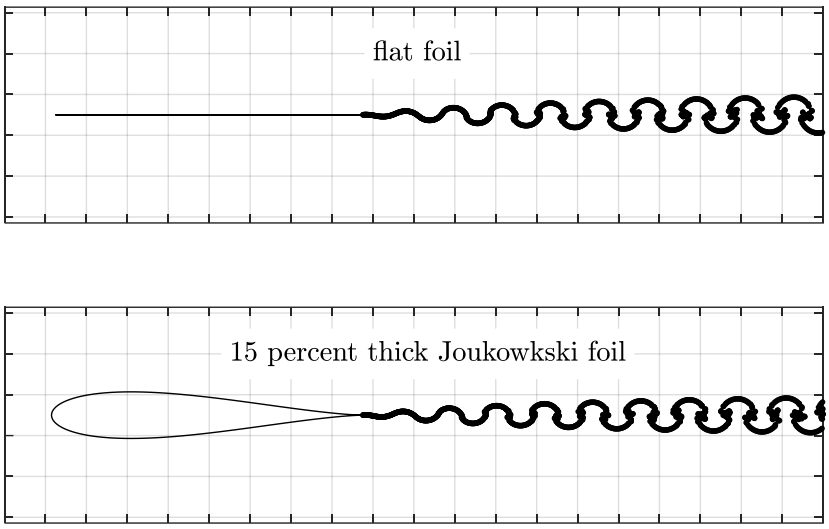

Figure 2.8. Example visualization of the shed point vortices for the flat and 15% Joukowski foils

The UPF calculations are a blended approach where explicit potential flow expressions are combined for specified unsteady flow conditions, and the necessary shed vorticity is deterministically tracked. Figure 2.9 provides a simple flow chart of this approach, which has been discussed throughout this chapter. As illustrated, the only portion of the calculations that require time marching involve the shed point vortices. Implementing the induced motion of the vortices, the application of the Kutta condition, and then sampling the velocity and flow potential fields at any desired locations (predominantly along the circle surface) by populating the full potential flow expressions are the distinct steps which require time stepping.

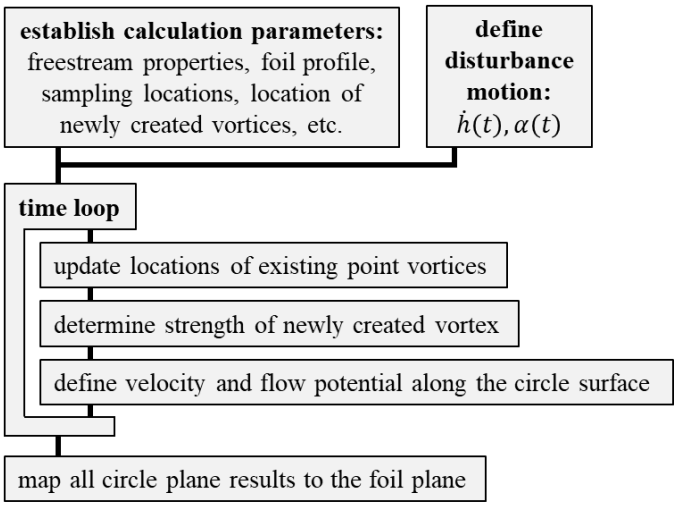

Figure 2.9. Consolidated flow chart of the UPF calculation approach

2.6 Determination of Pressures, Forces, and Moments

As discussed in the preceding sections, the mixed numerical and analytical Unsteady Potential Flow calculation approach provides the unsteady velocity and flow potential fields, sampled at any desired locations, for foils undergoing arbitrary, small-scale motion in the framework of potential flow. While these unsteady fields and vorticity wakes, as examples, are useful and worthwhile to analyze, it is the leveraging of the Unsteady Bernoulli equation which provides for the determination of the unsteady pressures on the foil surface and the subsequent unsteady force and pitching moment responses. This expression is,

$$\nabla\left(\frac{P}{\rho}+\frac{d\phi}{dt}+\frac{W^2}{2}+g\tilde{Z}\right)=0 \quad \rightarrow \quad \frac{P}{\rho}+\frac{d\phi}{dt}+\frac{W^2}{2}+g\tilde{Z}=Constant \tag{2.33}$$

where the complex flow potential expressed in the foil plane is defined as, $F=\phi+i\psi$. The unsteady pressure due to the change in the relative height of the foil, $\tilde{Z}$, is assumed negligible. With the complex velocity and flow potential explicitly known as a function of space and time in the foil plane (and equally in the circle, if desired), the unsteady pressure is determined throughout the flow field and along the foil surface as,

$$P(Z,t)=-\rho\left(\frac{W(Z,t)W^*(Z,t)}{2}+\frac{d\phi(Z,t)}{dt}\right)+Constant \tag{2.34}$$

where the pressure constant is taken to be zero throughout these efforts; this would cancel regardless, when assessing unsteady results. The [ ]* denotes the complex conjugate of the complex velocity.

The unsteady pressure and subsequent differential pressure acting across the foil is defined as,

$$\Delta P(Z,t)=P(Z_L,t)-P(Z_U,t) \tag{2.35}$$

where Z_L and Z_U represent the lower and upper sides, as pressure and suction sides are ill-defined for symmetric foils. Given the distributed pressures across the foil, the orthogonal forces and in-plane pitching moment are determined by integration along the foil surface. Within the UPF results, this integration is performed discretely and the standard practice for these results are based on evaluation at 801 evenly

distributed points around the circle circumference in the circle plane. This uniform distribution in the circle plane results in a non-uniform distribution in the foil plane with points being clustered more densely in the regions of the foil leading and trailing edges (this is discussed and illustrated in Section 2.8).

As illustrated by Figure 2.10, knowledge of the unsteady pressure distribution around the foil allows for the subsequent determination of the unsteady lift, streamwise force, and pitching moment responses. For either of the force directions, this is defined generically as,

$$F_n(Z,t) = \int_{foil} P(Z,t)\hat{n}(Z) \cdot \hat{e}\, dZ \tag{2.36}$$

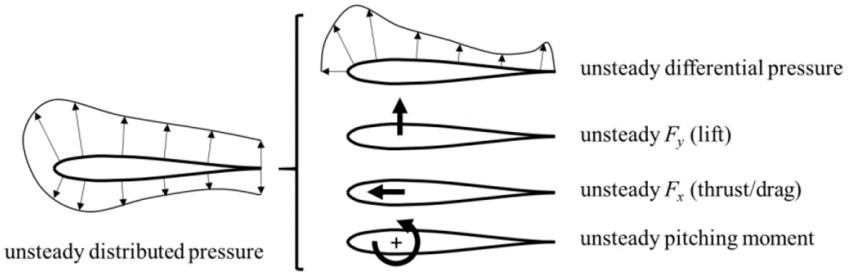

Figure 2.10. Generalized illustration of foil responses

In determining these responses, the orientation of the normal direction of the foil surfaces is necessary in order to project the subsequent pressure distribution. As a result of the implemented approach and foil shapes being considered, this information is always known. Figure 2.11 conveys this definition, and it is noted that most of the handling of the integration of pressure distributions, both numerically and analytically, is discussed within the Appendices.

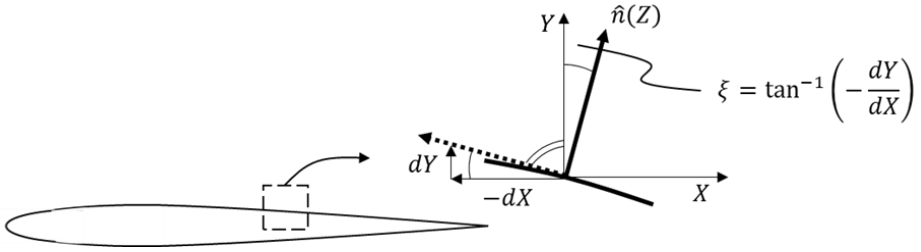

Figure 2.11. Illustration of the outward normal projection along the foil surface

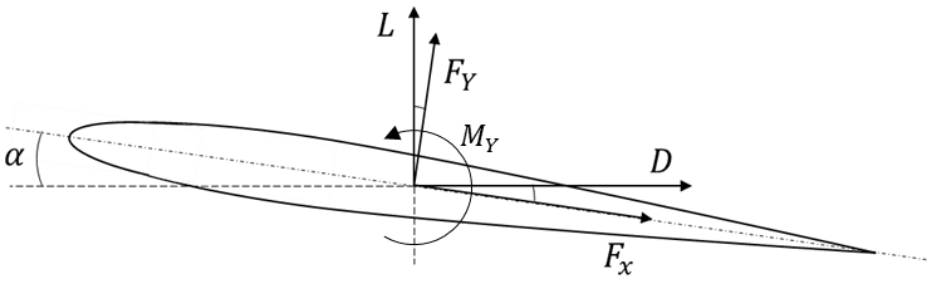

Figure 2.12. Illustration of the force and moment orientations

Within this work, the force and pitching moment definitions utilize standard orientations; these are illustrated in Figure 2.12. The pressure distributions are integrated to achieve the chordwise and chord-normal forces, F_X and F_Y. Subsequently, even for the small disturbance motion being considered presently, the unsteady lift and drag forces are determined by the projection of these forces into the fixed frame. The pitching moment is also accordingly determined by integration of the pressures with the corresponding moment arms. It is recognized that M_Y should more appropriately be labeled M_Z, however the current notation is utilized for consistency with the Theodorsen model; it is hoped that the intent of the current definition is clear from the context.

Given the explicit definitions of the velocity and flow potential terms, a distinctive and interesting analysis is available for the unsteady results. The individual contributions to the unsteady pressures can be defined for what are denoted as the source terms, which are the freestream, doublet, and rotational velocity contributions, and the wake terms, these being the shed wake and image vortices, by a decomposition in the following way,

$$P = -\rho\left(\frac{(W_S + W_W)(W_S + W_W)^*}{2} + \frac{\partial(\phi_S + \phi_W)}{\partial t}\right) \tag{2.37}$$

where the subscripts S and W are used for source and wake, respectively. This expression is expanded to,

$$P = -\rho\left(\frac{W_S W_S{}^*}{2} + Re(W_S W_W{}^*) + \frac{W_W W_W{}^*}{2} + \frac{\partial \phi_S}{\partial t} + \frac{\partial \phi_W}{\partial t}\right) \tag{2.38}$$

where $Re(\quad)$ denotes the real component of the specified argument.

The individual pressure contributions of the five terms in the parenthesis above are denoted by subscripts 1 through 5 and are defined in the following way,

$$P_1 = \frac{-\rho W_S {W_S}^*}{2} \; ; \; P_2 = -\rho Re(W_S {W_W}^*) \; ; \; P_3 = \frac{-\rho W_W {W_W}^*}{2} \; ; \; P_4 = -\rho \frac{\partial \phi_S}{\partial t} \; ; \; P_5 = -\rho \frac{\partial \phi_W}{\partial t} \quad (2.39)$$

such that each contribution can be assessed individually. Further, each of these contributions to the unsteady foil responses can be individually integrated $\left(\text{ex. } C_{L,1}\,, C_{L,2}\,, \ldots\right)$ to assess which terms contribute to or control the overall responses. This is similar, but not identical, to how prior works (and Theodorsen originally) have delineated between non-circulatory and circulatory contributions. While this decomposition originates with being on pressure, the decomposed foil responses are also determined where the following meaning is attributed to each of the five terms: contributions of the unsteady 1) source velocity, 2) source-wake velocity interaction, 3) wake velocity, 4) source flow potential, and 5) wake flow potential. A major utility of this decomposition is that if responses are determined to be controlled by terms that are only defined by source contributions, then they can be populated without any consideration for the contributions of the wake of shed vorticity (by definition). Conversely, it is also possible to identify responses that are dominated by wake contributions, which is also a useful observation.

Lastly, during the development and utilization of the UPF calculations, a standard Reynolds decomposition of the velocity is performed to achieve a first order approximation of the unsteady pressures by neglecting the product of the unsteady terms. These results are subsequently compared to those for when this approximation is not made. This is defined as,

$$P = -\rho\left(\frac{(\bar{W} + W')(\bar{W} + W')^*}{2} + \frac{\partial \phi}{\partial t}\right) \; ; \; P_{O(1)} = -\rho\left(\frac{\bar{W}\bar{W}^* + 2Re(\bar{W}W'^*) + \cancel{W'W'^*}}{2} + \frac{\partial \phi}{\partial t}\right) \quad (2.40)$$

This assessment is noteworthy as the Theodorsen model implements this same approximation on the pressures in order to achieve its direct expressions. Though not explored in this document, it was found during development and utilization of UPF calculations, and is shown briefly in prior work, Catlett (2018), that the contributions from the product of unsteady terms were in fact negligible.

2.7 Application of the Analytical Theodorsen Model

A central motivation for this work is to interrogate the analytic aeroelasticity model of Theodorsen in terms of how and in what ways unsteady foil responses vary for when the underlying model assumptions are not imposed. The Theodorsen model was developed in an unsteady potential flow framework for the flow about a circle which is then conformally mapped to an infinitely thin flat plate; which is often termed the Joukowski mapping. The major assumptions of 1) the foil being modeled as an infinitely thin flat plate, 2) undergoing harmonic heaving and pitching disturbance motion, 3) with a shed wake defined by a planar vorticity sheet moving with the freestream, allows for analytic expressions for unsteady lift, pitching moment, and differential pressure to be achieved. This is a two-dimensional model and correspondingly these terms are all per unit span. Directly following the development of Bisplinghoff et al., section 5-6, these expressions for the unsteady lift and pitching moment from the Theodorsen model are,

$$L = \pi\rho b^2\left[\ddot{h} + U_\infty\dot{\alpha} - ba\ddot{\alpha}\right] + 2\pi\rho U_\infty bC(k)\left[\dot{h} + U_\infty\alpha + b\left(\frac{1}{2} - a\right)\dot{\alpha}\right] \tag{2.41}$$

$$M_y = \pi\rho b^2\left[ba\ddot{h} - U_\infty b\left(\frac{1}{2} - a\right)\dot{\alpha} - b^2\left(\frac{1}{8} + a^2\right)\ddot{\alpha}\right] \ldots$$

$$+ 2\pi\rho U_\infty b^2\left(a + \frac{1}{2}\right)C(k)\left[\dot{h} + U_\infty\alpha + b\left(\frac{1}{2} - a\right)\dot{\alpha}\right] \tag{2.42}$$

where $h, \dot{h},$ and $\ddot{h}$ are the position, velocity, and acceleration due to heaving motion, $\alpha, \dot{\alpha},$ and $\ddot{\alpha}$ are the same for pitching motion (expressed in radians), a is the center of pitch rotation for the foil, b is the half chord length, U_∞ is the mean freestream velocity, $C(k)$ is the frequency-dependent Theodorsen function, and k is the reduced frequency defined as, $k = \omega b/U_\infty$. The Theodorsen function is a frequency-dependent, complex-valued expression defined as a combination of Hankel functions, which prescribe the combined effect of the shed vorticity on the foil responses (it is shown at the end of this subsection).

As written, these expressions can be implemented in either the time or frequency domains, however the Theodorsen function, $C(k)$, is defined in the frequency domain; therefore requiring convolution should the time domain be the desired frame for comparison. In the present work, a primary assessment of the

unsteady foil responses is the behavior defined in the frequency domain. Specifically, non-dimensional transfer functions between the input disturbance motion and the resulting output lift force, pitching moment, and differential pressures are principal metrics. Algebraic manipulation of the expressions above yield concise transfer functions, which are the topics of the subsequent subsections. In the present work, either heaving-only or pitching-only disturbances about the foil mid-chord are considered, which allows for some simplification as subsequent terms are set to zero. Further, the unsteady foil responses are expressed as standard aerodynamic coefficients. The following subsections provide these complex-valued transfer functions for the different motions.

In a manner directly analogous to the lift and pitching moment expressions above, the Theodorsen model also provides an expression for the differential pressure experienced across the foil chord as a result of the disturbance motion,

$$\begin{aligned}\Delta P = -2\rho \Bigg[& -\dot{h}U_\infty \cot(\theta) + \ddot{h}b \sin(\theta) - \alpha U_\infty^2 \cot(\theta) \dots \\ & + \dot{\alpha}U_\infty b \left(\sin(\theta) - \cot(\theta) \left[\frac{1}{2}\cos(\theta) - a \right] + \frac{1}{2}\sin(\theta) \right) \dots \\ & + \ddot{\alpha}b^2 \sin(\theta) \left[\frac{1}{2}\cos(\theta) - a \right] \Bigg] \dots \\ & - 2\rho U_\infty \left[\dot{h} + U_\infty \alpha + b\left(\frac{1}{2} - a \right)\dot{\alpha} \right] \left[\cot(\theta) + \left(\frac{1 - \cos(\theta)}{\sin(\theta)} \right) C(k) \right] \end{aligned} \tag{2.43}$$

where θ is the angle which defines the circle in the complex plane.

The Theodorsen function, $C(k)$, is plotted in Figure 2.13 in the complex plane and also for its magnitude and phase as a function of reduced frequency. Beyond visualizing this function, these views are shown in order to express the point that this function quickly approaches a constant value for reduced frequencies greater than one. Therefore, according to the Theodorsen model, the effect of the wake on the foil responses at high reduced frequency conditions becomes correspondingly constant.

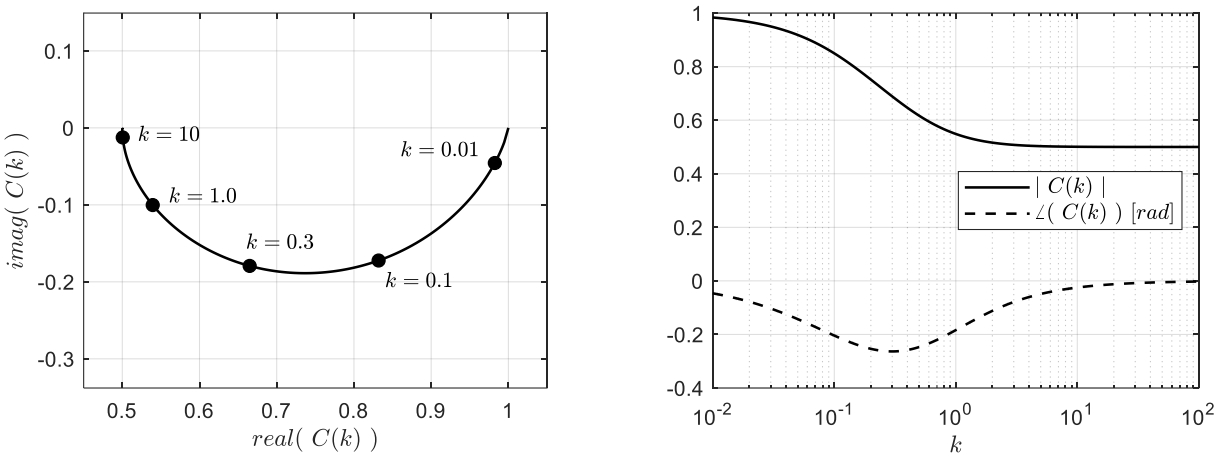

Figure 2.13. The Theodorsen function

A final note is offered on the utilization of transfer functions for the unsteady foil responses, these being either the Theodorsen-based expressions developed in the next subsections or calculated results. When transfer function results are presented it is in terms of Bode plots, clearly isolating the magnitude and phase properties of the unsteady results in the frequency domain. The magnitude portions of these plots are assessed and presented in terms of decibels, which for clarity, are defined as,

$$20\log_{10}\left(\frac{\tilde{y}}{\tilde{x}}\right) \tag{2.44}$$

where $\tilde{y}/\tilde{x}$ is a unit-less ratio of an output quantity (ex. $C_L(k)$) relative to a input quantity (ex. $\dot{h}(k)/U_\infty$). The units of this definition are decibels, and are often listed with the shorthand dB. Whenever necessary, the conversion to the frequency domain is facilitated by the use of a Fourier transform. Instead of presenting the frequency axes of these plots according to ω, these are presented according to the reduced frequency, $k = \omega b/U_\infty$. The phase angle of these complex-valued transfer functions,

$$\angle\left(\frac{\tilde{y}}{\tilde{x}}\right) \tag{2.45}$$

are presented in units of degrees, with positive phase relating to phase lead of the output signal. Lastly, when the unsteady foil responses are presented in the time domain, they are normalized by the corresponding magnitude of the disturbance motion.

2.7.1 Heave-only Motion

For heave-only disturbance motion, the unsteady pitch position, α, and its derivatives, $\dot{\alpha}$ and $\ddot{\alpha}$, are set to zero. From the Theodorsen lift expression this yields,

$$L = \pi\rho b^2[\ddot{h}] + 2\pi\rho U_\infty bC[\dot{h}] \tag{2.46}$$

As a non-dimensional transfer function is sought, the unsteady lift is expressed as an aerodynamic coefficient,

$$C_L = \frac{L}{0.5\rho U_\infty^2(2b)} = \frac{\pi b\ddot{h}}{U_\infty^2} + \frac{2\pi\dot{h}}{U_\infty}C \tag{2.47}$$

where the chord length is $2b$. The development of the Theodorsen model relies upon an assumption that the disturbance motion is harmonic, therefore, conversion between the motion and its derivatives is easily definable as, $\dot{h} = he^{i\omega t}, \ddot{h} = i\omega\dot{h}, etc$. Normalizing the disturbance heave velocity on the freestream yields,

$$C_L = i\pi\frac{\omega b}{U_\infty}\frac{\dot{h}}{U_\infty} + 2\pi\frac{\dot{h}}{U_\infty}C \tag{2.48}$$

Utilizing the reduced frequency definition, and expressing as a transfer function yields a very concise expression,

$$\frac{C_L U_\infty}{\dot{h}} = 2\pi C + i\pi k \tag{2.49}$$

Written in this way, the low frequency $(2\pi C)$ and high frequency $(i\pi k)$ characteristics are plainly evident.

Expressions for the unsteady pitching moment and differential pressures are developed similarly. The expression for the pitching moment due to heave-only motion is significantly simplified,

$$M_y = \pi\rho b^2[ba\ddot{h}] + 2\pi\rho U_\infty b^2\left(a + \frac{1}{2}\right)C[\dot{h}] \tag{2.50}$$

where the pitch axis for the pitching moment remains as a variable, denoted as a,

$$C_M = \frac{M_y}{0.5\rho U_\infty^2 (2b)^2} = i\frac{\pi}{2}\frac{\omega b}{U_\infty} a \frac{\dot{h}}{U_\infty} + \pi\left(a + \frac{1}{2}\right)\frac{\dot{h}}{U_\infty} C \tag{2.51}$$

$$\frac{C_M U_\infty}{\dot{h}} = \pi\left(a + \frac{1}{2}\right) C + i\frac{\pi}{2} ak \tag{2.52}$$

The corresponding expression for the differential pressure is,

$$\Delta P = -2\rho\left[-\dot{h} U_\infty \cot(\theta) + \ddot{h} b \sin(\theta)\right] - 2\rho U_\infty\left[\dot{h}\right]\left[\cot(\theta) + \left(\frac{1-\cos(\theta)}{\sin(\theta)}\right) C\right] \tag{2.53}$$

$$C_{\Delta P} = \frac{\Delta P}{0.5\rho U_\infty^2} = -4\left[-\frac{\dot{h}}{U_\infty}\cot(\theta) + \frac{\ddot{h}}{U_\infty^2} b \sin(\theta)\right] - 4\frac{\dot{h}}{U_\infty}\left[\cot(\theta) + \left(\frac{1-\cos(\theta)}{\sin(\theta)}\right) C\right] \tag{2.54}$$

$$C_{\Delta P} = -4i\frac{\omega b}{U_\infty}\frac{\dot{h}}{U_\infty}\sin(\theta) - 4\frac{\dot{h}}{U_\infty}\left(\frac{1-\cos(\theta)}{\sin(\theta)}\right) C \tag{2.55}$$

$$\frac{C_{\Delta P} U_\infty}{\dot{h}} = -4\left[\left(\frac{1-\cos(\theta)}{\sin(\theta)}\right) C + ik\sin(\theta)\right] \tag{2.56}$$

where again, the terms which control the low and high frequency character of this transfer function are clearly exposed.

As the Theodorsen model assumes a thin foil, there is no corresponding unsteady streamwise force expression as there is no projected area in that direction for this disturbance motion; $C_D U_\infty/\dot{h} \equiv 0$. However, foils of finite profile are implemented in the UPF calculations and subsequent assessment is made of the resulting unsteady streamwise force. For these results, a similarly defined transfer function is utilized,

$$\frac{C_D U_\infty}{\dot{h}} \ , \ where \ C_D = \frac{D}{0.5\rho U_\infty^2 (2b)} \tag{2.57}$$

Note that the term unsteady streamwise force is utilized instead of the more commonly used thrust and drag terminology. As the current focus is on the unsteady response of this force, which could be superimposed on a mean value, this makes the delineation between thrust and drag orientations less important. Throughout this work unsteady thrust and drag, and their subsequent aerodynamic coefficients, C_T and C_D, are often used interchangeably depending upon the configuration.

2.7.2 Pitch-only Motion

This subsection presents the development of similar transfer function expressions for the unsteady foil responses, though for pitch-only motion. The unsteady heave velocity, $\dot{h}$, and heave acceleration, $\ddot{h}$, are set to zero, however, the pitch axis, a, is left variable. From the Theodorsen lift expression this yields,

$$L = \pi\rho b^2[U_\infty\dot{\alpha} - ba\ddot{\alpha}] + 2\pi\rho U_\infty bC\left[U_\infty\alpha + b\left(\frac{1}{2}-a\right)\dot{\alpha}\right] \tag{2.58}$$

where harmonic pitch motion is assumed such that, $\dot{\alpha} = i\omega\alpha \quad , \quad \ddot{\alpha} = -\omega^2\alpha$,

$$C_L = \frac{L}{0.5\rho U_\infty^2(2b)} = \pi\left[i\frac{\omega b}{U_\infty}\alpha + \frac{\omega^2 b^2}{U_\infty^2}a\alpha\right] + 2\pi C\left[\alpha + i\frac{\omega b}{U_\infty}\left(\frac{1}{2}-a\right)\alpha\right] \tag{2.59}$$

$$\frac{C_L}{\alpha} = \pi[ik + k^2 a] + 2\pi C\left[1 + ik\left(\frac{1}{2}-a\right)\right] \tag{2.60}$$

$$\frac{C_L}{\alpha} = 2\pi C + i\pi\left[1 + 2C\left(\frac{1}{2}-a\right)\right]k + \pi a k^2 \tag{2.61}$$

For this response, there is low, mid, and high frequency contributions (i.e. k^0, k^1, k^2 dependence) which exhibits variable character based on the location of the pitch axis.

The subsequent pitching moment expression is,

$$M_y = \pi\rho b^2\left[-U_\infty b\left(\frac{1}{2}-a\right)\dot{\alpha} - b^2\left(\frac{1}{8}+a^2\right)\ddot{\alpha}\right] + 2\pi\rho U_\infty b^2\left(a+\frac{1}{2}\right)C\left[U_\infty\alpha + b\left(\frac{1}{2}-a\right)\dot{\alpha}\right] \tag{2.61}$$

$$C_M = \frac{M_y}{0.5\rho U_\infty^2(2b)^2} = \cdots$$

$$\frac{\pi}{2}\left[-i\frac{\omega b}{U_\infty}\left(\frac{1}{2}-a\right)\alpha + \frac{\omega^2 b^2}{U_\infty^2}\left(\frac{1}{8}+a^2\right)\alpha\right] + \pi\left(a+\frac{1}{2}\right)C\left[\alpha + i\frac{\omega b}{U_\infty}\left(\frac{1}{2}-a\right)\alpha\right] \tag{2.62}$$

$$\frac{C_M}{\alpha} = \frac{\pi}{2}\left[-ik\left(\frac{1}{2}-a\right) + k^2\left(\frac{1}{8}+a^2\right)\right] + \pi\left(a+\frac{1}{2}\right)C\left[1 + ik\left(\frac{1}{2}-a\right)\right] \tag{2.63}$$

$$\frac{C_M}{\alpha} = \pi\left(a+\frac{1}{2}\right)C + i\pi\left[\left(\frac{1}{4}-a^2\right)C - \left(\frac{1}{4}-\frac{a}{2}\right)\right]k + \frac{\pi}{2}\left(\frac{1}{8}+a^2\right)k^2 \tag{2.64}$$

Again, this expression takes a very similar form to the prior unsteady response expressions in terms of the distinct contributions to the unsteady response.

The associated differential pressure response is found to be,

$$\Delta P = -2\rho\left[-\alpha U_\infty^2\cot(\theta) + \dot{\alpha}U_\infty b\left(\sin(\theta) - \cot(\theta)\left[\frac{1}{2}\cos(\theta) - a\right] + \frac{1}{2}\sin(\theta)\right)\ldots\right.$$
$$\left. + \ddot{\alpha}b^2\sin(\theta)\left[\frac{1}{2}\cos(\theta) - a\right]\right]\ldots$$
$$- 2\rho U_\infty\left[U_\infty\alpha + b\left(\frac{1}{2} - a\right)\dot{\alpha}\right]\left[\cot(\theta) + \left(\frac{1-\cos(\theta)}{\sin(\theta)}\right)C\right] \quad (2.65)$$

$$C_{\Delta P} = \frac{\Delta P}{0.5\rho U_\infty^2} = -4\left[-\alpha\,cot(\theta) + i\alpha\frac{\omega b}{U_\infty}\left(\frac{3}{2}sin(\theta) - cot(\theta)\left[\frac{1}{2}cos(\theta) - a\right]\right)\ldots\right.$$
$$\left. - \alpha\frac{\omega^2 b^2}{U_\infty^2}sin(\theta)\left[\frac{1}{2}cos(\theta) - a\right]\right]\ldots$$
$$- 4\left[\alpha + i\alpha\frac{\omega b}{U_\infty}\left(\frac{1}{2} - a\right)\right]\left[cot(\theta) + \left(\frac{1-cos(\theta)}{sin(\theta)}\right)C\right] \quad (2.66)$$

$$\frac{C_{\Delta P}}{\alpha} = -4\left[-cot(\theta) + ik\left(\frac{3}{2}sin(\theta) - cot(\theta)\left[\frac{1}{2}cos(\theta) - a\right]\right) - k^2\,sin(\theta)\left[\frac{1}{2}cos(\theta) - a\right]\right]\ldots$$
$$- 4\left[1 + ik\left(\frac{1}{2} - a\right)\right]\left[cot(\theta) + \left(\frac{1-cos(\theta)}{sin(\theta)}\right)C\right] \quad (2.67)$$

$$\frac{C_{\Delta P}}{\alpha} = -4\left[\left(\frac{1-cos(\theta)}{sin(\theta)}\right)C + i\left(\frac{3}{2}sin(\theta) - cot(\theta)\left[\frac{1}{2}cos(\theta) - \frac{1}{2}\right] + \left(\frac{1}{2} - a\right)\left(\frac{1-cos(\theta)}{sin(\theta)}\right)C\right)k\ldots\right.$$
$$\left. - sin(\theta)\left(\frac{1}{2}cos(\theta) - a\right)k^2\right] \quad (2.68)$$

While this is a more involved expression, it still maintains the same form of the prior expressions, with distinct contributions at powers of the reduced frequency, k. Lastly, similar to the heave disturbance motion, the Theodorsen model does not provide a predictive expression for the unsteady streamwise force. These are available in the UPF calculated results however, and are assessed as C_D/α.

2.8 UPF Calculation Conditions

The UPF calculation approach has been implemented for different disturbance motion conditions and for various finite thickness foil profiles. This subsection provides the corresponding description of these conditions. In all UPF cases the nominal foil chord is either 0.015 or 0.15 meters, and the mean freestream velocity is variable. Correspondingly, the circle trailing edge location, a_c, was set to a value of either 0.0375 or 0.375, respectively. As it was not varied between foil thickness cases, there is a slight increase in the chord for the finite foil cases as a result of the conformal mapping.

The pressure on the circle surface, and therefore also the foil surface, is sampled at 801 evenly distributed points around the circle circumference. Figure 2.14, Figure 2.15, and Figure 2.16 provide visualizations of this in both the circle and foil planes for the 15% thick Joukowski foil profile configuration. Figure 2.14 shows both planes where the calculation nodes have been down-sampled by a factor of 10. As is well established, the fixed spacing of the calculation node distribution along the circle yields a distribution in the foil plane which preferentially clusters points in the regions of the foil leading and trailing edges. This is a convenient characteristic as the spatial variation of the unsteady pressures is often highest at these locations.

Figure 2.15 provides a view of the distribution within the circle plane for the 801 calculation nodes. Simply for clarity, a zoomed view along the circle surface is also offered. Figure 2.16 provides similar views of the calculation nodes within the foil plane. Zoomed views at the foil leading edge, trailing edge, and a portion along the foil chord are provided. A note is reiterated on these distributions; these are the points at which the potential flow solution is sampled, and is not a mesh or grid, in the sense of most numerical work. Because of the nature of the UPF framework, the flow field need only be sampled in space and time once all contributions to the flow field expressions are populated. Convergence studies on the effect of sampling density along the foil profile were performed during early stages of the development of the UPF calculations. Implementation of 801 points yielded consistent results relative to coarser and finer distributions, and was deemed very acceptable (results of these studies are not presented).

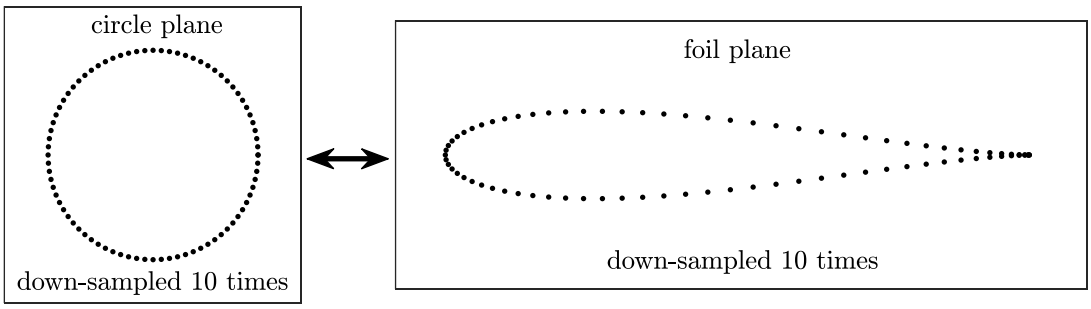

Figure 2.14. Example of the distribution of the calculation nodes in the circle and foil planes

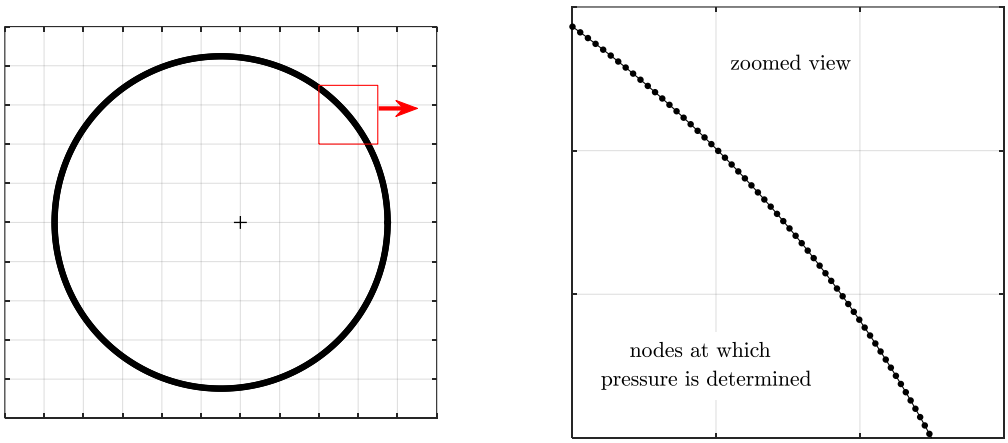

Figure 2.15. Example of the calculation nodes in the circle plane

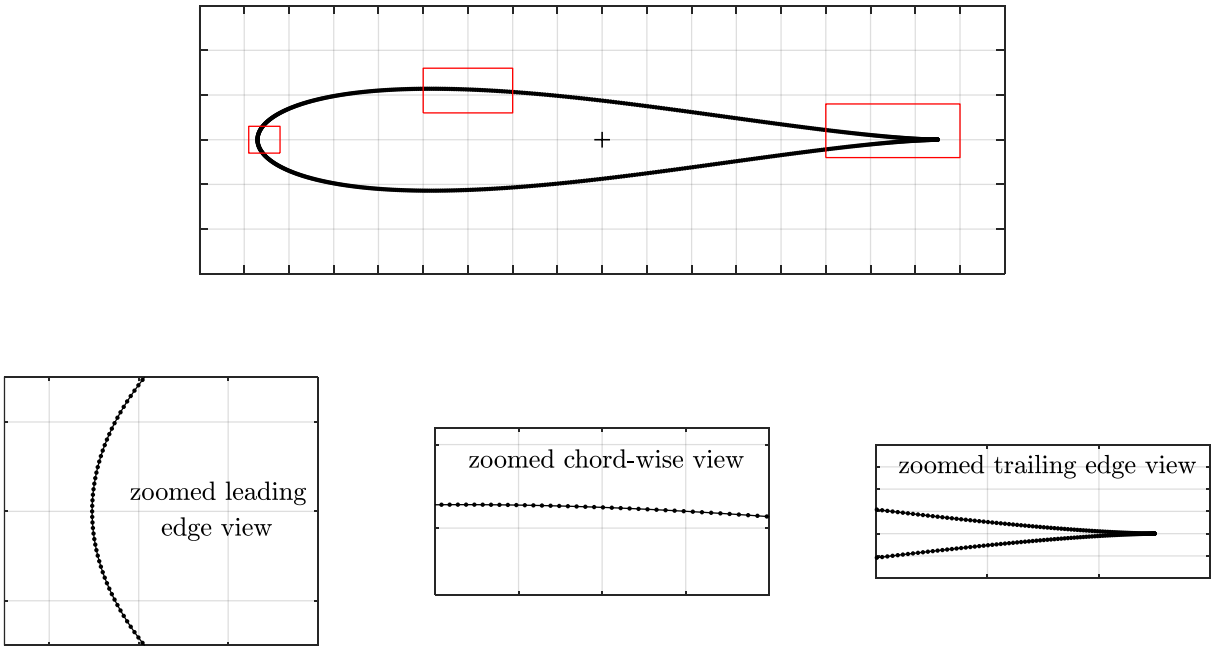

Figure 2.16. Example of the calculation nodes in the foil plane

A range of heaving disturbance conditions, pitching disturbance conditions, and foil thicknesses are examined in this work. The amplitudes of the variable sinusoidal disturbance motions were such that the maximum instantaneous angle of attack was either $0.01, 0.1,$ or 1.0 degrees. For the pitching disturbances, this is implemented directly as an amplitude on the sinusoidal distribution of pitch position, α. For the heaving disturbances, this was implemented by setting the necessary amplitude of the heaving velocity, $\dot{h}$, based on the freestream velocity. This yields varying heaving amplitudes for each reduced frequency, however, a common maximum effective angle of attack between calculations. These variable disturbance amplitude conditions were implemented only for the thin foil conditions. Calculations for the four separate Joukowski foils (0, 5, 10, and 15% thickness-to-chord ratios) were all performed for an unsteady angle of attack amplitude of 0.1 degrees.

Other than the desire for the calculations to be representative of high Reynolds number, incompressible flow about rigidly vibrating foils, the selection of the calculation parameters was arbitrary. Further, the calculation parameters were selected such that a wide range of reduced frequencies could be investigated; $10^{-2} < k < 10^{2}$. Table 2.1 presents the pertinent parameters for the UPF calculations that were specifically implemented for the varying conditions. For reference, assuming a fluid medium of air within the UPF calculations at $k = 2.0$ yields $Re_c = 9.62 * 10^5$, though Reynolds number is an ill-defined, infinite quantity for potential flow. All of the UPF calculations were performed for a total of 0.5 seconds at a sampling rate of 6 kHz, unless otherwise specified. Convergence exercises were performed on the sampling frequency of the UPF calculations throughout development, and given the temporal frequencies of the disturbance motion, this selected sampling frequency was deemed acceptable.

Table 2.1. Summarized parameters for UPF calculations

k	0.02	0.06	0.20	0.60	2.0	6.0	19.8	59.4
c $[m]$	0.15	0.15	0.15	0.15	1.5	1.5	1.5	1.5
U_∞ $[m/s]$	100	33.33	100	33.33	100	33.33	10.0	3.33
dist. freq. $[Hz]$	4.0	4.0	42.0	42.0	42.0	42.0	42.0	42.0
sampling freq. $[kHz]$	6.0	6.0	6.0	6.0	6.0	6.0	6.0	6.0

2.9 Description of uRANS Calculations

The present calculated results focus almost exclusively on the UPF calculations, which were developed by the author specifically based on the motivations of this work. However, accompanying unsteady Reynods-Averaged Navier-Stokes (uRANS) calculations were also performed with a primary purpose of providing an independent check on the newly developed UPF results (in the present context). The generally large Reynolds numbers and small amplitude disturbance motions under consideration were also motivating factors for implementing and testing the uRANS calculations at these conditions. These uRANS calculations however, were not executed by the author and therefore are not extensively highlighted throughout the present document. The author has analyzed portions of the results from these calculations, which are presented in select sections as they provide important supplemental results and help to establish the veracity of the current work. The author maintains a strong gratitude towards Dr. Camli Badrya for her collaboration on this work.

As results from these uRANS calculations are presented, a brief but informative discussion on the methodology of these calculations is provided. The CFD solver used to compare and verify the UPF calculation approach was the in-house developed Transonic Unsteady Rotor Navier-Stokes 2D (TURNS2D) fluid dynamic solver (Srinivasan and Baeder (1992)). TURSN2D has been widely used for airfoil and rotor blade flow conditions at high Reynolds numbers with confidence. TURNS2D uses a dual volume formulation to solve for the Reynolds-Averaged Navier-Stokes (RANS) equations. The inviscid fluxes are computed using a third-order MUSCL (Monotonic Upwind Scheme for Conservation Laws) reconstruction scheme in conjunction with Roe's scheme which has a modified dissipation term in order to better handle the low Mach numbers being presently considered (Rieper (2011)). The viscous fluxes are evaluated using a second-order central difference. For unsteady problems, an Euler implicit formulation is used for time marching with dual-time stepping to ensure sub-iterative convergence. Matrix inversion is performed using a lower-upper symmetric line-Gauss Seidel (LU-SGS) approach.

In these TURNS2D simulations the Reynolds number is set to 10^6, such that the viscous effects are expected to be small compared to the inertial force, and the freestream Mach number was set to either 0.1 or 0.01. Prior experience shows that it is imperative that the solver not assume a fully laminar or fully turbulent flow over the foil. A key feature in TURNS2D is the inclusion of a laminar-turbulent transition model coupled with the Spalart-Allmaras turbulence model (Medida and Baeder (2011)), which improves the fidelity of the numerical solution by better predicting the physics of flow transition. This formulation keeps track of the intermittency in the flow, whose value varies between 0 and 1, indicating a fully laminar or fully turbulent flow, respectively.

A C-mesh was used around the foil with an outer boundary at 50 chord lengths away from the foil surface, as shown in Figure 2.17. The reference mesh contained 400 grid points in the surface-wrap direction, 78 grid points in the wall-normal direction, and 200 points in the wake cut along the downstream direction. Grid spacing within the boundary layer in the normal direction was 0.001% of the chord length.

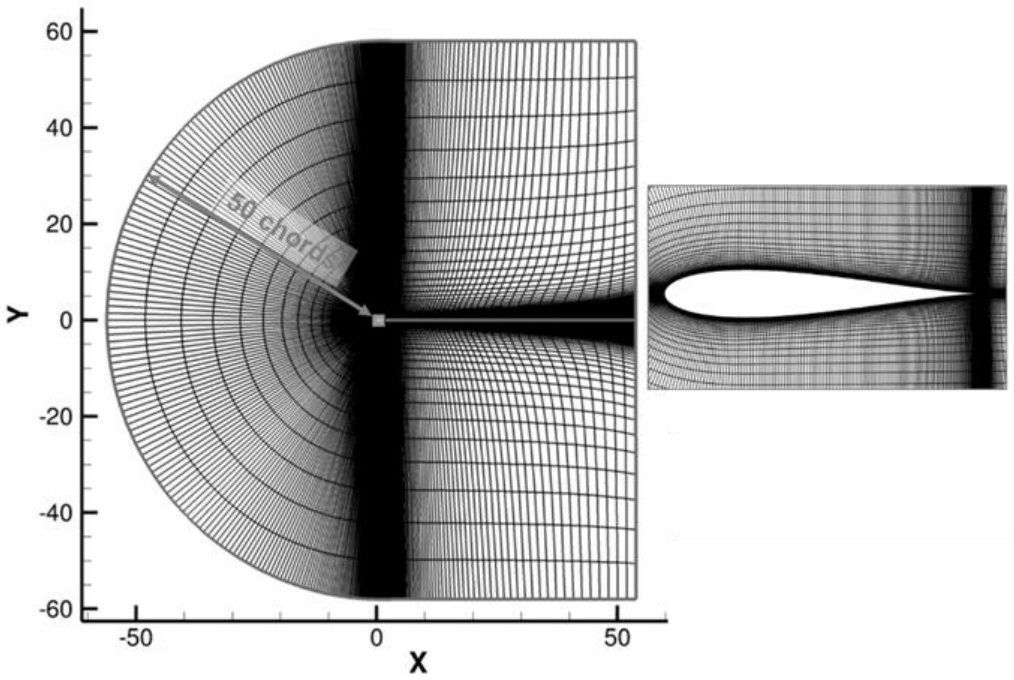

Figure 2.17. View of the C-mesh used for TURNS2D calculations

A concise evaluation of the sensitivity of the TURNS2D calculation results at a single reduced frequency for the thin foil condition was performed for the reference mesh density and time step size in

order to check that the calculated results were sufficiently independent of these selected parameters. Relative to the reference C-mesh shown above, calculations were also performed for a fine and coarse mesh, which corresponded to implementing 800 and 200 points in the surface-wrap direction, respectively. Additionally, time step sizes of half and twice the reference time step were implemented; the reference sampling frequency in this case being 28.8 kHz. The flow conditions for these sensitivity study calculations are pitching about the mid-chord with an amplitude of 0.1 degrees at a reduced frequency of 20.0 and freestream Mach number of 0.1. The results of this sensitivity study are presented in Figure 2.18 as partial time series of the unsteady lift coefficient.

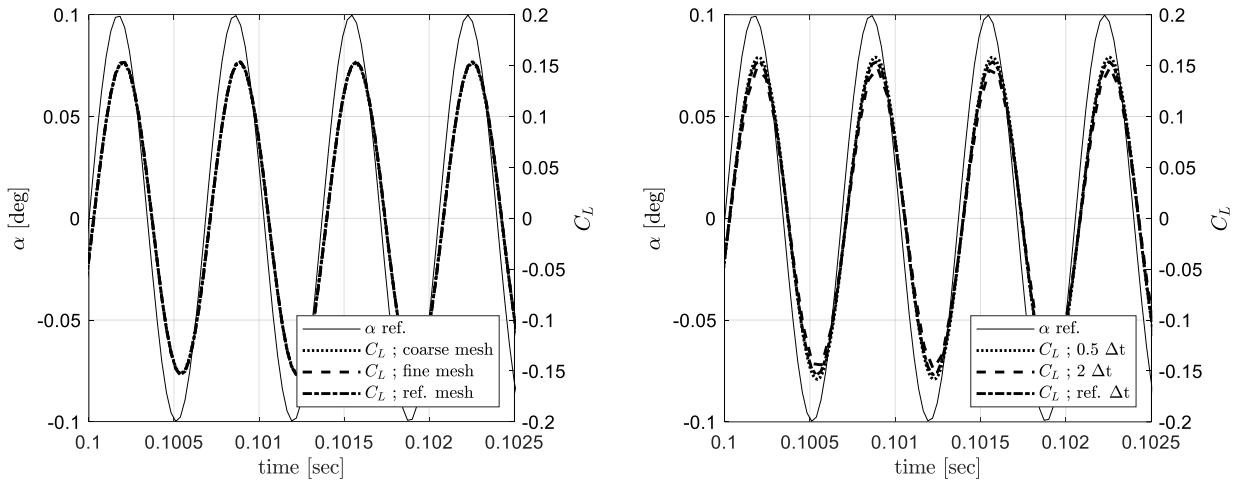

Figure 2.18. Lift coefficient time series from CFD sensitivity calculations; $k = 20.0$

It can be seen that varying the mesh density along the surface of the foil yields indiscernible differences in the unsteady response of the lift coefficient, and therefore the reference foil mesh was deemed acceptable. Varying the time step size yields minor shifts in the oscillation amplitude, but no perceptible shift in the phase of the unsteady lift response. The lower sampling rate results appear as an under-sampled sine wave, leading to jagged peaks at the extrema of the signal (note, these are not the same dimensional conditions as the UPF calculations). Given these results of the C_L response from this quick sensitivity study, the reference mesh and time step size were deemed acceptable. An identical assessment of the C_M response yields very similar results for the lack of sensitivity to mesh density and time step size.

Analysis of the specific amplitude and phase characteristics of these calculated results is left for the Results chapter, however, the phase of these high reduced frequency responses shown in Figure 2.18 is not that which is predicted by the Theodorsen model. This discussion is provided in Chapter 4. In terms of the motivation of performing a convergence study, it was deemed that these calculated results were sufficiently independent of the selected spatial and temporal discretizations.

For all of the TURNS2D calculations, the chord based Reynolds number was set to 10^6. Only pitching disturbances about the foil mid-chord were considered, and effectively all calculations were performed for a maximum angle of attack amplitude of 0.1 degrees ($k = 50.0$ and $|\alpha| = 0.01^o$ was also computed). The TURNS2D calculations were performed at the specified reduced frequencies for a variable number of periods of the disturbance motion and a variable sampling rate between the distinct calculations. The sampling rates for the TURNS2D calculations however, were greater than the fixed value of the UPF calculations, and were typically greater than 20 kHz. For the flat foil condition, the TURNS2D calculations implemented a 1% thickness-to-chord ratio Joukowski foil profile as an approximation to the infinitely thin foil profile, as meshing an increasingly thin body can become intractable. Table 2.2 presents the pertinent parameters for the TURNS2D calculations. It should be noted that not all UPF calculations have an accompanying TURNS2D calculation, and this is clarified in the following sections as needed.

Table 2.2. Summarized parameters for TURNS2D calculations

k	0.02	0.05	0.20	0.50	2.0	5.0	20.0	50.0
Re_c	10^6	10^6	10^6	10^6	10^6	10^6	10^6	10^6
M_∞	0.1	0.1	0.1	0.1	0.1	0.1	0.01	0.01

Some final commentary is offered towards the shedding of vorticity within both the UPF and TURNS calculations. As described earlier, it is the intention and interest of the present work that vorticity is only shed from the foil trailing edge. For the UPF calculations, this is specified explicitly; no accommodation is made for shedding from the leading edge. Within the TURNS2D calculation framework, leading edge vorticity shedding is possible; however, the disturbance conditions were not anticipated to nor

did they result in this behavior. One reference, amongst others, which offers summarizing discussion and linkage to further relevant references on this behavior is Platzer et al. (2008). They identify a threshold for leading edge vortex shedding as beginning approximately when conditions exceed $kh = 0.35$ for heaving motion (h in this instance being normalized on chord). While not identical to pitching motion, it is assumed that this is sufficiently relatable in terms of the induced angle of attack. This threshold corresponds to a maximum instantaneous angle of attack of approximately 19 degrees. As detailed above, all of the disturbance amplitudes for the pitching results are exceedingly below this limit. Additionally, the induced angles of attack due to angular velocity contributions, $\dot{\alpha}$, do not exceed this limit for all of the 0.01 and 0.1 degree conditions. This limit would be reached for $k = 50$ and $|\alpha| = 1.0^o$, however, a TURNS2D calculation was not performed for this condition.

3. Comparison of the Theodorsen Model to Selected Historical Data

Since its introduction, the Theodorsen model has been utilized in various manners for analysis of foils undergoing motion within a fluid stream. The focus of the present work is to concentrate on motion which is representative of vibration of a structure; for example, of a high aspect ratio, cantilevered wing or rotor blade. As the current focus is on vibration, often smaller amplitude disturbances and higher disturbance frequencies are the pertinent conditions relative to those typically available in the technical literature. Despite this, there is a substantial number of references and body of work reaching across decades for the effects of unsteady foil motion within a fluid stream. The references that are reviewed here in detail include: 1) both older and newer works, 2) works with results for either the foil responses or shed vorticity wake, and 3) which have fairly close association with the current focus.

The presentation of this subsequent analysis is intended to address the following two topics. First, to serve as a consolidated assessment of the Theodorsen model relative to various experimental and numerical results. The intention is to confirm where the Theodorsen is seen to be robust, where it may be lacking, where its assumptions would seem to be stretched, and what the impact may be. Second, it is the author's experience that within the numerous technical references that there are several manners in which results are presented and assessed, and that the focus of references can substantively vary. As such, a direct comparison to and assessment of the corresponding results in relation to the Theodorsen model is not always immediately apparent or available in a consistent manner. The subsequent analysis of this section presents these applicable results in a common format to that used throughout this work.

A final note on these comparisons is that when feasible, the nomenclature of the referenced works is utilized in the subsequent presentation and analysis of results in order to retain continuity to the references. This inevitably causes some discrepancies in variable definitions. It is hoped that this is clarified by the context and description of each configuration. Lastly, to serve as a quick summary, Table 3.1 provides a list of these references, along with an identification of the type of results and a very brief description of the key relevant results. Though they are not immediately pertinent to this section, the

references which are also utilized in the analysis of the unsteady streamwise force response in Section 4.7 are listed as well.

Table 3.1. Summary of detailed review references (*E*: experimental, *C*: computational)

	Reference	Results	Key Points *(relative to the present context)*
literature review	Silverstein and Joyner (1939)	*E*	partial unsteady C_L results for pitching motion
	Bratt (1945)	*E*	unsteady C_M for pitching motion for various flow conditions and foil profiles
	Halfman (1952)	*E*	unsteady C_L and C_M for heaving and pitching motions and various flow conditions
	Rainey (1957)	*E*	unsteady C_L and C_M for pitching motion and various mean α conditions
	Leishman (1993)	*E*	unsteady C_L for pitching motion
	Cordes et al. (2017)	*E*	unsteady $C_{\Delta P}$ for pitching motion and various mean and unsteady α conditions
	Satyanarayana and Davis (1978)	*E*	unsteady $C_{\Delta P}$ for pitching motion with data concentrated at the foil trailing edge
	Ohashi and Iskikawa (1972)	*E*	visualization of the shed wake at conditions of $k > 1$ which identifies roll-up of the vorticity in the wake
	Bratt (1953)	*E*	visualization of the shed wake at conditions of $k > 1$ which identifies roll-up of the vorticity in the wake
	Poling and Telionis (1986)	*E*	observations of the velocity field in the immediate region around the foil trailing edge
	Münch et al. (2010)	*E C*	unsteady foil responses which exhibit altered behavior for $k > 1$ and visualization of the flow field
	Liu et al. (1990)	*E*	observations of the velocity field in the immediate region around the foil trailing edge
	Basu and Hancock (1978)	*C*	unsteady C_L and C_M for pitching motion for high k
	Strangfeld et al. (2015)	*E C*	unsteady C_L for pitching motion
	Ashraf et al. (2011)	*C*	unsteady C_L for large amplitude heaving motion
streamwise force	Read et al. (2003)	*E*	time series of C_L and C_D for large amplitude disturbance motion
	Young and Lai (2004)	*E C*	mean and unsteady C_L and C_T for pitching motion, as well as flow field results
	Lu et al. (2013)	*C*	unsteady foil responses for pitching motion; includes non-sinusoidal motion
	Hammer et al. (2019)	*E C*	unsteady foil responses and flow field results for pitching motion; conditions also include a sheared inflow

3.1 Silverstein and Joyner

The work of Silverstein and Joyner (1939) is a NACA-era experimental wind tunnel effort which consists of the measurement of unsteady lift for an airfoil undergoing sinusoidal pitching motion. The results are provided by a mechanical balance which provide the phase difference between the unsteady lift and the unsteady angle of attack across a range of reduced frequencies for both zero and finite mean lift conditions. The exact foil profile is unspecified within the reference, however, the foil is listed as being symmetric, with 18 percent thickness, a chord length of 5.1875 inches, and a span of 36.75 inches. The axis of rotation for the pitching motion is listed as being about the quarter chord. The wind tunnel side walls served as the end plates for the airfoil in order to attempt to minimize tip effects of the foil, while the top and bottom walls of the wind tunnel (in the normal to chord direction) were removed. For reference, based on the varying freestream conditions listed, the chord-based Reynolds numbers are $Re_c = 0.6 - 2.9 * 10^5$.

Of particular relevance to the present work is the measured phase relationship between the unsteady pitching motion and unsteady lift as a function of reduced frequency, and the subsequent comparison to the Theodorsen model. Figure 3.1a is a directly copied version of this plot from the Silverstein and Joyner reference, while Figure 3.1b provides this same data after having been digitized and replotted. This data is then plotted in Figure 3.2 in the same manner as the results of the present work, namely having the abscissa be k and not $1/k$. Also present on Figure 3.2 is the subsequent phase difference predicted by the Theodorsen model. As the airfoil is oscillating about the quarter chord in this instance, the unsteady lift Theodorsen expression written as a complex transfer function is taken from Section 2.7, where $\dot{h} = \ddot{h} = 0$, $a = -0.5$,

$$\frac{C_L}{\alpha} = 2\pi C + i\pi[1 + 2C]k - \frac{\pi}{2}k^2 \tag{3.1}$$

The phase of this Theodorsen model expression is plotted in Figure 3.2 alongside the digitized data of Silverstein and Joyner where it can be seen that there is generally good agreement relative to the modeled phase distribution, though there is certainly non-negligible scatter within the measured data. It is acknowledged in the document of Silverstein and Joyner that the cause of the positive phase at reduced

frequencies of approximately 0.1 and less is not understood, and would be a topic of future exploration. It is of interest to reiterate that this dataset includes both a relatively thick airfoil and mean lift conditions, which if strictly applied, violate the assumptions of the Theodorsen model. This dataset is not comprehensive enough to make claims about either the effects, or lack of effects, on the unsteady airfoil responses due to foil thickness or mean lift, however they do begin to provide insight into these considerations.

a)

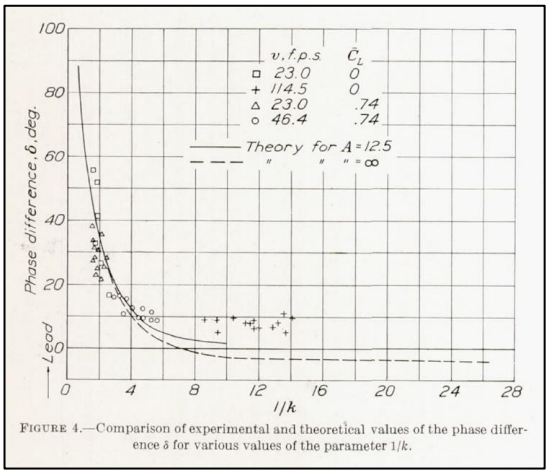

FIGURE 4.—Comparison of experimental and theoretical values of the phase difference δ for various values of the parameter $1/k$.

b)

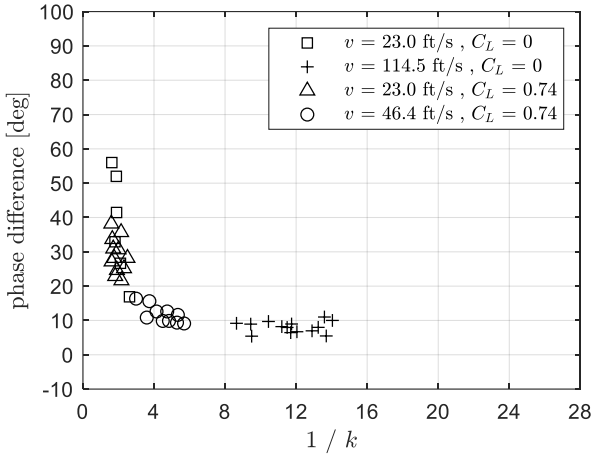

Figure 3.1. Phase difference between unsteady lift and angle of attack from Silverstein and Joyner
a) figure copied directly from source material, b) source data digitized and replotted

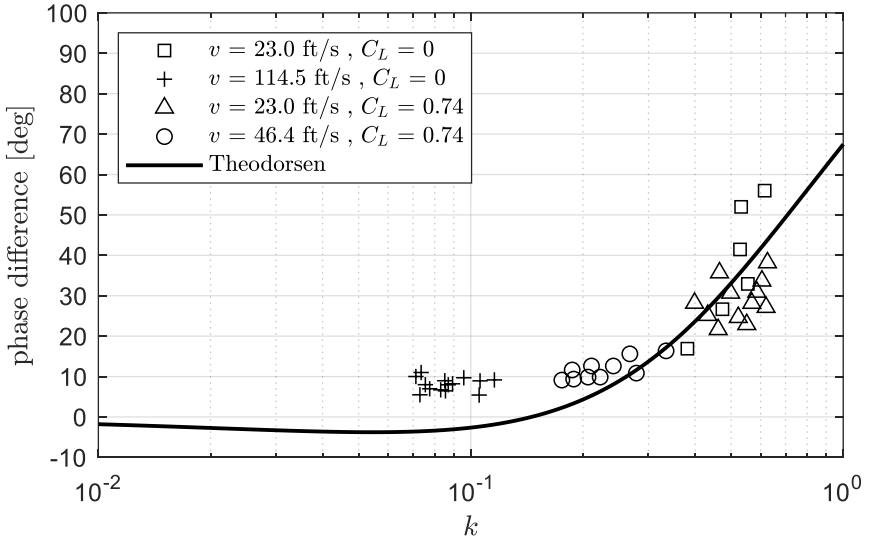

Figure 3.2. Phase difference between unsteady lift and angle of attack from Silverstein and Joyner

3.2 Bratt (1945)

The work of Bratt (1945) is an experimental wind tunnel effort that interrogates the unsteady pitching moment of a two dimensional airfoil as a result of pitching motion, where several operating characteristics were varied in order to identify any effects. In addition to reporting results for standard variations in reduced frequency and Reynolds number conditions, variable conditions are also explored for mean incidence of the airfoil, amplitude of the pitching motion, pitch axis location, airfoil profile, as well as aspect ratio for three-dimensional airfoil configurations. The various conditions will be described in the subsequent presentation and discussion of the results, however, in general the Reynolds number based on chord is between $Re_c = 1.4 - 2.8 * 10^5$, and the range of reduced frequencies is approximately $0.1 < k < 0.8$. The results in this reference are presented in numerous figures, however all of these results are fortunately tabulated for ease of use. Generally, the Theodorsen model is seen to provide reliable results for the measured data, though some differences are identified.

The transfer function expression for the unsteady pitching moment as a result of pitching motion about the airfoil mid-chord location is found by using the unsteady pitching moment Theodorsen expression written as a complex transfer function as taken from Section 2.7, where $\dot{h} = \ddot{h} = 0$, $a = 0.0$,

$$\frac{C_M}{\alpha} = \pi\left(\frac{1}{2}\right)C + i\pi\left[\left(\frac{1}{4}\right)C - \left(\frac{1}{4}\right)\right]k + \frac{\pi}{2}\left(\frac{1}{8}\right)k^2 \tag{3.2}$$

$$\frac{C_M}{\alpha} = \frac{\pi}{2}C + i\frac{\pi}{4}k[C-1] + \frac{\pi}{16}k^2 \tag{3.3}$$

The expression above pertains to the pitching moment transfer function as a result of pitching motion about the airfoil mid-chord, for which most of the data from this reference pertains. However, a portion of the results are for unsteady pitching moment measurements where the pitch axis is at one-third chord ($X/c = 1/3$). This yields a different pitching moment transfer function expression, where $a = -\frac{1}{3}$,

$$\frac{C_M}{\alpha} = \pi\left(-\frac{1}{3}+\frac{1}{2}\right)C + i\pi\left[\left(\frac{1}{4}-\frac{1}{9}\right)C - \left(\frac{1}{4}+\frac{1}{6}\right)\right]k + \frac{\pi}{2}\left(\frac{1}{8}+\frac{1}{9}\right)k^2 \tag{3.4}$$

$$\frac{C_M}{\alpha} = \frac{\pi}{6}C + i\pi\left[\frac{5}{36}C - \frac{5}{12}\right]k + \frac{17\pi}{144}k^2 \tag{3.5}$$

Both of these expressions are utilized where it should be clear from the context which expression applies. These have the same form, though the coefficients for each term are different. Also, while there are distinct contributions from the three terms of order k^0, k^1, k^2, it is mostly the first and second terms which control the Theodorsen model results as the reduced frequencies in this reference are always less than one.

The first assessment of these results comes from Tables 1 and 2 of the reference document, and are presented in Figure 3.3. These results are for a Joukowski airfoil profile of 15% thickness which is pitching about the 1/3 chord location. Different mean angles of attack are implemented of 0, 8, and 10 degrees, with oscillation amplitudes of $\pm$ 6 and 2 degrees, and the chord-based Reynolds numbers are also listed in the legend. The magnitude and phase of the pitching moment response are fairly well represented by the associated Theodorsen model expression over the lower range of reduced frequencies. At reduced frequencies greater than approximately 0.3, the magnitude of the measured pitching moment is seen to be appreciably lower than the modeled results, while the phase of the measured results compare well with the Theodorsen model. Unfortunately, it is not clear from the reference what the cause is for this deviation between measured and modeled results. Most of these conditions (all black symbols and the red triangles) correspond to when the airfoil nominally has fully attached flow, as determined by the mean pitching moment versus angle of attack relationship. This mean distribution is plotted within the reference document. Despite the somewhat good agreement between the model and measured results, there are still upwards of 6 decibels and 15 degrees of difference between the magnitude and phase of these responses, respectively.

The results which most notably deviate from the Theodorsen model correspond to a mean incidence of 10 degrees and oscillation amplitude of 6 degrees at a reduced frequency of approximately 0.08 (the red open circle). Over a significant portion of the pitch oscillation motion the airfoil is at an angle of attack which would imply transient separated flow. It is assumed that this is the cause of the significantly attenuated magnitude and altered phase of the pitching moment response, though it is not immediately clear

why only the lowest reduced frequency is affected while the response at the higher reduced frequencies are much closer to the other results. It is possible that this is an effect of dynamic stall, where the oscillation rate of the airfoil pitching motion prevents (or delays) the ability for the flow to separate. It is also possible that these elevated angles of attack induce vorticity to be shed at the leading edge of the airfoil, which would be a distinct departure from the Theodorsen framework and not a condition for which the model would be applicable. Unfortunately, this reference does not provide the means with which to test these speculations.

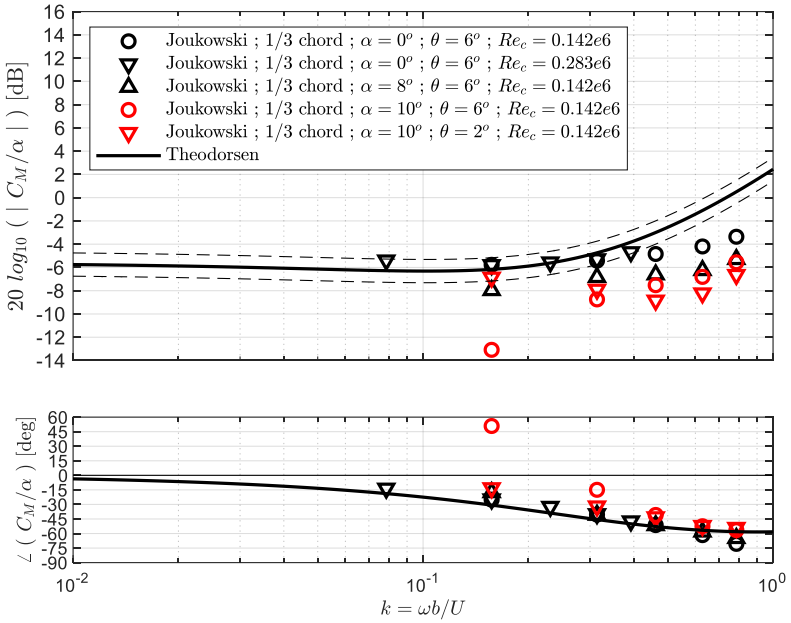

Figure 3.3. Comparison of unsteady pitching moment response from Bratt for pitching motion

The results for the same Joukowski airfoil pitching about is mid-chord are presented in Figure 3.4 in an identical manner as the previous figure. The magnitude of the pitching moment response across the range of lower reduced frequencies is significantly elevated relative to the conditions of the prior figure, as a result of the shifted pitch axis. Generally these results compare quite favorably to the Theodorsen model for both magnitude and phase of the unsteady pitching moment. The operating conditions appear such that there is an expectation that the flow is fully attached (for at least most of the cycle), and therefore is compatible with the predictive Theodorsen model. Also, there appears to be essentially no effect of doubling the Reynolds number in this instance of zero mean incidence angle.

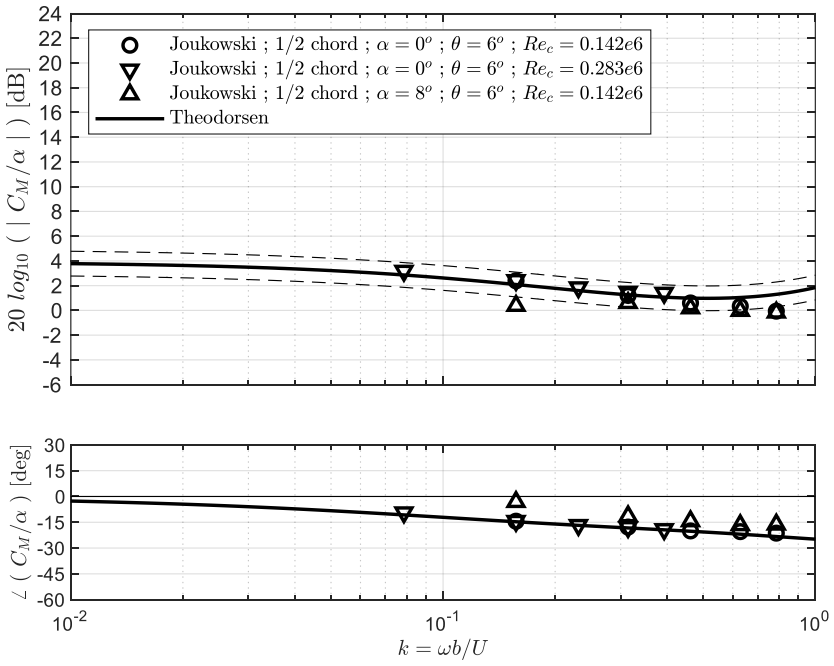

Figure 3.4. Comparison of unsteady pitching moment response from Bratt for pitching motion

One of the parametric changes made within this reference is that various airfoil profiles were tested. These profiles are shown and described within the reference document and not recreated here. Figure 3.5 provides the same type of pitching moment results for the EC1550 airfoil pitching about its mid-chord. This airfoil is a 15% thick, symmetric profile characterized by the maximum thickness being pushed further aft. Two plots are presented, which correspond to oscillation amplitudes of 6 and 2 degrees. Similar to the prior results, these measurements are also nominally well represented by the corresponding Theodorsen model. The exception to this statement is for operating conditions which include elevated angles of attack, such that it is assumed the airfoil is experiencing transient flow separation. Whether this is the cause or another phenomenon is occurring, the effect on the unsteady pitching moment response is for the magnitude to attenuate and the phase of the response to change significantly from lagging the pitching motion to leading. This behavior is seen to become less prominent for the smaller amplitude oscillations, which agrees with the understanding that the threshold for applying the Theodorsen model is to maintain well within the linear portion of the mean pitching moment distribution.

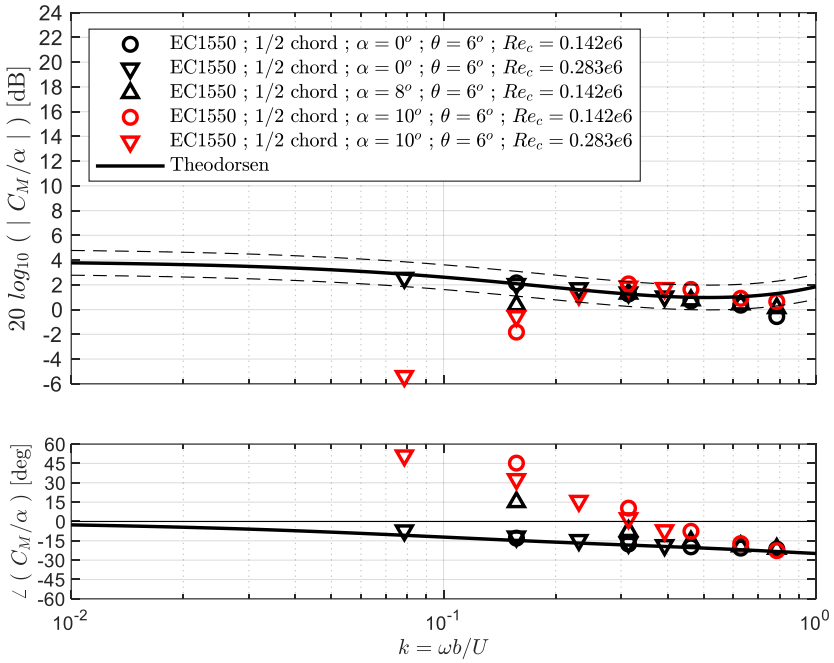

a)

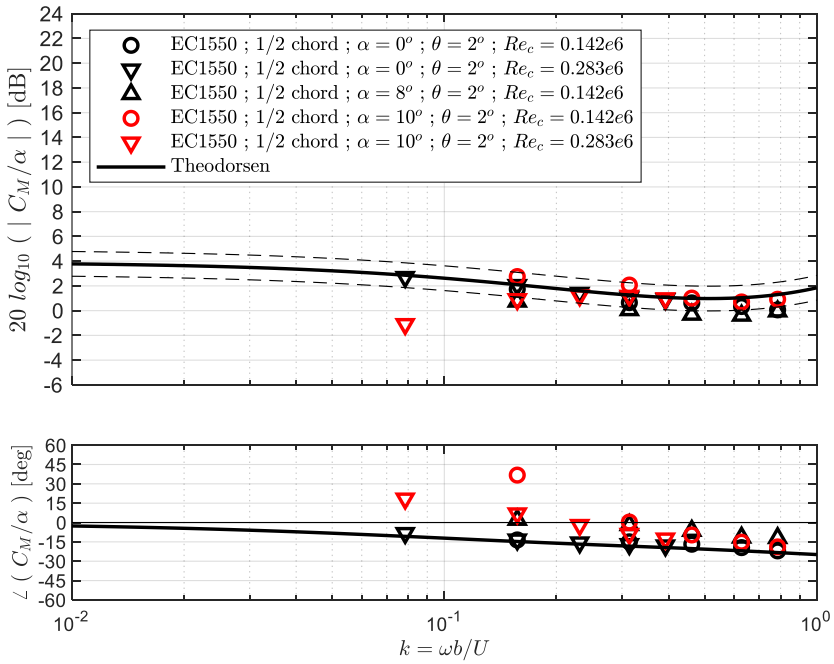

b)

Figure 3.5. Unsteady pitching moment response: a) 6^o oscillation amplitude, b) 2^o oscillation amplitude

Within this reference, results are presented for four separate airfoil profile configurations: Joukowski and EC1550 (previously mentioned), in addition to an elliptic profile and a profile termed Hollow-ground. This Hollow-ground profile is identical to the elliptic over the forward half of the profile,

but then tapers to a sharp trailing edge by a fourth order polynomial which is specified within the document. All of these airfoils have a 15% thickness-to-chord ratio. Unsteady pitching moment results for these profiles pitching about their respective mid-chords is presented is Figure 3.6 for mean incidence angles of both 0 and 8 degrees. Again, these measured results appear to be reasonably well represented by the Theodorsen model, though there are two notable deviations. First, the magnitude results for the elliptic airfoil at zero mean angle of attack is below the modeled levels by as much as 3 decibels. It is unclear specifically why the response at this mean incidence condition is attenuated and it is not for the higher incidence condition. It is speculated that some uncertainty likely stems from this profile having a significantly blunt (i.e. rounded) trailing edge, therefore complicating the manifestation of a Kutta condition. Second, at the lowest reduced frequency condition of this figure, the phase of the unsteady pitching moment responses for the high angle of attack conditions are prominently altered; in agreement with the previously presented results.

The final comparison of the measured data from this reference is presented in Figure 3.7, where unsteady pitching moment responses are presented for the Joukowski airfoil pitching about its mid-chord, but where the aspect ratio of the tested airfoils varies between infinite (i.e. two-dimensional) and a value of one. While this variation does not have a direct correlation to the present study, it is of significant practical interest, and the effect of aspect ratio is seen to be quite prominent. The data points are denoted (red and black) based on the two available Reynolds numbers of the reference.

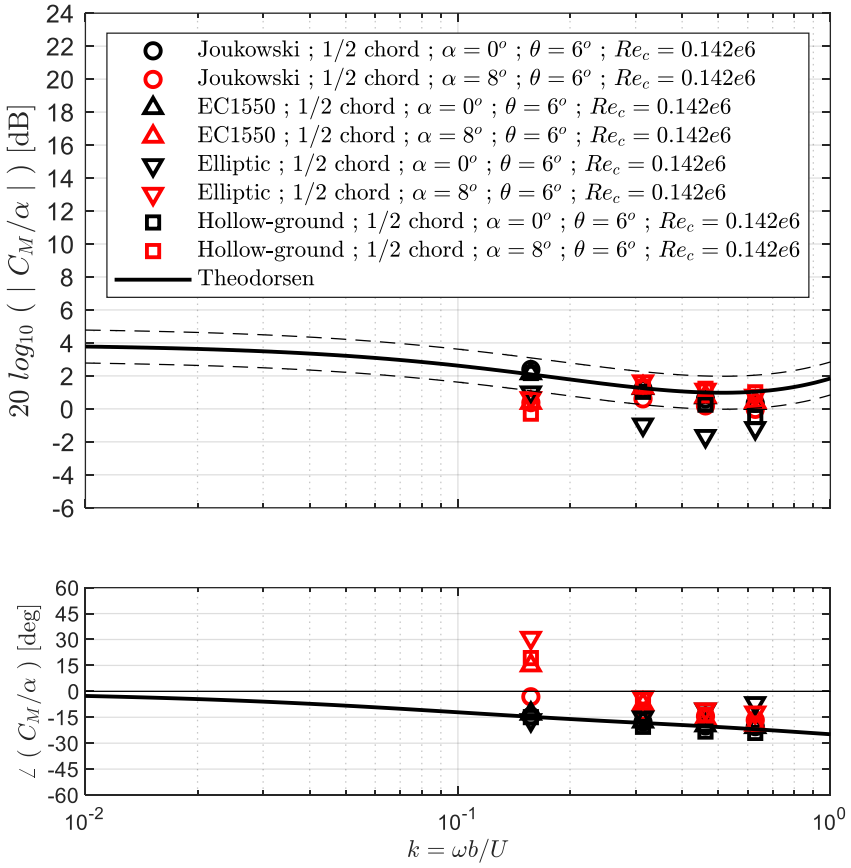

Figure 3.6. Unsteady pitching moment response for multiple airfoil profiles

For the two-dimensional airfoil, the measured unsteady pitching moment is seen to be represented quite well by the Theodorsen model for both magnitude and phase characteristics. However, as the aspect ratio is lowered, there is a clear trend to how this response is altered. The magnitude is seen to diminish almost uniformly across these reduced frequencies, and the phase is also seen to diminish back towards a value of zero. The pitching moment response for the aspect ratio of 4.44, in this instance, is seen to border very closely to the one decibel threshold of the Theodorsen model; therefore it is assumed that for greater aspect ratios through to two-dimensional conditions that the Theodorsen model would yield similarly favorable comparisons.

This reference does not provide additional results with which to conclusively identify the root cause for this altered behavior for low aspect ratio configurations. However, the attenuation of the unsteady

pitching moment response is understood in the context that for progressively smaller aspect ratios, the end effects at the spanwise extremities of the airfoil become more prominent. Flow leaking around the spanwise edges of the airfoil and generating markedly three-dimensional flow fields is assumed to be a contributing factor to these altered pitching moment responses.

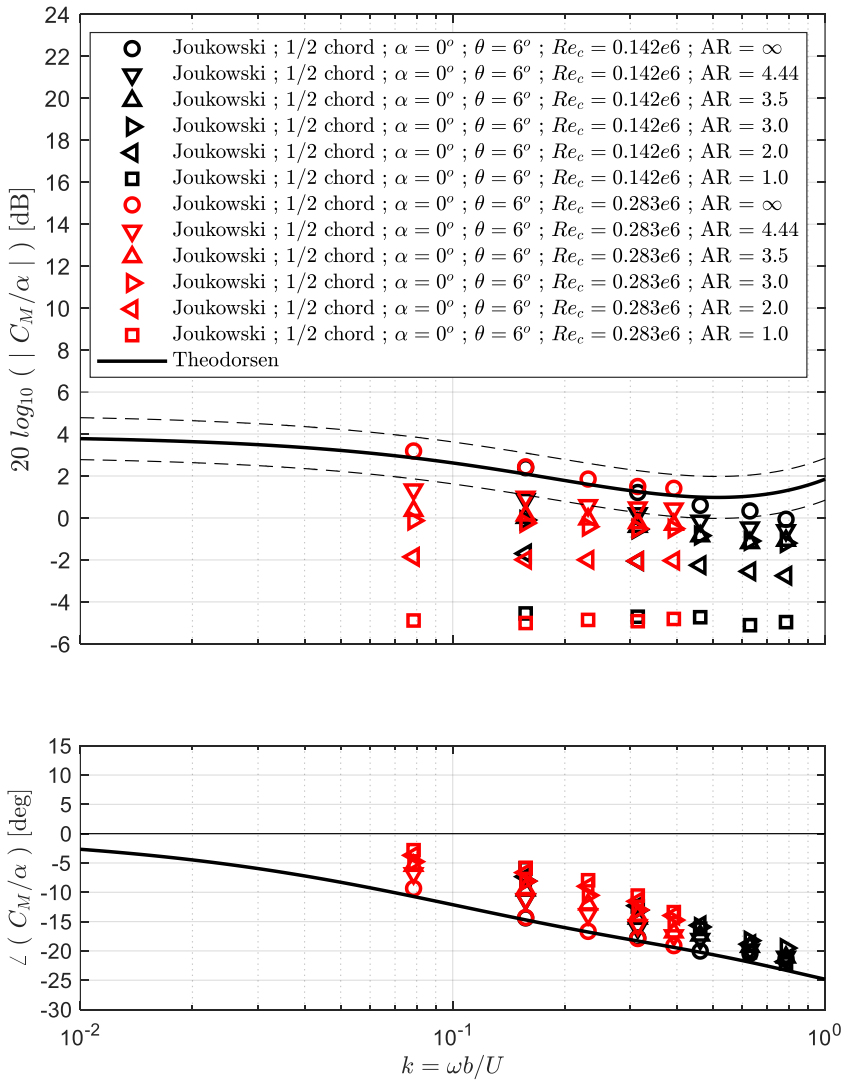

Figure 3.7. Unsteady pitching moment response for multiple airfoil aspect ratios

3.3 Halfman

The reference of Halfman (1952) is also a NACA-era experimental, subsonic, wind tunnel effort which consists of the measurement of unsteady airfoil responses due to various harmonic disturbance motions. Both unsteady lift and pitching moment are measured for pure pitch, plunge, and combined motion operating conditions. Both zero and finite mean lift conditions are investigated where the reduced frequency range is typically kept below a value of 0.5. The airfoil utilized in this series of testing is of a NACA 0012 profile with a nominal 1 foot chord and 2 foot span (the specific half-chord listed within the results is 5.8 inches). The utilized wind tunnel was modified with end walls at the spanwise extents of the airfoil in order to ensure two-dimensional flow over the airfoil. For the pitching motion, the elastic axis (i.e. pitching axis) is listed as being at 37 percent chord, and based on the varying freestream velocities, the chord-based Reynolds numbers ranged from $Re_c = 7.0 - 9.2 * 10^5$. The disturbance motions are sinusoidal, implemented at various reduced frequencies, and are characterized by the amplitudes of the disturbance motions. For heaving motion, this is listed as the airfoil sweeping through a displacement of either ± 1 or 2 inches. For the pitching motion, this is listed as sweeping through angles of attack of either $\pm$ 6.74 or 13.48 degrees. While these are particularly large pitching amplitudes, no definitive results or statements are listed with regard to flow separation, though some reference is made to this possibility. Additionally, mean angle of attack conditions were either 0 or 6.1 degrees (when not listed in the figures below, the mean angle of attack is 0 degrees).

A primary motivation for this section is the comparison of the referenced data to the Theodorsen model, where the comparisons and analysis are performed in the same manner as the calculated results of the present study. As such, the following transfer function expressions are generated from the Theodorsen model expressions for both the unsteady lift and pitching moment for both heaving (i.e. plunging) and pitching motions. For the unsteady lift resulting from pitching motion, this transfer function expression is found by using the unsteady lift Theodorsen expression taken from Section 2.7, where $\dot{h} = \ddot{h} = 0$, $a = -0.26$,

$$\frac{C_L}{\alpha} = 2\pi C + i\pi[1 + 2C(0.5 + 0.26)]k - 0.26\pi k^2 \tag{3.6}$$

$$\frac{C_L}{\alpha} = 2\pi C + i\pi[1 + 1.52C]k - 0.26\pi k^2 \tag{3.7}$$

Similarly, the unsteady lift resulting from heaving motion is,

$$\frac{C_L U_\infty}{\dot{h}} = 2\pi C + i\pi k \tag{3.8}$$

The transfer function expression for the unsteady pitching moment as a result of pitching motion is also found by utilizing the expression from Section 2.7,

$$\frac{C_M}{\alpha} = \pi(-0.26 + 0.5)C + i\pi[(0.25 - (0.26)^2)C - (0.25 + 0.13)]k + \frac{\pi}{2}(0.125 + (0.26)^2)k^2 \tag{3.9}$$

$$\frac{C_M}{\alpha} = 0.24\pi C + i\pi k[0.1824C - 0.38] + 0.0963\pi k^2 \tag{3.10}$$

Lastly, the unsteady pitching moment as a result of heaving motion is,

$$\frac{C_M U_\infty}{\dot{h}} = \pi\left(-0.26 + \frac{1}{2}\right)C + i\frac{\pi}{2}(-0.26)k \tag{3.11}$$

$$\frac{C_M U_\infty}{\dot{h}} = 0.24\pi C - i0.13\pi k \tag{3.12}$$

The unsteady airfoil response data from the reference of Halfman are presented in several figures within the source material for the various configurations and conditions which are studied. One of these

representative figures is copied and presented here as Figure 3.8, simply for reference; this example is of the unsteady lift due to heaving motion. The magnitude and phase of the unsteady airfoil responses are plotted as a function of reduced frequency. Instead of having to digitize all of the pertinent data from the figures of this reference, all of the data from this study are tabulated within the document and easily accessible, however a quick note is warranted with regard to the interpretation of the results. The phase results are presented relative to heaving position, and not heaving velocity, therefore a phase shift of 90 degrees is assumed and implemented. Additionally, phase shifts of 180 and 360 degrees are assumed for the results of both motions as needed, such that the low frequency responses approach a value of zero, and given possible polarity differences in the orientation of the variables.

The Halfman data of the unsteady lift and pitching moment transfer functions due to heaving motion are plotted in Figure 3.9 in a Bode plot format with the magnitude expressed on a decibel scale. Multiple conditions are present in these figures, for heaving position amplitudes of $\pm$ 1 inch about a zero mean, $\pm$ 2 inches about a zero mean, and $\pm$ 1 inch about a mean angle of attack of 6.1 degrees. The Theodorsen model (corresponding expressions above) is presented as the thick black line, where the dotted lines on the magnitude plots represent a $\pm$ 1 decibel visual aid. As can be seen, generally the Halfman data compare well to the Theodorsen model; though some notable characteristics and differences do exist. The first notable feature of these comparisons is the visual effect of the logarithmic versus the linear scale for the magnitude of the airfoil responses, as well as for the reduced frequency. The purpose of the logarithmic scales however, is that within the present work the range of reduced frequencies and magnitude of the responses span orders of magnitude, while the Halfman data exist over a more limited range.

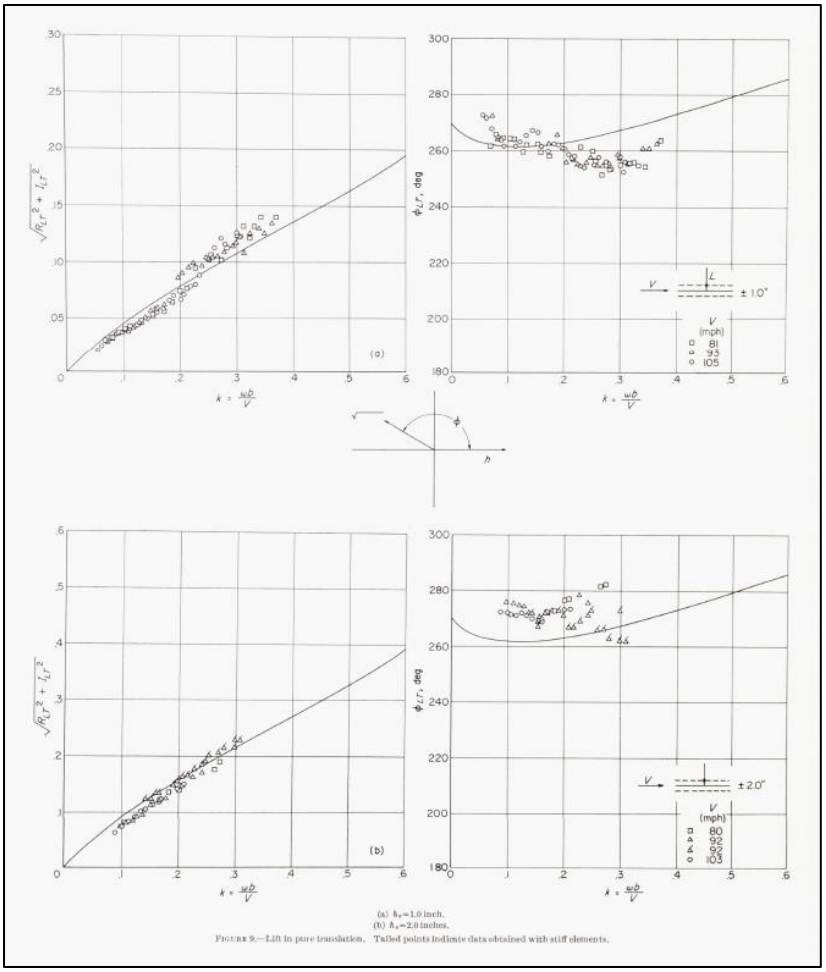

Figure 3.8. Characteristic example of the unsteady airfoil response figures provided by Halfman (figure copied directly from reference)

The results in Figure 3.9 that are seen to deviate the most from both the Theodorsen model and each other are the magnitude of the unsteady pitching moment response. The measured data for the mean angle of attack condition exhibit an attenuated response by as much as 4 decibels relative to the results at a zero mean angle of attack. A specific cause for this is not identified; however it is noted that as the airfoil is oscillating through several degrees of angle attack, that some transient flow separation may be occurring with this motion superimposed onto the mean angle of attack. The phase results for this data however, are nominally well predicted by the Theodorsen model.

The Theodorsen model lines presented in Figure 3.9 correspond to implementing the stated elastic axis position within the reference, and it is assumed that the pitching moment is calculated about this

chordwise location. There is however a discrepancy of unknown cause with regard to the Theodorsen model presently shown and that presented within the figures of the reference material. Specifically, Figure 10 within the Halfman document presents the pitching moment due to heaving motion, and the magnitude results show a much better agreement between the model and the measured data. Based on the magnitude distribution, this would appear to be from implementing an elastic axis positioned closer to mid-chord; however, this is not in agreement with the phase distribution. As stated earlier, there is not a clear understanding about the cause of this discrepancy: a misunderstanding of the elastic axis location, the location about which the pitching moment is calculated, etc. Simply for reference, Figure 3.10 presents the same pitching moment response due to heaving motion figure as above, but includes the predicted distribution for an elastic axis assumed about the mid-chord. Lastly, the mean angle of attack condition appears to have no appreciable effect on the unsteady lift response.

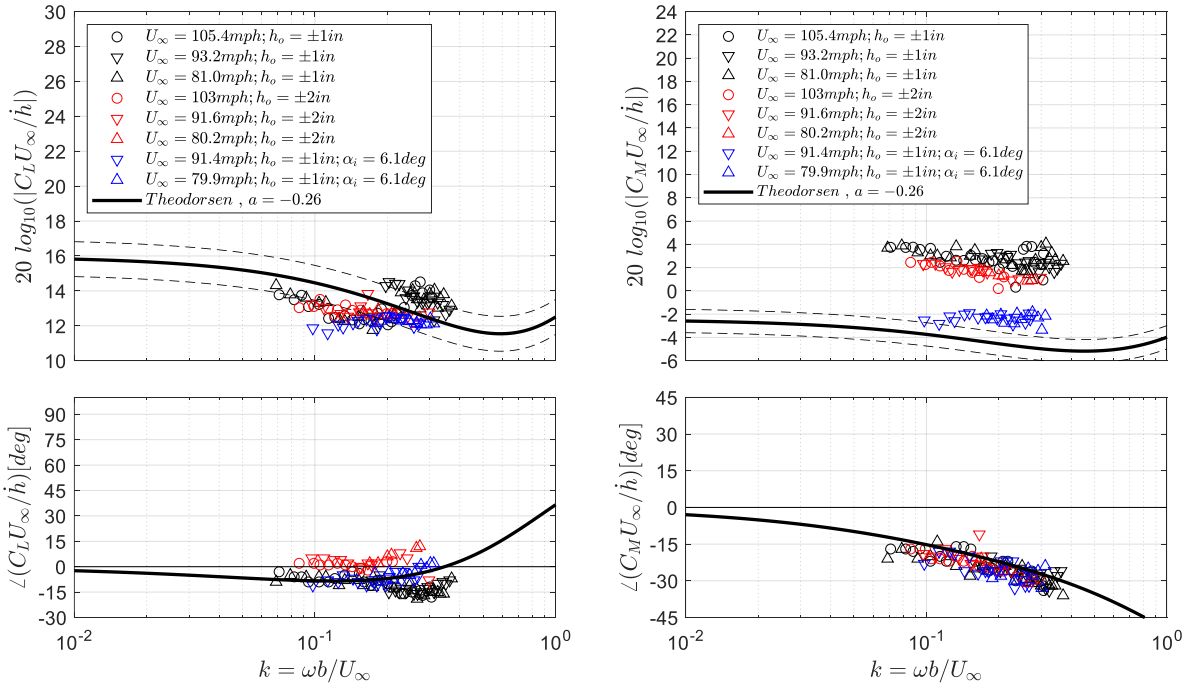

Figure 3.9. Comparison of unsteady lift and pitching moment responses from Halfman for heaving motion

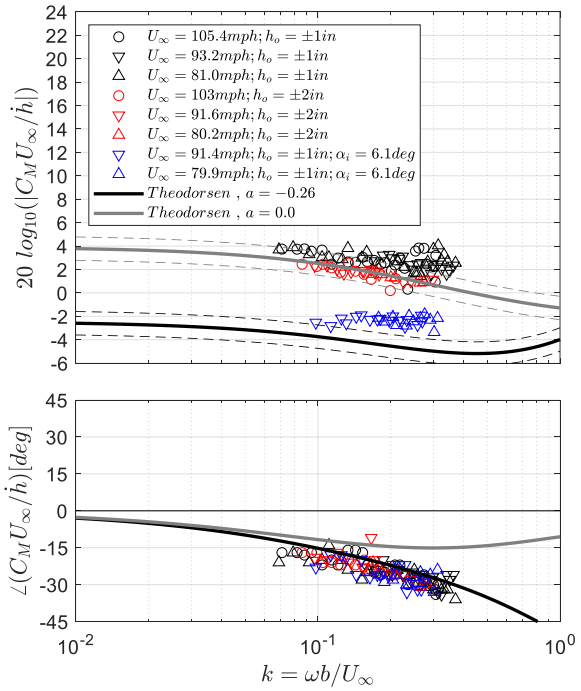

Figure 3.10. Comparison of unsteady pitching moment response from Halfman for heaving motion

Presented in an identical format, the unsteady lift and pitching moment responses due to pitching motion are provided in Figure 3.11. Nominally, the magnitude and phase of these responses are also predicted well by the Theodorsen model, with the notable exception again being the magnitude of the pitching moment. The magnitude of the unsteady lift is slightly over-predicted by the Theodorsen model, while the phase distribution is modeled well, capturing the transition into phase lead of the response. While the phase of the pitching moment response is seen to be modeled particularly well, the magnitude is similarly off as in the case for heaving motion. Again, it is unclear what the root cause of this discrepancy is. Simply for reference, the corresponding Theodorsen model for an assumed elastic axis of mid-chord is provided in Figure 3.12. Separate from the Theodorsen model however, the presence of a mean angle of attack appears to have little to no appreciable effect on the pitching moment response due to pitching motion, as it did for the case of heaving motion. This data also exhibits no appreciable effect of a mean angle of attack on the unsteady lift response due to pitching motion.

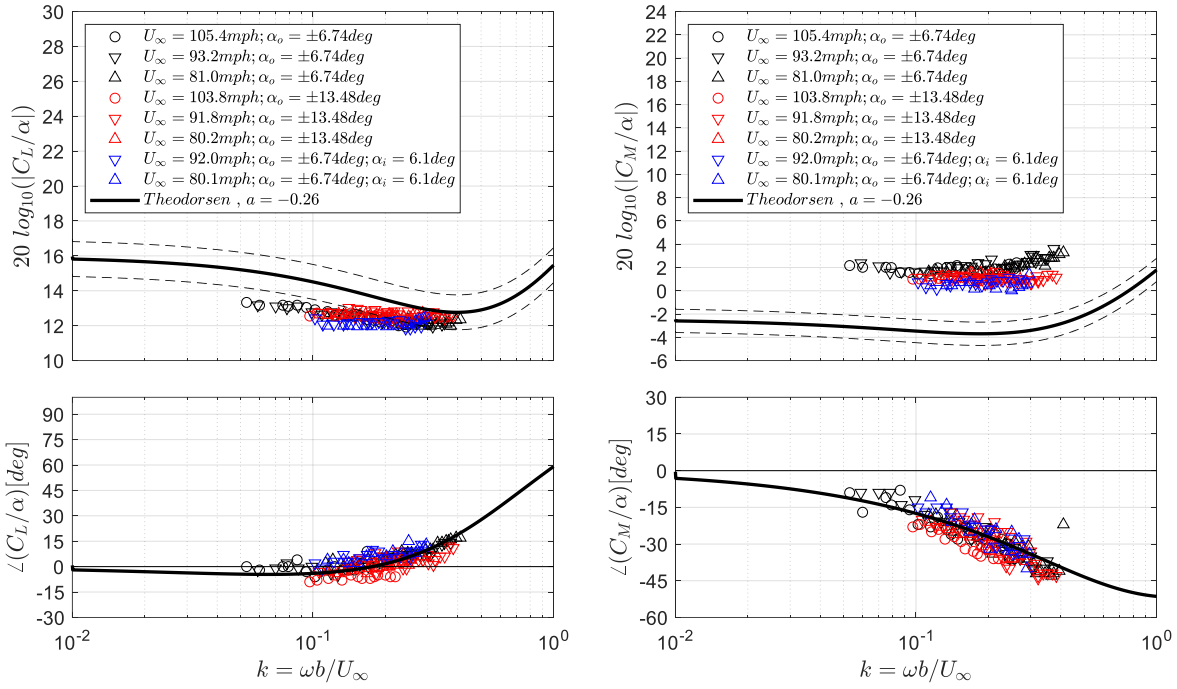

Figure 3.11. Comparison of unsteady lift and pitching moment responses from Halfman for pitching motion

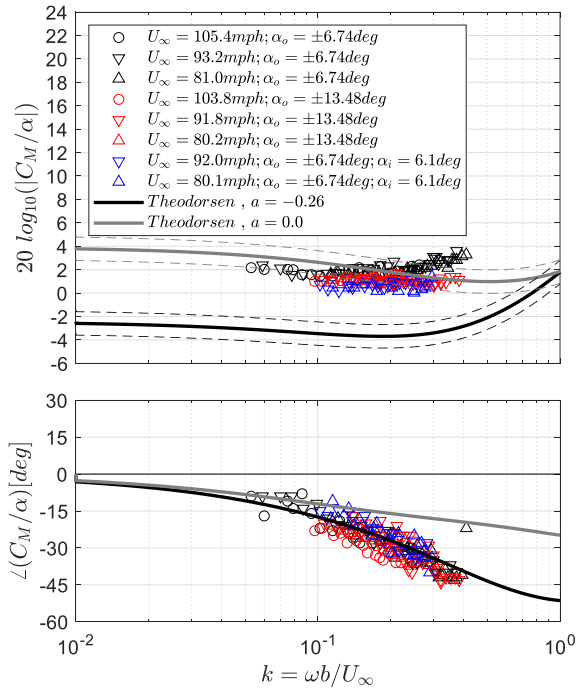

Figure 3.12. Comparison of pitching moment response from Halfman for pitching motion

3.4 Rainey

The reference of Rainey (1957) is another experimental, wind tunnel study which investigates the unsteady response of airfoils due to harmonic disturbance motion through direct measurement. Various operating conditions and configurations are considered, though only the subsonic and small amplitude disturbance conditions are utilized presently. The implemented airfoil is a NACA 65A010 with a chord of 1 foot and span of 2 feet, which covers the extent of the utilized test section (i.e. end walls are present in order to help enforce two-dimensionality of the flow). The chord-based Reynolds number is listed as $Re_c = 5.3 * 10^6$, where the fluid medium is Freon-12. Two separate Mach numbers were implemented in this reference study, though only the results from the 0.35 Mach number condition have been utilized.

The unsteady lift and pitching moment results were determined from discrete measurements of the unsteady pressure across the chord by pressure sensor pairs, where the differential pressures were subsequently weighted and integrated. The airfoil disturbance motion is pitching about the mid-chord for an amplitude of nominally 1.2 degrees. One of the distinguishing attributes of this study is that this disturbance motion is implemented for several mean angle of attack conditions, some of which range into transient and full stall conditions. Within the present analysis, only the results for where fully attached flow is assumed were retained. This corresponds to mean angles of attack of 0, 4, and 8 degrees.

For the unsteady lift resulting from pitching motion about the mid-chord, the subsequent transfer function is found by using the expression from Section 2.7, where $\dot{h} = \ddot{h} = 0$, $a = 0.0$,

$$\frac{C_L}{\alpha} = 2\pi C + i\pi[1 + C]k \tag{3.13}$$

Similarly, the unsteady pitching moment transfer function based on the Theodorsen model is,

$$\frac{C_M}{\alpha} = \frac{\pi}{2}C + i\pi\left[\frac{1}{4}C - \frac{1}{4}\right]k + \frac{\pi}{2}\left(\frac{1}{8}\right)k^2 \tag{3.14}$$

$$\frac{C_M}{\alpha} = \frac{\pi}{2}C + i\frac{\pi}{4}[C - 1]k + \frac{\pi}{16}k^2 \tag{3.15}$$

This unsteady lift and pitching moment data with respect to reduced frequency is presented for the various mean angle of attack conditions in Figure 3.13. The data presented in this reference was digitized and used directly. Both the magnitude and phase distributions of these unsteady lift and pitching moment results are predicted quite well by the Theodorsen model for the 0 and 4 degree mean angle of attack conditions. Though the range of reduced frequencies is somewhat limited, and there appears to be a slight systematic offset of the phase, the character of the magnitude and phase distributions are captured well.

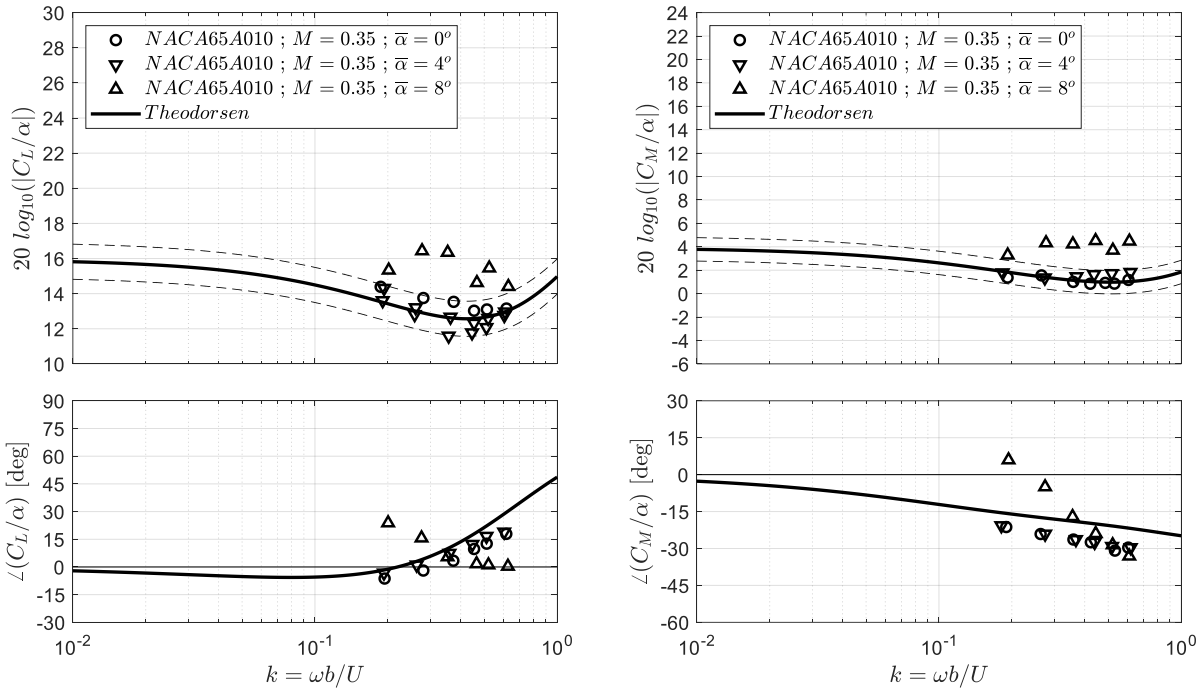

Figure 3.13. Comparison of unsteady lift and pitching moment responses from Rainey for pitching motion

The results for the 8 degree angle of attack condition however, exhibit notable deviations from the other data and the Theodorsen model. The magnitudes of both the unsteady lift and pitching moment responses are amplified, and the phase distributions are markedly altered. This is certainly acknowledged within the reference document, however a definitive understanding of this behavior is not established. However, within Appendix B of the reference document, strip charts showing the time traces of the individual pressure measurements collected across the chord are presented for the case of 8 degrees mean angle of attack at various reduced frequencies. These plots are copied directly from the reference and

presented here in Figure 3.14. It can be seen that for the positive portions of the sinusoidal disturbance, $\alpha(t) > 8^o$, that the measured pressures, particularly near the leading edge, exhibit random fluctuations. This is termed 'flow breakdown' within the reference, and is presumed to be some form of transient flow separation or leading edge shedding. These fluctuations vanish for the portion of the wavelength which is below the mean incidence angle. It is difficult to ascertain quantitatively, though qualitatively these fluctuations are seen to occur at a slight time delay for locations moving aft along the chord, presumably as these disturbances convect with the flow. Within this reference document of Rainey, Figure 27 presents a standard static pitching moment versus angle of attack plot for this airfoil, and it can be seen that this 8 degree condition is right on the edge of the stall threshold.

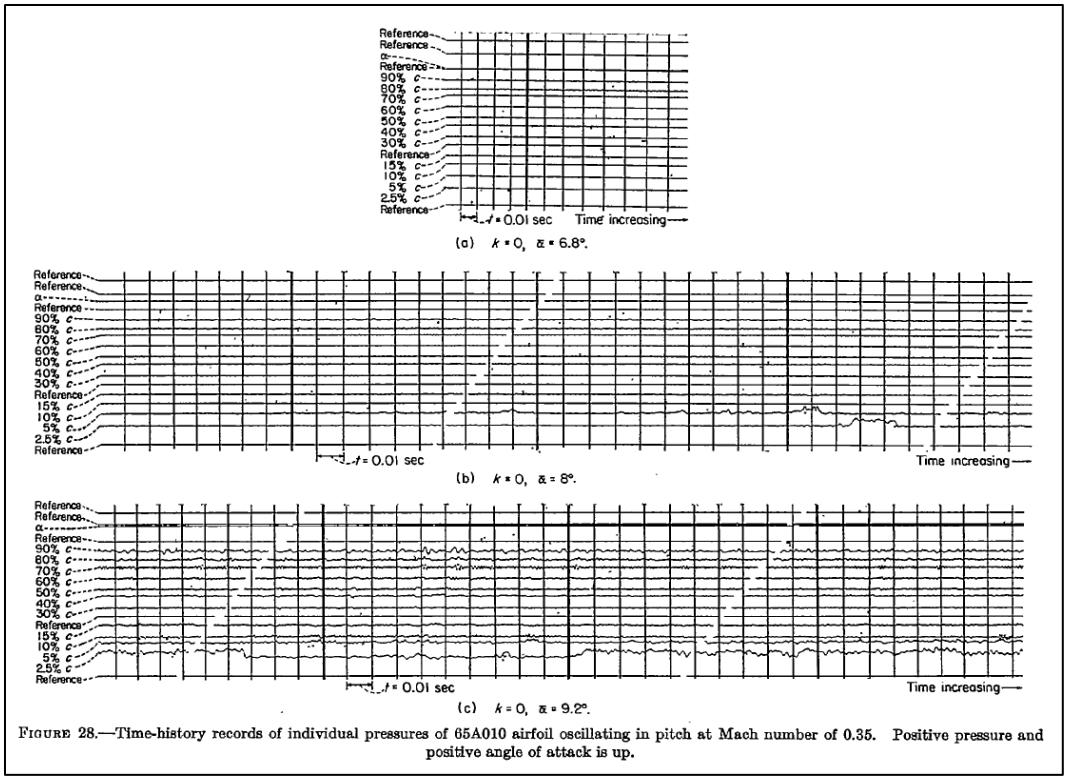

(a) $k = 0$, $\bar{\alpha} = 6.8°$.

(b) $k = 0$, $\bar{\alpha} = 8°$.

(c) $k = 0$, $\bar{\alpha} = 9.2°$.

FIGURE 28.—Time-history records of individual pressures of 65A010 airfoil oscillating in pitch at Mach number of 0.35. Positive pressure and positive angle of attack is up.

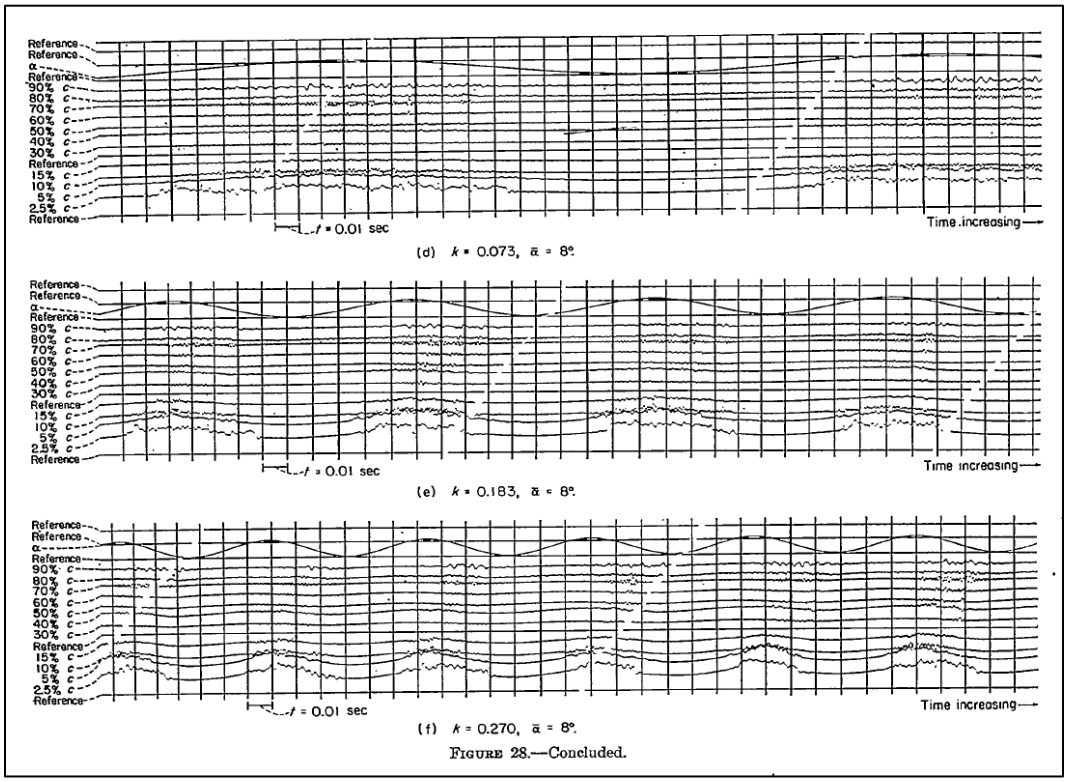

(d) $k = 0.073$, $\bar{\alpha} = 8°$.

(e) $k = 0.183$, $\bar{\alpha} = 8°$.

(f) $k = 0.270$, $\bar{\alpha} = 8°$.

FIGURE 28.—Concluded.

Figure 3.14. Time traces of unsteady pressure provided by Rainey (figure copied directly from reference)

3.5 Leishman

The work of Leishman (1993) is a document with comprises a mix of analytical development and a compilation of experimental results for airfoils subjected to unsteady motion. Of particular interest in this instance is the compilation of experimental data which comes from three different wind tunnel studies. The experimental data comes from Boeing, Aircraft Research Association (ARA), and NASA references (see Section 1.2). The freestream Mach numbers involve both subsonic and transonic operating conditions, though the current analysis only retains results for freestream Mach numbers of 0.5 or less. All of the experimental data pertain to the unsteady lift which results from various airfoil profiles (both symmetric and cambered) subjected to pitching about their respective quarter chords. The chord-based Reynolds numbers are not explicitly listed for the various experimental conditions, though they are generally high given a review of the reference documents. Importantly, the amplitudes of the disturbance pitching motion are listed as being small (such that fully attached flow conditions are maintained), though all of these specific conditions are referenced to their source material. The range of reduced frequencies for these compiled results is $k = 0.02 - 0.7$.

For the unsteady lift resulting from pitching motion about the quarter-chord, the subsequent transfer function is found by using the expression from Section 2.7, where $\dot{h} = \ddot{h} = 0$, $a = -0.5$,

$$\frac{C_L}{\alpha} = 2\pi C + i\pi[1 + 2C]k - \frac{\pi}{2}k^2 \tag{3.16}$$

This unsteady lift data is presented in a consolidated figure for the various configurations in Figure 3.15. The magnitude and phase of the unsteady lift transfer function results are plotted with respect to reduced frequency in an identical manner to the previous sections. The data presented in this reference were digitized and used directly, except for the following consideration. The reference describes a Mach number correction applied to the unsteady lift magnitude data; this was subsequently removed in the present analysis. The Theodorsen model, expressed above, is plotted in the same way as the prior comparisons.

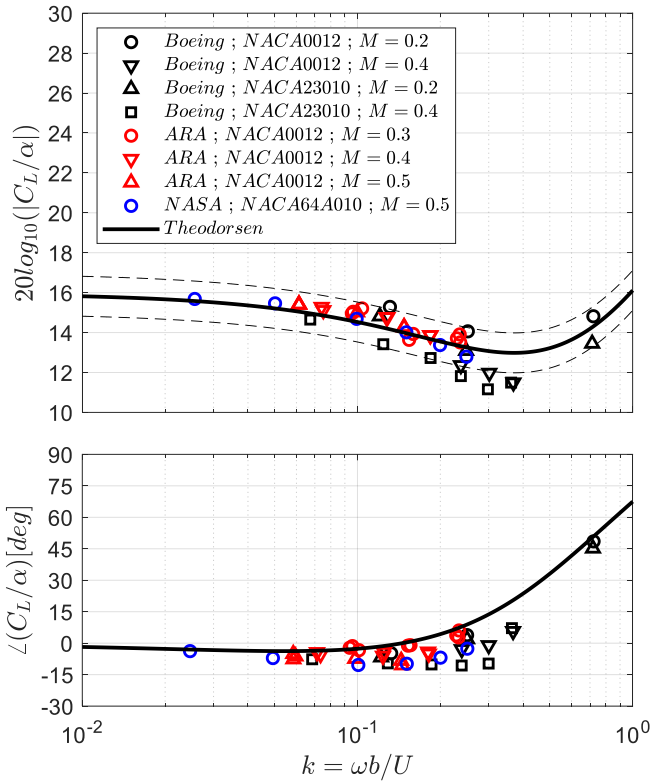

Figure 3.15. Comparison of unsteady lift coefficients from Leishman

As seen in Figure 3.15, both the magnitude and phase distributions of these experimental unsteady lift coefficient results are consistent with each other and predicted well by the Theodorsen model. The lift magnitudes mostly fall within a $\pm$ 1 decibel scatter of the model; and while the correct trend for the phase of the response is exhibited, some data points can be seen to vary by as much as 15 degrees. The agreeable comparison between the model and two data points at a reduced frequency of approximately 0.7 is also noteworthy as around these higher reduced frequency conditions the lift response exhibits different characteristics, where the magnitude grows and the onset of a marked phase lead begins.

The comparison of this data is particularly noteworthy as the experimental conditions include both cambered foils and freestream Mach numbers for which compressibility effects would certainly be expected to be present. However, despite these conditions, the unsteady lift response over this range of reduced frequencies is not seen to be drastically altered from that dictated by the Theodorsen model.

3.6 Cordes et al.

The work of Cordes et al. (2017) documents the results from another experimental wind tunnel study on the unsteady response of airfoils subjected to either unsteady motion or an unsteady inflow velocity field. The unsteady disturbance motion is concentrated on presently, where this is pitching motion about the airfoil leading edge for various amplitudes of pitch motion superimposed onto various mean pitch angles. Most operation conditions stay within the bounds of fully attached flow, though there are instances where this condition is breached. The utilized airfoil is two-dimensional with a Clark Y profile, a chord length of 0.12 m, and a span of 0.45 m. The resulting range of Reynolds numbers based on chord length is $Re_c = 1.2 - 3.0 * 10^5$.

The specific unsteady response which is interrogated in this study is the unsteady lift response, however this is achieved by an indirect measurement. The utilized airfoil is instrumented with multiple embedded pressure sensors, such that the unsteady differential pressure across the airfoil is measured at three distinct locations in the vicinity of the airfoil leading edge. This measured, unsteady, differential pressure is utilized as a surrogate for the unsteady lift. The term used within their analysis is further normalized by the quasi-steady amplitude. Further description and review of their analysis steps is deferred to the reference document. The airfoil is oscillating about the leading edge in this instance, and therefore the unsteady differential pressure Theodorsen expression written as a complex transfer function is taken from Section 2.7, where $\dot{h} = \ddot{h} = 0$, and $a = -1.0$,

$$\frac{C_{\Delta P}}{\alpha} = -4\left[\left(\frac{1-cos(\theta)}{sin(\theta)}\right)C + i\left(\frac{3}{2}sin(\theta) - cot(\theta)\left[\frac{1}{2}cos(\theta) - \frac{1}{2}\right] + \left(\frac{1}{2}+1\right)\left(\frac{1-cos(\theta)}{sin(\theta)}\right)C\right)k \ldots \right.$$
$$\left. - sin(\theta)\left(\frac{1}{2}cos(\theta)+1\right)k^2\right] \tag{3.17}$$

$$\frac{C_{\Delta P}}{\alpha} = -4\left(\frac{1-cos(\theta)}{sin(\theta)}\right)C - i2k\left(3\,sin(\theta) - cot(\theta)\,[cos(\theta)-1] + 3\left(\frac{1-cos(\theta)}{sin(\theta)}\right)C\right)\ldots$$
$$+ 2k^2\,sin(\theta)\,(cos(\theta)+2) \tag{3.18}$$

Further manipulation of this expression is needed however, in order to compare to the data of this reference. The reference text states that the transfer function is additionally normalized by the quasi-steady level, which in this instances is $-4\left(\frac{1-cos(\theta)}{sin(\theta)}\right)$, for $C(k \approx 0) \approx 1.0$. Therefore,

$$\frac{C_{\Delta P}}{\alpha} = C + i\frac{1}{2}k\left(\frac{3\,sin^2(\theta)}{1-\cos(\theta)} + \cos(\theta) + 3C\right) - \frac{1}{2}k^2\frac{sin^2(\theta)}{1-\cos(\theta)}(cos(\theta)+2) \tag{3.19}$$

Additionally, there exists some ambiguity into the specific pressure measurement location which is utilized in the analysis of this reference. The description of the analysis states the location as the leading edge, which corresponds to $\theta = -\pi$ radians, and this specific value is used as an approximation. This results in the following simplified expression for the equivalent transfer function term for which to compare to the data of this reference,

$$\frac{C_{\Delta P}}{\alpha} = C + i\frac{1}{2}k(-1+3C) \tag{3.20}$$

A check of the expression developed above is given by Figure 3.16, where the relevant figures from this reference are copied and presented alongside the digitized data and Theodorsen expression above. Comparison of the 'First-order theory' and the Theodorsen expression show that they are effectively identical, and therefore valid to compare.

The data from this reference were digitized and are presented relative to the Theodorsen model expression for the differential pressure transfer function developed above within Figure 3.17. The first plot corresponds to variations in the mean angle of attack, and the second plot corresponds to variations in the pitching amplitude. The figure title from Figure 3.16a (a copy of the reference material) should be leveraged for additional description. As can be seen in Figure 3.17a, the variation in mean angle of attack between -4^o and 5^o over these operating conditions are not seen to result in drastic variation of the differential pressure response, and in fact compare fairly well with the Theodorsen model. Variations in the magnitude of the response of up to 2 decibels are seen at $k = 0.3$. This is however, in stark contrast to the response for a mean angle of attack of 8^o, at which this airfoil is very near to its stall region on its mean lift curve

distribution. The pitch amplitude is stated to be 4^o, such that it is inferred that the foil is experiencing transitory flow separation over a significant portion of its oscillation cycle. This is seen to result in significant attenuation in the magnitude of the unsteady response at the specified reduced frequencies. No discussion is offered in terms of possible response at non-driven frequencies.

The results presented in Figure 3.17b correspond to variations in the pitch amplitude at a mean angle of attack of 2^o. These distributions are very consistent and compare well to the Theodorsen model such that the system is responding linearly for these conditions.

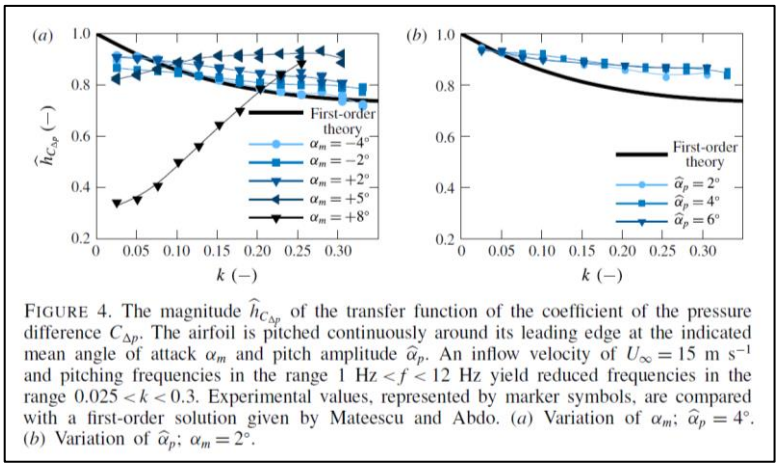

FIGURE 4. The magnitude $\widehat{h}_{C_{\Delta p}}$ of the transfer function of the coefficient of the pressure difference $C_{\Delta p}$. The airfoil is pitched continuously around its leading edge at the indicated mean angle of attack α_m and pitch amplitude $\widehat{\alpha}_p$. An inflow velocity of $U_\infty = 15$ m s^{-1} and pitching frequencies in the range 1 Hz $< f <$ 12 Hz yield reduced frequencies in the range $0.025 < k < 0.3$. Experimental values, represented by marker symbols, are compared with a first-order solution given by Mateescu and Abdo. (*a*) Variation of α_m; $\widehat{\alpha}_p = 4°$. (*b*) Variation of $\widehat{\alpha}_p$; $\alpha_m = 2°$.

a)

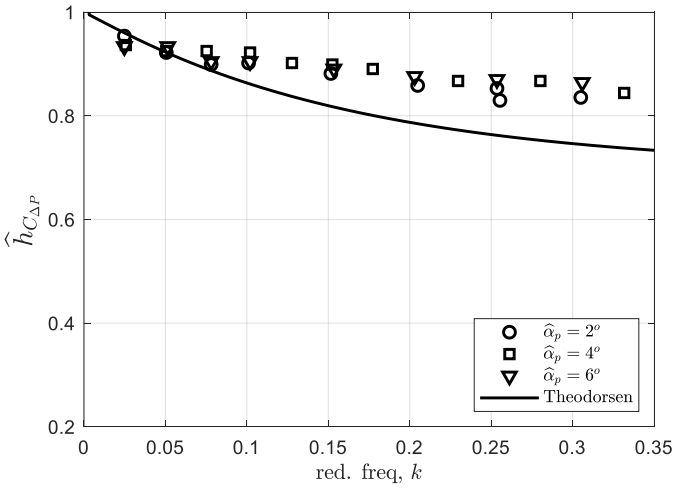

b)

Figure 3.16. Unsteady differential pressure responses from Cordes et al.
a) figure copied directly from reference b) digitized data of variable oscillation amplitudes

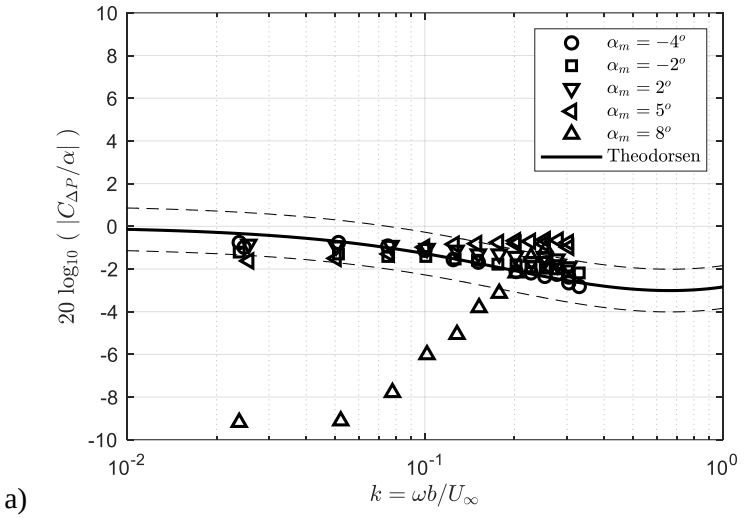

a)

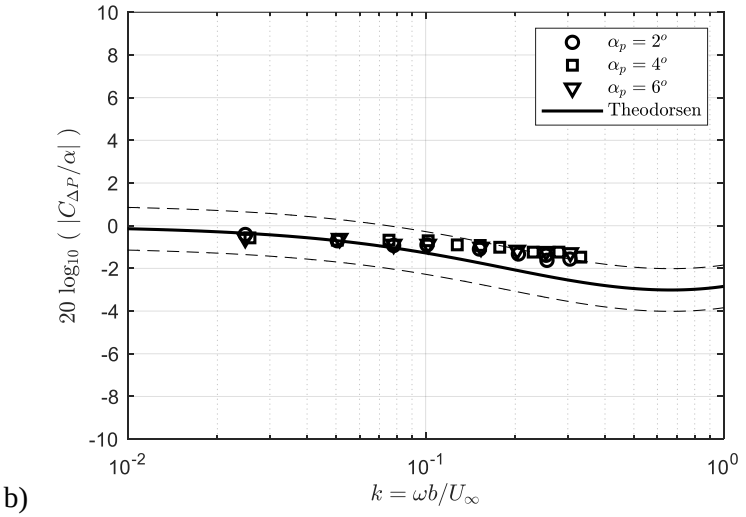

b)

Figure 3.17. Comparison of unsteady differential pressure responses from Cordes et al.: a) variable mean angles of attack, b) variable oscillation amplitudes

3.7 Satyanarayana and Davis

The work of Satyanarayana and Davis (1978) is an experimental, subsonic wind tunnel study where an instrumented airfoil was subjected to sinusoidal pitching about the quarter chord. The airfoil which was utilized had a NACA 64A010 profile and a 15 cm chord. Results are presented for a single freestream velocity, which corresponds to a chord-based Reynolds number of $Re_c = 5.6 * 10^5$. The disturbance pitching motion is stated to be of an amplitude of approximately ± 1 degree and to oscillate about a zero degree mean. The range of reduced frequencies is $k = 0.05 - 1.2$.

The experimental results presented within this reference are unsteady surface pressures measured by embedded pressure transducers within the airfoil. Symmetric measurement pairs were implemented on either side of the airfoil in order to determine the differential pressures acting across it at the following normalized chordwise locations, $x/c = 0.40, 0.893, 0.920, 0.947,$ and 0.973. The resulting time series were phase averaged from the inclusion of approximately 100 oscillation cycles, where it is stated that more variability was witnessed in the trailing edge measurements than those at the 40% chordwise location. Throughout the reference, the experimental results are compared to linear, incompressible, small disturbance theory; however it is never definitively stated or referenced which model or expressions are utilized. It is therefore assumed that the Theodorsen model was used. Further, while not elucidated here, it should be acknowledged that a corrective calibration procedure was implemented within the reference results based on the instrumentation calibration used for determining the unsteady angle of attack being observed to be frequency dependent. It is assumed that the presented data from this reference is valid, and it is recommended that the reference be sought for further details (section "Data Reduction and Presentation of Results" within the reference document).

The expression from the Theodorsen model for the differential pressure acting across the foil chord is manipulated into a transfer function of differential pressure coefficient to pitching motion by utilizing the expression from Section 2.7 where $\dot{h} = \ddot{h} = 0$, $a = -0.5$,

$$\frac{C_{\Delta P}}{\alpha} = -4\left[\left(\frac{1-cos(\theta)}{sin(\theta)}\right)C + i\left(\frac{3}{2}sin(\theta) - cot(\theta)\left[\frac{1}{2}cos(\theta) - \frac{1}{2}\right] + \left(\frac{1-cos(\theta)}{sin(\theta)}\right)C\right)k \ldots \right.$$
$$\left. - sin(\theta)\left(\frac{1}{2}cos(\theta) + \frac{1}{2}\right)k^2\right] \quad (3.21)$$

$$\frac{C_{\Delta P}}{\alpha} = -4\left(\frac{1-cos(\theta)}{sin(\theta)}\right)C - i2k\left(3\,sin(\theta) - cot(\theta)\,[cos(\theta) - 1] + 2\left(\frac{1-cos(\theta)}{sin(\theta)}\right)C\right) \ldots$$
$$+ 2k^2\,sin(\theta)\,(cos(\theta) + 1) \quad (3.22)$$

Two of the most pertinent figures which present data from the reference have been extracted, the data digitized, and these are presented and discussed below. Figure 3.18 presents the magnitude and phase of the $C_{\Delta P}$ responses at the multiple measurement locations across the foil chord at four distinct reduced frequencies. Both the reference figure and the digitized version are presented. Within the reference, delineation is made between the experiment results for when a boundary layer trip was or was not installed on the airfoil leading edge. This demarcation was not carried into the digitized analysis and figures. In order to be clear, within the legend of Figure 3.18b the label "Theo." stands for Theodorsen and the corresponding model results expressed above are plotted. This is clarified because the "theory" line in the reference figure appears to be not quite the same. Differences between the magnitudes of these theoretical curves appear indistinguishable, however some differences in the phase are present; the source of these differences is not clear. Lastly, in order to make the comparisons of the Theodorsen model to the data from this reference, the following definition was needed for the phase from the Theodorsen model, $\angle(C_{\Delta P}/\alpha) = -\angle(-C_{\Delta P}/\alpha)$, which clearly has no influence on the magnitude results. This flipping of the phase results was deemed acceptable as it only involves orientation definitions of the variables, which it is presumed could be different.

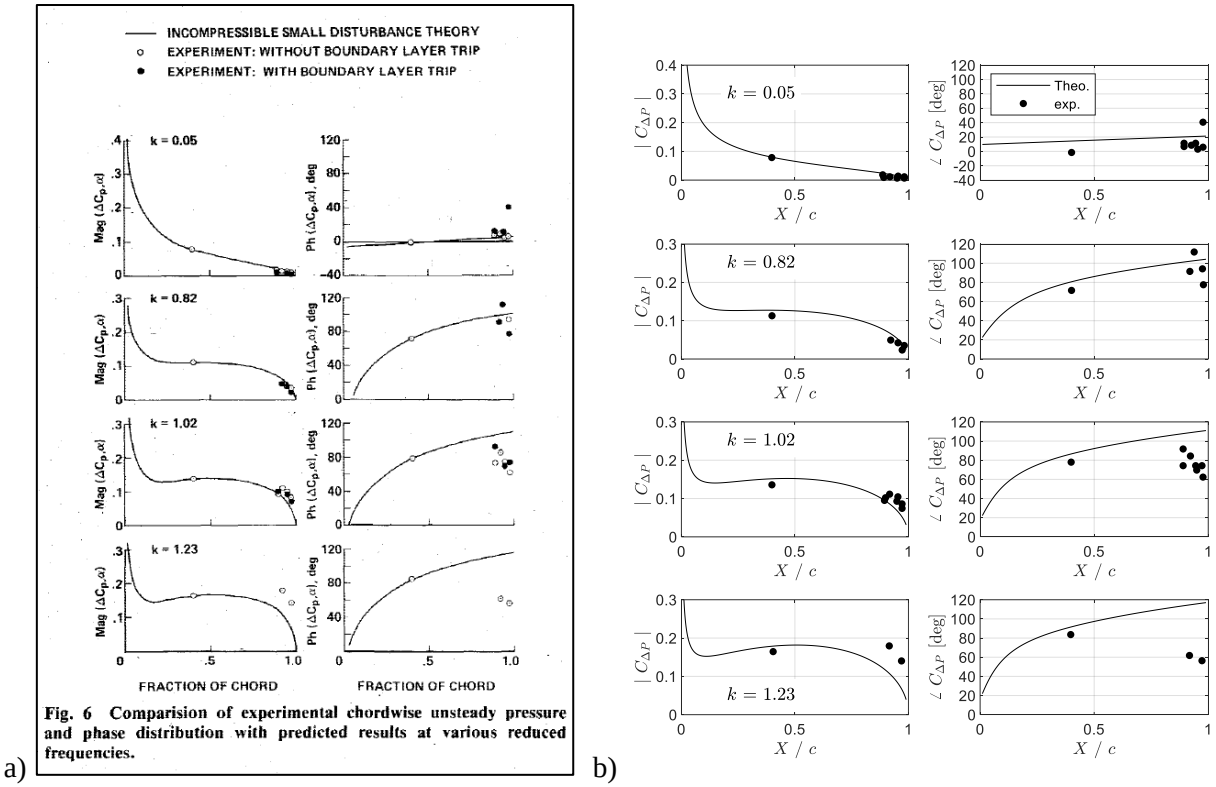

Figure 3.18. Comparison of unsteady differential pressure coefficients from Satyanarayana and Davis a) figure copied directly from source material, b) figure recreated from digitized data

In Figure 3.19 this same data is re-plotted, but in the format utilized for the analysis of the present study. Based on this data the results of Satyanarayana and Davis do compare fairly well to the Theodorsen model, but there are some differences which are notable. Generally, the magnitude and phase of the differential pressure response at the 40% chord location compares best with theory, though the phase of the experimental data is consistently less than the theoretical.

The bulk of the experimental data are based on measurements clustered at the trailing edge. The magnitude and phase of the differential pressure responses are also generally in agreement with the analytic Theodorsen model, though this data is markedly more scattered. However, it must be acknowledged that the magnitude data points were extracted from a condensed linear scale which makes viewing these points on a logarithmic scale much more prone to uncertainty. Despite the scatter in this data, which is further discussed in the reference document, there does appear to be a consistent difference between the measured

data and the theoretical results for increasing reduced frequencies. Specifically, the magnitude of the measured differential pressure response appears amplified relative to the theoretical results and the phase is seen to lag. Though not explicitly explored and discussed within this section, this type of result appears consistent with the calculations and analysis of the present study for airfoils of finite thickness at high reduced frequencies.

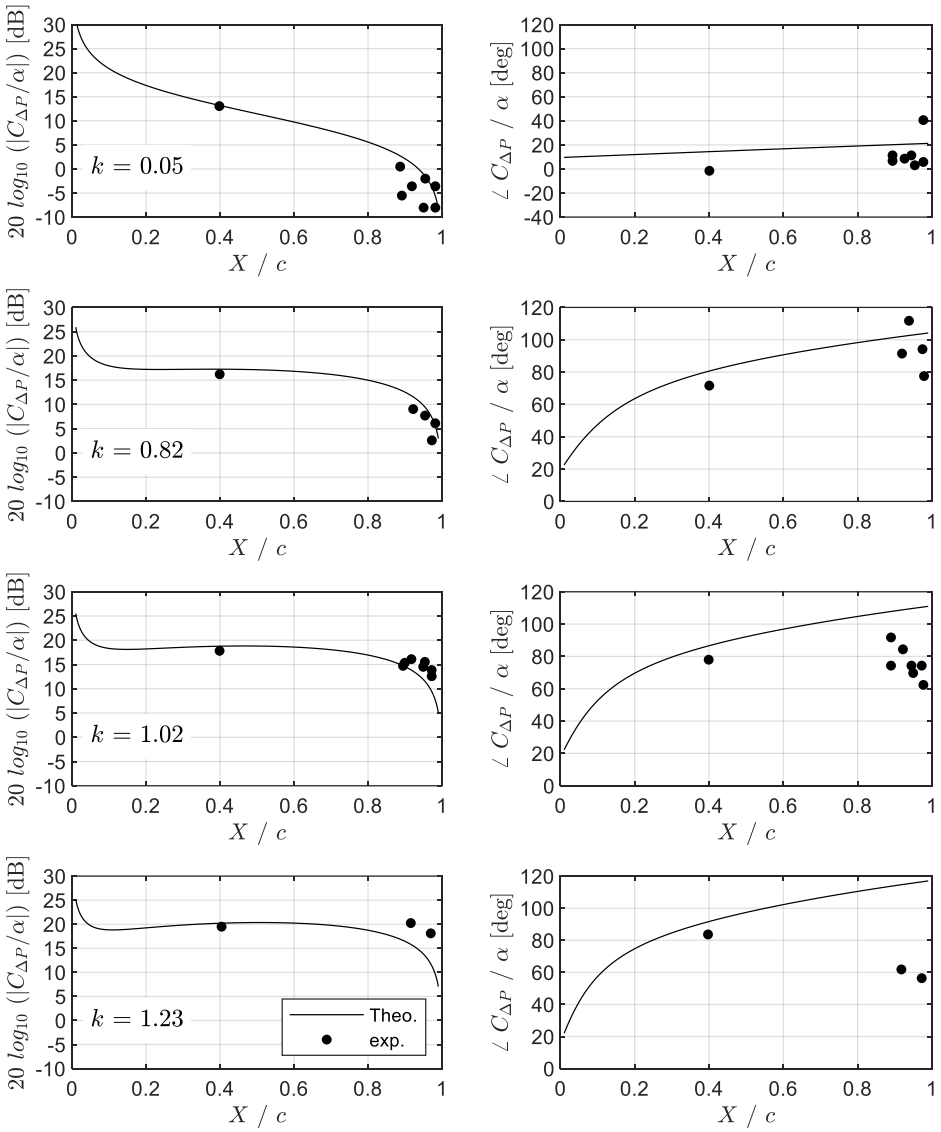

Figure 3.19. Comparison of unsteady differential pressure coefficients from Satyanarayana and Davis

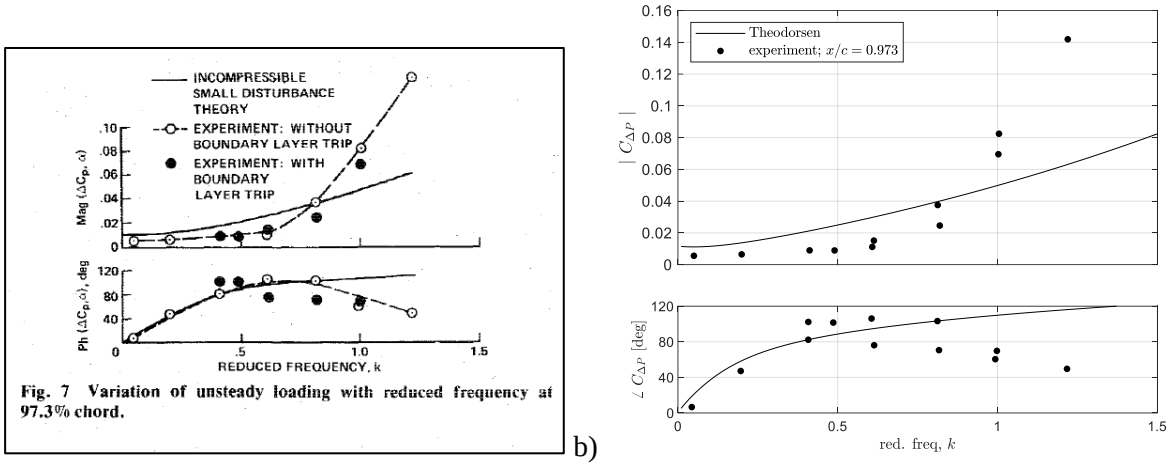

Figure 3.20. Comparison of unsteady differential pressure coefficients from Satyanarayana and Davis
a) figure copied directly from source material, b) figure recreated from digitized data

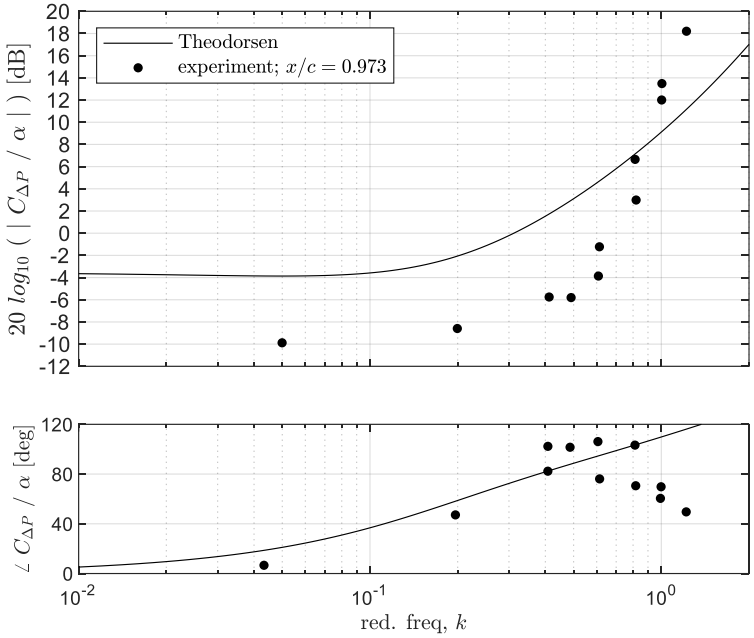

Figure 3.21. Comparison of unsteady differential pressure coefficients from Satyanarayana and Davis

In a very similar manner to the previous example, Figure 3.20 presents another copied figure from this reference and its corresponding digitized form. The data in this instance is the differential pressure response at the 97.3% chord location as a function of reduced frequency. Again, this same digitized data is then provided in Figure 3.21 in the presentation format of the present study. This view of the results in the immediate vicinity of the trailing edge shows that there is a notable difference between the experimental

and theoretical results. For reduced frequencies below a value of approximately one, the magnitude of the theoretical response over-predicts the experimental data, while for reduced frequencies greater than one theory under-predicts the experimental data. At both of the extremities of these differences, the experimental and theoretical results vary by as much as a factor of two. For the phase of the differential pressure response, the experimental and theoretical results agree responsibly well for lower reduced frequencies. Over the range of higher reduced frequencies the results begin to diverge such that the experimental data tends towards lower values of phase angle.

3.8 Ohashi and Ishikawa

The work of Ohashi and Ishikawa (1972) consists of an experimental, subsonic wind tunnel study where the wake pattern of a heaving airfoil was captured through Schlieren visualization over a range of reduced frequencies which are mostly greater than one. The motivations and results of this reference aim directly at critical assumptions enforced within the Theodorsen model, namely that 1) the shed vorticity from the trailing edge propagates downstream along a planar trajectory at the freestream velocity, and 2) the Kutta condition is applicable at the trailing edge.

Within this wind tunnel study the airfoil utilized is a NACA 65-010 with a chord of 100 mm and span of 200 mm, such that the spanwise ends of the airfoil corresponded with the end walls of the wind tunnel jet exit. Various freestream velocities, frequencies of heaving motion, and amplitudes of heaving motions were implemented for fully attached flow conditions, which yields chord-based Reynolds numbers and reduced frequencies between $Re_c = 1 - 4 * 10^4$ and $k \approx 0.5 - 10$, respectively. Additionally, the majority of the conditions were such that shedding of vorticity from the leading edge was not apparent nor believed to be occurring.

As this is a low-speed wind tunnel study, the variable density of the fluid medium necessary for the Schlieren imaging method is not induced by compressibility of the fluid, but rather by surface heating of only one side of the airfoil. The temperature difference between the flow as it leaves the airfoil yields a sufficient density gradient in the airfoil wake at the dividing streamline, which is understood to be the wake centerline. A characteristic view of the types of Schlieren images that are presented in this reference are reproduced here as Figure 3.22.

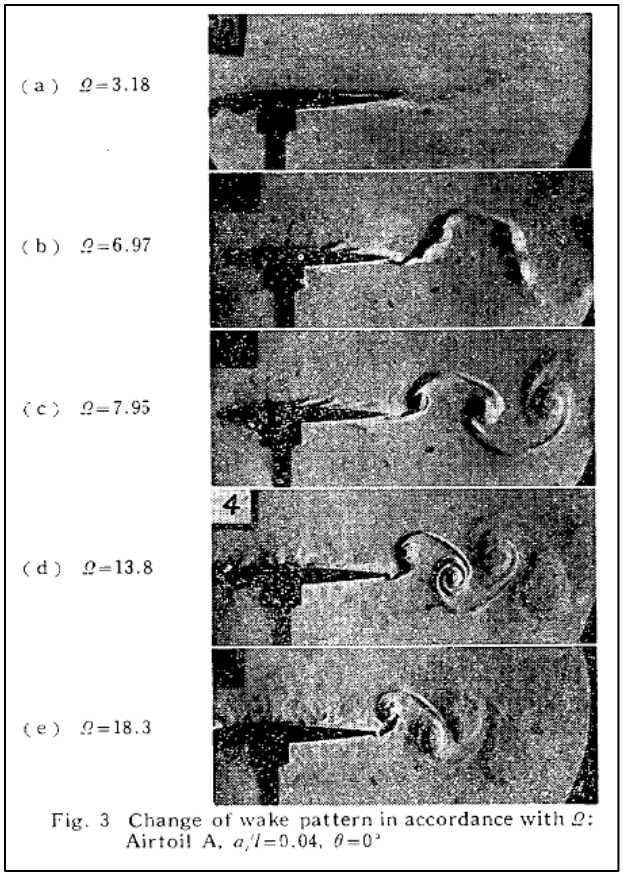

Fig. 3 Change of wake pattern in accordance with Ω: Airtoil A, $a/l=0.04$, $\theta=0°$

Figure 3.22. Characteristic example of the Schlieren images provided by Ohashi and Ishikawa (figure copied directly from reference)

Summarizing the results of Ohashi and Ishikawa, the assumption of a planar vorticity sheet appears reasonable for lower reduced frequencies and lower disturbance amplitudes. However, as either reduced frequency or disturbance amplitude are increased, or more downstream locations are considered, the assumption of a planar distribution of vorticity does not hold. Further, as evidenced by these images, the vorticity can even roll-up in the immediate vicinity of the airfoil trailing edge. The increased vorticity strength needed to enforce the Kutta condition results in the vorticity sheet rolling up into larger vortical structures prior to displacing downstream. Within the nomenclature of Ohashi and Ishikawa, Ω represents reduced frequency, however this value is twice what is presently used, k, as they utilize the chord length as opposed to the half chord.

Additionally, this reference attempts to provide numerical thresholds classifying the behavior and motion of the wake vorticity, between a slowly undulating wake through to rolled-up vortices similar to Figure 3.22. This is provided as a two-dimensional plot with normalized heaving amplitude versus reduced frequency. However, as stated in the reference, the transitions between these regions (of varying wake behavior) is not abrupt, but rather fairly continuous. Finally, this reference provides additional experimental scrutiny on the Kutta condition, specifically seeking to confirm that the flow does leave the airfoil at its sharp trailing edge even at the high reduced frequency conditions being considered. In addition to visual inspection of the Schlieren imagery, a configuration was implemented where a chemical reaction would take place if the flow from one side of the airfoil came into contact with the airfoil surface on the opposing side. For high reduced frequency conditions their results did find that this chemical reaction was occurring; however, this was determined not to be a breach of the Kutta condition, but rather a result of fluid mixing taking place due to the creation of the large vortex structures forming in the immediate vicinity of the airfoil trailing edge. In all cases, they found that the flow detached from the sharp airfoil trailing edge.

In terms of relevance of this reference to the present work, it provides visual results which clearly show that for unsteady, attached flow conditions the vorticity shed from the foil trailing edge can undergo very non-planar motion for reduced frequencies which are nominally characterized as being greater than a value of one. Specifically, counter-rotating vortex pairs manifest in the wake in a very similar manner to the development of a von-Kármán vortex street. Further, it is found that this non-planar wake behavior is exacerbated by the amplitude of the disturbance motion.

3.9 Bratt (1953)

The work of Bratt (1953) is also a flow visualization study performed in a subsonic wind tunnel which focuses specifically on the motion of the airfoil wake for nominally high reduced frequency conditions. The study utilizes a NACA 0015 airfoil subjected to sinusoidal heaving motion across a range of chord-based Reynolds numbers, $Re_c = 2.6 * 10^4 - 3.5 * 10^5$, and an approximate range of reduced frequencies, $k = 0.6 - 20$. The airfoil motion was a single frequency sinusoidal motion for various disturbance frequencies and freestream velocity conditions, and the chord and span of the airfoil were 20 inches and 60 inches, respectively. It is assumed that the flow is fully attached across the airfoil, though this particular condition is not explicitly confirmed. The flow visualization technique in this specific instance is a smoke trace introduced upstream of the airfoil, which is illuminated within the immediate vicinity of the airfoil trailing edge and downstream wake region.

A characteristic example of the visual results provided by this reference are copied directly and presented in Figure 3.23. In the nomenclature of Bratt, ω is the non-dimensional frequency parameter which utilizes chord length; therefore, ω listed within this reference is twice the value used within the present work, k. As can be seen in the characteristic example, for progressively increasing reduced frequency conditions the smoke trace is seen to undulate and then succinctly roll-up revealing a system of counter-rotating vortices in the airfoil wake, in a visually similar manner to a von-Kármán vortex street.

There is certainly a close visual similarity between these results and those of Ohashi and Ishikawa, however the lack of referenceable scale within these images largely prevents more direct and quantifiable comparisons. Further, the amplitudes of the heaving disturbances are different between the studies, which makes quantitative comparison not possible without a scale reference. Despite this, the visual results of this reference further corroborate that for higher reduced frequency conditions the shed vorticity does not follow a strictly planar trajectory, and in fact induces a non-trivial flow field in the immediate vicinity of the airfoil trailing edge. For high reduced frequency, sinusoidal disturbance motion conditions, this behavior of the flow field is understood to be a direct result of both the short wavelength of the shed vorticity distribution

the relatively large vorticity strength needed to enforce the Kutta condition. Conversely, for lower reduced frequencies (ex. frame 5 of Figure 3.23) the trace through the flow field appears much more benign, implying a planar and weaker vorticity distribution, at least within these zoomed views which only capture a fraction of the wavelength.

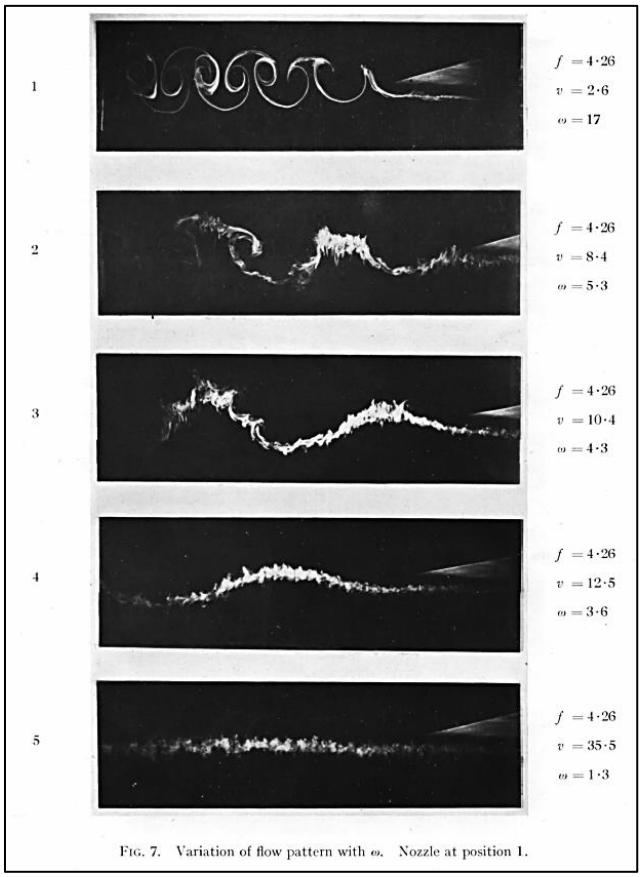

Figure 3.23. Characteristic example of the smoke trace images provided by Bratt (figure copied directly from reference)

3.10 Poling and Telionis

The work of Poling and Telionis (1986) involve an analytic assessment and review of the unsteady Kutta condition and its implications for attached flow at a high reduced frequency, as well as experimental LDV measurements and analysis of the unsteady velocity field for a two-hydrofoil system in a water tunnel. The upstream hydrofoil undergoes pitching about its quarter chord, where its wake then provides an unsteady inflow to the downstream hydrofoil positioned aft by 2 chord lengths. Both hydrofoils have a NACA 0012 profile and chord length of 4 inches. The chord-based Reynolds number is $2.0 * 10^4$, the reduced frequency is 2.4, and the peak-to-peak amplitude of the pitch oscillations is rather large, at 20 degrees. Significant discussion is provided about the implications of the Kutta condition and what evidence exists for the varying characteristics of the flow field in the immediate vicinity of the trailing edge.

All of the experimental data involves the unsteady velocity field, which does not permit a direct comparison to the Theodorsen model. However, conditionally-averaged measurements of the unsteady, trailing edge velocity field indicate that the flow certainly does oscillate according to the unsteady induced angle of attack. Additionally, a limited amount of interesting discussion is provided with regard to the unsteady streamwise velocities found at different flow field locations aft of the upstream, oscillating hydrofoil. The unsteady velocity at a location almost a chord length away from the hydrofoil in the chord-normal direction oscillates at the disturbance frequency, while the velocity at a location directly aft of the hydrofoil exhibits oscillations at twice the disturbance frequency.

3.11 Münch et al.

The work of Münch et al. (2010) is a mixed numerical and experimental effort for the forced and free motion of a pitching foil over a wide range of reduced frequencies from 0.02 to 100, at a chord-based Reynolds number of approximately 10^6. The foil utilized in this work is listed as having a "rounded trailing edge NACA 0009" profile, where a visual of the profile is provided. The chord and maximum thickness are listed as being 100 mm and 9.27 mm, respectively. The forced pitching motion is sinusoidal with a zero mean angle and a maximum amplitude of 2 degrees. The pitching axis is listed to be located at the foil center of mass, however, the specific chordwise location to which this corresponds does not appear to be listed. It is therefore assumed to be in the vicinity of the mid-chord.

The experiment was conducted in a water tunnel for freestream velocities of $5, 10,$ and 15 m/s, where the two-dimensional foil profile extended across the 150 mm span of the test section. Though the foil extends to the tunnel side walls, which should help minimize foil end effects, it is not fully clear if the low aspect ratio of the foil had an impact on these results. Six pressure sensors where installed on a single side of the foil in order to measure the unsteady pressure acting across the chord. These distinct pressure signals were utilized to calculate the subsequent pitching moment of the foil, under an assumption of symmetry across the foil thickness. It is the author's impression that this spatial discretization is likely too coarse, however, their experimental results are corroborated by their numerical results. Their CFD calculations are briefly summarized as URANS calculations on a structured mesh with a maximum cell thickness at the foil surface of $y^+ = y\, u_\tau/\nu = 5$, where u_τ is the friction velocity. All other pertinent details of the experimental and numerical conditions are left to the reference.

In the beginning sections of their results, example time series for a reduced frequency of 0.21 are provided for the coefficient of pressure at a single location and the pitching moment. It is the author's suspicion that there may be an error in the presentation of the pitching moment. It is listed as being in dimensional units (Nm), however, the magnitude appears to more appropriate for C_M. There is some added

uncertainty, as the location of the pitching axis is not specifically clear. For these reasons, direct comparisons of these time series results with the Theodorsen model are not presented.

A result that is extracted for direct comparison is the phase angle determined between the pitching motion and resulting pitching moment from their array of numerical results. This is copied and presented directly in Figure 3.24. Beside this is the digitized version of these results (labeled as ref. data) plotted with the corresponding phase dictated by the Theodorsen model for three different values of the pitching axis. These selected pitch axis locations are representative values as the specific location is not quite clear, as well as they convey the sensitivity of this variable. As a note, a negative sign was applied to the Theodorsen-based phase angle, in order to coincide with the apparent orientation of this reference. As can be seen, the trend of the phase angle between the pitching moment and pitching motion is certainly captured well by the Theodorsen model, however the prediction is generally 5 to 10 degrees higher than the values of this reference, which come from calculations in this instance.

a)

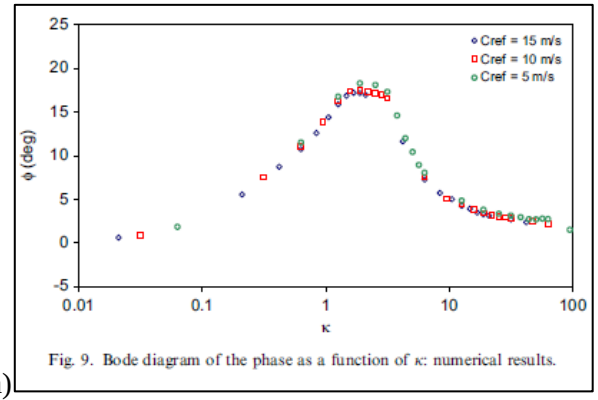

b)

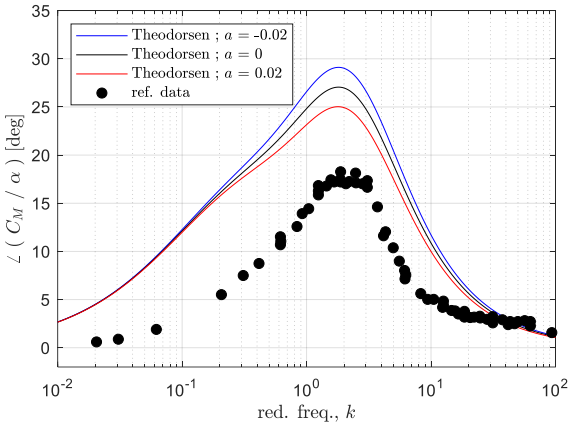

Figure 3.24. Phase of the pitching moment response as a function of reduced frequency
a) figure copied directly from source material, b) application of Theodorsen model

This reference also presents views of the calculated flow field in the immediate vicinity of the foil trailing edge. Figure 3.25 provides these views, copied directly from the reference, which plot the scaled vorticity field at four distinct reduced frequencies, all of which are greater than a value of one. These views

of the flow field reinforce the observations that for representatively high reduced frequencies the shed vorticity clearly deviates from the planar assumption, and coalesces into counter-rotating vortices.

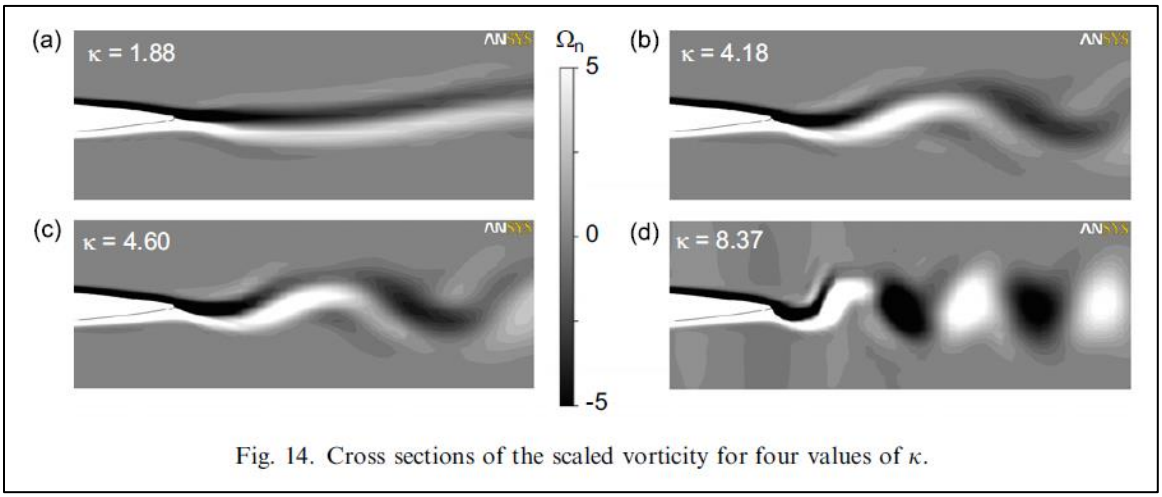

Fig. 14. Cross sections of the scaled vorticity for four values of κ.

Figure 3.25. Flow field of shed vorticity from Münch et al. (copied directly from reference)

3.12 Liu et al.

The reference of Liu et al. (1990) consists of Laser Doppler Anemometry (LDA) and hot-wire anemometry measurements in the immediate vicinity of an airfoil that is subjected to unsteady pitching conditions. Their work consists of a wind tunnel configuration at incompressible flow conditions utilizing a two-dimensional, NACA 0012 airfoil at a chord-based Reynolds number of $Re_c = 1.25 * 10^5$ and a reduced frequency of $k = 2.0$. The foil is placed at a mean angle of attack of 0 degrees (as stated in the figure captions) with an oscillation amplitude of $\pm$ 4.6 degrees. For reference, the foil is static and the disturbances are induced by a downstream rotating ellipse.

Limited results are presented within this reference, however, it is shown and discussed that the mean wake streamline does deviate from a chordline-extended trajectory in an oscillatory motion for this nominally high reduced frequency operating condition. The mean wake streamline is defined as both the location of the minimum tangential velocity component (mean cross-stream component) and where the Reynolds stress changes sign for measurement locations traversing in the chord-normal direction; these criteria yielded effectively the same spatial location. Though this reference is limited to a single condition, it adds to the evidence that for high reduced frequency conditions the wake vorticity, even in the immediate vicinity of the airfoil trailing edge, does not follow a strictly planar trajectory. Simply for visual clarity, the final two figures of this reference are copied and presented here as Figure 3.26.

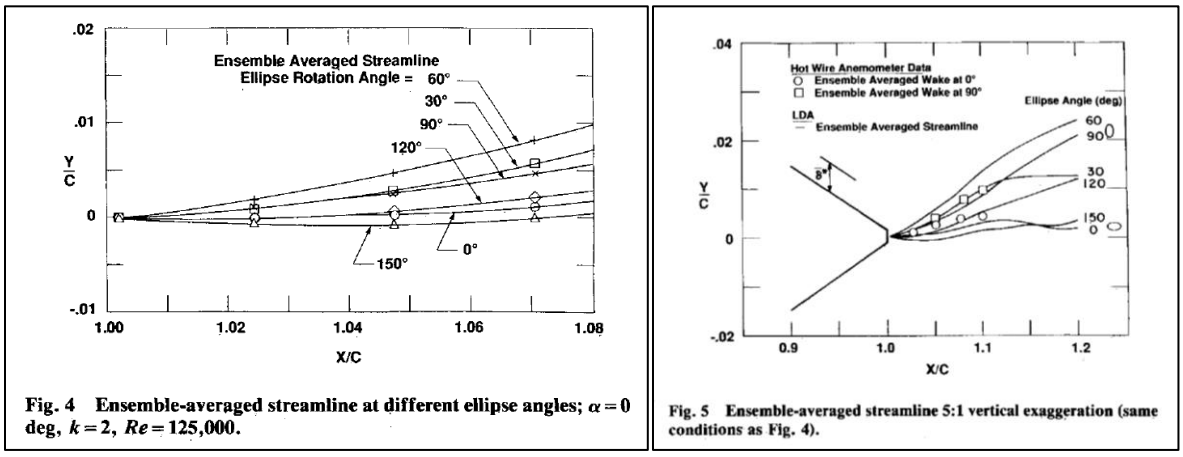

Fig. 4 Ensemble-averaged streamline at different ellipse angles; $\alpha = 0$ deg, $k = 2$, $Re = 125{,}000$.

Fig. 5 Ensemble-averaged streamline 5:1 vertical exaggeration (same conditions as Fig. 4).

Figure 3.26. Mean wake streamlines from Liu et al. (figures copied directly from reference)

3.13 Basu and Hancock

The work of Basu and Hancock (1978) involves the discussion of its development and the demonstration of a potential flow panel method utilized for arbitrary unsteady motion. Specifically, the following unsteady conditions are implemented: 1) an impulsive change in angle of attack, 2) high frequency pitching oscillations, and 3) an airfoil encountering a sharp-edged upwash gust. Of direct consequence to the present work is the high frequency pitching oscillation configuration. The opening material of Basu and Hancock concentrates on a description of the calculation approach and the treatment and handling of the Kutta condition. Several important analytical and practical considerations are discussed relative to the trailing edge flow region, the shedding of vorticity, and the appropriate conditions which should exist (or be enforced) in this very sensitive region of the flow field.

It is however the numerical results for the airfoil undergoing unsteady pitching motion that are of direct interest in the present setting. As their results are from a potential flow, panel method calculation the Reynolds number is an ill-defined quantity, and it is the reduced frequency which fully describes the flow condition. In the nomenclature of Basu and Hancock, the reduced frequency is $\nu = \frac{\omega c}{U_\infty} = 20$, which under the present definition corresponds to $k = 10$. The implemented airfoil is an 8.4% thick, symmetric, Von Mises profile section which is undergoing pitching about its leading edge over an amplitude of 0.01 radians (i.e. 0.573 degrees) with no mean angle of attack or separated flow. The numerical results from these conditions are quite interesting in relation to the Theodorsen model, as the disturbance motion is small, however, the reduced frequency is high, the airfoil occupies finite area, and the shed vorticity within the flow field is not constrained. Simply for visual orientation, the following two figures pertaining to these results are copied directly out of this reference and presented in Figure 3.27. These figures illustrate that the shed vorticity rolls up into larger vortical structures, as well as how the specific point vortices are distributed.

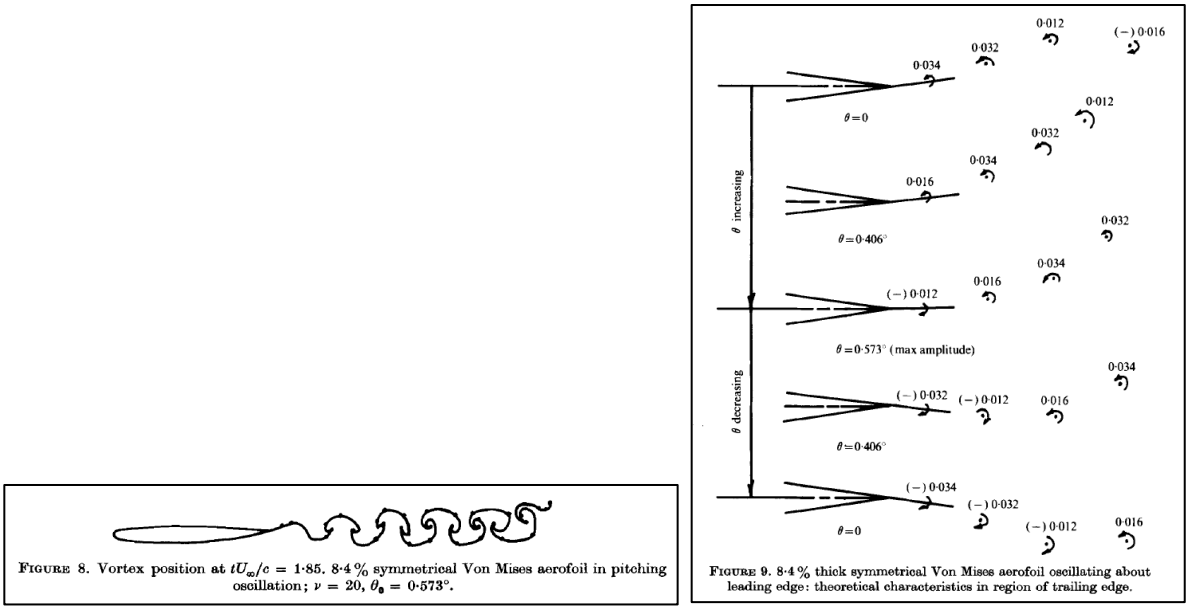

FIGURE 8. Vortex position at $tU_\infty/c = 1{\cdot}85$. 8·4 % symmetrical Von Mises aerofoil in pitching oscillation; $\nu = 20$, $\theta_0 = 0{\cdot}573°$.

FIGURE 9. 8·4 % thick symmetrical Von Mises aerofoil oscillating about leading edge: theoretical characteristics in region of trailing edge.

Figure 3.27. Nature of the shed wake from Basu and Hancock (figures copied directly from reference)

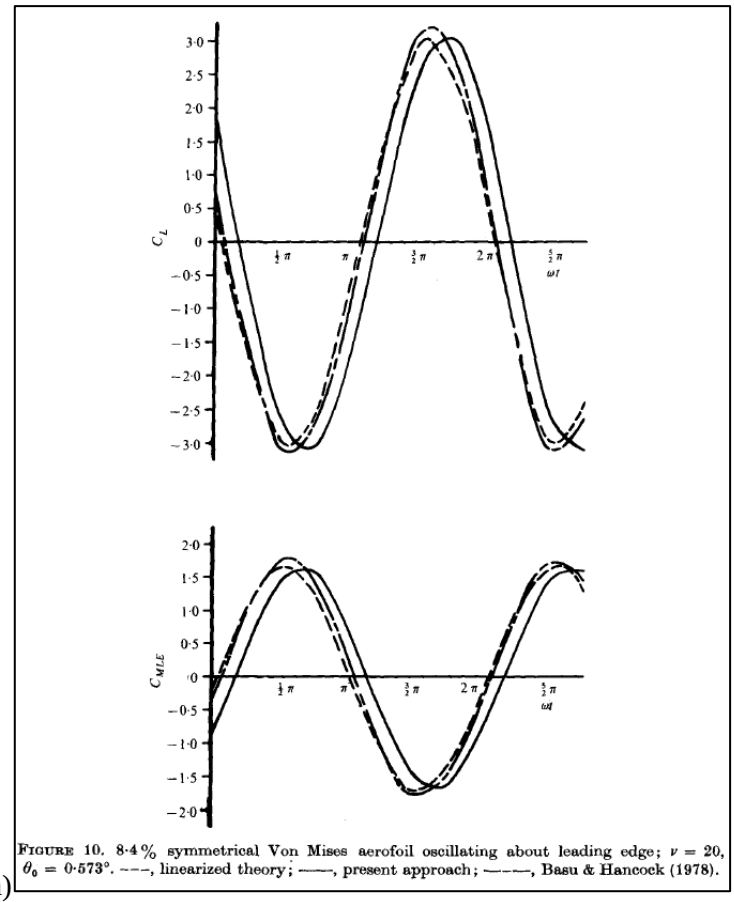

FIGURE 10. 8·4 % symmetrical Von Mises aerofoil oscillating about leading edge; $\nu = 20$, $\theta_0 = 0{\cdot}573°$. – – –, linearized theory; ——, present approach; — — —, Basu & Hancock (1978).

a)

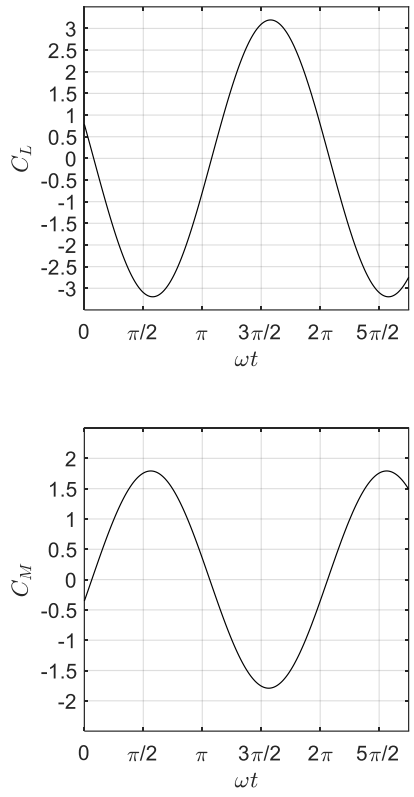

b)

Figure 3.28. Comparison of unsteady lift and pitching moment coefficients from Basu and Hancock

a) figure copied directly from source material, b) application of Theodorsen model

The figure from Basu and Hancock which presents time series of the unsteady lift coefficient and pitching moment coefficient are again copied directly from the reference, and presented here as Figure 3.28a. Correspondingly, Figure 3.28b presents the time series which result from a strict application of the Theodorsen model. Beginning with the unsteady lift expression from the Theodorsen model as presented in Section 2.7 where $\dot{h} = \ddot{h} = 0$, $a = -1$,

$$\frac{C_L}{\alpha} = 2\pi C + i\pi[1 + 3C]k - \pi k^2 \tag{3.23}$$

For the present conditions, this results in,

$$\left|\frac{C_L}{\alpha}\right| = 319.6 \quad ; \quad \angle\frac{C_L}{\alpha} = \phi_{C_L} = 2.89\, rad \quad ; \quad C_L = \left|\frac{C_L}{\alpha}\right| |\alpha| \sin(\omega t + \phi_{C_L}) \tag{3.24}$$

An identical development is followed for the unsteady pitching moment coefficient,

$$\frac{C_M}{\alpha} = -\frac{\pi}{2}C + i\pi\left[-\frac{3}{4}C - \frac{3}{4}\right]k + \frac{\pi}{2}\left(\frac{1}{8} + 1\right)k^2 \tag{3.25}$$

$$\frac{C_M}{\alpha} = -\frac{\pi}{2}C - i\frac{3\pi}{4}[C + 1]k + \frac{9\pi}{16}k^2 \tag{3.26}$$

which yields,

$$\left|\frac{C_M}{\alpha}\right| = 179.2 \quad ; \quad \angle\frac{C_M}{\alpha} = \phi_{C_M} = -0.199\, rad \quad ; \quad C_M = \left|\frac{C_M}{\alpha}\right| |\alpha| \sin(\omega t + \phi_{C_M}) \tag{3.27}$$

These corresponding C_L and C_M time series are plotted directly alongside the results of Basu and Hancock in Figure 3.28. It is not directly clear, but the "linearized theory" time traces within the Basu and Hancock figure are described in the text as being from "standard linearized theory" which is presumed to be the Theodorsen model, though again, it is not certain. The comparison between the results of Basu and Hancock to those of implementing the Theodorsen model is quite good in terms of magnitude and phase properties of these unsteady airfoil responses, at least as far as can be discerned from these figures. The lack of definitive demarcation along the abscissa of the source material renders detailed evaluation and comparison of the phase properties of these responses difficult; however, the results are certainly close.

It is of direct interest to the present study that these results are for conditions of an airfoil of finite profile, at a high reduced frequency, and with an un-constrained wake of shed vorticity; however, further

assessment beyond the time series comparison is difficult given that this is for a single condition and more results are not available. The Theodorsen model is found to certainly provide an admirable prediction of these numerical results, though it remains unclear as to if the motion of the shed vorticity or the foil profile, as examples, have specific effects on these airfoil responses. It is noted however, that these calculated foil responses are slightly phase lagged from the linearized theory responses, which would seem to corroborate with the results found in the present work.

3.14 Strangfeld et al.

The work of Strangfeld et al. (2015) incorporates a combined experimental, computational, and theoretical campaign on the effects of pitching and surging disturbances for a NACA 0018 airfoil at various operating conditions and flow regimes. It focuses on several conditions which are of interest (ex. an oscillating freestream, and dynamic stall) and assesses various theoretical models, though this discussion is not specifically germane to the present emphasis of the Theodorsen model. However, one of their conditions is an airfoil undergoing oscillations in pitch and is compared directly to the Theodorsen model. Both experimental and numerical (URANS) results are presented for the NACA 0018 airfoil at a chord-based Reynolds number of $3 * 10^5$ at two distinct reduced frequencies, $k = 0.08$ and 0.263. The airfoil is assumed to be pitching about its midchord (as this is not explicitly clear within the reference), sweeping through an amplitude of $\pm$ 2 degrees at a mean angle of attack of 2 degrees. The unsteady lift results from these two reduced frequency conditions are presented as hysteresis loops, which have been copied directly from the reference and presented here in Figure 3.29. The experimental and numerical results are compared directly to the Theodorsen model within the reference, which is seen to provide a reliable prediction of the experimental results.

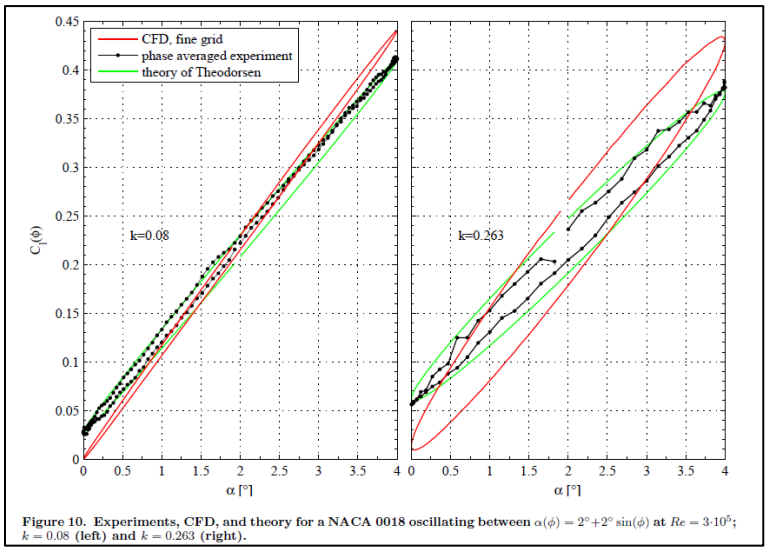

Figure 10. Experiments, CFD, and theory for a NACA 0018 oscillating between $\alpha(\phi) = 2° + 2° \sin(\phi)$ at $Re = 3{\cdot}10^5$; $k = 0.08$ (left) and $k = 0.263$ (right).

Figure 3.29. Hysteresis loops of C_L as a function of α for a pitching airfoil, as provided by Strangfeld et al. (figures copied directly from reference)

In the spirit of assessing these results in a similar manner as to the analysis of the present work, the unsteady lift transfer function from Section 2.7 of the Theodorsen model expression is utilized where $\dot{h} = \ddot{h} = 0$, and $a = 0$,

$$\frac{C_L}{\alpha} = 2\pi C + i\pi[1 + C]k \tag{3.28}$$

Expressing the unsteady lift transfer function in this way fully describes the normalized unsteady response, and in order to compare to the Strangfeld et al. results the following is considered. The unsteady lift is superimposed onto the steady contribution of the lift from the mean angle of attack, $\bar{\alpha}$, from lifting line theory, and the magnitude of the unsteady lift response is scaled by the disturbance amplitude, α'. The maximum and minimum predicted lift coefficients are expressed in the following way and tabulated in Table 3.2 for the two distinct reduced frequencies. As can be seen, the maximum and minimum C_L values from Table 3.2 compare very favorably to the results of Strangfeld et al. represented here in Figure 3.29.

$$C_L = 2\pi\bar{\alpha} + \left|\frac{C_L}{\alpha}\right|\alpha' \sin(\omega t + \phi) \quad ; \quad \phi = \angle\left(\frac{C_L}{\alpha}\right) \quad ; \quad \alpha = \bar{\alpha} + \alpha' \sin(\omega t) \tag{3.29}$$

$$C_{L,max} = 2\pi\bar{\alpha} + \left|\frac{C_L}{\alpha}\right|\alpha' \quad ; \quad C_{L,min} = 2\pi\bar{\alpha} - \left|\frac{C_L}{\alpha}\right|\alpha' \tag{3.30}$$

Table 3.2. Maximum and minimum unsteady C_L from the Theodorsen model for Strangfeld et al. results

k	$C_{L.max}$	$C_{L,min}$
0.08	0.410	0.028
0.263	0.375	0.064

Although the results of Strangfeld et al. are presented with a direct comparison to the Theodorsen model (as stated), the corresponding hysteresis loops based on the expressions above are presented for reference in Figure 3.30. These also compare favorably to the prior figure; however, with detailed inspection of the theoretical hysteresis loops some differences are present, the source of which is unclear (this is possibly due to the uncertainty of the pitch axis). Specifically, there is a slight difference in the eccentricities of the Theodorsen loops for the higher reduced frequency condition. Despite these slight

differences, it can be seen that the experimental results of this reference are predicted well by the Theodorsen model.

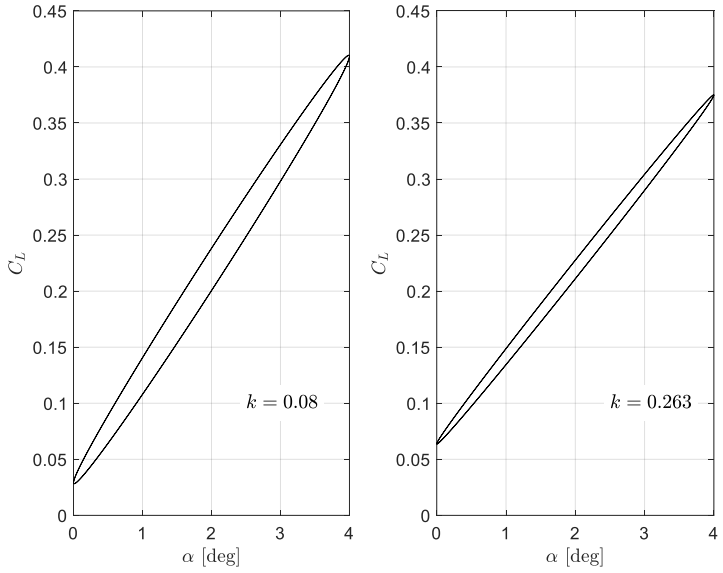

Figure 3.30. Hysteresis loops of C_L from implementing the Theodorsen model

3.15 Ashraf et al.

The work of Ashraf et al. (2011) is a parametric computational study using unsteady RANS of variable thickness, two-dimensional NACA airfoils undergoing various plunging and combined plunging and pitching motions across a wide range of chord-based Reynolds numbers from $2 * 10^2 - 2 * 10^6$ at a distinct reduced frequency of 2.0 (under their definition). This reference of Ashraf et al. is not particularly well-aligned in relation to the motivations and enforced constraints of the present study, in that generally large airfoil motions are considered such that leading edge vorticity shedding is induced, the role of viscosity is particularly important, and a majority of the results are presented and assessed in terms of mean thrust and propulsive efficiency metrics. However, a select set of results are presented as time series, which can be assessed relative to the Theodorsen model. An example of these results is copied directly from the Ashraf et al. document and provided as Figure 3.31. This involves time traces of C_L which are presented for airfoils of two different thicknesses. A complex C_L response is seen despite the sinusoidal variation of the plunging (i.e. heaving) motion, which is attributed to the non-linearity of the flow field and the leading edge shed vorticity. However, these unsteady C_L responses do exhibit harmonic character and appear to be generally dominated by a single-frequency sinusoid.

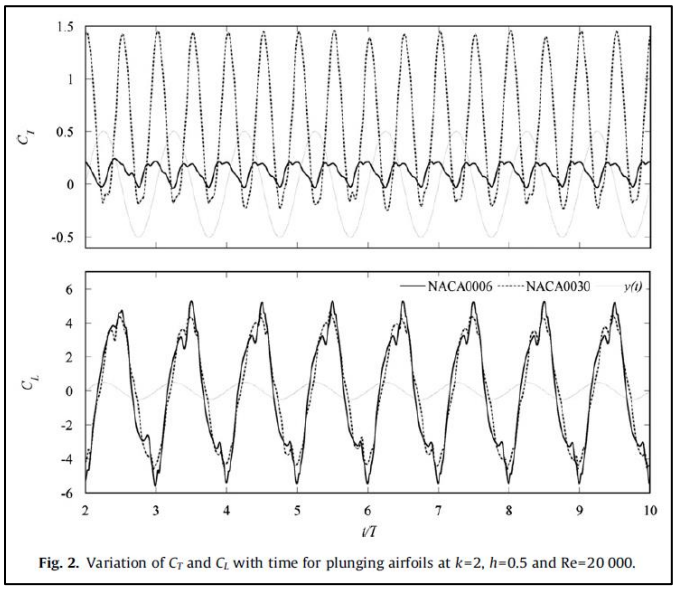

Fig. 2. Variation of C_T and C_L with time for plunging airfoils at k=2, h=0.5 and Re=20 000.

Figure 3.31. Time traces of unsteady thrust and lift coefficients from Ashraf et al. (figure copied directly from reference)

Beginning with the unsteady lift expression as a result of heave-only motion from the Theodorsen model as presented in Section 2.7,

$$\frac{C_L U_\infty}{\dot{h}} = 2\pi C + i\pi k \tag{3.31}$$

Strictly assessing the C_L results of Figure 3.31 in terms of the Theodorsen model, the magnitude of the C_L response and phase relative to the disturbance motion can be found; however two points need to be acknowledged. First, the reduced frequency of Ashraf et al. is defined with the chord length and not half chord as in the Theodorsen model. Second, their variable h is a non-dimensional plunge amplitude which is normalized on chord. Both of these considerations are accounted for in the following analysis of the predicted unsteady lift coefficient magnitude and phase from the Theodorsen model.

$$C_L = \left(\frac{\dot{h}}{U_\infty}\right)(2\pi C + i\pi k) = \left(\frac{i\omega h}{U_\infty}\right)(2\pi C + i\pi k) = \cdots$$
$$\left(i\frac{\omega b}{U_\infty}\frac{h}{b}\right)(2\pi C + i\pi k) = \left(ik\frac{h}{b}\right)(2\pi C + i\pi k) \tag{3.32}$$

For the specific reduced frequency of 2.0 (under the Ashraf et al. definition; $k = 1.0$ under the present definition),

$$C_L|_{k=1} = \left(i(1)\left(\frac{(0.5)(2b)}{b}\right)\right)\left(2\pi C|_{k=1} + i\pi(1)\right) = -2.51 + i3.39 \tag{3.33}$$

this yields the following C_L magnitude and phase relative to the heaving motion,

$$\left|C_L\right|\Big|_{k=1} = 4.22 \;\; ; \;\; \angle C_L = 126.5^o \tag{3.34}$$

The values above define the unsteady C_L response, however, for visual assessment and confirmation Figure 3.32 presents the earlier C_L plot from Ashraf et al. alongside sinewaves of the disturbance motion and unsteady lift response with the characteristics listed above. A negative sign was applied to the C_L trace of Figure 3.32b given the potential ambiguity between the specific orientations of the variables.

As can be seen, the predicted results from implementing the Theodorsen model do reliably account for the bulk characteristics of the unsteady C_L response for this heaving motion. As this is a single-input single-output model, it does not (and cannot) capture the complex response being induced at other

frequencies from more complex flow behavior. However, despite this character and the fact that a range of foil thicknesses are being considered (6% and 30%), which could be seen as violations of the Theodorsen model assumptions, this model yields admirable results.

a) 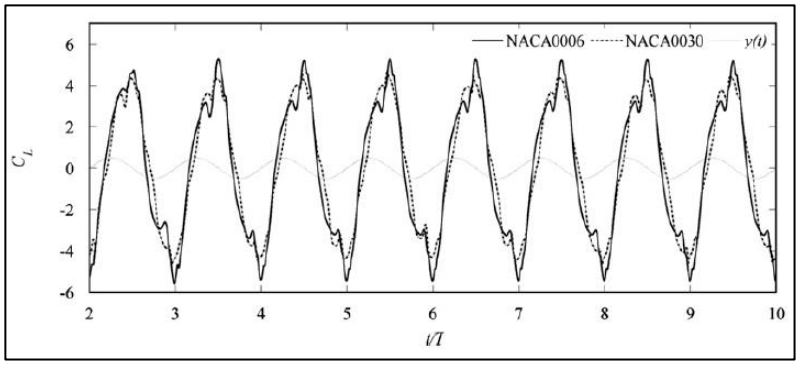

b) 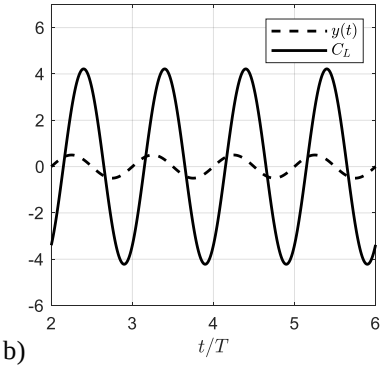

Figure 3.32. Comparison of C_L time traces from a) Ashraf et al. to b) the Theodorsen model

3.16 Summary of Literature Review Findings

The previous subsections reviewed the data and findings of several references with respect to the unsteady responses and associated flow fields for foils experiencing both heaving and pitching motion disturbances. The review of these results are cast specifically such that they are assessed in the same approach as that used for the findings of the present study. Specifically, assessing the reference results relative to the Theodorsen model in a Bode plot format, when possible, and attempting to identify any deviations resulting from not strictly adhering to the assumptions made by the model. It is additionally beneficial to review and assess these results in a common format, as direct comparison is often difficult because of the various ways in which results are provided. The following lists provide the major findings from this review of the technical literature, in terms of how they apply directly to the motivations and results of the present effort. These are broken into two categories: Unsteady Foil Responses, and Shed Vorticity and Velocity Field.

Unsteady Foil Responses:

- Examples of unsteady lift, pitching moment, and differential pressure are assessed relative to the associated predictive expressions of the Theodorsen model within this technical review
- This data is generally available for reduced frequencies between the approximate range of $10^{-2} < k < 10^{0}$, which is a primary consequence of most cases being aerodynamic configurations
- Some results are available for conditions where $k > 1$, though they are less prevalent
- Over the lower range of reduced frequencies, the Theodorsen model is seen to be robust and to reliably predict unsteady foil responses for the following conditions:
    - low amplitude oscillations
    - low to moderate mean angles of attack
    - fully attached flow conditions

    - symmetric and lightly cambered foil profiles of moderate thickness
    - subsonic freestream conditions
- When differences between the measured and modeled results do occur, the cause is not always explicitly clear
- In terms of observed uncertainty of magnitude and phase differences in the unsteady responses between applicable measured data and the Theodorsen model as assessed through Bode plots, magnitude differences of $\pm\ 2\ dB$ and phase angle differences of $\pm\ 10$ degrees are typical
- As larger disturbance motions and mean angles of attack are considered, transient flow separation occurs, which can significantly alter the unsteady foil responses
- Altered responses are affected both in terms of magnitude and phase characteristics, where the particular effects are dependent upon the implemented configuration and operating conditions

Shed Vorticity and Velocity Field:

- For small disturbance motions and attached flow conditions, the validity of the Kutta condition is maintained, even at progressively elevated reduced frequency conditions
- The assumption of a planar shed vorticity wake appears valid for lower reduced frequency conditions, as the subsequent wavelength of the vorticity distribution extends over a large spatial extent
- As reduced frequency is increased above an approximate threshold of $k \approx 1$, the shed vorticity is seen to become non-planar, from both measured and calculated results
- Through self-interaction, the shed vorticity is seen to undulate and roll-up onto itself forming prominent vortical structures of opposing strength
- It is unclear if or in what specific ways this behavior of the shed vorticity affects any of the unsteady foil responses

4. Results

As a supplement to the titles of the subsequent subsections, the following is a brief description of each. Section 4.1 presents dimensional analysis of the governing equations in order to provide criteria for which results based in potential flow should be expected to compare to either higher fidelity numerical calculations or experimental results. The criteria are equally applicable to all conditions, however have particular application to high reduced frequency conditions where $k > 1$. Sections 4.2 and 4.3 concentrate on the unsteady responses from flat foils for small-scale, sinusoidal heaving and mid-chord pitching motions, respectively. A primary purpose for these is to compare directly to the Theodorsen model, in addition to showing the distinct decomposition of results offered by UPF, and effects of mobility of the shed vorticity from the foil trailing edge on the foil responses. While development of the Theodorsen model is based strictly on sinusoidal motion at a single frequency, it can be equally applied for broadband, statistically stationary motion; Section 4.4 presents an example of this for flat foil conditions.

Sections 4.5 and 4.6 again concentrate on unsteady foil responses from heaving and pitching motions, but for Joukowski foils of variable finite thickness. Attention is paid to when deviations from the Theodorsen model are seen, and analytically based expressions for these augmented responses are developed. Section 4.7 concentrates on the unsteady response of the streamwise force, where UPF and open literature results are presented along with newly developed predictive expressions for this response. Table 4.1 provides a quick summary of these topic areas and the associated disturbance motion.

Table 4.1. Summary of UPF results

	heaving	mid-chord pitching
thin foil UPF results compared to Theodorsen model	✓	✓
effects of wake non-linearity due to disturbance motion of variable amplitude	-	✓
analysis of UPF calculations with broadband disturbance motion	-	✓
altered responses for thick foil UPF results and development of augmented predictive expressions	✓	✓
discussion of unsteady streamwise force response, development of modeling expressions, and analysis of thin and thick foil UPF results	✓	✓

4.1 Criteria for Comparing to Potential Flow Results at High Reduced Frequencies

As discussed in the opening material, a central motivation of the present work is that the foil disturbance motions that are to be considered are small. From this, qualitative and quantitative criteria can be established for acceptable motion conditions. However, it is not always clear what the effects of these various considerations for real flows are (i.e. vorticity shedding from the leading edge, compressibility effects, viscosity effects, etc.) across the wide range of reduced frequencies to be presently considered relative to the potential flow framework of the Theodorsen model, as well as the present UPF calculations. Therefore, in addition to the description discussed earlier, the development within this section establishes further conditions for the applicability of results based on potential flow for elevated reduced frequency values.

The following analysis culminates in a set of criteria that are necessary to be met in order for the results from unsteady potential flow calculations, the Theodorsen model, and the Euler equations (i.e. compressibility effects) to be equitably compared given that their underlying governing equations are different. This begins with the Continuity equation,

$$\frac{\partial \rho}{\partial t} + \nabla \cdot \left(\rho \vec{V}\right) = 0 \tag{4.1}$$

which can be recast into the following by employing the definition of the velocity as the gradient of a potential, $div\left(\vec{V}\right) = div(\nabla\phi) = \nabla^2\phi$, such that,

$$\nabla^2\phi + \frac{1}{\rho}\frac{\partial \rho}{\partial t} + \frac{1}{\rho}\vec{V} \cdot \nabla\rho = 0 \tag{4.2}$$

Written in this way, it is clear that this expression simplifies to Laplace's equation, $\nabla^2\phi = 0$, for an incompressible fluid. The goal is to then define these additional two terms based on velocity and flow potential, and not fluid density. This is achieved by arriving at the unsteady Bernoulli equation from the Momentum equation (which is not recreated here, as it was discussed earlier and is readily available). In order to populate the term above, two expressions are developed from the following steps: 1) taking the

time derivative of the unsteady Bernoulli equation, and 2) taking the velocity dot product with the gradient of the unsteady Bernoulli equation. Taking these steps (also available in several texts, for example Bisplinghoff et al.) yields the following,

$$1)\quad \frac{\partial}{\partial t}\left[\frac{\partial \phi}{\partial t}+\frac{V^2}{2}+\int\frac{\partial P}{\rho}\right]=0\quad;\quad 2)\quad \vec{V}\cdot\nabla\left[\frac{\partial \phi}{\partial t}+\frac{V^2}{2}+\int\frac{\partial P}{\rho}\right]=0 \tag{4.3}$$

$$\frac{\partial^2\phi}{\partial t^2}+\frac{1}{2}\frac{\partial V^2}{\partial t}+\frac{1}{\rho}\frac{\partial P}{\partial t}=0\quad;\quad \vec{V}\cdot\left[\frac{\partial \nabla\phi}{\partial t}+\nabla\left(\frac{V^2}{2}\right)+\frac{1}{\rho}\nabla P\right]=0 \tag{4.4}$$

$$\frac{1}{\rho}\frac{\partial P}{\partial \rho}\frac{\partial \rho}{\partial t}=-\frac{\partial^2\phi}{\partial t^2}-\frac{1}{2}\frac{\partial V^2}{\partial t}\quad;\quad \vec{V}\cdot\left[\frac{\partial \vec{V}}{\partial t}+\nabla\left(\frac{V^2}{2}\right)+\frac{a_\infty^2}{\rho}\nabla\rho\right]=0 \tag{4.5}$$

$$\frac{a_\infty^2}{\rho}\frac{\partial \rho}{\partial t}=-\frac{\partial^2\phi}{\partial t^2}-\frac{1}{2}\frac{\partial V^2}{\partial t}\quad;\quad \frac{1}{\rho}\vec{V}\cdot\nabla\rho=-\frac{1}{a_\infty^2}\left[\vec{V}\cdot\frac{\partial \vec{V}}{\partial t}+\vec{V}\cdot\nabla\left(\frac{V^2}{2}\right)\right] \tag{4.6}$$

$$\frac{1}{\rho}\frac{\partial \rho}{\partial t}=-\frac{1}{a_\infty^2}\left[\frac{\partial^2\phi}{\partial t^2}+\frac{1}{2}\frac{\partial V^2}{\partial t}\right]\quad;\quad \frac{1}{\rho}\vec{V}\cdot\nabla\rho=-\frac{1}{a_\infty^2}\left[\frac{1}{2}\frac{\partial V^2}{\partial t}+\vec{V}\cdot\nabla\left(\frac{V^2}{2}\right)\right] \tag{4.7}$$

using $\partial P/\partial\rho = a_\infty^2$, where a_∞ is the freestream speed of sound. Substituting the right-hand sides of the two expressions above into Equation 4.2 yields the following expression applicable to unsteady, compressible potential flow,

$$\nabla^2\phi-\frac{1}{a_\infty^2}\left[\frac{\partial^2\phi}{\partial t^2}+\frac{\partial\, V^2}{\partial t}+\vec{V}\cdot\nabla\left(\frac{V^2}{2}\right)\right]=0 \tag{4.8}$$

It is on this expression that dimensional analysis is performed. The bracketed term needs to be negligible relative to the Laplacian of the flow potential in order for there to be an expectation that unsteady potential flow results would be comparable to unsteady results based on the Euler equations, Reynolds-Averaged Navier-Stokes, or experimentation.

The Prandtl-Glauert compressibility correction due to elevated freestream Mach numbers (which incorporates a factor of $1/\sqrt{1-M_\infty^2}$) is based on neglecting the time derivative terms in the governing expression above. The present consideration however, is to not make this assumption and to ensure the

following, where it is broadly assumed that the velocity, flow potential, and subsequent spatial derivative terms are all of the order of ϵ, such that,

$$O(\epsilon) \gg \frac{1}{a_\infty^2}[O(\ddot{\epsilon}) + O(\dot{\epsilon}) + O(\epsilon)] \tag{4.9}$$

while the time derivatives lead to the higher order terms. It is recognized that the units of $O(\epsilon)$ are $1/s$, and therefore the following is written utilizing the general flow parameters which define the reduced frequency,

$$\frac{U_\infty}{b} \gg \frac{1}{a_\infty^2}\left[\omega^2 U_\infty b + \omega U_\infty^2 + \frac{U_\infty^3}{b}\right] \tag{4.10}$$

Rearranging this expression,

$$1 \gg \frac{U_\infty^2}{a_\infty^2}\left[\frac{\omega^2 b^2}{U_\infty^2} + \frac{\omega b}{U_\infty} + 1\right] \tag{4.11}$$

$$1 \gg M_\infty^2[k^2 + k + 1] \tag{4.12}$$

where M_∞ is the freestream Mach number.

This dimensional analysis yields the following three criteria in order for higher fidelity calculations or experimental results to be at appropriate conditions to be compared to potential flow results. Each of the following must be true,

$$M_\infty^2 \ll 1 \quad ; \quad kM_\infty^2 \ll 1 \quad ; \quad k^2 M_\infty^2 \ll 1 \tag{4.13}$$

Therefore, in addition to only considering subsonic freestream Mach numbers, for conditions of $k > 1$ (generally considered high reduced frequency conditions in the present work) the Mach number must be further reduced in order to avoid compressibility effects. The calculation conditions which are considered include reduced frequencies which are significantly greater than one, and therefore the Mach number for these conditions has been subsequently lowered as needed according to these criteria.

During the development of the current work, high reduced frequency TURNS2D calculations were executed which violated these conditions and some effects on the unsteady foil responses were seen.

Specifically, these conditions and the associated C_L responses were implemented in the CFD sensitivity study provided in Figure 2.18. For these calculations, the implemented reduced frequency was 20.0 and the freestream Mach number was 0.1. Though this is certainly a subsonic Mach number, this operating condition yields $kM_\infty^2 = 0.2$ and $k^2M_\infty^2 = 4.0$, which clearly violates the third criterion. While these C_L responses appear sinusoidal and do not exhibit any obvious oddity, upon closer inspection it is clear that the phase relative to the disturbance motion does not follow the Theodorsen model. The characteristics of the unsteady lift transfer function are presented and discussed throughout the present work. At a high reduced frequency condition the C_L response of the Theodorsen model approaches a 90 degree phase lead relative to the disturbance pitch motion about the foil mid-chord, while the results of Figure 2.18 exhibit a slight phase lag. Though not explicitly presented as in the following sections, the amplitude of these C_L responses do agree with that of the Theodorsen model. In this instance, it appears that the phase of the C_L response is the characteristic which is primarily affected by violating these criteria on the flow conditions. These results should be considered anecdotal however, and consequently be seen as a practical example of these criteria on the flow conditions, as this is not a systematic assessment. Additional examples could come from the results within the references of Young and Lai (2004) and Münch et al. (2010) which also exhibit foil response behavior which varies at elevated reduced frequencies. A systematic assessment of the implications of these criteria is suggested as an avenue for further study.

4.2 Heave Disturbances for Flat Foils at Discrete Frequencies

4.2.1 Unsteady Lift and Pitching Moment Responses Compared to the Theodorsen Model

This section concentrates on the foil responses determined from UPF calculations relative to the Theodorsen model for numerically thin foils undergoing unsteady, small-scale, sinusoidal heaving motion at several discrete frequencies. To begin, two examples of time series from these UPF results are presented in Figure 4.1 for reduced frequencies, k, of 0.2 and 2.0 . There are two vertical axes on these plots, one for the normalized heave velocity signal (left) and one for the unsteady lift coefficient (right). As can be seen, the sinusoidal disturbance heave velocity is the same between these two calculations, but the sinusoidal lift response is varied in both amplitude and phase, as a result of the varied reduced frequency. Despite the small magnitude of the disturbance motion (corresponding to $|\alpha| = 0.1^o$), these initial views of the UPF results do not exhibit numerical aberrations, which provides confidence that the calculation is adequately sampled in both time and space (across the foil and in the wake). Convergence of results was performed separately during development of the UPF calculation approach, however these UPF results are based in potential flow and therefore do not have the same convergence considerations as most typical CFD configurations.

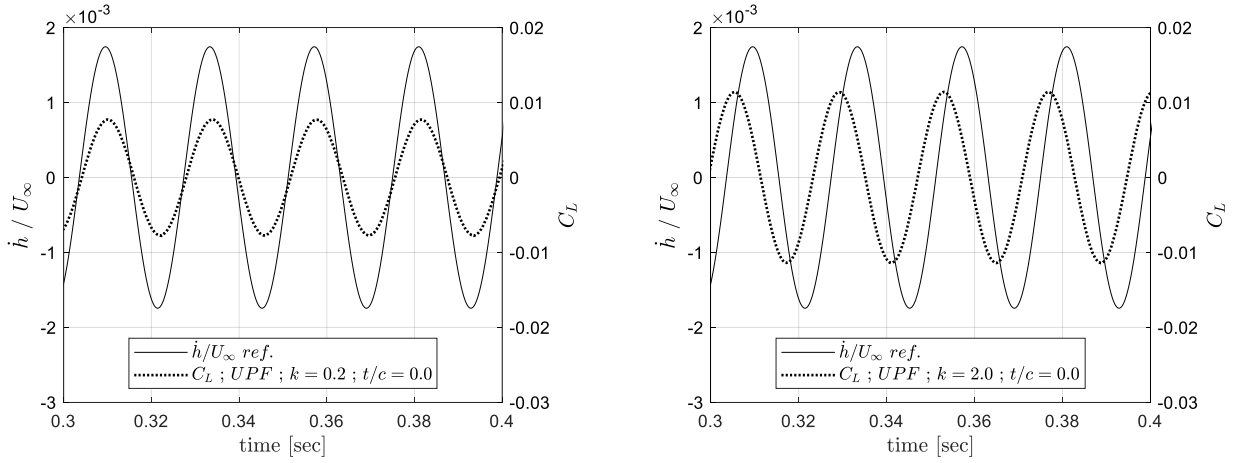

Figure 4.1. Time series of unsteady heave velocity and lift coefficient for sinusoidal heave calculations

While all UPF calculations are performed explicitly in the time domain, a primary motivation of this work is to assess the complex-valued transfer functions of unsteady foil response in the frequency domain. Figure 4.2 and Figure 4.3 present Bode plots of the calculated unsteady lift and pitching moment, respectively, for numerically thin foils undergoing unsteady heaving motion. These UPF results are performed at discrete reduced frequencies and compared directly to the associated Theodorsen expressions (Eq. 2.49 and Eq. 2.52). The reduced frequency axes of the top (magnitude) and bottom (phase) plots are aligned, and the gray band around the Theodorsen line is a $\pm$ 1 decibel visual aid. The comparison of these UPF results to the Theodorsen model is very good for both magnitude and phase characteristics for both unsteady lift and pitching moment responses over the wide range of reduced frequencies being considered. These results are taken as foundational towards the veracity of the UPF calculation approach, from which varied results are to be inferred.

For the lift coefficient response, the initial drop in magnitude over lower reduced frequencies, as well as the transition to the high frequency slope of k^1 is captured well. Additionally, the initial slight phase lag of the lift followed by a progression into a 90 degree phase lead for high reduced frequencies is also captured, where multiple UPF calculations span the reduced frequency range. Similarly good results are seen for the pitching moment response, where the pitching moment is taken about the foil mid-chord. For this configuration, the pitching moment response occupies a much smaller dynamic range across the reduced frequency range. From the low frequency limit, this pitching moment response falls and reaches a high frequency constant value. Correspondingly, the phase of this response lags the motion and then approaches zero phase delay for progressively larger reduced frequencies. The comparison between the magnitude and phase of these UPF and Theodorsen pitching moment responses are within approximately 0.5 decibels and 2 degrees, respectively.

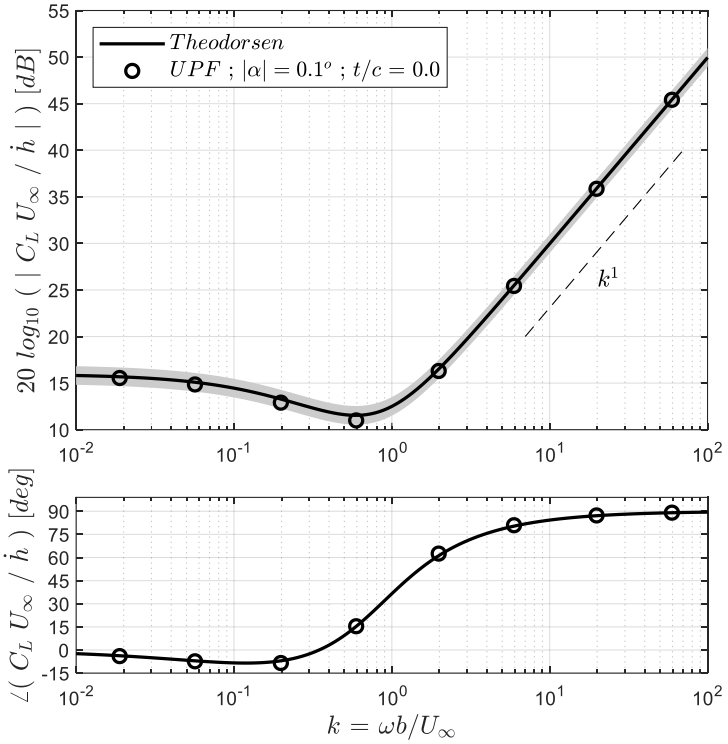

Figure 4.2. Analytical and calculated transfer functions of unsteady lift coefficient to normalized heave velocity for flat foils undergoing sinusoidal motion

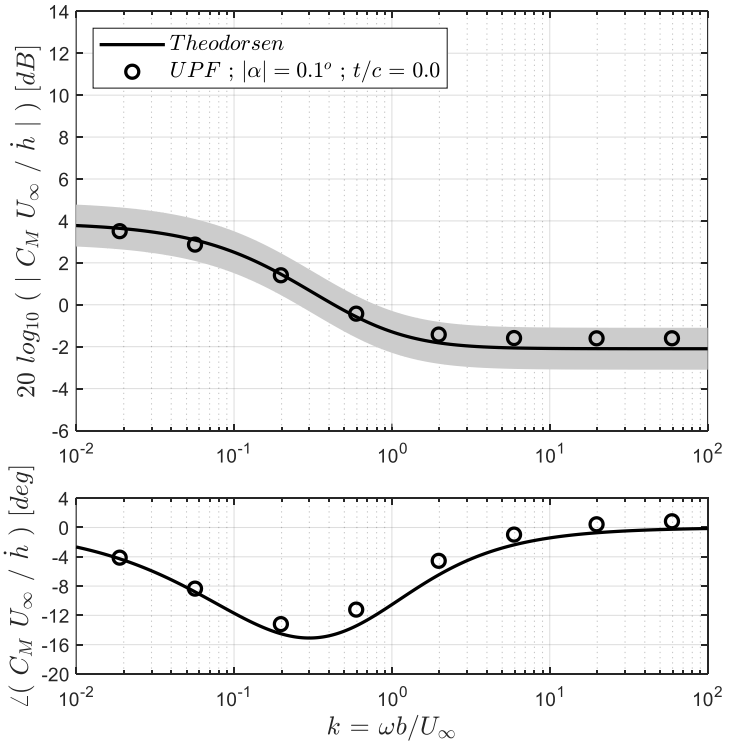

Figure 4.3. Analytical and calculated transfer functions of unsteady pitching moment coefficient to normalized heave velocity for flat foils undergoing sinusoidal motion

In addition to comparing the UPF results to the Theodorsen model expressions for unsteady lift and pitching moment response, assessment can also be made for the response of the unsteady differential pressure acting across the foil. As can be imagined, adding the additional spatial dimension (i.e. distribution along the foil chord) could yield a considerable amount of comparable material; however, given the successful comparisons to the integrated responses above, it seems not fully warranted to exhaustively attempt to present these comparisons. The differential pressure coefficient transfer function due to heaving motion is restated (see Section 2.7),

$$\frac{C_{\Delta P} U_\infty}{\dot{h}} = -4\left[\left(\frac{1-\cos(\theta)}{\sin(\theta)}\right)C + ik\sin(\theta)\right] \tag{4.14}$$

where there are clearly low and high reduced frequency limits.

$$\lim_{k\to 0}\frac{C_{\Delta P} U_\infty}{\dot{h}} = -4\left(\frac{1-\cos(\theta)}{\sin(\theta)}\right) \quad \text{and} \quad \lim_{k\gg 1}\frac{C_{\Delta P} U_\infty}{\dot{h}} = -4ik\sin(\theta) \tag{4.15}$$

Two example comparisons are provided in Figure 4.4 and Figure 4.5. Figure 4.4 presents the differential pressure distribution across normalized chord, X/c, at a single instance of time, denoted by the black open circle, for a low reduced frequency condition of $k = 0.02$. This time step is approximately at the maximum heave velocity disturbance and the predicted pressure distribution compares very favorably to the calculated UPF results, being in-phase (though of opposing sign) and exhibiting the anticipated leading edge singularity behavior. A very similar comparison is provided in Figure 4.5 for a high reduced frequency condition of $k = 19.8$, however now the time index has been moved to be at an approximate zero-crossing for the heaving velocity. This is necessitated by the $\pi/2$ phase shift of the response, which is both specified in the predictive expression and seen in the UPF results. The $\sin(\theta)$ distribution and amplitude of this response are also both captured well. These positive comparisons for the differential pressure are expected given the integrated responses above. While further comparisons at intermediate reduced frequencies are certainly available, where multiple contributions interact and the phase of the responses varies, the presented material is left with the current.

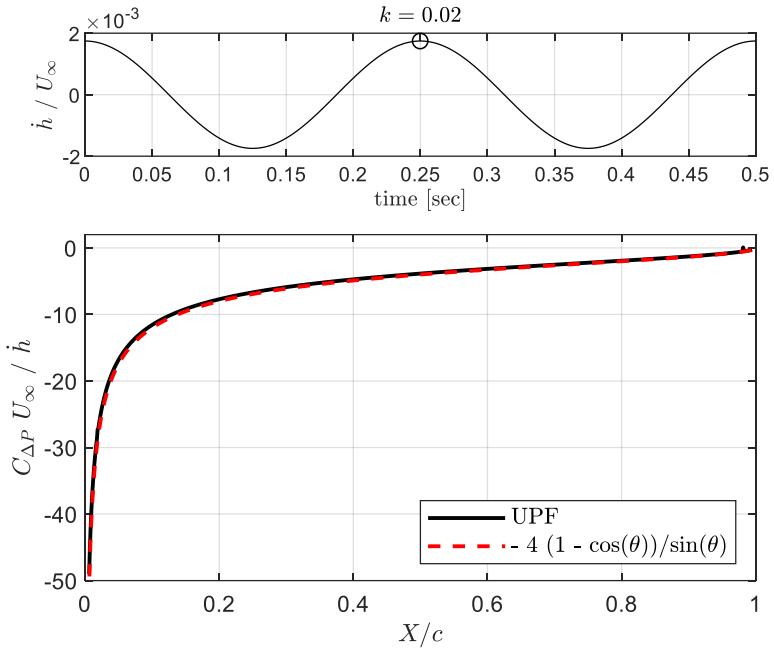

Figure 4.4. Unsteady differential pressure distribution from a low reduced frequency UPF calculation for heaving motion compared to the approximate dominant term from the Theodorsen model

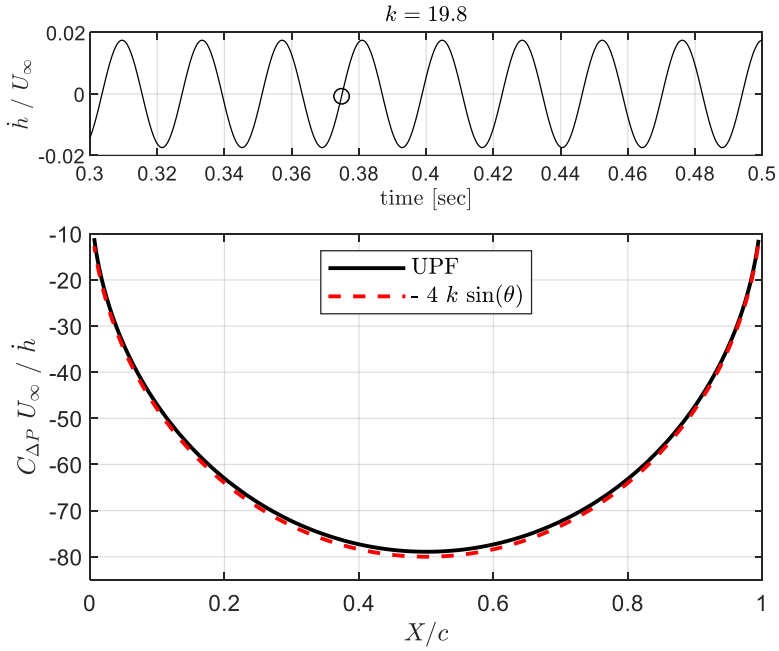

Figure 4.5. Unsteady differential pressure distribution from a high reduced frequency UPF calculation for heaving motion compared to the approximate dominant term from the Theodorsen model

4.2.2 Decomposition of the Unsteady Foil Responses

A unique and useful trait of the UPF calculation framework is that the unsteady velocities and flow potentials can be decomposed according to being contributions attributed to either the source or the wake; the subsequent terms are developed and discussed in Section 2.6. This decomposition is carried through to unsteady pressures, forces, and pitching moment, such that the hierarchy of contributions for these terms can be assessed. Beyond identification, it is important to recognize that for the terms which are solely dependent on source contributions, that they are populated simply by knowledge of the disturbance motion; no consideration is needed for the shed vorticity.

This source and wake decomposition is defined by Eq. 2.39, such that the corresponding unsteady lift and pitching moment decomposed signals can be determined. Figure 4.6 presents time traces of the unsteady lift, expressed as lift coefficients normalized on the maximum normalized heave velocity, for the total lift and for each individual component at a reduced frequency of $k = 0.06$. Decomposing the response in this way, it is clear that the velocity term associated with the interaction of the source and wake, $C_{L,2}$, dominates this unsteady lift response. The flow potential terms register much smaller levels at this reduced frequency and are phase shifted relative to the response from the velocity term.

This same decomposition of the unsteady lift coefficient for a reduced frequency of $k = 19.8$ is presented in an identical way in Figure 4.7. The higher reduced frequency condition clearly shifts the controlling terms for this response, such that the flow potential terms dominate and the velocity terms are negligible. This is understood as a direct impact of the time derivative within the unsteady Bernoulli equation. Specifically, the strongest contribution for this C_L response comes from the flow potential attributed to the source terms alone.

Presented in the same way, Figure 4.8 and Figure 4.9 also present decomposed signals for the same, representative, low and high reduced frequency conditions, but instead for the unsteady pitching moment responses. A similar trend as before is observed for the low reduced frequency condition in that terms associated with velocities control this response. The $C_{M,1}$ term (defined by source velocity contributions)

strongly controls the C_M response at this low reduced frequency, which is information known without the need for a dedicated calculation tracking the shed vorticity. For the high reduced frequency response, multiple contributions are seen to influence the overall response, both velocity and flow potential terms. As a result of the flattening of the magnitude of the pitching moment response over high reduced frequencies for this configuration, the levels between these two reduced frequency conditions are comparable. While not explicitly shown, the differential pressure acting across the foil can be similarly decomposed and analyzed. The hierarchy and interaction of the various terms changes across the foil chord, in addition to being controlled by the reduced frequency condition.

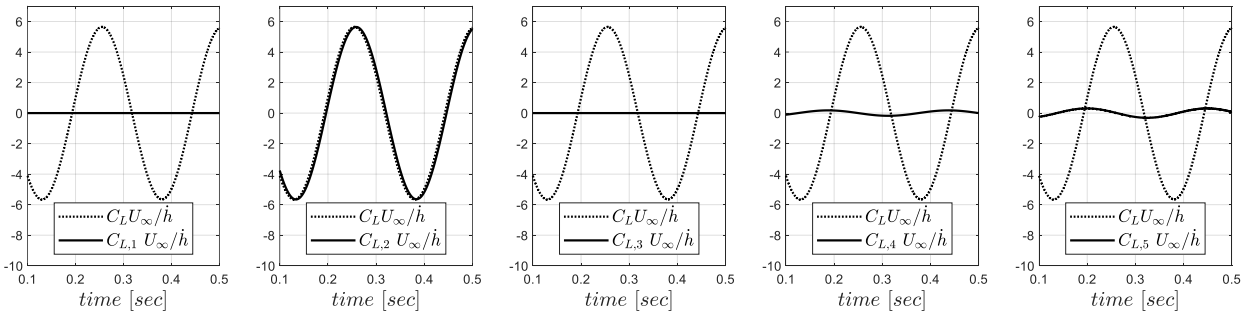

Figure 4.6. Varying contributions to unsteady C_L from UPF for $k = 0.06$ and $\left|\frac{\dot{h}}{U_\infty}\right| = 0.0017$; see Eq. 2.39

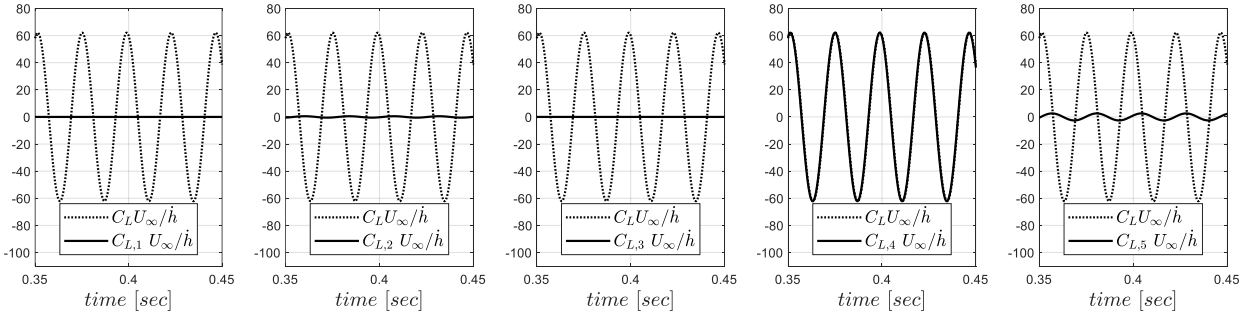

Figure 4.7. Varying contributions to unsteady C_L from UPF for $k = 19.8$ and $\left|\frac{\dot{h}}{U_\infty}\right| = 0.0017$

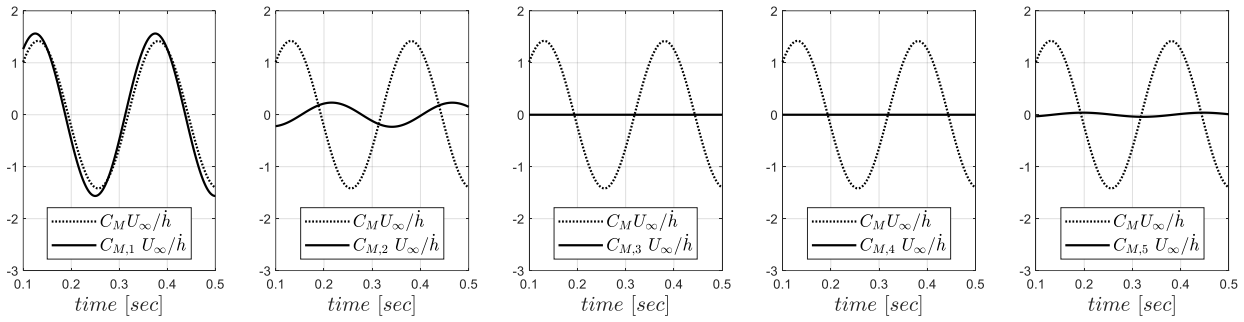

Figure 4.8. Varying contributions to unsteady C_M from UPF for $k = 0.06$ and $\left|\frac{\dot{h}}{U_\infty}\right| = 0.0017$

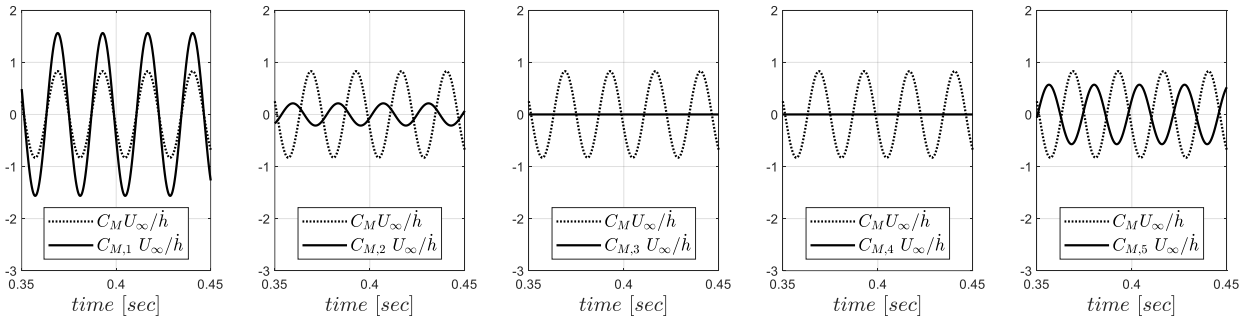

Figure 4.9. Varying contributions to unsteady C_M from UPF for $k = 19.8$ and $\left|\frac{\dot{h}}{U_\infty}\right| = 0.0017$

4.2.3 Effect of Variable Small Amplitude Heaving Motion

The considerations of variable amplitude disturbance motion are explored in the subsequent section for pitching motion, and is not considered for heaving motion as the results are largely redundant.

4.3 Pitch Disturbances for Flat Foils at Discrete Frequencies

4.3.1 Unsteady Lift and Pitching Moment Responses Compared to Theodorsen Model

In a manner very similar to the results of the previous section, the unsteady lift and pitching moment responses from flat foils subjected to small-scale, sinusoidal pitching disturbance motions at discrete frequencies are concentrated on in this section. Examples of time traces of these results are presented in Figure 4.10 where the unsteady lift coefficient from both UPF and TURNS2D calculations are plotted relative to the pitching disturbance motion for two separate reduced frequencies. The time axes are normalized by the periods, T, of the specific signals. As should be expected, these sinusoidal pitch motions result in sinusoidal lift forces. The amplitudes of the pitching motions are all the same, however, the reduced frequencies vary, and this results in different magnitude and phase properties of the lift coefficient response relative to the motion. Comparison of the foil responses will be made in the frequency domain directly, though it can be seen in these views that the results from the two calculations are in very good agreement.

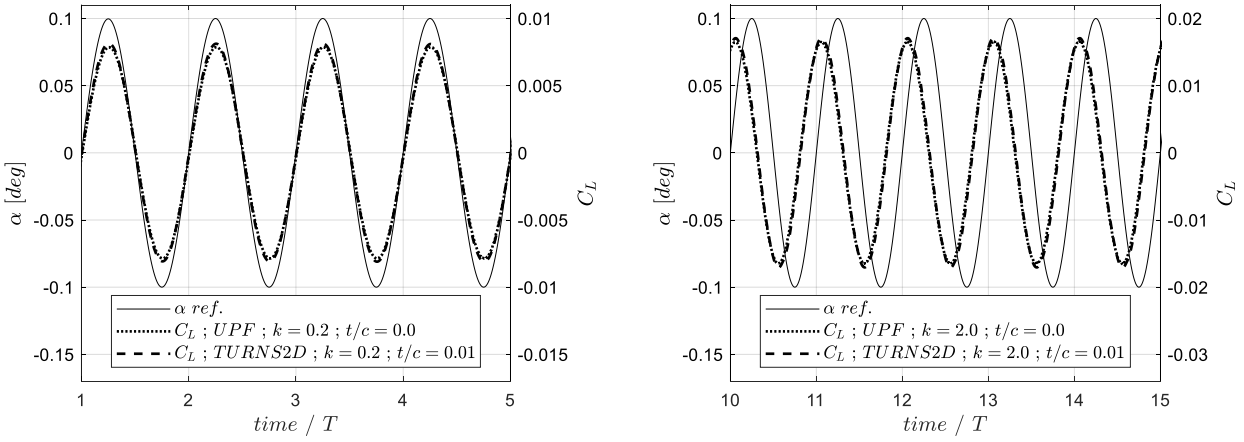

Figure 4.10. Time series of unsteady pitch angle and lift coefficient for sinusoidal pitch calculations

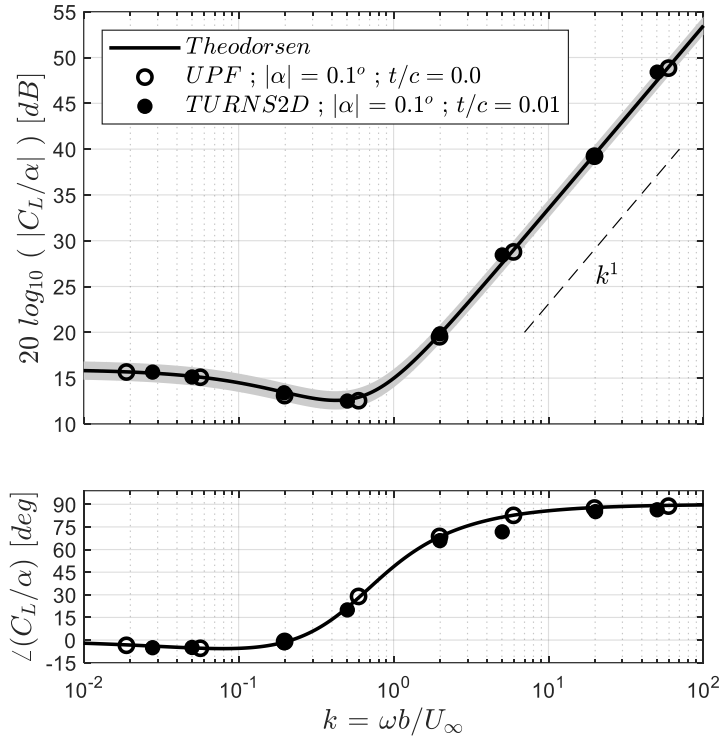

Figure 4.11. Analytical and calculated transfer functions of unsteady lift coefficient to pitch position for flat foils undergoing sinusoidal motion

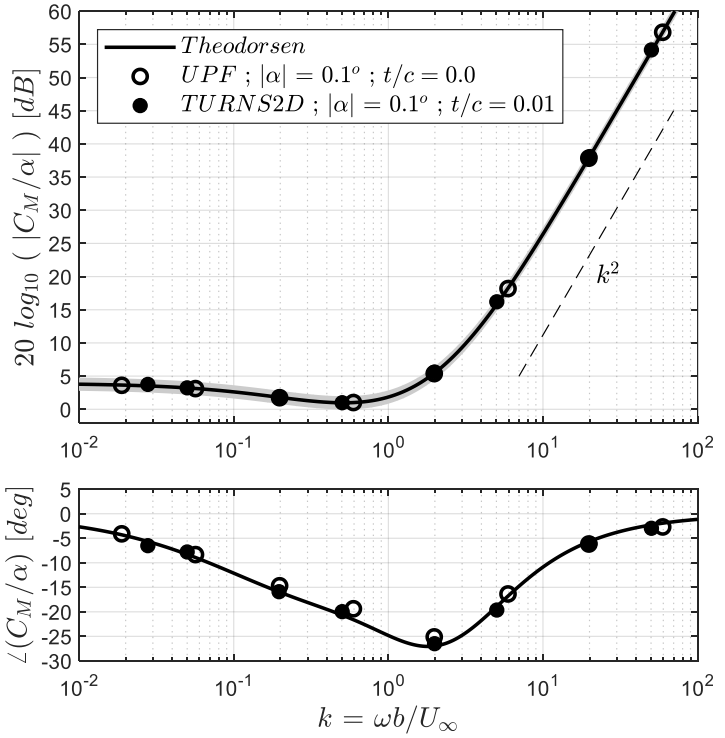

Figure 4.12. Analytical and calculated transfer functions of unsteady pitching moment coefficient to pitch position for flat foils undergoing sinusoidal motion

A primary motivation of this work is to assess the complex-valued transfer functions of unsteady foil responses in the frequency domain, and therefore Figure 4.11 and Figure 4.12 present Bode plots of the calculated unsteady lift and pitching moment for mid-chord pitch motion for the thin foil condition at the baseline disturbance condition of $|\alpha| = 0.1^o$. These calculated results at discrete reduced frequencies are compared directly to the associated Theodorsen expressions (Eq. 2.61 and Eq. 2.64). The reduced frequency axes of the top (magnitude) and bottom (phase) plots are aligned, and the gray band around the Theodorsen line is a ± 1 decibel visual aid. The comparison of these results from the UPF and TURNS2D calculations relative to the Theodorsen mode is very good for both magnitude and phase characteristics for both the lift and pitching moment responses over the wide range of reduced frequencies being considered.

The drop in magnitude of the lift coefficient around the mid-reduced frequency range and the subsequent transition to the high frequency slope of k^1 are captured well. Additionally, the phase relationship of slight initial lag of the lift followed by a transition into a 90 degree phase lead for high reduced frequencies is reliably captured. Similarly good results are seen for the pitching moment calculated about the mid-chord, where for increasing reduced frequencies the magnitude of the response initially drops and then transitions into a high frequency slope of k^2. All lift and pitching moment magnitudes are within 1 decibel of the Theodorsen expressions, and the phase angles also compare acceptably well. The lowest reduced frequency condition for the TURNS2D pitching calculation was performed at 0.02; however, the plotted result is positioned off of this value due to the available frequency resolution given the temporal conditions of the calculation. What is plotted is the result from the resolved frequency bin closest to this value of the disturbance motion. The reliable comparison of these calculated results to the Theodorsen model is foundational for this work as the calculations implemented thin foils in these instances, which is a critical assumption within the modeling framework of Theodorsen.

It should also be noted that these UPF and TURNS2D results are achieved independently; and in addition to being two separate calculations, the computational effort and perceived modeling fidelity is different between them. Though the computational cost between the calculations is not explicitly explored

and compared, the computational burden of the UPF calculations is significantly less, with results being able to be achieved rapidly (dependent upon the discretization conditions). While the expedience with which results can be achieved is of interest, this is not a current area of focus.

Interestingly, the added fidelity of utilizing the unsteady RANS equations provides little perceptible benefit in this instance of analyzing the unsteady lift and pitching moment responses for small disturbance pitching motion at a high Reynolds number, low Mach number, and for which the foil maintains fully attached flow conditions. For these operating conditions, any unsteady effects associated with compressibility or viscosity in either the boundary layer or foil wake appear to be sufficiently negligible. An additional implication is that the sheared wake generated by the coalescing of the boundary layers on either sides of the foil appears to yield little impact on these unsteady results.

In an identical manner as to how the previous heaving motion results were presented, an assessment is also made for the response of the unsteady differential pressure acting across the foil due to pitching motion about the foil mid-chord. Again, given the successful comparisons to the integrated responses above, an exhaustive set of these comparisons is not presented. The differential pressure coefficient transfer function due to mid-chord pitching motion is listed in Eq. 2.68, and not restated here; however, given the form in which it is written it is clear that there are low and high reduced frequency limits.

$$\lim_{k\to 0}\frac{C_{\Delta P}}{\alpha} = -4\left(\frac{1-\cos(\theta)}{\sin(\theta)}\right) \quad \text{and} \quad \lim_{k\gg 1}\frac{C_{\Delta P}}{\alpha} = 2k^2\sin(\theta)\cos(\theta) \tag{4.16}$$

Not surprisingly, the limiting low reduced frequency expression is the same as that for heaving motion, though the high reduced frequency is certainly different, with changes to both the chordwise distribution and response phase. Two example comparisons are provided in Figure 4.13 and Figure 4.14, for low and high reduced frequency conditions of $k = 0.02$ and $k = 19.8$, respectively. Figure 4.13 presents the differential pressure distribution across normalized chord, X/c, at a single instance of time, denoted by the black open circle, for a low reduced frequency condition of $k = 0.02$. This time step is approximately at the maximum pitch position disturbance and the predicted pressure distribution compares

very favorably to the calculated UPF results, being in-phase and exhibiting the anticipated leading edge singularity behavior. Figure 4.14 provides the comparison for a high reduced frequency condition of $k = 19.8$, where the corresponding time index is also at an approximate maximum in the pitch position disturbance motion, as this response is predicted to be in-phase with the motion (and is seen in the UPF results). The $\sin(\theta)\cos(\theta)$ chordwise distribution and amplitude of this response, which is growing as k^2, are also both captured well. These positive comparisons for the differential pressure are expected given the integrated responses above. For clarity, the equivalent TURNS2D results were not extracted and analyzed.

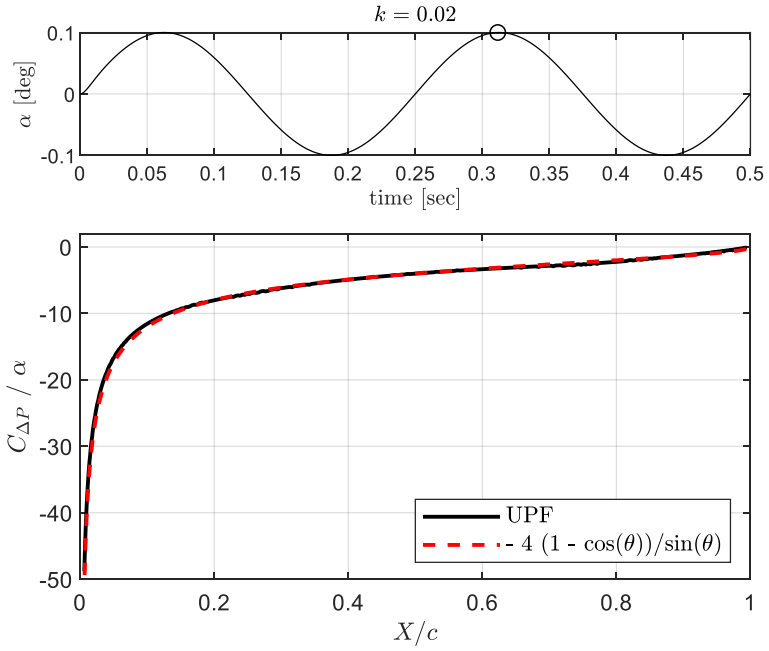

Figure 4.13. Unsteady differential pressure distribution from a low reduced frequency UPF calculation for mid-chord pitching motion compared to the approximate dominant term from the Theodorsen model

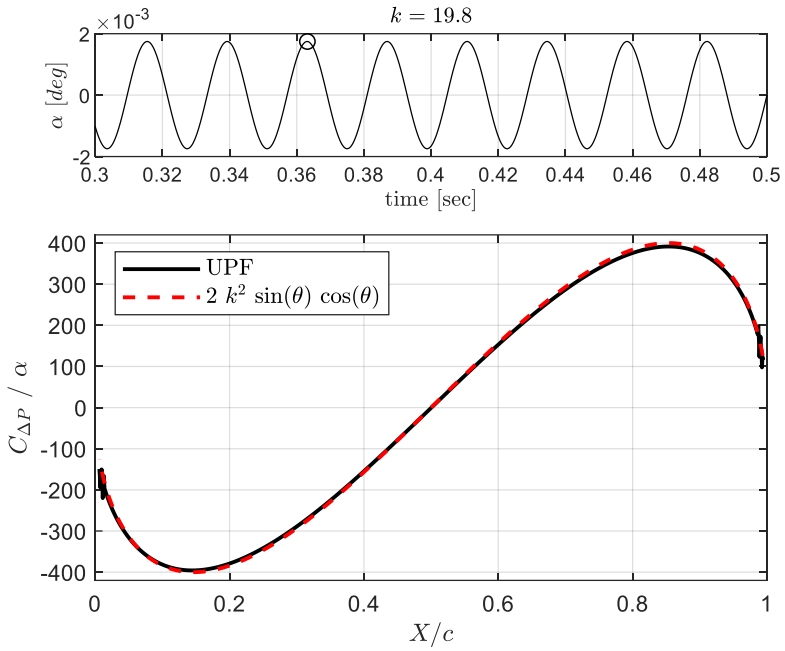

Figure 4.14. Unsteady differential pressure distribution from a low reduced frequency UPF calculation for mid-chord pitching motion compared to the approximate dominant term from the Theodorsen model

4.3.2 Decomposition of the Unsteady Foil Responses

Leveraging the unique trait of the UPF calculation framework, the contributions to the unsteady pressure acting across the foil can be decomposed into the source and wake controlled terms according to Eq. 2.39, and then the corresponding unsteady lift and pitching moment decomposed signals can be determined. Figure 4.15 presents time traces of the unsteady lift, expressed as lift coefficients normalized on the maximum pitch amplitude, for the total lift and for each individual component at a reduced frequency of $k = 0.06$. Decomposing the response in this way, it is clear that the velocity term associated with the interaction of the source and wake, $C_{L,2}$, dominates this unsteady lift response. The flow potential terms register much smaller levels at this reduced frequency and are phase shifted relative to the response from the velocity term. The decomposed contributions to the unsteady lift coefficient for a reduced frequency of $k = 19.8$ are presented in an identical way in Figure 4.16. The higher reduced frequency condition clearly reorders the hierarchy of the controlling terms for this response, such that the flow potential terms dominate. This is understood as a direct impact of the time derivative within the unsteady Bernoulli equation.

Specifically, the strongest contribution comes from the flow potential attributed to the source terms alone. This is particularly intriguing because, by definition, this term is defined without regard for the shed wake of vorticity, and can therefore be populated simply with knowledge of the unsteady motion. The dominance of this $C_{L,4}$ term is a fact that will be leveraged in the later section dealing with the responses from foils of finite thickness.

Figure 4.17 and Figure 4.18 also present decomposed signals for the same, representative, low and high reduced frequency conditions in an identical manner to the prior figures, but instead for the unsteady pitching moment. A similar trend is observed in that terms associated with velocities control the low reduced frequency responses, while responses at high reduced frequency are controlled by flow potential terms. The $C_{M,1}$ term (defined by source velocity contributions) strongly controls the C_M response at this low reduced frequency, which is information known without the need for a dedicated calculation tracking the shed vorticity. Also similar to the C_L results, the C_M response at this high reduced frequency condition is dominated by the flow potential of source contributions. While not explicitly shown in the present work, the differential pressure acting across the foil can be similarly decomposed and analyzed, this however adds another dimension to the presentation of results. The hierarchy and interaction of the various terms changes across the foil chord, in addition to being similarly controlled by the reduced frequency condition.

As a final point for this subsection, Figure 4.19 and Figure 4.20 present the same type of decompositions for the C_L responses at intermediate reduced frequencies of $k = 0.6$ and 2.0, respectively. In conjunction with the earlier figures, these views show the evolving hierarchy of the multiple contributions to the overall unsteady lift response. Views at these additional reduced frequencies show, with some increased specificity, that the magnitude of the velocity-based term, $C_{L,2}$, falls with increasing reduced frequency, while the terms based on flow potential, $C_{L,4}$ and $C_{L,5}$, increase. Views of these decomposed signals also exhibit the importance of the correct handling of these various components of the calculation, as for at these intermediate reduced frequencies the combination of the magnitude and phase properties of these various contributions compete at similar levels towards the overall responses.

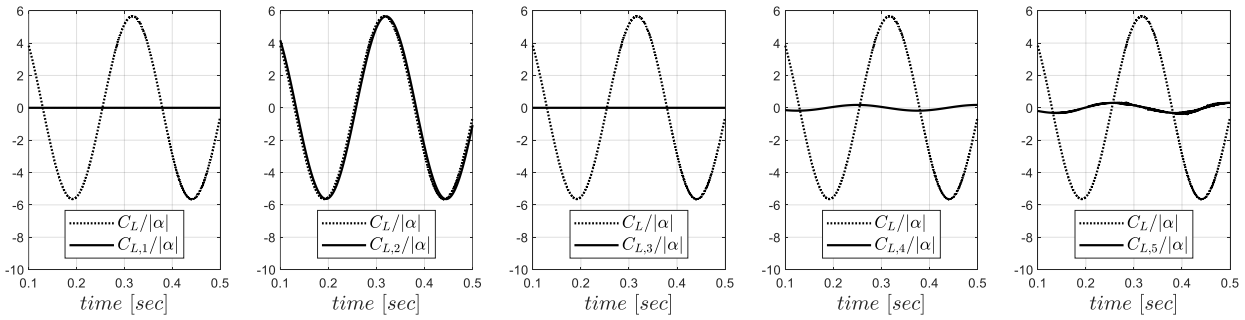

Figure 4.15. Varying contributions to the unsteady C_L from UPF for $k = 0.06$ and $|\alpha| = 0.1^o$; see Eq. 2.39

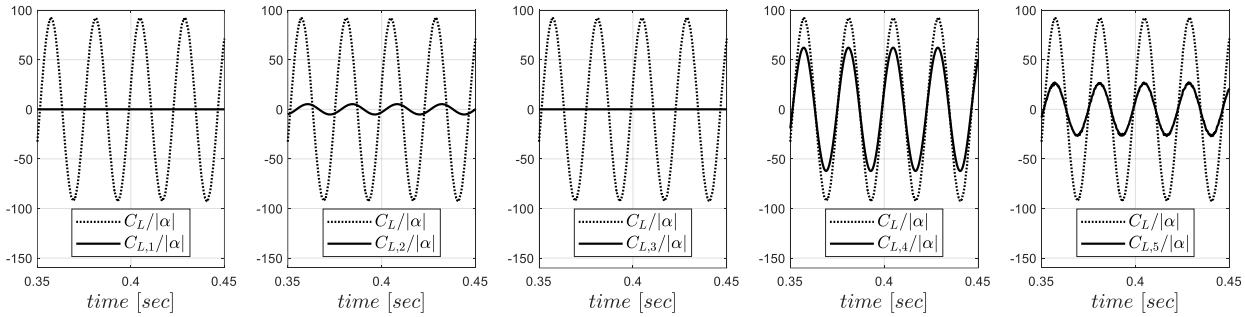

Figure 4.16. Varying contributions to the unsteady C_L from UPF for $k = 19.8$ and $|\alpha| = 0.1^o$

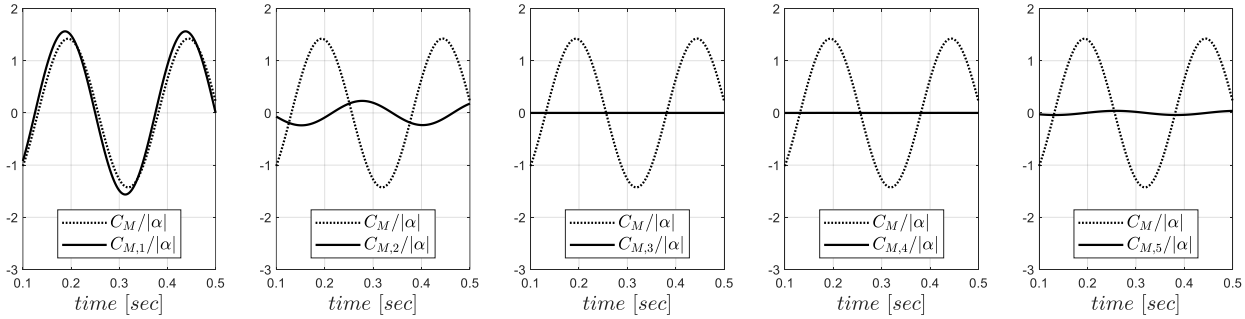

Figure 4.17. Varying contributions to the unsteady C_M from UPF for $k = 0.06$ and $|\alpha| = 0.1^o$

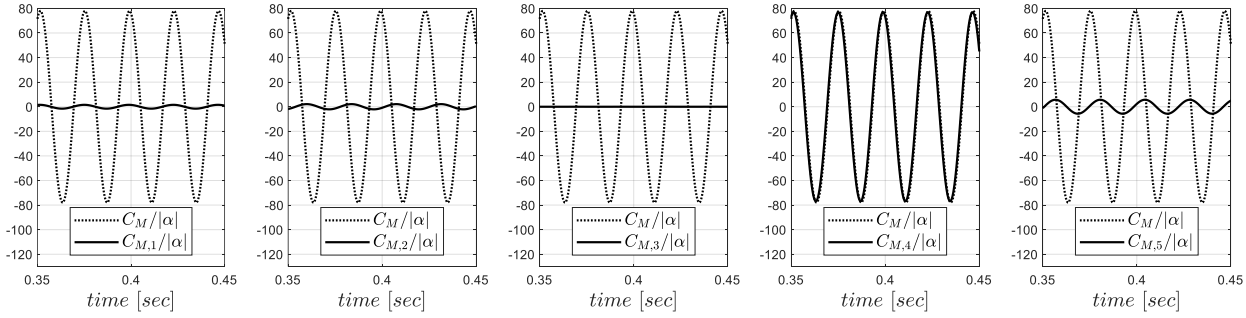

Figure 4.18. Varying contributions to the unsteady C_M from UPF for $k = 19.8$ and $|\alpha| = 0.1^o$

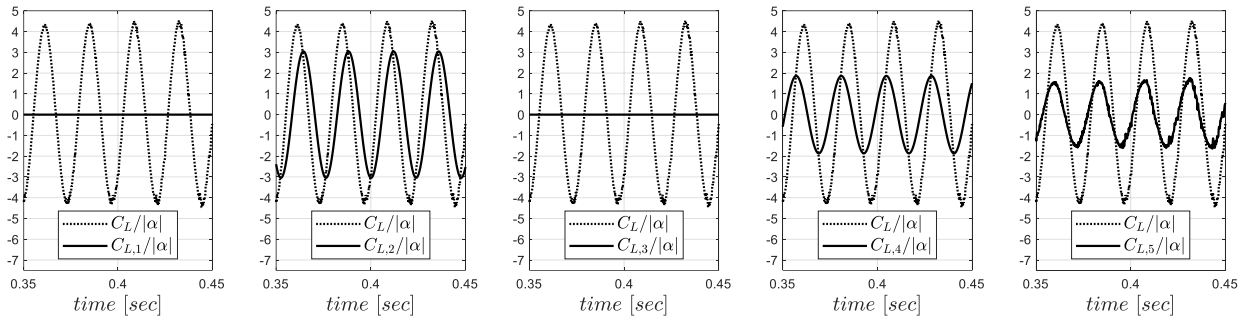

Figure 4.19. Varying contributions to the unsteady C_L from UPF for $k = 0.6$ and $|\alpha| = 0.1^o$

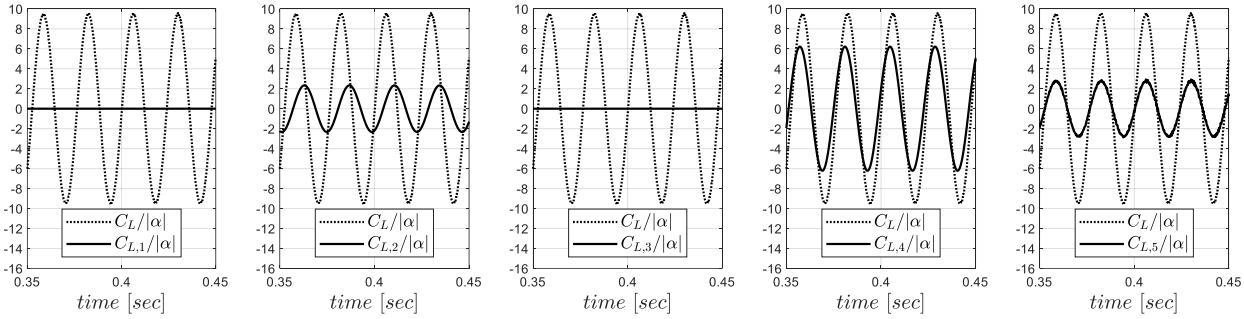

Figure 4.20. Varying contributions to the unsteady C_L from UPF for $k = 2.0$ and $|\alpha| = 0.1^o$

4.3.3 Effect of Variable Small Amplitude Pitching Motion

The results of this subsection are for the same thin foils undergoing sinusoidal pitching motion, however now for variable amplitudes of $0.01^o, 0.1^o$, or 1.0^o. Figure 4.21 and Figure 4.22 present Bode plots of the normalized C_L and C_M responses for these different amplitude calculations. Just for clarity, note that the only TURNS2D results present on these plots are for $k = 50$, and that they are very consistent. Viewing the results in this way illustrates that there is little difference in the normalized responses over this range of disturbance amplitudes; hence the appropriateness of assessing these responses as transfer functions. Put another way, these figures show the apparent linearity of these transfer function relationships.

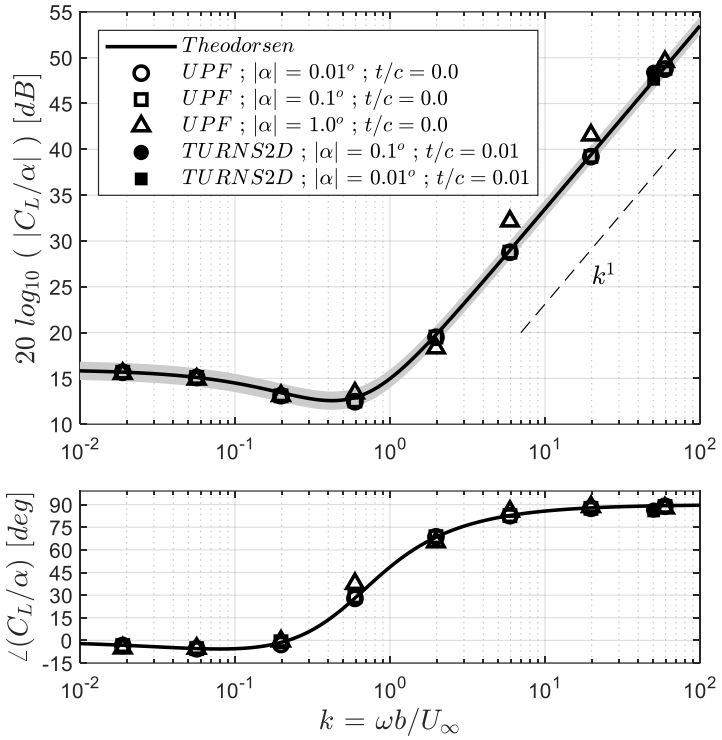

Figure 4.21. Analytical and calculated transfer functions of unsteady lift coefficient to pitch position for flat foils undergoing variable, small amplitude, sinusoidal motion

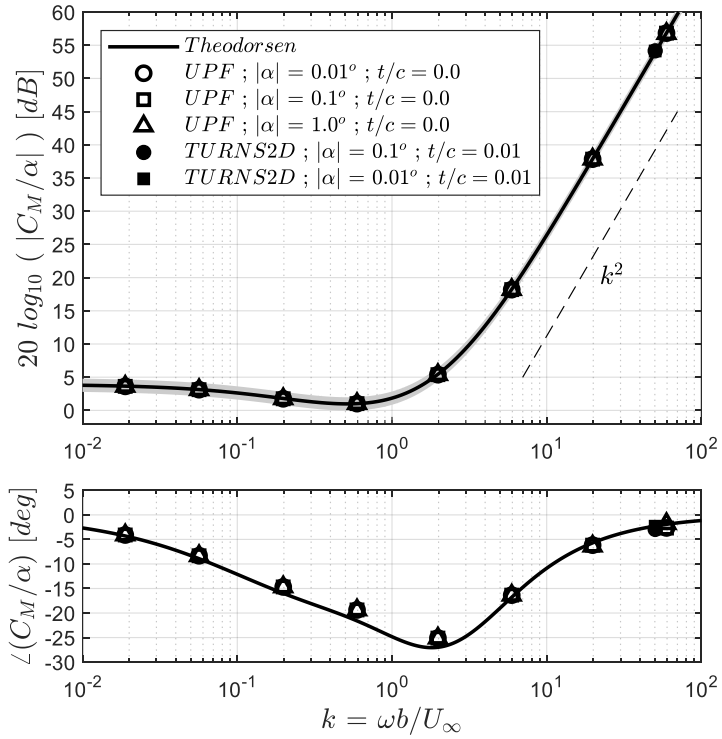

Figure 4.22. Analytical and calculated transfer functions of unsteady pitching moment coefficient to pitch position for flat foils undergoing variable, small amplitude, sinusoidal motion

The clear exception to this is the C_L response at the largest amplitude disturbance for the $k = 6.0$ and 19.8 conditions; where the magnitudes of these responses are seen to be elevated, but the phase angles are unaltered. The cause for this deviation is understood to be a result of the induced motion of the shed wake of vorticity. Utilizing the decomposition technique on the unsteady C_L responses, it is found that the flow potential contributions of the wake terms are amplified, which coincide directly with enhanced motion of the shed vortices away from the planar sheet assumption. This decomposition of the unsteady lift signals at $k = 19.8$ for the array of disturbance amplitudes for the flow potential source and wake contributions is provided in Figure 4.23. As should be expected, the normalized source contributions, $C_{L,4}/|\alpha|$, between the three calculations are all the same. The wake contributions, $C_{L,5}/|\alpha|$, for the lowest two amplitude conditions are effectively identical, however this contribution for the 1.0^o amplitude configuration is elevated and is the cause of the amplified levels of the corresponding overall response. Figure 4.24 provides an expanded view along the time axis for just the $C_{L,5}$ portion of the unsteady response. As can be seen, the amplitude envelope of the signal for the $|\alpha| = 1.0^o$ disturbance motion is growing with time and has not yet reached a steady state. This has implications on the analysis of the signal across the frequency domain, and should warrant continued scrutiny for continued work on high reduced frequency conditions.

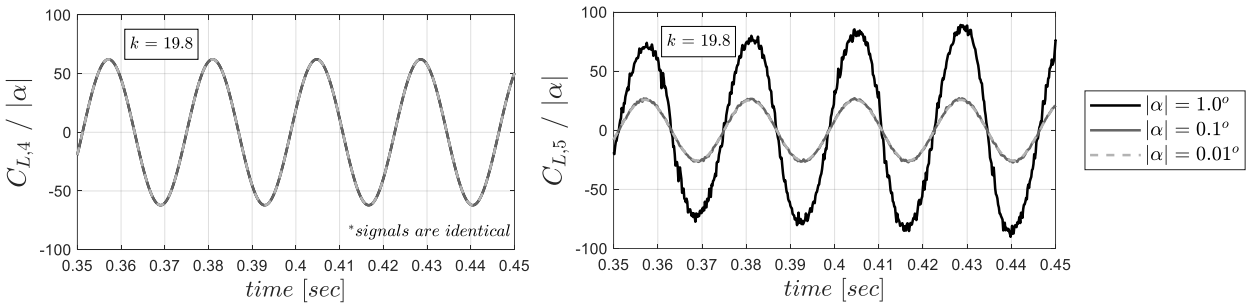

Figure 4.23. Decomposition of flow potential contributions to the normalized lift coefficient at $k = 19.8$

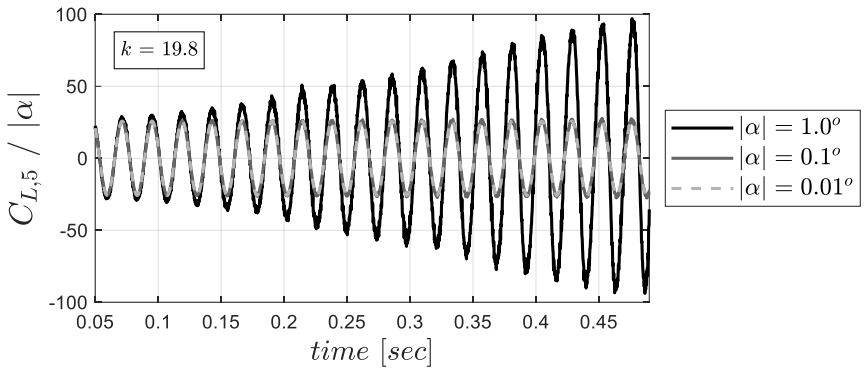

Figure 4.24. Decomposition of the wake flow potential for the normalized lift coefficient at $k = 19.8$

The results of Figure 4.21 earlier can be somewhat misleading however, in that the single-input single-output form of these transfer functions implies that for an input (the pitch disturbance) at a specified reduced frequency that the output only occurs at that reduced frequency. Because of the relaxation of the planar shed wake assumption within the UPF calculations, this is not true for the higher amplitude and higher reduced frequency conditions. Effectively the same example of this is seen in the time traces presented in Figure 4.25, where the total normalized C_L is plotted for the three different disturbance amplitudes at $k = 19.8$. The responses at the $|\alpha| = 0.01^o$ and 0.1^o conditions are seen to be quite sinusoidal and to overlay each other (the lighter gray traces). The C_L response for the 1.0^o condition is also predominantly a sinusoid; however, there is a slight distortion of the sinusoidal response and additional energy is present, both of which are attributed to the non-linearity of the development of counter-rotating structures in the shed wake (this is broken out specifically in Figure 4.23).

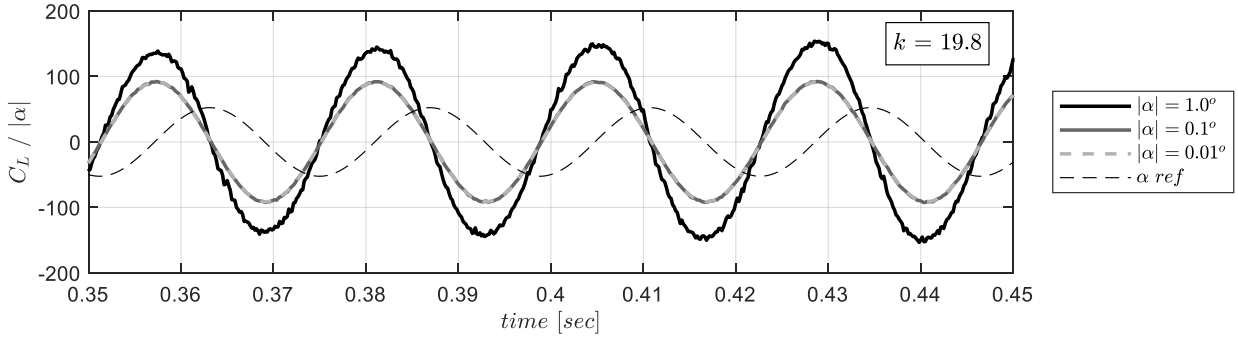

Figure 4.25. Normalized lift coefficient for variable amplitude pitch calculations at $k = 19.8$

Figure 4.26 presents the power spectral density of these C_L signals, Φ_{C_L}, normalized by pitch amplitude for the three different disturbance amplitudes at reduced frequencies of 0.6 and 19.8. While the disturbance motion is defined to be a single frequency sine wave, these plots present the frequency domain content of the unsteady lift signals. For the smaller amplitude results, it is clear that the unsteady lift is effectively a response at a single frequency. From these examples, the $|\alpha| = 1.0^o$ results for both reduced frequencies differ by exhibiting notable elevation of the response at the non-driven frequencies. However, the behavior of these example responses are different. For $k = 0.6$ the added response manifests at multiples of the disturbance reduced frequency along with elevated broadband levels for frequencies greater than the disturbance motion. In contrast, for $k = 19.8$ the added response manifests as a broadening of the nearly tonal character to the immediately adjacent frequencies and less pronounced broadband increases. The broadening of the tonal response and elevated levels over the range of lower reduced frequencies is at least partially attributed to the increasing amplitude envelope as shown in Figure 4.24.

The complete implications of the generation of unsteady lift response at non-driven frequencies due to single-frequency, small-scale motion while maintaining attached flow is a suggested area for future attention. While these UPF calculations are identifying variable response behavior, it is recognized that viscous effects and very specific behavior of the shed vorticity are likely to have important influence on these aspects of the responses. Given the linear nature of the contributions to the lift response by the source terms, this character must be linked with the shed vorticity and its development in the wake.

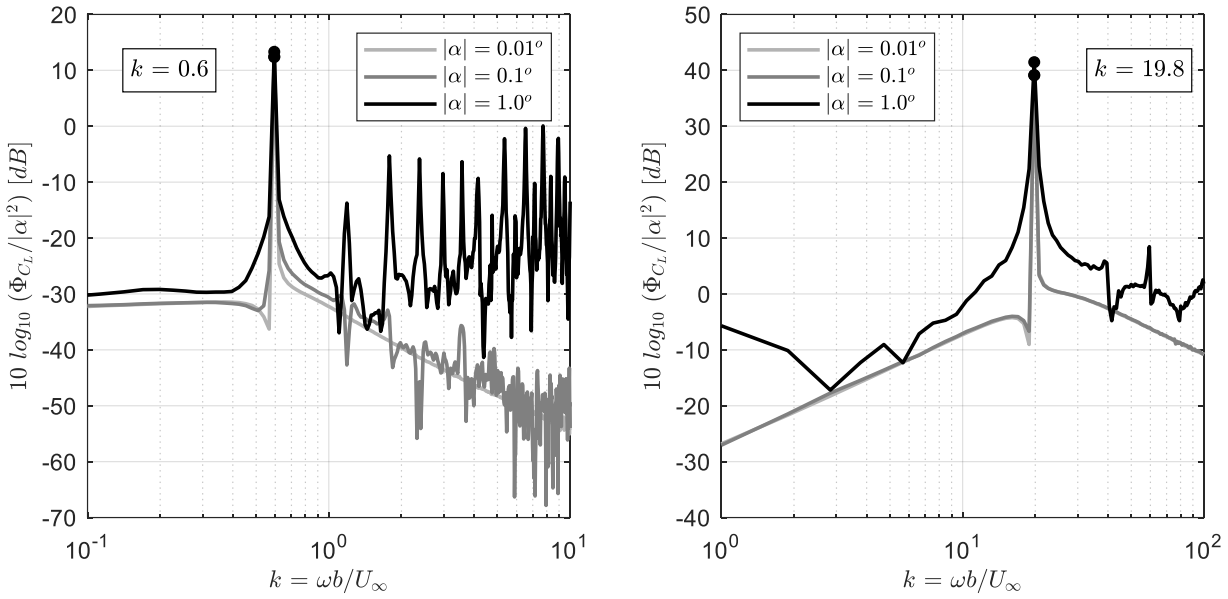

Figure 4.26. Power spectral densities of lift coefficient normalized by pitch magnitude for variable amplitude pitch calculations for two representative reduced frequency conditions

The effective linearity of the foil responses at the disturbance frequency for the present conditions is not overly surprising given that prior works and studies (several of which are presented earlier) have presented similar findings, though at reduced frequencies which are often less than a value of one. What is interesting though, are the wake patterns that establish downstream of the foils, and the subsequent inference that they apparently have little to no influence on the foil responses for low reduced frequency disturbances, though can have effect at higher reduced frequency conditions (see Figure 4.21). This point is of particular interest because older studies with flow visualization like Bratt (1953) and Ohashi and Ishikawa (1972), in addition to more recent references of Münch et al. (2010) and Young and Lai (2004), were performed for high reduced frequency conditions of $k > 1$ which clearly show the existence of shed vorticity which does not follow a planar trajectory. However, accompanying unsteady force and moment results, of the kind studied presently, are often not available for these operating conditions.

For all of the UPF calculations the assumption of a planar wake, as imposed in the Theodorsen model, has been relaxed and all point vortices are treated as particles which displace within the field

according to the influence of the unsteady velocity field. For low reduced frequency conditions and low disturbance amplitude, moderate reduced frequency conditions the resulting wake of point vortices still resemble a nearly planar distribution. However, as either the disturbance amplitude or the reduced frequency are raised, undulations in the wake pattern become more pronounced. Examples of this behavior are presented in Figure 4.27 for a single time index, where the spatial coordinates are normalized on chord, the flat foil is plotted for reference, and the point vortices are denoted by dots (which can appear as a line given the temporal resolution of the calculations). Undulation of the wake is seen for the larger disturbance amplitude calculation, signifying a departure from the planar wake assumption. The strengths of the vortices are not explicitly signified in these views, though in the subsequent figures this can be inferred by the breakdown of the sheet into counter-rotating vortical structures.

In an identical way, Figure 4.28 presents examples of the shed wake for a representative high reduced frequency. Even at the smallest disturbance amplitude condition considered here, the shed vortices are seen to undulate. The wake pattern for the $|\alpha| = 0.1^o$ condition almost immediately forms counter-rotating vortex clusters which continue to grow and interact as they propagate downstream. Note that as the point vortices are displacing they are effectively following the spatial distribution shown in Section 2.5, $= 2\pi b/k$, or equally, $\lambda/c = \pi/k$.

Figure 4.29 shows zoomed views in the immediate proximity of the foil trailing edge and at a downstream wake location for these same flow conditions. Unlike the prior figures, the aspect ratio of these axes are not square. These views highlight both the subtle breakdown of the vorticity sheet occurring near the foil trailing edge in the $|\alpha| = 0.1^o$ case, and the establishment of the counter-rotating vortex structures which manifest in a very similar way to a von-Kármán vortex street in the wake of streamlined bodies, bluff bodies, and free shear flows.

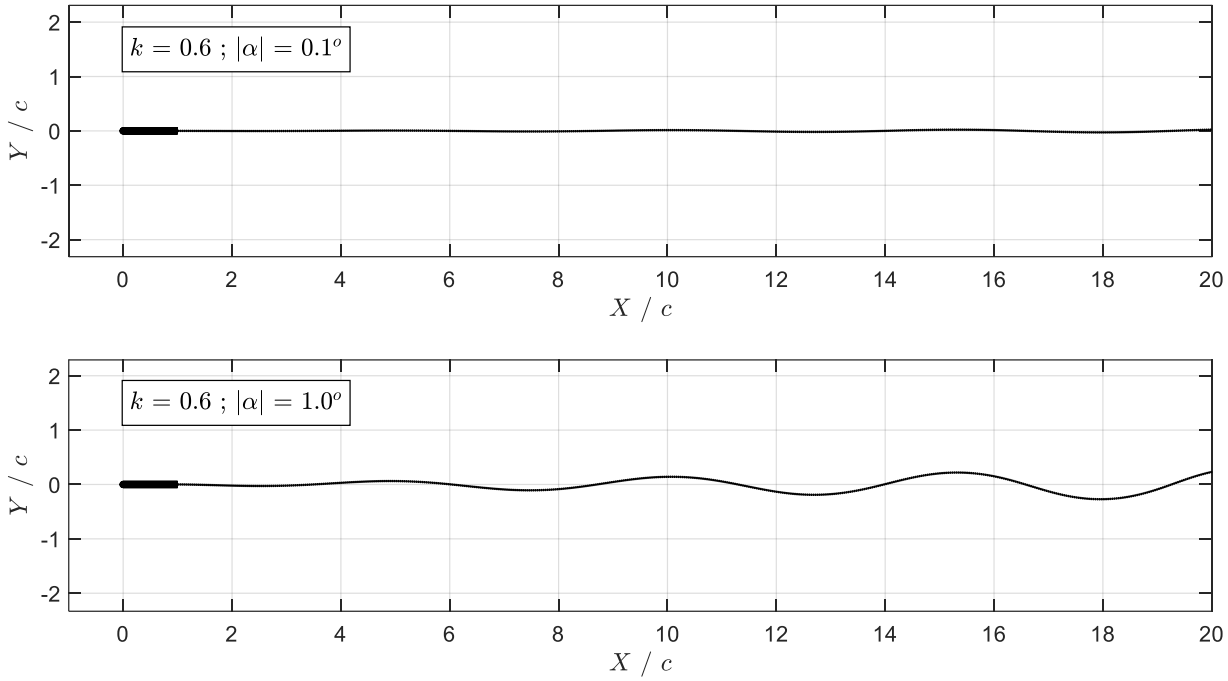

Figure 4.27. Visualization of the wake of shed point vortices at a single instance of time for $k = 0.6$

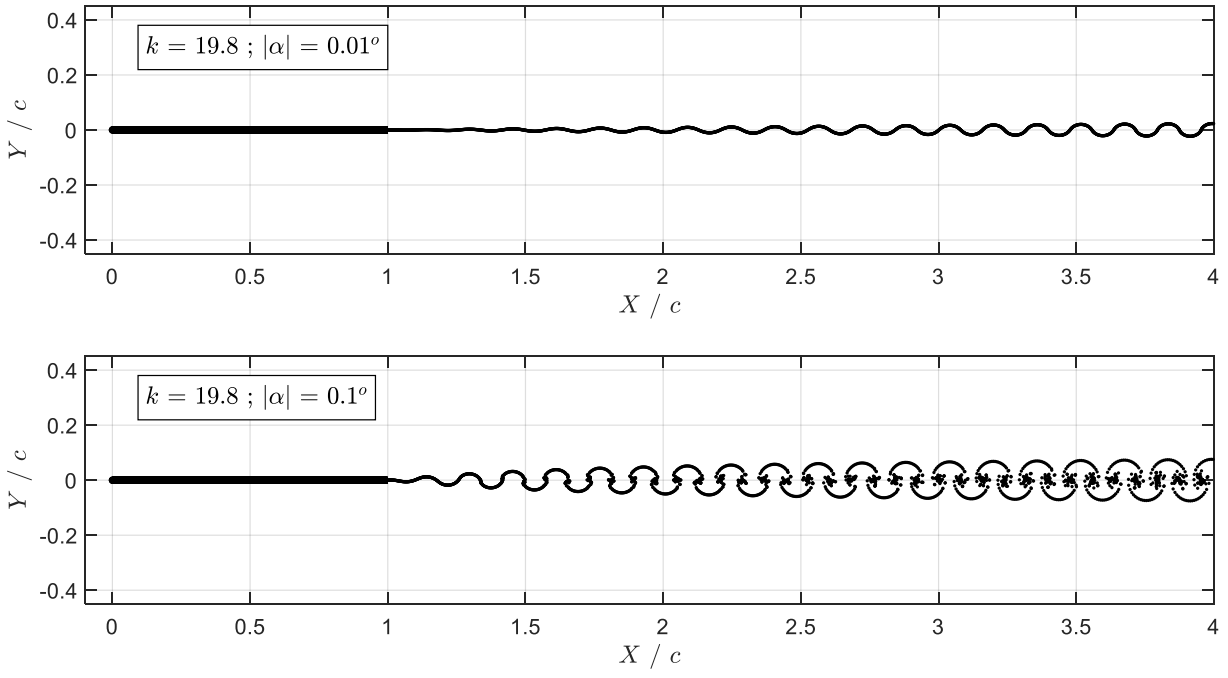

Figure 4.28. Visualization of the wake of shed point vortices at a single instance of time for $k = 19.8$

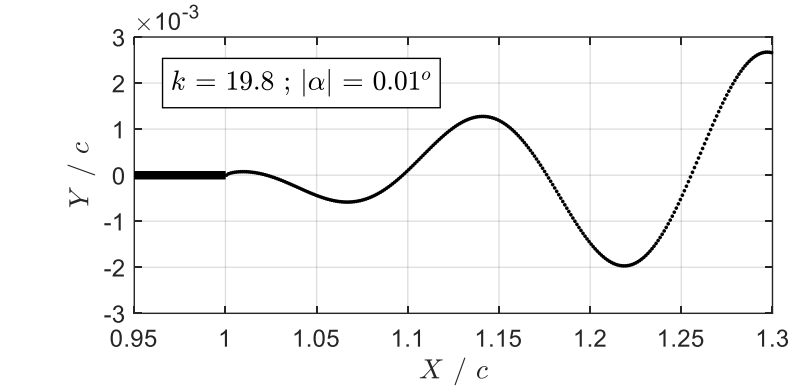

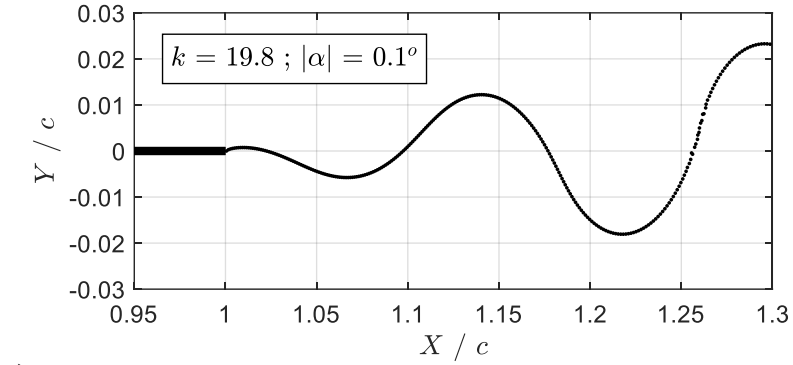

a)

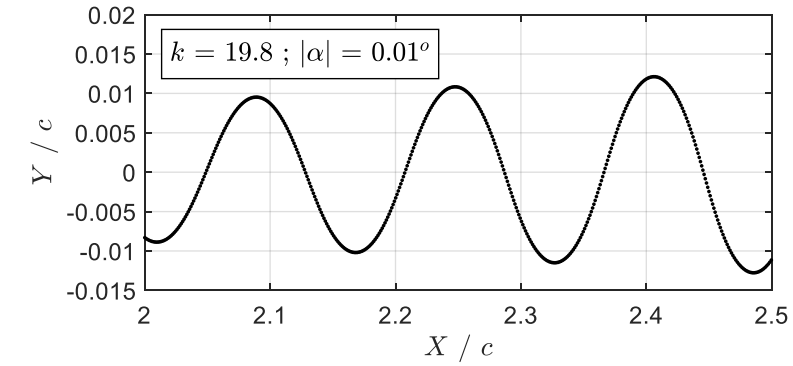

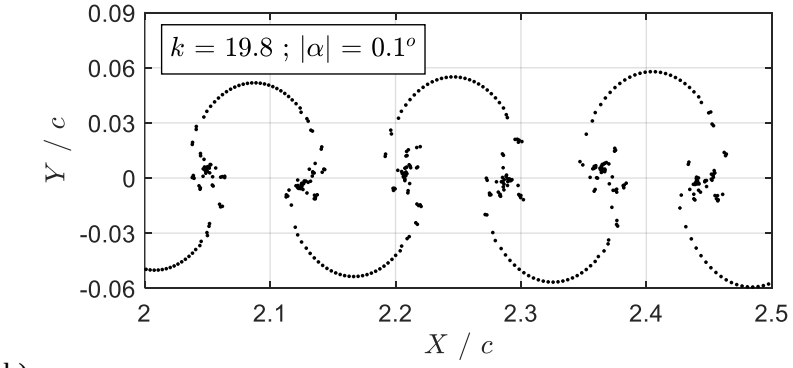

b)

Figure 4.29. Zoomed views of the wake of shed point vortices for $k = 19.8$; a) trailing edge, b) downstream wake

This vortex behavior in the foil wake is consistent with the references of Platzer et al. (2008) and Young and Lai (2004) which pertain to force responses and wake behavior for pitching and heaving motions. As described in these references, the slight clockwise inclination of the wake structures present in the UPF results are indicative of being a thrust-producing wake. Though the mean streamwise force (i.e. thrust) is not a concentration of the present analysis, this wake behavior and the mean thrust due to unsteady motion are closely linked through a momentum balance of the force and wake velocity field. The model of Garrick (1936) is a contemporary to the Theodorsen model, and yields predictive expressions for the mean streamwise force as a result of small-scale foil motion. Comprehensive analysis is left for future effort; however, a quick utilization of the Garrick model expects that mean thrust should occur for this high reduced frequency condition of $k = 19.8$, which directly corroborates with the wake orientation.

While the spatial extent of the wake is of interest in the present work, it can be a primary concern for other configurations (ex. the downstream interaction from a cascade of foils). More central to the present motivations is the determination that while this wake behavior clearly violates the planar wake assumption, there appears to be limited effect on the foil response transfer functions at the reduced frequency involved (though there can be response induced at other frequencies as previously shown). Subsequently, two considerations are offered as to why this is. Referencing back to Figure 4.16 and Figure 4.18, for high reduced frequency conditions the contributions from the source terms are the dominant terms for the foil responses; therefore, changes in the wake contributions would need to be strong enough relative to these source terms in order to appreciably alter the overall responses. Second, the flow potential for a point vortex takes the following form, $i\log(z)$, with the contribution to the unsteady pressure coming from the complex argument of the spatial dimension, $i\log\left(re^{i\theta}\right) = i\log(r) + i\log\left(e^{i\theta}\right) = i\log(r) - \theta$. While the vortex strengths are not explicitly presented in Figure 4.28 and Figure 4.29, it should be clear that the strongest vortices are within the centers of the vortex clusters. As these features are not seen to stray significantly from the real axis (i.e. chordline-extended) their effect at the disturbance reduced frequency is inferred to not be radically different from if they were forced to follow a strictly planar trajectory.

4.4 Broadband Disturbance Motion for Flat Foils

This section explores the results and ramifications for disturbance motion that is statistically stationary, however not sinusoidal for a specific isolated frequency. For many realistic scenarios of a steady-state, vibrating foil structure within a freestream, the resulting motion will not occur as a pure sinusoidal disturbance at a single frequency, but rather as a response with resonant character across the frequency domain (clearly, dependent upon the structure involved). Remaining indifferent to specific structural considerations and assuming that the disturbance motion is known for a given configuration, it is of interest to assess the same unsteady foil responses as a result of this motion.

Strict adherence to the Theodorsen model and its underlying assumptions could lead to the conclusion that it is only applicable to sinusoidal disturbance motion. The conditions for utilizing the model expressions are however, not that strict, due to the use of the principle of superposition in the frequency domain, or equivalently, the convolution theorem. As long the disturbance motion remains small enough such the flow about the foil remains attached, that vorticity is only shed from the foil trailing edge, and that it follows a planar trajectory which convects with the freestream (critical assumptions of the Theodorsen model), then the Theodorsen model expressions are applicable for variable broadband disturbances expressed in the frequency domain. An example of these expressions is presented prior to numerical results.

The Theodorsen expression for unsteady lift due only to mid-chord pitching motion is,

$$L = \pi\rho b^2[U_\infty\dot{\alpha}] + 2\pi\rho U_\infty bC(k)\left[U_\infty\alpha + \frac{b}{2}\dot{\alpha}\right] \tag{4.17}$$

$$L = \pi\rho b\,[bU_\infty\dot{\alpha} + 2U_\infty^2C(k)\alpha + bU_\infty C(k)\dot{\alpha}] \tag{4.18}$$

$$L = \pi\rho b\left[2U_\infty^2C(k)\alpha + bU_\infty\big(1 + C(k)\big)\dot{\alpha}\right] \tag{4.19}$$

where the pitching motion can be defined by a summation of any number of sinusoidal contributions. This is expressed here for the unsteady pitch position as,

$$\alpha = \sum_{n=1}^{N} \alpha_n \tag{4.20}$$

and an equivalent summation applies for the subsequent pitch velocity. This yields,

$$L = \pi\rho b \left[2U_\infty^2 C(k)(\alpha_1 + \cdots + \alpha_N) + bU_\infty\big(1 + C(k)\big)(\dot{\alpha}_1 + \cdots + \dot{\alpha}_N)\right] \tag{4.21}$$

which applies equally in either the time or frequency domains. If utilization of the expression is desired for a pitch disturbance defined in the time domain, then the pitch position and velocity terms would need to be convolved with the Theodorsen function, $C(k)$, which is defined in the frequency domain. If however, the pitch disturbance is defined in the frequency domain (through a Fourier transform, as is done throughout this work), then the combinations of the Theodorsen function and the pitching motion components are simple products. This utilizes the concept of convolution theorem, and the corresponding lift expression is,

$$L(k) = \pi\rho b \left[\Big(2U_\infty^2 C(k)\alpha_1(k) + bU_\infty\big(1 + C(k)\big)\dot{\alpha}_1(k)\Big) + \cdots \right.$$
$$\left. + \Big(2U_\infty^2 C(k)\alpha_N(k) + bU_\infty\big(1 + C(k)\big)\dot{\alpha}_N(k)\Big)\right] \tag{4.22}$$

$$L(k) = L_1(k) + \cdots + L_N(k) \tag{4.23}$$

showing that the lift from a mid-chord pitching motion that is composed of components from multiple frequencies is also governed by the principle of superposition. It should be clear that this concept and implementation applies equally to the unsteady lift, pitching moment, and differential pressure expressions for both heaving and pitching disturbance motions. Analysis of broadband results in this way is a common occurrence for work associated with unsteady inflow velocities to a foil (i.e. inflow gusts or turbulence) when utilizing the Sears model, Sears (1941) (these are but a few examples, Anderson et al. (2015), Catlett and Anderson (2016), and Glegg and Devenport (2009)); however, this does not seem as prevalent in work associated with the current problem of unsteady foil motion.

UPF calculations for a flat foil configuration which implement a broadband mid-chord pitching motion are provided with the remainder of this section. This disturbance motion is generated by the

summation of sinusoids of varying amplitude and phase properties superimposed over white noise, in an attempt to emulate realistic, but completely arbitrary, small-scale motion. In an experimental configuration, data would be collected for sufficiently long amounts of time such that results exhibit adequate statistical convergence and can benefit from averaging across numerous ensembles. Presently, instead of a single long calculation, ten distinct calculations with disturbance motion of very similar statistical properties were performed such that the results in the frequency domain could benefit from ensemble-averaging.

For these pitching calculations, the maximum instantaneous pitch angle within each calculation was normalized to a value of $|0.1|$ degrees. Each calculation was performed at a sampling frequency of $2\ kHz$ and for a length of 1.0 second. Figure 4.30 presents the time series of the unsteady pitch position, $\alpha(t)$, and UPF calculated unsteady lift coefficient, $C_L(t)$, for one of these calculations; a zoomed view is also provided. The unsteady pitch position and lift coefficient signals are similar, but are certainly not a scaled version of each other. This is due to the varied magnitude and phase properties of the C_L/α transfer function across frequency, where in these cases the disturbance motion contains rich frequency content.

Given that these disturbance motions and foil responses are broadband signals, viewing them as time series provides little insight beyond initial diagnostics; they are more appropriately assessed in the frequency domain. Figure 4.31 presents the auto-spectral densities of the unsteady pitch position, $\Phi_\alpha = \alpha\alpha^*/\Delta f$, and unsteady lift coefficient, Φ_{C_L}, for each of the ten ensemble calculations as a function of reduced frequency. Which is now evident in these plots, the unsteady pitch signals were constructed with three arbitrarily-placed, moderately damped, resonant features across the range of resolved reduced frequencies. While these pitch signals were constructed to have the same statistical properties, each are unique, and the variability in the signals is indicated by the spread between these spectra. As an example, the variability at frequencies away from these resonant peaks is significantly greater than those at the peaks. In addition to the resonant features, these pitch and calculated unsteady lift signals contain non-trivial content across the entire resolved frequency range and involve spectral levels over several orders of

magnitude. Simply for visual reference, the approximate frequency ranges for the resonant features are highlighted.

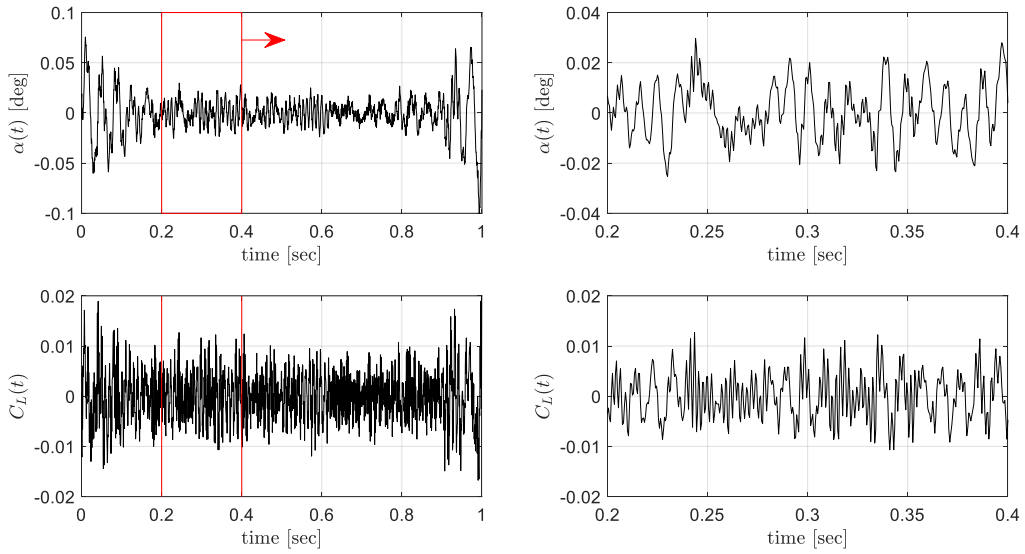

Figure 4.30. Example UPF calculated lift coefficient for a broadband pitch disturbance

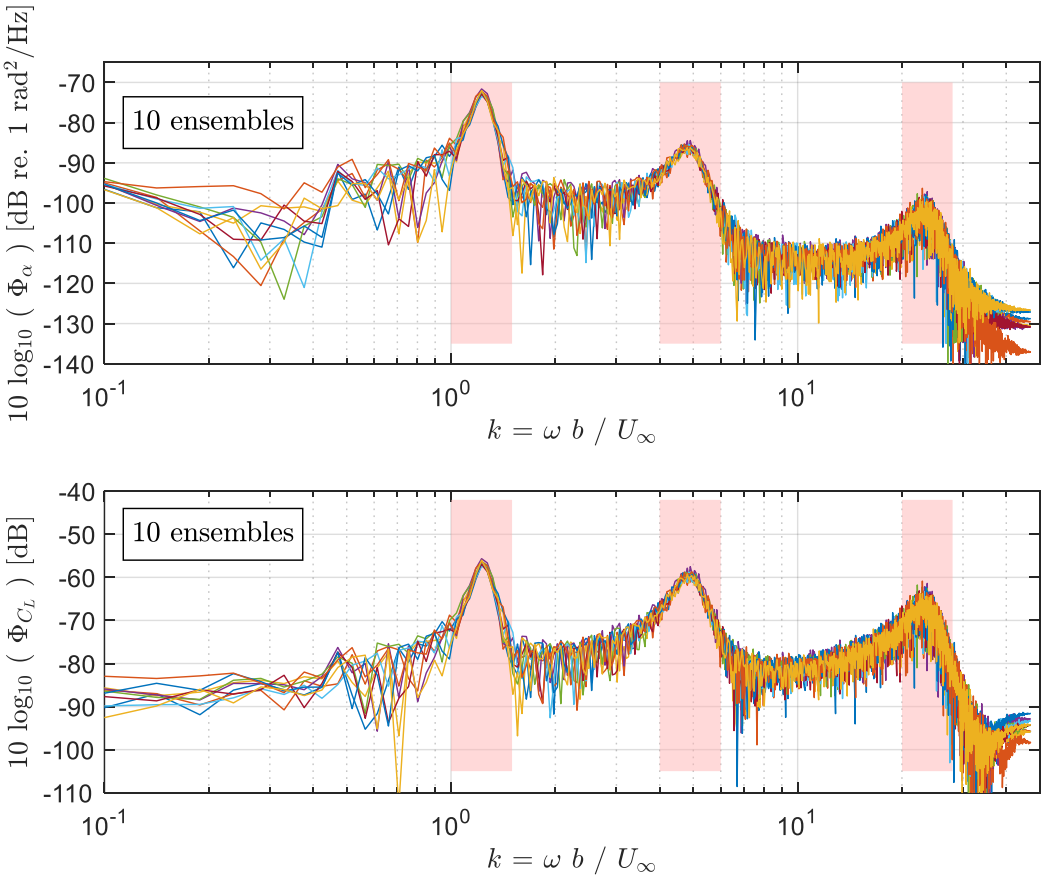

Figure 4.31. Auto-spectra of the unsteady pitch position and lift coefficient for ten distinct calculations

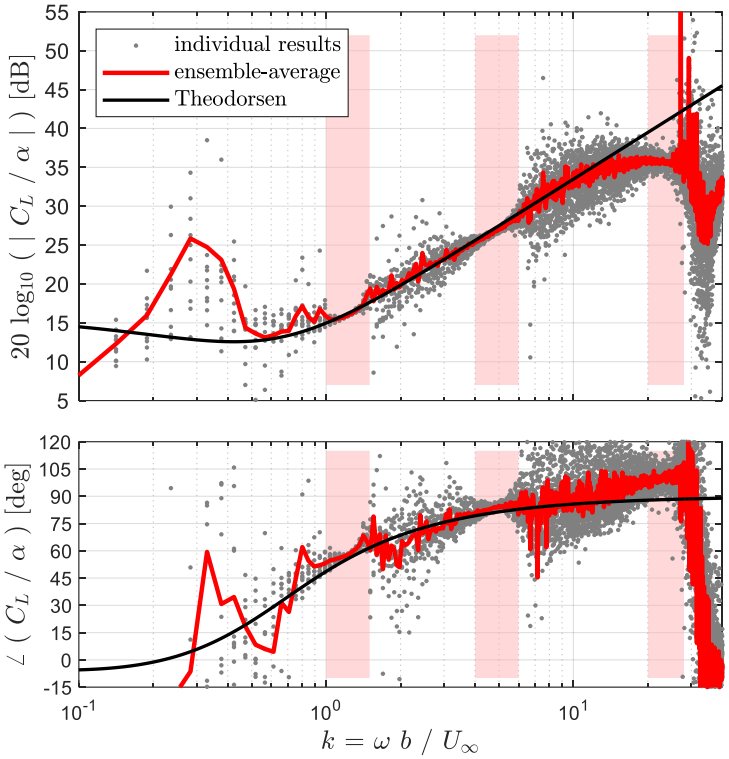

Figure 4.32. Analytical and calculated transfer functions of unsteady lift coefficient to pitch position for flat foils undergoing broadband motion

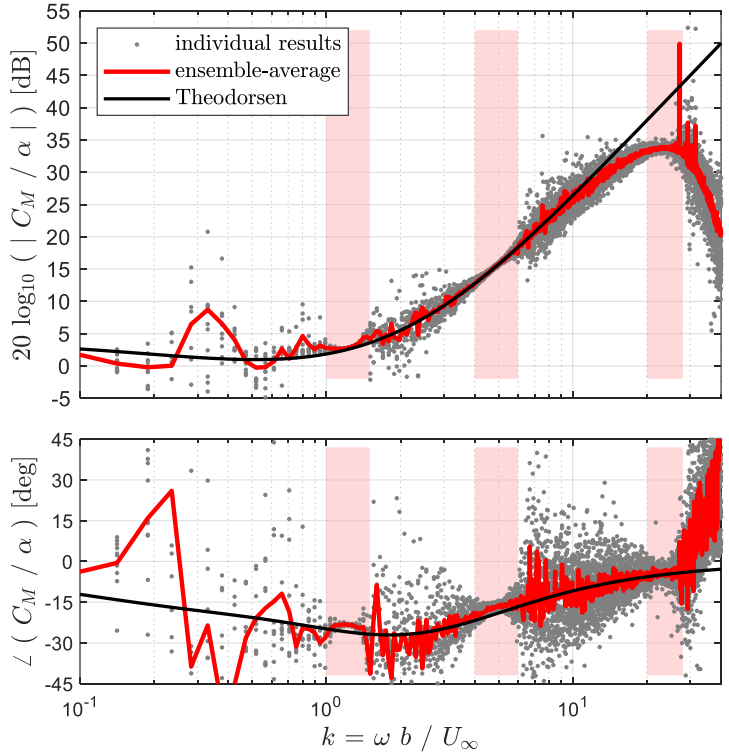

Figure 4.33. Analytical and calculated transfer functions of unsteady pitching moment coefficient to pitch position for flat foils undergoing broadband motion

Presented in an identical manner as for the results for sinusoidal disturbance motion, Bode plots of the calculated unsteady lift and pitching moment transfer functions are provided in Figure 4.32 and Figure 4.33, respectively. Where the results for sinusoidal motion populate the frequency domain at distinct values, the broadband signals provide results across the range of resolved frequencies. As can be inferred from the spectra of Figure 4.31, since these are relatively short signals in terms of providing statistical convergence, the result of any individual calculation yields a substantial amount of variability. This is why several calculations were performed, such that the magnitude and phase properties can be averaged across the number of ensembles to significantly improve the determined results. Within Figure 4.32 and Figure 4.33 the results for each frequency bin for all of the calculations are plotted as gray dots, which provides an insight into the substantial variability. The red line is the ensemble-averaged magnitude and phase results for each response, and the black line is the corresponding Theodorsen expression. As can be seen, the ensemble-average, calculated transfer function results follow the Theodorsen model quite adequately in both magnitude and phase properties over much of the reduced frequency range, specifically for the range of reduced frequencies directly at and between the resonant features.

While the calculated results generally compare well to the Theodorsen model, there are some interesting features worth discussing. As the same highlighted reduced frequency ranges are carried between these figures, it can be seen that these are the portions of the calculated results which exhibit the least variability and therefore tightest collapse. This makes intuitive sense, as these frequencies dominate the disturbance motion signals and correspondingly the response signals. While there remains variability in the results at frequencies away from these resonances, it should be recognized that ensemble-averaging over ten samples is a fairly low sample count, and these results should only improve with an increased sample size.

There is an intriguing behavior in both the unsteady lift and pitching moment responses at the highest reduced frequencies resolved in these calculations. This is the clear attenuation of the magnitudes and altering of the phase distributions of these responses at an approximate threshold of $k > 20 - 30$.

Ultimately, comprehensive analysis and understanding of the source of this behavior is left for future work; though it would seem that immediate efforts should involve calculations at a higher sampling rate, in order to expand the range of resolved reduced frequencies and better discretize the shed wake of vorticity.

Figure 4.34 provides two sample views for a limited range of the downstream flow field from a single instance of time from one of these broadband calculations. The spatial coordinates are normalized on the foil chord and the two views correspond to the same time index; simply the top plot has axes which are equal in size and the other does not. As before, each point vortex is represented by a dot, though the distribution is now connected. From the top plot of this figure, the spatial distribution of the shed vorticity can still be generally considered to follow a chordline-extended trajectory, as there appears to be no substantial deviations. The bottom plot provides a zoomed view, where it is evident that the point vortices are displaced. The vorticity distribution does not appear to establish a coherent vortex pattern, as seen previously, but rather appears relatively chaotic. The linking of the ramifications of this flow field behavior to the unsteady foil responses is left for future pursuit.

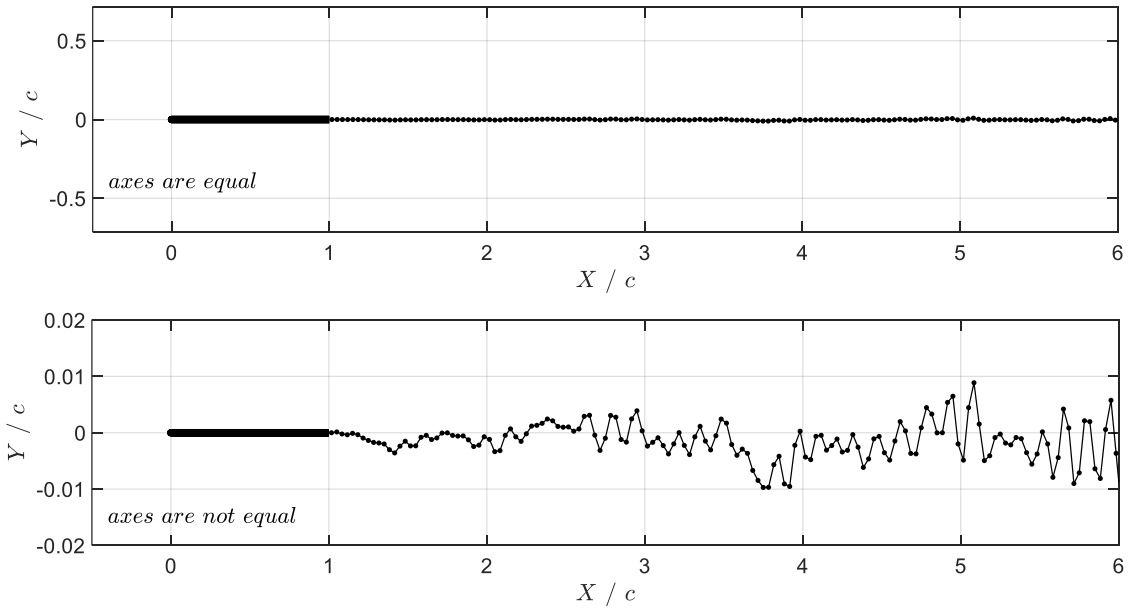

Figure 4.34. Example views of the wake of shed point vortices for broadband pitch motion

4.5 Heave Disturbances for Finite Thickness Joukowski Foils

Upon initial review and orientation to the Theodorsen model, it is seen that the assumption of treating a foil as an infinitely thin flat plate is critical in the analytical development of the model, as it provides considerable advantages and simplifications towards the potential flow and conformal mapping framework, which ultimately yields direct expressions for the unsteady foil responses. As necessary as this assumption is, it is of interest to attempt to identify for what conditions and in what possible ways this assumption would appear to be restrictive. As shown and discussed earlier, a considerable amount of work on the topic of unsteady responses to foil motion exists. Many references present experimental and numerical results for various foils of finite profile which generally exhibit the robustness and acceptability of the Theodorsen model, leading one to conclude that the flat foil assumption is correspondingly quite acceptable. However, much of this available work does not extend above an approximate threshold of $k \approx 1$, and for those that do, unsteady foil response data is not always available.

The same array of UPF calculation conditions were performed for foils of Joukowski profile which have a maximum thickness-to-chord ratio of $5, 10,$ and 15%, in addition to the flat foil conditions. Bode plots of the C_L and C_M responses are presented in Figure 4.35 and Figure 4.36, respectively, and the unsteady heave conditions are such that the maximum induced angles of attack are 0.1 degrees. For the unsteady lift responses, there is minimal alteration to either the magnitude or phase properties as a result of implementing these Joukowski foil profile sections.

This is certainly different for the C_M response, as there is a clear alteration to the response for the series of finite thickness foils. At low reduced frequencies, the effect on the magnitude is between 1 and 2 decibels and the phase is seen to be minimally altered. However, over the range of higher reduced frequencies there is a prominent increase in the magnitude of the response and an equally significant progressive change towards a 90 degree phase lead. These augmented responses exhibit a direct dependence on the foil thickness, with the changes being more prominent for increasing foil thickness. The dotted lines on the magnitude portions of these figures are visual aids at the specified slopes of k^1.

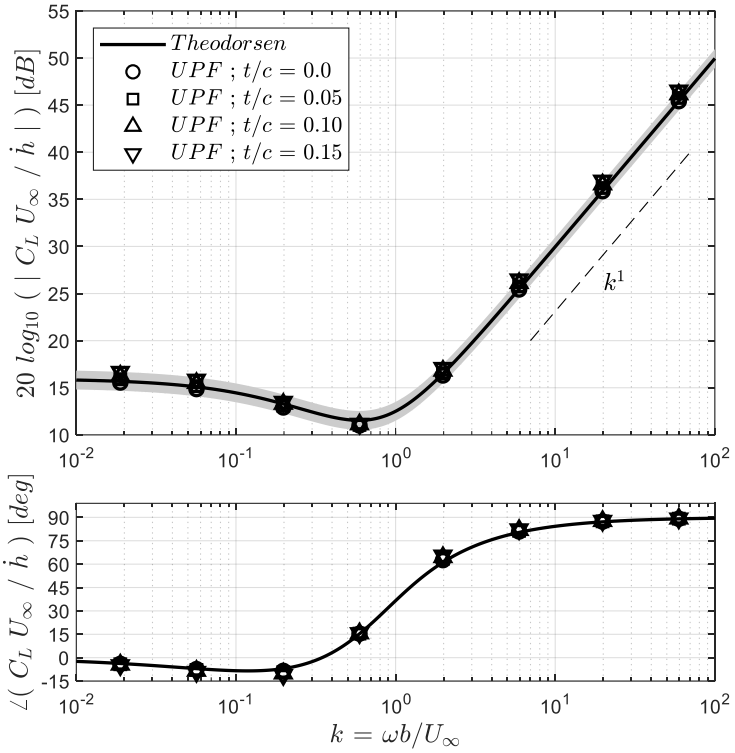

Figure 4.35. Analytical and calculated transfer functions of unsteady lift coefficient to normalized heave velocity for variable thickness Joukowski foils undergoing sinusoidal motion

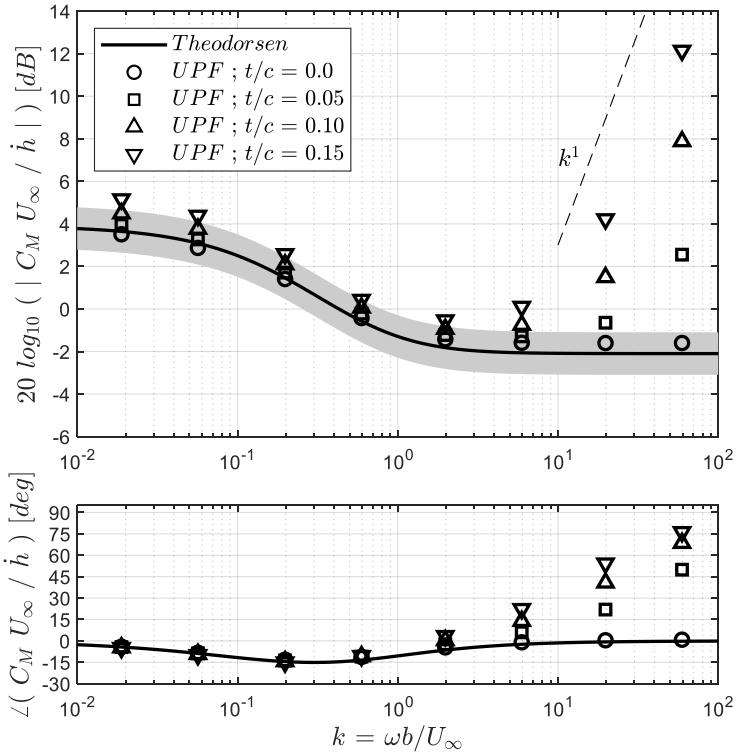

Figure 4.36. Analytical and calculated transfer functions of unsteady pitching moment coefficient to normalized heave velocity for variable thickness Joukowski foils undergoing sinusoidal motion

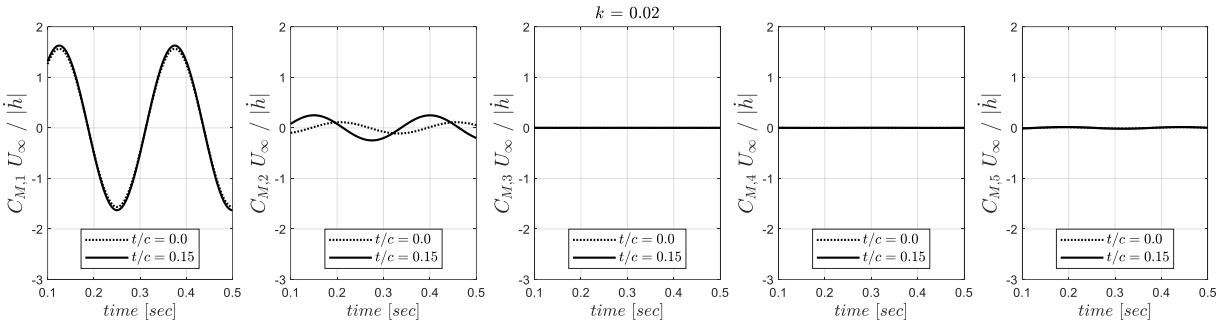

Figure 4.37. Contributions to the unsteady pitching moment due to heaving motion for thin and 15% thick foils at $k = 0.02$; see Eq. 2.39

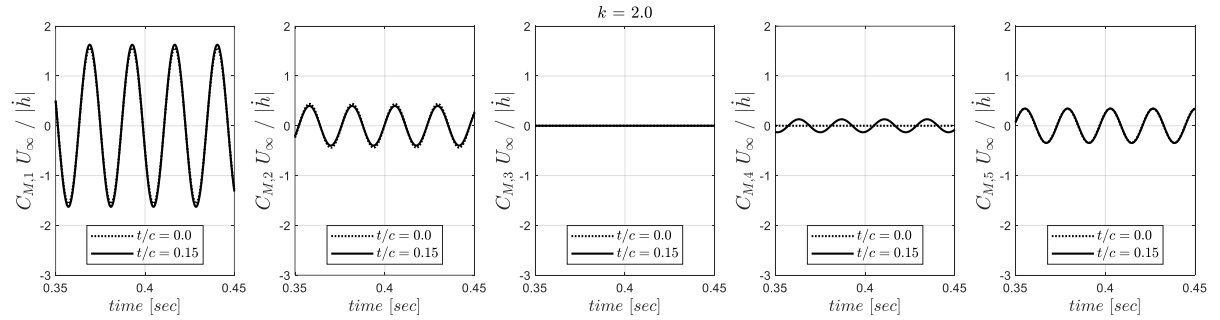

Figure 4.38. Contributions to the unsteady pitching moment due to heaving motion for thin and 15% thick foils at $k = 2.0$

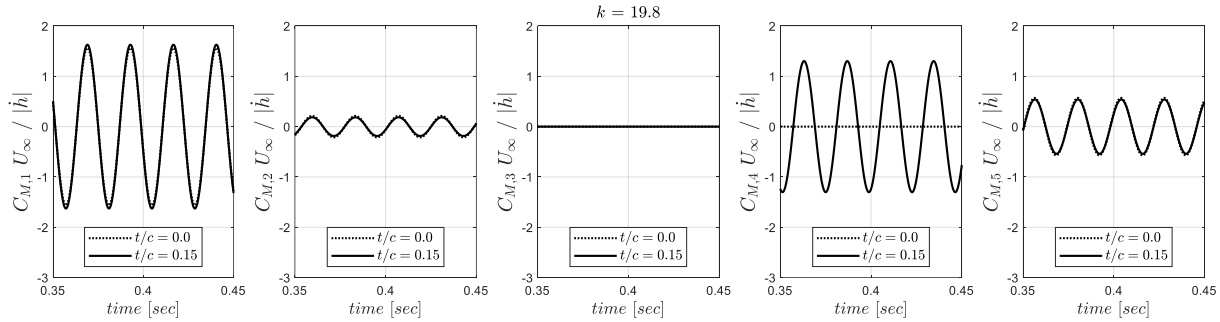

Figure 4.39. Contributions to the unsteady pitching moment due to heaving motion for thin and 15% thick foils at $k = 19.8$

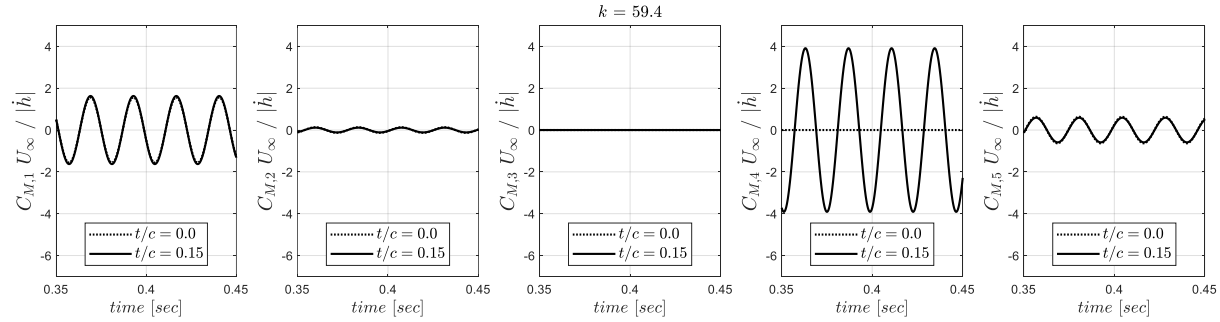

Figure 4.40. Contributions to the unsteady pitching moment due to heaving motion for thin and 15% thick foils at $k = 59.4$

Beyond identifying these altered high reduced frequency C_M responses for finitely thick, symmetric Joukowski foils relative to what the Theodorsen model specifies, it is the intention of this work to understand why this would be occurring. Further, the development of explicit expressions for these augmented foil responses is pursued from analysis within the potential flow framework. The rest of this section presents the most pertinent aspects of this analysis and the subsequent results. All of the detailed analysis and development is deferred to Appendix A and Appendix B, in order to maintain a manageable scope for the presentation of results.

The series of Figure 4.37 through Figure 4.40 exhibit the critical feature used to better understand these altered C_M responses attributed to foil thickness. The figures show the decomposed pitching moment terms, $C_{M,1}, \ldots, C_{M,5}$, as defined in Section 2.6, for a progression of reduced frequencies, $k = 0.02, 2.0, 19.8,$ and 59.4, respectively. Each plot shows a portion of the corresponding time series for the flat and 15% thick foils. Beginning with Figure 4.37, at this lowest reduced frequency of 0.02, it is the $C_{M,2}$ term which shows any significant difference between the foil cases; this term being the interaction of the source and wake velocities. In relation to the overall response though, this change is somewhat muted given the dominance of the $C_{M,1}$ term. This is an example of the low reduced frequency behavior, and is not however the changes that are occurring at the high reduced frequency conditions.

Figure 4.38 provides this C_M decomposition for $k = 2.0$ and little difference is seen between the thin and thick foil responses, other than for $C_{M,4}$ which is for the source flow potential. As is seen for the increasing reduced frequency conditions in the subsequent figures however, this altered $C_{M,4}$ response for the 15% thick Joukowski foil grows and begins to dominate the overall response. It is particularly important that it is this source term which exhibits an altered response because as a result of its definition, it is a known quantity simply from the foil geometry and disturbance motion. No consideration is needed for the shed wake of vorticity, and therefore analysis can be pursued strictly on these source contributions.

This analysis of the flow potential of the source contributions (i.e. the freestream and doublet, in this instance of heaving motion) is fully pursued in Appendix B. Beginning with the source flow potential terms and the definition of the circle (which is subsequently mapped to the Joukowski foils),

$$f = U_o z e^{-i\,\alpha_o} + U_o \frac{a_c^2 e^{i\alpha_o}}{z - \delta_x} \qquad ; \qquad z = r_c e^{i\theta} + \delta_x \tag{4.24}$$

a progression of analysis is followed which links the time derivative of the flow potential with the pressure through the Unsteady Bernoulli equation. This subsequently leads to a transfer function expression for the differential pressure across the foil chord as a result of normalized heave velocity,

$$\frac{C_P U_\infty}{\dot{h}} = -i2k \frac{r_c}{b}\left[1 + \frac{a_c^2}{r_c^2}\right] sin(\theta) \tag{4.25}$$

where symmetry of the foil is utilized for $C_{\Delta P} = 2C_P$, and all of these terms are known based on the circle and foil geometry, in addition to the reduced frequency, k.

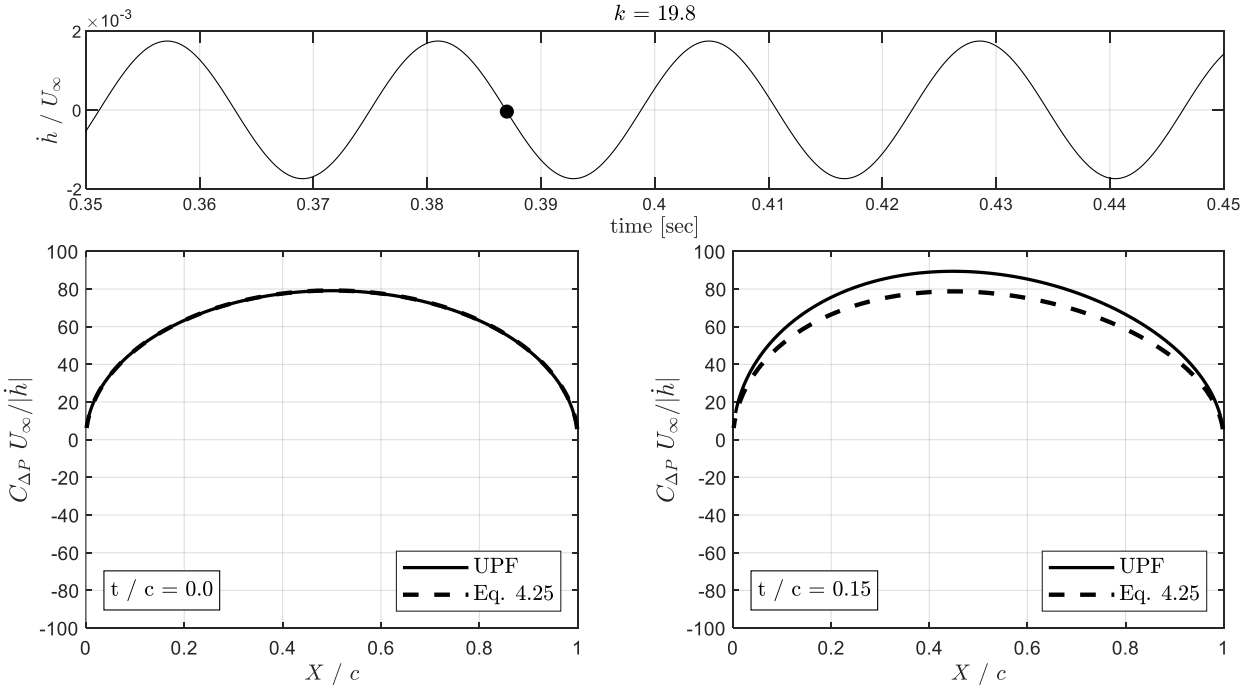

Figure 4.41. Instantaneous differential pressure distributions for the thin and 15% thick Joukowski foils for heaving motion at $k = 19.8$

An example of this expression relative to the corresponding UPF calculated results is presented in Figure 4.41 for a reduced frequency of $k = 19.8$. The top plot is a partial time series of the normalized heave velocity, where the black dot denotes the instance of time for which the differential pressure results below are plotted. As can be seen, Eq. 4.25 reverts back to the limiting high frequency value of the Theodorsen model, see Eq. 2.56, for a flat foil condition (see Appendix B). The comparison of both the $\sin(\theta)$ distribution and the amplitude of the response is very favorable between the prediction and the calculated UPF results for the thin foil condition. This specific instance of time within the calculated results corresponds with an approximate zero-crossing of the heave velocity, which was selected given the phase implications of the i within the transfer function expression.

Similarly, the differential pressure distribution for the 15% thick foil is also presented in Figure 4.41 at this same instance of time. The comparison between the calculated and predicted distributions is not ideal, though generally considered acceptable. What is most notable and important for this condition is that an asymmetry of the differential pressure across the foil chord is both seen in the calculated results and exhibited by the predictive expression. For the thin foil case at progressively large reduced frequencies, the differential pressure distribution becomes symmetric about the mid-chord; as a result, this portion of the pitching moment response cancels (being determined about the foil mid-chord), leading to the flattening of the response as seen in Figure 4.36. Breaking this mid-chord symmetry for the finitely thick foils however, results in residual contributions to the pitching moment response which grows as k^1 (again, seen in Figure 4.36). While the chordwise distribution remains a function of $\sin(\theta)$, the asymmetry results from the implications of the circle being displaced from the origin.

Building from these differential pressure results, the pitching moment response can be pursued through analytic integration of the differential pressure across the foil chord. As earlier, effectively all of this detailed analysis is deferred to Appendix A and Appendix B, and the culminating highlights are presented in this section. Utilizing the pressure expression above, knowledge of the foil geometry, and the definition of the pitching moment about the mid-chord, a transfer function expression for the pitching

moment as a result of normalized heaving velocity for high reduced frequency conditions is developed. This development involves several considerations and specific simplifications of the expressions for the foil geometry, which are facilitated by the conformal Joukowski mapping. Jumping directly to the concluding result, this expression is found to be,

$$\left.\frac{C_M\, U_\infty}{\dot{h}}\right|_{source,\ \ flow\ potential} \approx -i\frac{\pi}{2}k\frac{\delta_x r_c^2}{b^3}\left[1+\frac{a_c^2}{r_c^2}\right]\left[1+\frac{a_c^2}{2r_c^2}-\frac{a_c^4}{2r_c^4}\right] \tag{4.26}$$

This represents the high reduced frequency contribution to the pitching moment calculated about the foil mid-chord from the source flow potential terms for Joukowski foil profiles of variable thickness. These variables are known, being defined by the implemented geometry. Given that this contribution is for thick foil conditions (and drop for a flat foil condition, $\delta_x = 0$) it can be added to the Theodorsen expression to yield the following,

$$\left.\frac{C_M\, U_\infty}{\dot{h}}\right|_{thick} \approx \left.\frac{C_M\, U_\infty}{\dot{h}}\right|_{Theo.} - i\frac{\pi}{2}k\frac{\delta_x r_c^2}{b^3}\left[1+\frac{a_c^2}{r_c^2}\right]\left[1+\frac{a_c^2}{2r_c^2}-\frac{a_c^4}{2r_c^4}\right] \tag{4.27}$$

This expression is compared directly to the UPF calculated results for the 5% and 15% Joukowski foils in Figure 4.42. This is the same Bode plot format as earlier, however the reduced frequency axes have been windowed to only include the high reduced frequency range where this augmentation takes effect. This added contribution does not influence the response over lower reduced frequencies as it is appreciably below the corresponding portions of the Theodorsen model. As can be seen, this augmented expression captures both the magnitude and phase properties of these pitching moment responses for the varying thick foil conditions. The rise of the pitching moment response to a dependence on k^1, the shifting of the response towards a 90 degree phase lead, and the corresponding influence of the variable foil thickness condition are captured well by this expression. The slight offset between the calculated and predicted magnitude results is assumed to be a result of the assumptions necessary to reach the final expression.

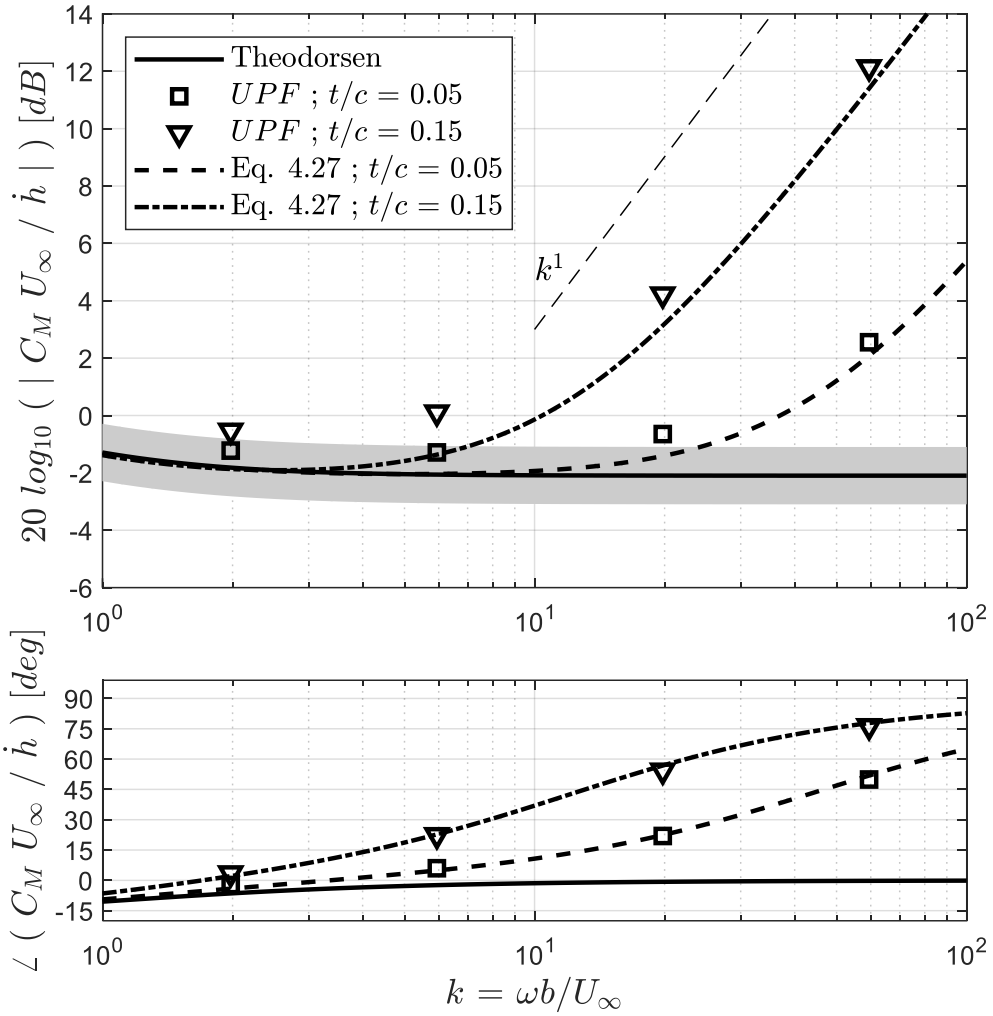

Figure 4.42. High reduced frequency portion of the unsteady pitching moment transfer function for the 5% and 15% thick Joukowski foils undergoing heaving motion

Though not an inherent topic of the present analysis and effort, the shifting of the phase of the pitching moment response due to heaving motion into a regime of phase lead is significant as this can be indicative of unstable foil response behavior. It is acknowledged that these calculated UPF results and corresponding potential-flow based expressions are applicable to small disturbance motion and are only for the pressure contributions to the response. Therefore, in the instance of a foil immersed in a specified working fluid, the effects of viscosity (as an example) may preclude or alter further this high reduced frequency behavior. The eventual assessment of these considerations are left for future efforts.

In the context of presenting these findings in a separate way as to be directly comparable to the results of other studies, the altered pitching moment response due to the consideration of foil thickness is recast into the following,

$$\frac{\left.\frac{C_M\,U_\infty}{\dot{h}}\right|_{thick}}{\left.\frac{C_M\,U_\infty}{\dot{h}}\right|_{Theo.}} \approx 1 - \frac{i\frac{\pi}{2}k\frac{\delta_x r_c^2}{b^3}\left[1+\frac{a_c^2}{r_c^2}\right]\left[1+\frac{a_c^2}{2r_c^2}-\frac{a_c^4}{2r_c^4}\right]}{\left.\frac{C_M\,U_\infty}{\dot{h}}\right|_{Theo.}} \tag{4.28}$$

As seen in the results above, the consideration of foil thickness induces strong alteration to both the magnitude and phase properties in the high reduced frequency region of the pitching moment response. Utilizing the recast expression of Eq. 4.28, the following are written,

$$\Delta dB = 20\log_{10}\left(\left|\left.\frac{C_M\,U_\infty}{\dot{h}}\right|_{thick}\Big/\left.\frac{C_M\,U_\infty}{\dot{h}}\right|_{Theo.}\right|\right) \;\; ; \;\; \Delta\phi = \angle\left(\left.\frac{C_M\,U_\infty}{\dot{h}}\right|_{thick}\Big/\left.\frac{C_M\,U_\infty}{\dot{h}}\right|_{Theo.}\right) \tag{4.29}$$

In this way, the reduced frequencies at which selected thresholds of the thick foil responses differ from the Theodorsen model, for both magnitude and phase properties, are plotted as a function of foil thickness in Figure 4.43 and Figure 4.44. For the foil thicknesses presently illustrated, changes to the magnitude of the pitching moment response of 3 decibels or greater are found when consideration is given to reduced frequencies greater than nominally a value of ten; where more significant alterations are certainly possible at elevated conditions. Changes to the phase of the response by 15 and even 30 degrees for most foils of practical thickness are predicted however for reduced frequencies which are less than a value of ten.

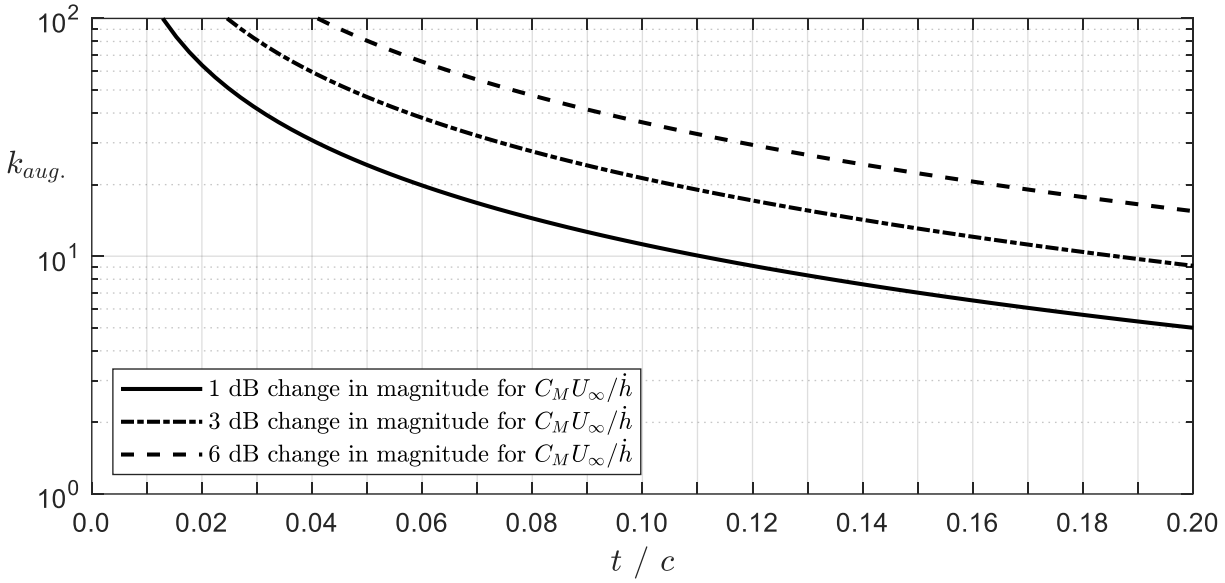

Figure 4.43. Identification of the reduced frequencies at which the magnitude of the unsteady pitching moment response crosses specific thresholds of alteration as a function of foil thickness-to-chord ratio

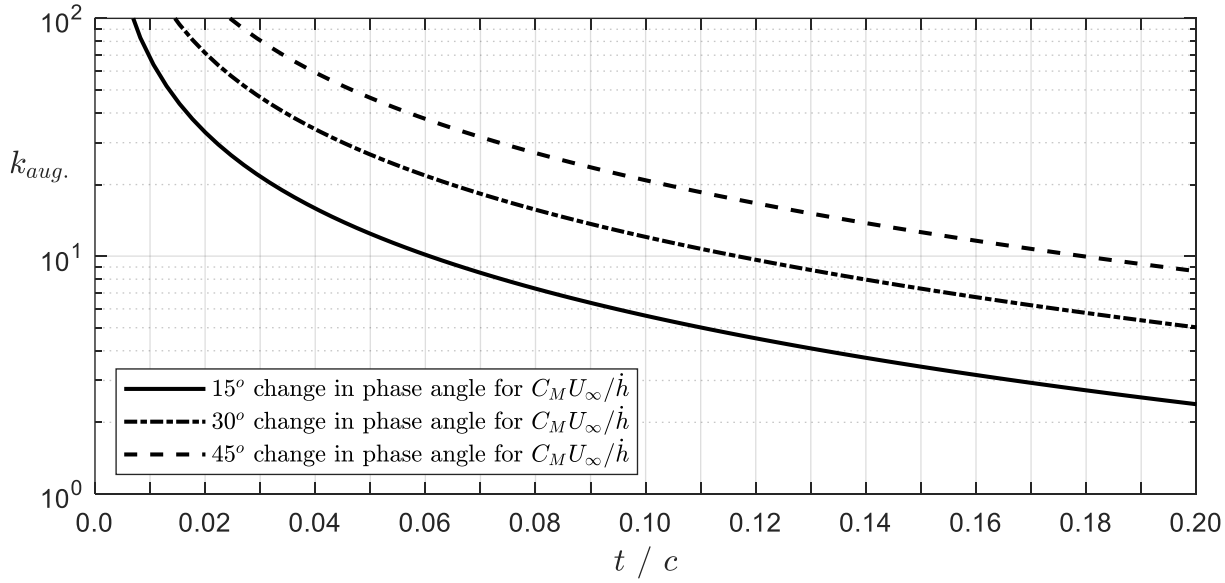

Figure 4.44. Identification of the reduced frequencies at which the phase of the unsteady pitching moment response crosses specific thresholds of alteration as a function of foil thickness-to-chord ratio

4.6 Pitch Disturbances for Finite Thickness Joukowski Foils

As in the previous section, an exploration and analysis of any substantial effects on the unsteady foil responses determined from UPF calculations due to a finite foil profile (i.e. thickness) is the present concentration. Again, the same array of Joukowski foil profile sections and operating conditions as have been common throughout this work are implemented. The complex-valued transfer functions of unsteady lift and pitching moment are presented in Figure 4.45 and Figure 4.46 for the variable thickness Joukowski foils for both the UPF and TURNS2D calculations. For reduced frequency conditions of $k \lesssim 1$, both the unsteady lift and pitching moment responses are seen to be relatively insensitive to these foils having variable thickness, symmetric profiles. There is a slight amplification of $\sim 1\ dB$ for the C_L response and $\sim 2\ dB$ for the C_M response for the 15% thick foil at the lowest reduced frequency conditions, though generally both responses follow the Theodorsen model fairly well and would appear to fall within the generalized uncertainty of prior results. To some extent this relative insensitivity of these foil responses to foil thickness for this sinusoidal, mid-chord pitching motion should also be a somewhat expected result, given that previous experimental studies (several of which are reviewed earlier) utilized physical foil models of various profile sections and also found agreeable results to the Theodorsen model. It is however an important distinction to note that few studies have covered a range of reduced frequencies as wide as the present work.

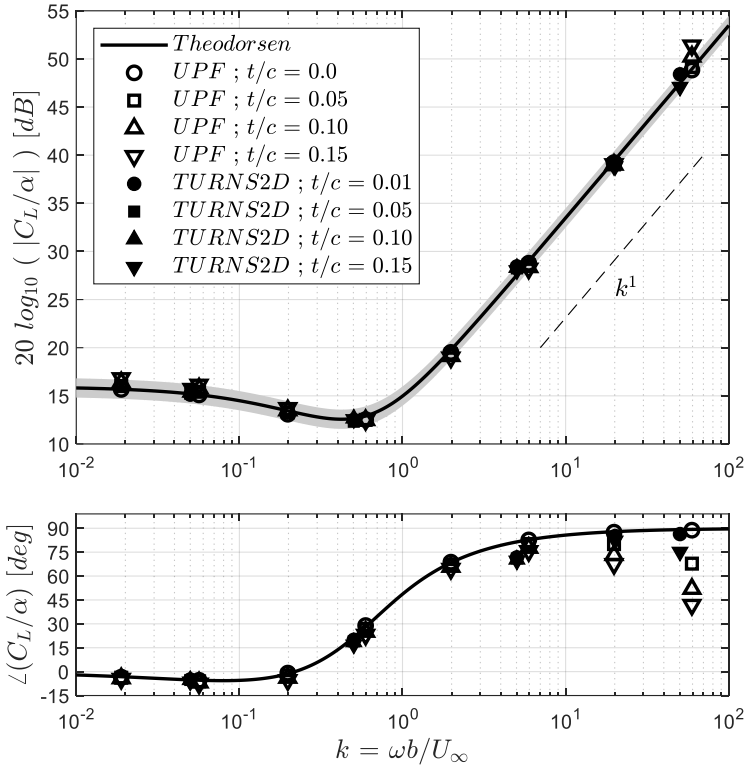

Figure 4.45. Analytical and calculated transfer functions of unsteady lift coefficient to pitch position for variable thickness Joukowski foils undergoing sinusoidal motion

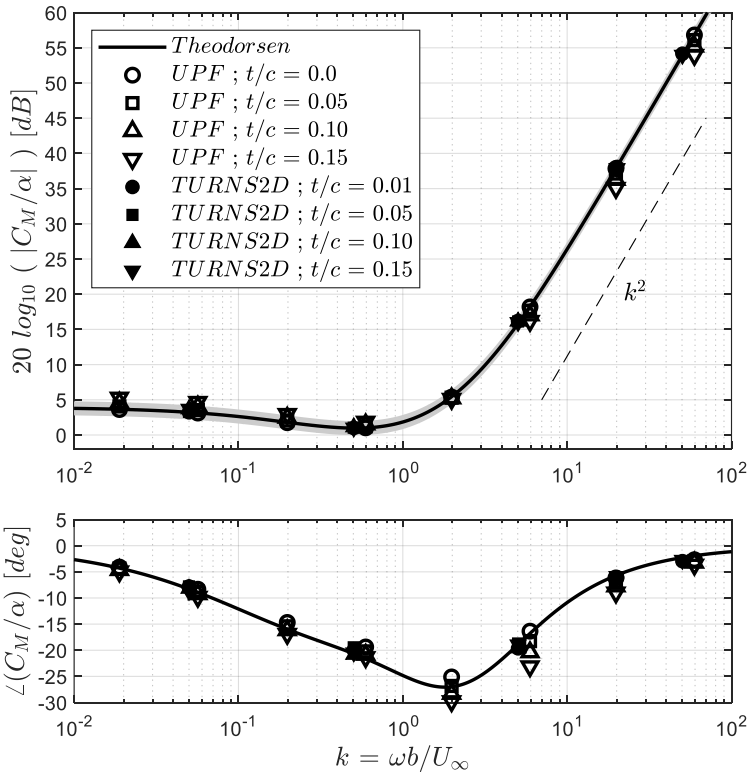

Figure 4.46. Analytical and calculated transfer functions of unsteady pitching moment coefficient to pitch position for variable thickness Joukowski foils undergoing sinusoidal motion

However, there does appear to be a threshold beginning around $k \gtrsim 1$ for which the unsteady lift responses of the finitely thick foils begin to deviate from the Theodorsen model. This manifests as both an amplification and a notable phase shift of the lift response, and shows direct dependence on foil thickness. The associated TURNS2D results do not exhibit deviations as prominent as those of the UPF results, and the specific causes for this have not yet been fully identified. In these cases, the disturbance motion is small, the freestream Mach numbers are low, and the flow remains attached. While these conditions involve rather high values of reduced frequencies, they do still conform to the general reduced frequency and Mach number constraints proposed in Section 4.1. It is speculated however, that some combinatory effects of viscosity and compressibility of the fluid medium could be involved and which could account for the differences between the UPF and TURNS2D results. Specific identification of the cause for the difference between the results remains open, however, the work and results from two references may provide insight to this. The works of Taha and Rezaei (2019) and Yates (1980) present corrections and extensions to potential flow, unsteady foil responses due to viscosity considerations. They focus on pitching foils and in very brief partial summary, find that the phase of the unsteady lift can be altered by effects of viscosity. While portions of their work consider similar Reynolds numbers, their presented results do not extend up to the elevated reduced frequencies being currently considered (in addition to other differing characteristics). In their range of reduced frequencies being considered, $k < 1.0$, the viscous correction to potential flow results is seen to induce a phase lag on the unsteady lift. For the present higher reduced frequency conditions for finite thickness foils, an additional phase lead would be needed for the UPF results to better match the TURNS2D results. It is unclear if their corrections and extensions from viscous considerations would yield this behavior at these higher reduced frequency conditions. Further assessment requires dedicated analysis, and is left for future effort.

After acknowledging this departure from the Theodorsen model for the UPF results of unsteady lift for finitely thick, symmetric foils at high reduced frequencies, the natural next step is to work to understand why this would occur. In particular, the development towards explicit expressions for this augmentation to

the foil responses are sought. The remainder of this section highlights this analysis and subsequent results, where much of the detailed analysis and development is deferred to Appendices A and C.

This explanation begins with the prior inference that the unsteady lift response at high reduced frequency conditions is primarily controlled by the flow potential, source terms. Again, these are known explicitly for a defined pitch disturbance. The same decomposition technique as has been implemented previously is used for the unsteady lift signals for the thin and 15% thick Joukowski foils at the highest UPF reduced frequency of 59.4; these are presented in Figure 4.47. The differences between the thin and thick foils that are induced in the unsteady lift response are predominantly introduced in the $C_{L,4}$ term, again defined by the flow potential of the source contributions. This observation is what initiates the analysis of Appendix C. The $C_{L,4}$ response for the thick foil is seen to be amplified and phase lagged from the thin foil counterpart. Interestingly, the $C_{L,1}$ and $C_{L,5}$ terms for the thick foil condition work to counteract each other.

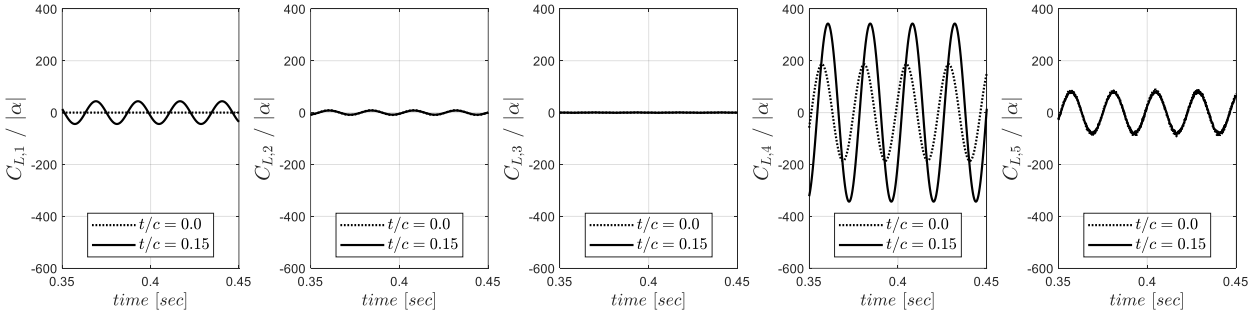

Figure 4.47. Contributions to the unsteady lift for thin and 15% thick foils at $k = 59.4$ and $|\alpha| = 0.1^o$

An analysis progression provided in Appendix C retains the dominant term for high reduced frequency conditions, which is taken to be the influence of the angular rotation rate of the pitching foil. The explicitly known expression for the flow potential of this contribution along the foil surface can be used to determine an expression for the complex transfer function between the coefficient of differential pressure and the disturbance motion, $C_{\Delta P}/\alpha$, for variably thick, symmetric Joukowski foils. This expression for the coefficient of differential pressure is found to be,

$$\frac{C_{\Delta P}}{\alpha} = 2k^2 \frac{r_c^2}{b^2}\left[\left(4 + 16\frac{\delta_x}{r_c}\right)\sin(\theta)\cos(\theta) + \left(4\frac{\delta_x}{r_c} + 8\frac{\delta_x^2}{r_c^2} - 4\frac{\Delta_x}{r_c}\right)\sin(\theta)\right] \tag{4.30}$$

where the following approximation is assumed for the coefficient of differential pressure, $\frac{C_{\Delta P}}{\alpha} = 2\frac{C_P}{\alpha}$, based on symmetry of the foil profiles. It should be noted that this expression is composed of variables defined both in the circle (r_c, δ_x, θ) and foil (b, Δ_x) planes. The differential pressure distributions from this expression and from the UPF results at a single time frame approximately at a local maximum of the pitch disturbance (signified by the black dot) are plotted for the thin and 15% thick foils at the reduced frequency condition of 19.8 in Figure 4.48. It is seen that Eq. 4.30 captures the calculated UPF pressure distributions for the thin and 15% thick foils quite reliably. While several additional figures could be generated for this type of result (the other foil thicknesses and high reduced frequencies), they would exhibit similarly positive comparisons between the calculated and modeled differential pressure distributions.

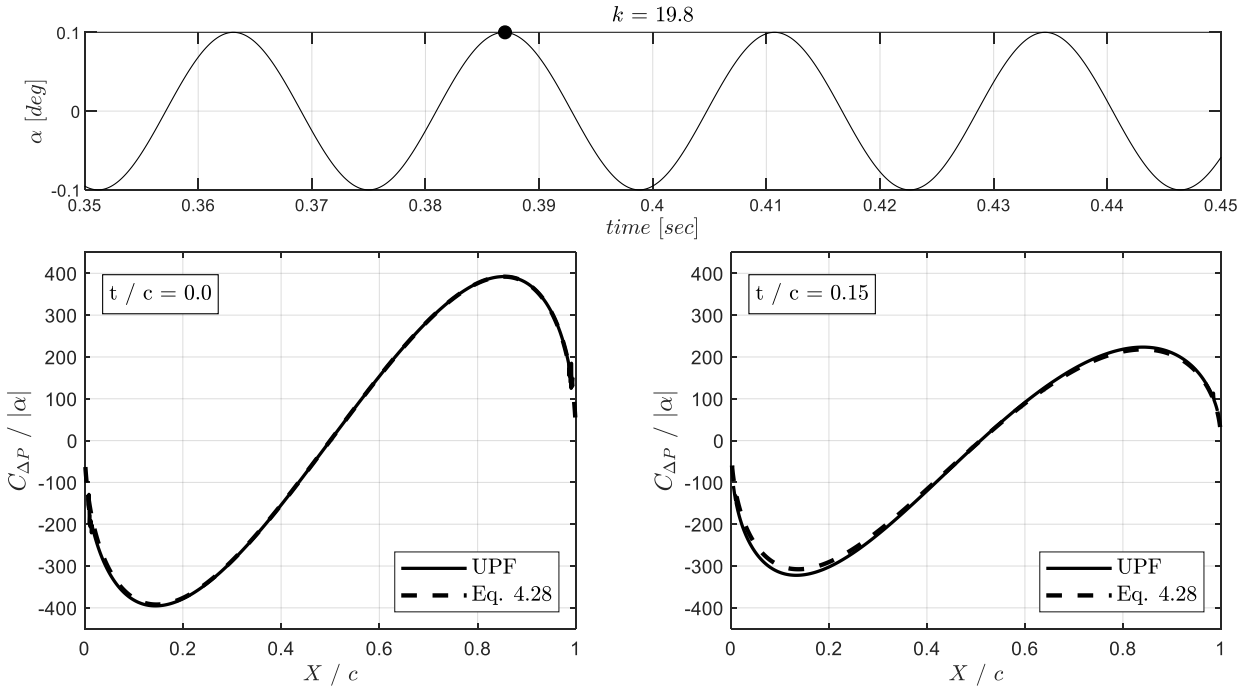

Figure 4.48. Instantaneous differential pressure distributions for the thin and 15% thick Joukowski foils for mid-chord pitching motion at $k = 19.8$

The thin foil pressure distribution follows closely the $\sin(\theta)\cos(\theta)$ distribution dictated by the high reduced frequency limit of the Theodorsen model according to Eq. 2.68, which is symmetric about the foil mid-chord. As such, the amplitudes of the unsteady pressures grow as k^2, while the unsteady lift amplitudes (for this mid-chord pitching condition) grow as k^1 since the pressure contributions from this term cancel due to the symmetry about the mid-chord. Similarly for the thin foil, unsteady pitching moment, these contributions reinforce, hence the k^2 dependence over high reduced frequencies for C_M.

For the finitely thick foils however, an asymmetry of the differential pressure develops from the combination of the $\sin(\theta)\cos(\theta)$ and $\sin(\theta)$ terms. This has a primary consequence on the C_L response that leads to amplified levels which are in-phase with the disturbance pitch motion. Correspondingly, the high reduced frequency C_M response for thick foils is not as strongly affected because the thin foil response is already growing as k^2 and approaching to be in-phase with the pitch motion. Interestingly, the amplitudes of the differential pressure across the chord for the thick foils are seen to decrease relative to the thin foil at these high reduced frequency conditions.

Referring to Appendices A and C for the detailed analysis progression and development, the pressure expression above can be further carried through to an unsteady lift expression by integrating across the foil chord. An expression for the unsteady pitching moment is presently omitted as no significant change is seen in the calculated results for this response over this range of high reduced frequencies. The expression for the unsteady lift is found to be,

$$\left.\frac{C_L}{\alpha}\right|_{source,\ \ flow\ potential} \approx -2\pi k^2\left(\frac{\delta_x r_c}{b^2} + 2\frac{\delta_x^2}{b^2} - \frac{\Delta_x r_c}{b^2}\right) \tag{4.31}$$

This term is effectively the added influence to the unsteady lift due to the finite thickness of the foil; therefore it is added as an augmentation to the Theodorsen expression, which is developed on the premise of an infinitely thin foil, to yield the following,

$$\left.\frac{C_L}{\alpha}\right|_{thick} \approx \left.\frac{C_L}{\alpha}\right|_{Theo.} - 2\pi k^2\left(\frac{\delta_x r_c}{b^2} + 2\frac{\delta_x^2}{b^2} - \frac{\Delta_x r_c}{b^2}\right) \tag{4.32}$$

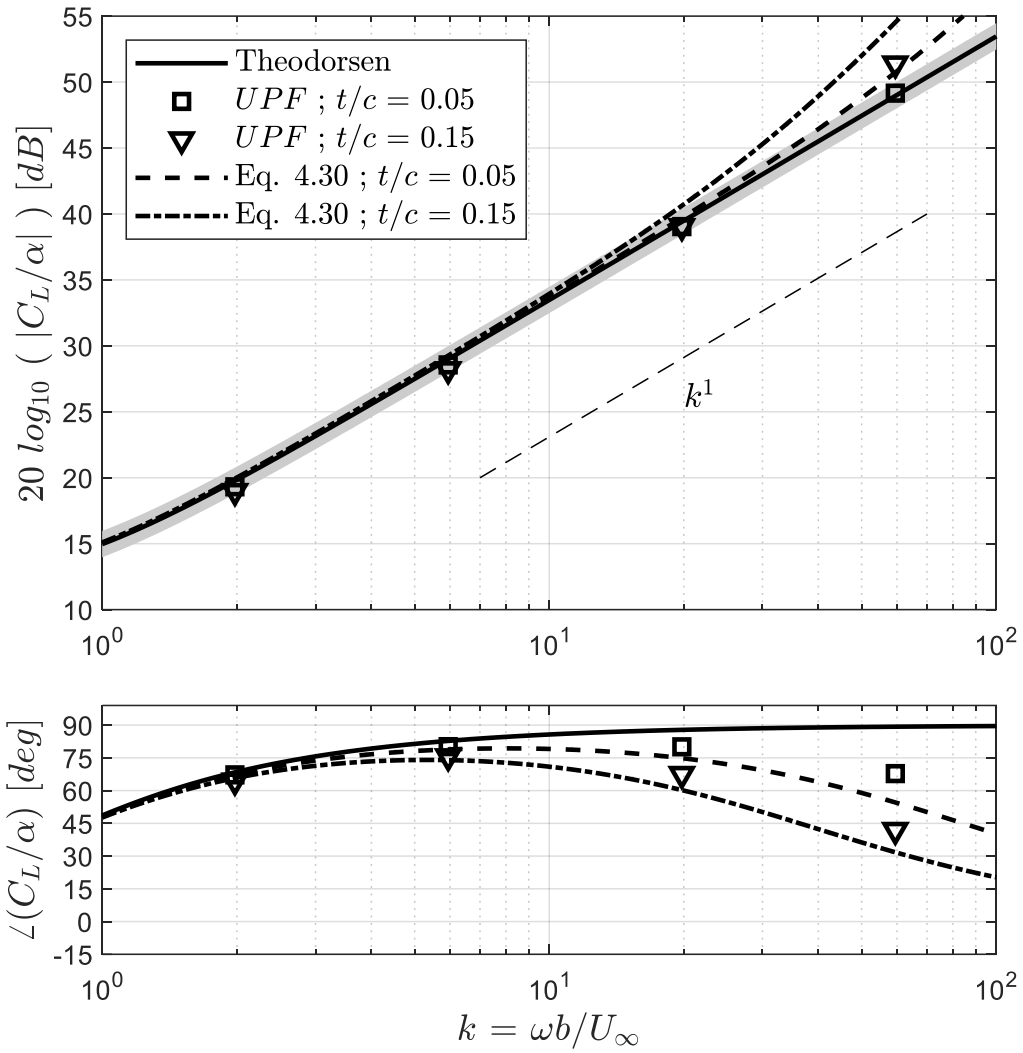

Figure 4.49. High reduced frequency portion of the unsteady lift transfer function for the 5% and 15% thick Joukowski foils undergoing mid-chord pitching motion

Figure 4.49 presents again the magnitude and phase of the unsteady lift responses for the UPF results, along with this expression for unsteady lift augmentation due to finitely thick 5% and 15% thick foil conditions. Within these plots, the reduced frequency axes have been limited to the high frequency region. It can be seen that this expression dependably captures the trends of both the slight increase in the UPF lift response magnitudes, as well as the clearly altered phase of the responses. The differences between the calculated results and the modeled expression are believed to be a result of the assumptions made in the analysis and development of the expression. The unsteady lift for the 5% thick foil is less augmented than

the corresponding 15% thick foil, with this dependency captured by the expression above. Again, this expression is founded in the framework of potential flow, and only accounts for the contributions of the flow potential source terms, neglecting all other contributions. While these results are strictly applicable to symmetric foils of Joukowski profile, it is assumed that symmetric foils with a different profile will exhibit a similar type of behavior. Further, cambered foils would also be expected to have an altered unsteady lift response at high reduced frequencies, though it is not yet clear how impactful the asymmetry of the profile would be on the projection and integration of the pressure distribution, not to mention induced differences in the shedding of vorticity. Analysis of results at these exceedingly high reduced frequencies remains a topic of investigation and a suggested area of future work.

As a final point in the interest of practical applicability towards other studies and results, the primary consequence of considering a thick foil in this pitching motion configuration is that the phase angle of the unsteady lift response is augmented. The altered expression above is rearranged in the following way,

$$\frac{\frac{C_L}{\alpha}\Big|_{thick}}{\frac{C_L}{\alpha}\Big|_{Theo.}} \approx 1 - \frac{2\pi k^2 \left(\frac{\delta_x r_c}{b^2} + 2\frac{\delta_x^2}{b^2} - \frac{\Delta_x r_c}{b^2}\right)}{\frac{C_L}{\alpha}\Big|_{Theo.}} \tag{4.33}$$

such that the altered phase angle relative to the Theodorsen model can be clearly determined,

$$\Delta\phi = \angle\left(\frac{C_L}{\alpha}\Big|_{thick} \Big/ \frac{C_L}{\alpha}\Big|_{Theo.}\right) \tag{4.34}$$

Based on this expression, Figure 4.50 plots the reduced frequency, $k_{aug.}$, at which the phase angle of the thick foil response is augmented enough relative to the Theodorsen model such that it crosses specific altered thresholds, in this case $-5, -15$, and -45 degrees, as a function of the thickness-to-chord ratio, t/c. It is reminded that this is specific to Joukowski foil profiles because of the development, and should be extended to different foil profiles with due caution. As can be seen, at least a 5 degree change in the phase of the response can be expected for most foils of practical thickness when consideration is given to reduced frequencies up to a value of 10. A phase alteration of -15 degrees is seen to asymptote at an

approximate reduced frequency of 10 as a function of foil thickness. For still higher reduced frequencies, $k \gtrsim 10$, significant alterations to the phase of the response can be expected for effectively all practical foil thicknesses.

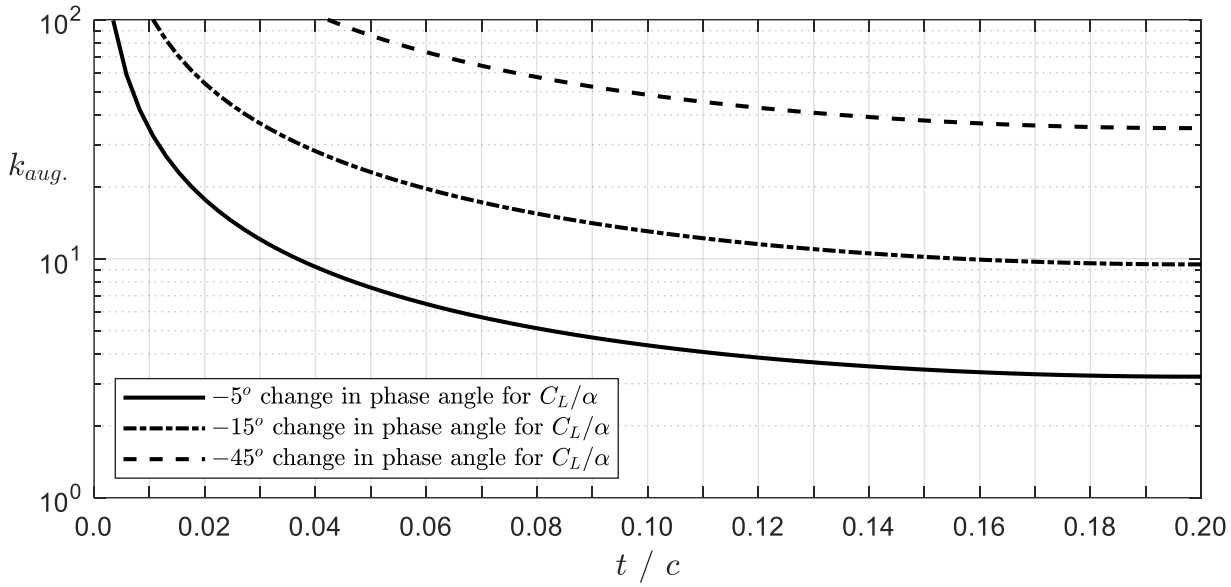

Figure 4.50. Identification of the reduced frequencies at which the phase of the unsteady lift response crosses specific thresholds of alteration as a function of foil thickness-to-chord ratio

4.7 Analysis and Development for the Fluctuating Streamwise Force Response

The unsteady force response along the streamwise direction is the concentration of this section. For flat foil conditions this precludes heaving motion as no area is projected into that direction, and therefore only pitching motion is considered. For finite thickness foils, results for both heaving and pitching motion are considered. The term unsteady streamwise force is often used in the discussion as the specific orientations connoted by thrust and drag are less paramount to the analysis of unsteady results. The variables C_D and C_T are effectively used interchangeably, especially when assessing the results from separate references, as these are the conventional variables for the streamwise force.

4.7.1 Development of an Unsteady Streamwise Force Response Expression

The primary motivation for the present work is to analyze the unsteady streamwise force response due to small-scale foil motion, and to develop a model expression for this response. In the way that the Theodorsen model provides a direct expression for the unsteady lift as a result of known motion, it is the author's experience and understanding that a similarly direct expression is not available for the unsteady streamwise force. Within the Theodorsen model, the unsteady streamwise force is assumed to be negligible, which is a result of the foil being enforced to be infinitely thin and the disturbance motion being assumed to be small (i.e. a negligible amount of foil area projects into the streamwise direction). The absence of this expression is supported in that the four distinct works from which results are extracted and are referenced in this section present results for both unsteady lift and unsteady streamwise force, however do not utilize or acknowledge a corresponding predictive expression for the unsteady streamwise force. The closest type of predictive expression for the streamwise force response comes from Garrick (1936), however the analysis and resulting model expressions are for the properties of the mean streamwise force due to foil motion, and not the character of the unsteady response.

A predictive expression for the unsteady streamwise force response is achieved through straightforward analysis. Consider Figure 4.51, which provides illustrations of the instantaneous force

components for infinitely thin and finite-sized foils due to unsteady pitching motion. As the Theodorsen and Garrick models and the UPF calculated results are based within the framework of potential flow, this development is in terms of pressure effects, and not viscous effects, which should become increasingly dominant for high Reynolds number conditions.

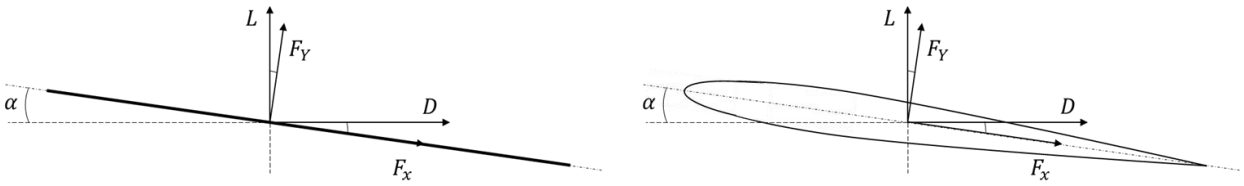

Figure 4.51. Illustration of foil and force coordinate system

The unsteady streamwise force is defined in terms of the projections of the chordwise and chord-normal forces in the time domain such that,

$$D(t) = F_X(t)\,cos\big(\alpha(t)\big) + F_Y(t)\,sin\big(\alpha(t)\big) \tag{4.35}$$

Under a small angle assumption for α this becomes,

$$D = F_X + F_Y\,\alpha \tag{4.36}$$

where the arguments of the variables have been dropped as this applies equally in the time and frequency domains. Further assuming a thin foil, as in the Theodorsen model, the chordwise force drops and the unsteady streamwise force is simply the modulation of the chord-normal force by the pitch motion. Two steps are now taken: 1) the forces are rewritten as transfer functions (as discussed earlier), and 2) as a further implication of the small angle assumption, the chord-normal force is approximated by the lift. This results in,

$$\frac{C_D}{\alpha} = \frac{C_L}{\alpha}\,\alpha \tag{4.37}$$

where it is acknowledged that this expression simply represents the product of two sinusoids; the lift coefficient transfer function having variable phase depending upon the reduced frequency condition. The

subsequent analysis involves applying multiple trigonometric sum and double angle identities in order to achieve an expression for the magnitude of the unsteady streamwise force transfer function.

As the expression above represents the product of two sinusoids, the right-hand side of this expression is rewritten with generalized variables in the time domain as,

$$A\sin\big(\omega t + \phi(\omega)\big)\ B\sin(\omega t) \tag{4.38}$$

where A and B represent the arbitrary magnitudes of the unsteady lift response and pitch disturbance, and $\phi(\omega)$ represents the variable phase of the lift response as a result of the reduced frequency condition. Utilizing the sine angle sum identity, $\sin(\alpha+\beta) = \sin(\alpha)\cos(\beta) + \cos(\alpha)\sin(\beta)$, for $\sin\big(\omega t + \phi(\omega)\big)$ yields,

$$AB\ [\sin(\omega t)\cos(\phi) + \cos(\omega t)\sin(\phi)]\ \sin(\omega t) \tag{4.39}$$

Distributing the $\sin(\omega t)$,

$$AB\sin^2(\omega t)\cos(\phi) + AB\sin(\omega t)\cos(\omega t)\sin(\phi) \tag{4.40}$$

Then using separate double angle identities, $\cos(2\alpha) = 1 - 2\sin^2(\alpha)$ and $\sin(2\alpha) = 2\sin(\alpha)\cos(\alpha)$, on the first and second terms involving ωt yields,

$$AB\left(\frac{1}{2} - \frac{1}{2}\cos(2\omega t)\right)\cos(\phi) + AB\frac{1}{2}\sin(2\omega t)\sin(\phi) \tag{4.41}$$

Rearranging terms,

$$\frac{1}{2}\ AB\ [\sin(2\omega t)\sin(\phi) - \cos(2\omega t)\cos(\phi) + \cos(\phi)] \tag{4.42}$$

Lastly, it is recognized that the first and second terms within the bracket can be simplified by the cosine angle sum identity, $\cos(\alpha+\beta) = \cos(\alpha)\cos(\beta) - \sin(\alpha)\sin(\beta)$,

$$\frac{1}{2}\ AB\ [-\cos(2\omega t + \phi) + \cos(\phi)] \tag{4.43}$$

This generalized expression is the basis of the expression for the magnitude of the unsteady streamwise force,

$$\left|\frac{C_D}{\alpha}(2k)\right| = \frac{1}{2}\left|\frac{C_L}{\alpha}(k)\right| \ |\alpha(k)| \tag{4.44}$$

The amplitude of the bracketed term above remains unity, therefore the magnitude of the unsteady streamwise force response is dictated by the generalized expression, $\frac{1}{2}AB$. The unsteady streamwise force response occurs at twice the frequency of the disturbance motion, as well as having variable phase and mean offset properties according to the reduced frequency condition.

This expression can be equally written as,

$$\left|\frac{C_D(2k)}{\alpha(k)}\right| = \frac{1}{2}\left|\frac{C_L}{\alpha}(k)\right| \ |\alpha(k)| \quad \leftrightarrow \quad \frac{|C_D(2k)|}{|\alpha(k)|^2} = \frac{1}{2}\left|\frac{C_L}{\alpha}(k)\right| \tag{4.45}$$

These simple expressions relate the magnitude of the unsteady streamwise force transfer function to the magnitudes of the corresponding unsteady lift transfer function and disturbance motion. For disturbance pitch motion occurring at a reduced frequency of k, the magnitude of the unsteady streamwise force occurs at twice this frequency, $2k$. In conjunction with the Theodorsen model lift transfer function expression, this is a readily implementable expression for the character of the unsteady streamwise force response. Additional implications for the mean offset and phase character of this streamwise force response can be inferred based on this development; however, it is acknowledged that if comparing to experimental or numerical results, neglecting the mean viscous drag, as an example, is likely to yield differences depending upon the configuration.

In addition to being readily implementable, the expressions above imply an important consideration, which is that while C_L scales with α, C_D scales with α^2. This is understood to be directly consistent with the expressions of the mean lift and drag coefficients derived through lifting line theory: $C_L = 2\pi\alpha$ and $C_D = C_{Do} + f(\alpha^2)$.

Lastly, this expression also provides for a simple ratio of the unsteady C_L and C_D magnitudes,

$$\frac{|C_L|}{|C_D|} = \frac{2}{|\alpha|} \tag{4.46}$$

which clearly shows how the C_L response becomes increasingly dominant relative to C_D for decreasing $|\alpha|$. The degree to which C_D is considered negligible certainly depends upon the specific motivations, configurations, and analyses being considered, and may not be as negligible as is often assumed. Examples of the relative magnitudes of these two forces are seen in the results below.

4.7.2 Analysis of Thin Foil, Sinusoidal, Mid-Chord Pitching UPF Results

Calculated UPF results have been introduced in the earlier sections, and the results discussed in this section are from the same calculations. As opposed to unsteady lift and pitching moment transfer functions, similar responses are analyzed for the unsteady streamwise force and are compared to the associated predictive expressions developed at the beginning of this section. As opposed to the Bode plots presented earlier, showing both magnitude and phase, these results are only assessed in terms of the magnitude portion of the unsteady streamwise force response, in conjunction with the previous section. This magnitude portion of the Bode plot for the unsteady streamwise force transfer function is provided in Figure 4.52 for the calculated UPF results for numerically thin foils where $|\alpha| = 0.1^o$, along with the associated predictive expression. The disturbance motion is defined to occur at k, however the streamwise force response occurs at $2k$. It should be noted this this figure presents C_D/α, and not the response relative to α^2, so that the magnitude difference relative to the unsteady lift is easily discernable. In the present instance there is an approximate offset of 60 decibels between the C_L/α and C_D/α responses which corroborates directly with the ratio expression listed earlier as the disturbance magnitude is $|\alpha| = 0.1^o$,

$$20\log_{10}\left(\frac{|C_L|}{|C_D|}\right) = 20\log_{10}\left(\frac{2}{|\alpha|}\right) = 20\log_{10}\left(\frac{2}{0.1\frac{\pi}{180}}\right) = 61.2\ dB \tag{4.47}$$

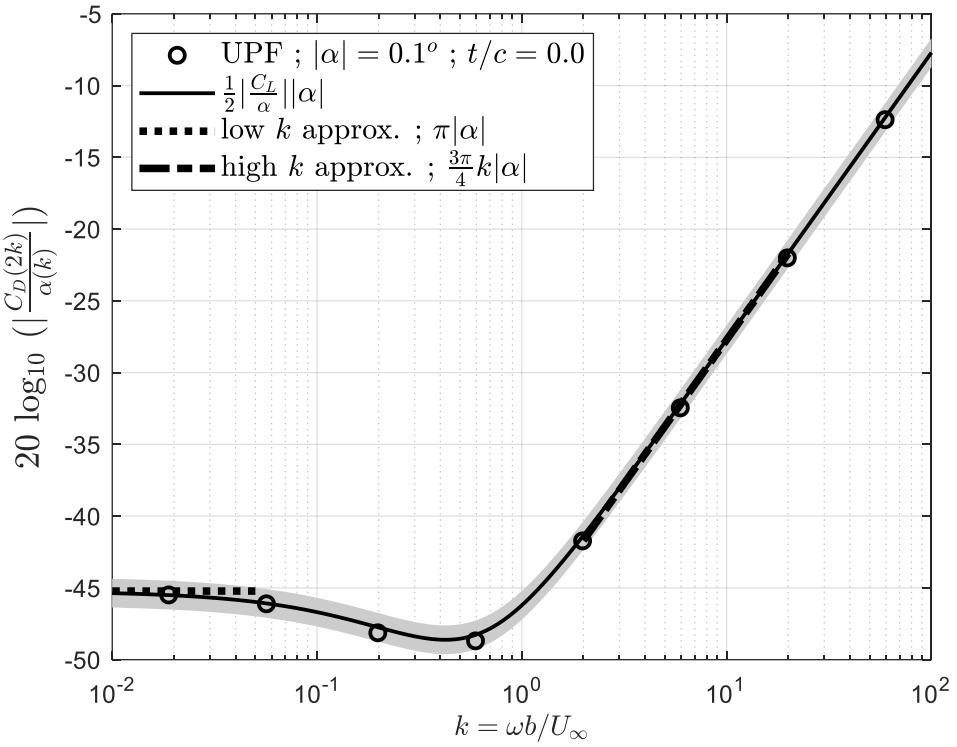

Figure 4.52. Predicted and calculated transfer functions of the unsteady streamwise force coefficient to pitch motion for numerically flat foils undergoing sinusoidal motion about the mid-chord

The calculated UPF results for the magnitude of the streamwise force response at $2k$ from disturbance pitching motion at k compare very favorably to the associated predictive expression, which was developed through application of the Theodorsen model (the gray band is a similar ± 1 decibel visual aid). This positive comparison is maintained across the entire range of reduced frequencies under consideration. What is also included in this figure, simply for reference, are expressions that result from implementing the Theodorsen model, unsteady lift transfer function taken at the low and high reduced frequency limits. These are quickly developed here for mid-chord pitching, where,

$$\lim_{k\to 0} C(k) = 1.0 \quad ; \quad \lim_{k\gg 1} C(k) = 0.5 \tag{4.48}$$

$$\frac{C_L}{\alpha} = 2\pi C + i\pi[1 + C]k \quad ; \quad \left.\frac{C_L}{\alpha}\right|_{low\ k} = 2\pi \quad ; \quad \left.\frac{C_L}{\alpha}\right|_{high\ k} = i\frac{3\pi}{2}k \tag{4.49}$$

$$\left|\frac{C_D}{\alpha}\right| = \frac{1}{2}\left|\frac{C_L}{\alpha}\right||\alpha| \quad ; \quad \left.\left|\frac{C_D}{\alpha}\right|\right|_{low\ k} = \pi\,|\alpha| \quad ; \quad \left.\left|\frac{C_D}{\alpha}\right|\right|_{high\ k} = \frac{3\pi}{4}k\,|\alpha| \tag{4.50}$$

The next topic to be discussed with these UPF results is the different normalization that is needed for the unsteady streamwise force, as compared to the unsteady lift. Specifically, this is the additional α which is present in the C_D magnitude expression. While C_L/α is a normalized expression, the unsteady streamwise force requires a normalization of C_D/α^2.

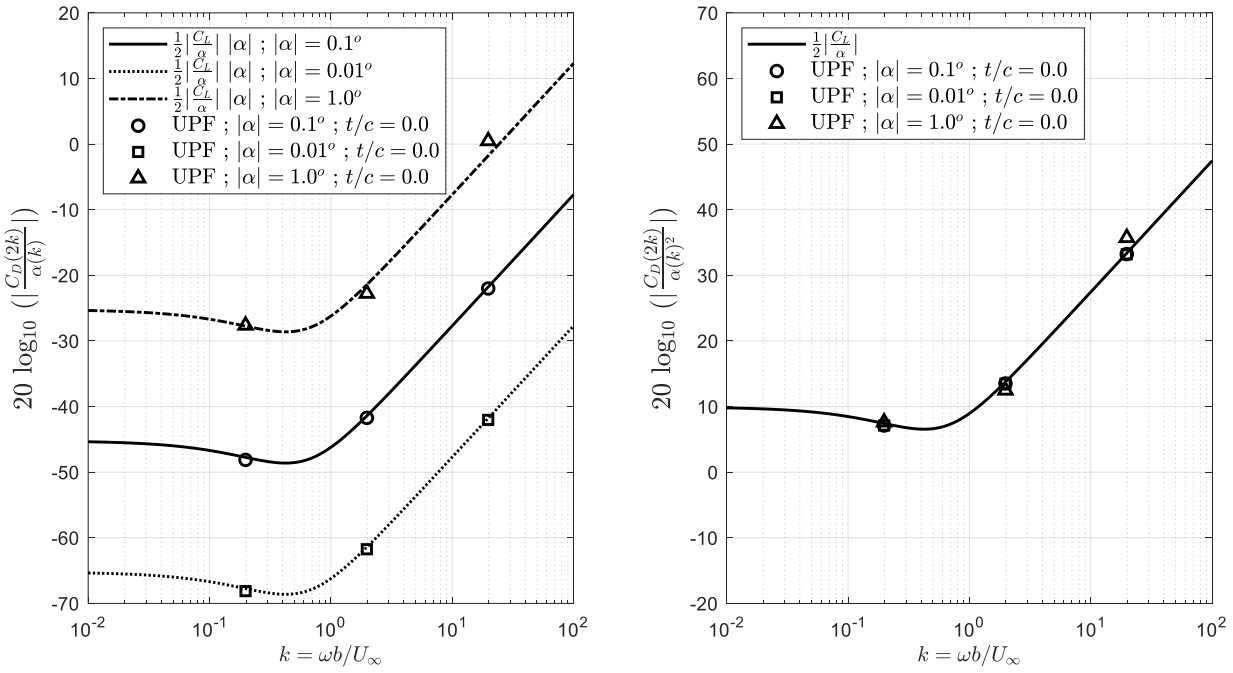

Figure 4.53. Predicted and calculated transfer functions of the unsteady streamwise force coefficient to pitch motion for numerically flat foils undergoing variable, small amplitude, sinusoidal motion

The necessity of this altered normalization for the unsteady streamwise force transfer function is seen with analysis of the calculated UPF results for multiple small disturbance magnitude conditions of $|\alpha| = 0.01, 0.1,$ and 1.0 degrees. Figure 4.53 presents these UPF results where the magnitudes of $C_D(2k)/\alpha(k)$ and $C_D(2k)/\alpha^2(k)$ are plotted for a subset of the reduced frequency conditions, simply for expedience. Regardless of the variation of the small-scale disturbance motion across multiple orders of magnitude, the numerical UPF results follow either expression. It is simply that the α^2 scaling provides a true normalization for this variable.

A notable feature of these streamwise force magnitude results is that the high reduced frequency, large amplitude (for these circumstances) condition, $k = 19.8$ and $|\alpha| = 1.0^o$, is slightly elevated from the other results and predictive expression. This is understood to be a direct consequence of the non-linearity of the shed wake of vorticity. Figure 4.54 plots associated views of the shed point vortices in the immediate region downstream of the flat foil trailing edges for the three disturbance magnitudes at this reduced frequency. The foil is plotted as a thin line, of which only the last quarter-chord is shown. The discrete point vortices are each a dot and are colored by their individual strengths, which have been normalized to the particular ranges of each case; the colorbar illustrates the polarity of the scheme. The specific time step corresponds to an instantaneous angle of attack of approximately zero, and these three views are all windowed to the same normalized spatial extent. The vorticity distribution for the smallest magnitude disturbance motion is nearly planar with small undulations developing downstream, while the vortices for the $|0.1^o|$ disturbance begin to form counter rotating structures as they convect downstream. Interestingly, the $|1.0^o|$ disturbance magnitude at this elevated reduced frequency results in a particularly energetic wake, with the vortices very near to the foil trailing edge experiencing significant motion relative to the foil in addition to the vortical structures downstream.

While the specific strengths of these vortices are not quantitatively discernable in these figures, it should be clear by the colorbar that the strongest concentrations of vorticity are at the centers of these structures (red being the largest positive values and blue being the largest negative values), and that these are causing the sheet to roll-up on itself. It is noteworthy to recognize that this wake structure is congruent with a thrust-producing wake as discussed in Young and Lai (2004), or equally, a reverse von-Kármán vortex street as discussed in Platzer et al. (2008), amongst others. As also discussed earlier, quick utilization of the corresponding model expression from Garrick (1936) corroborates the orientation of these wakes.

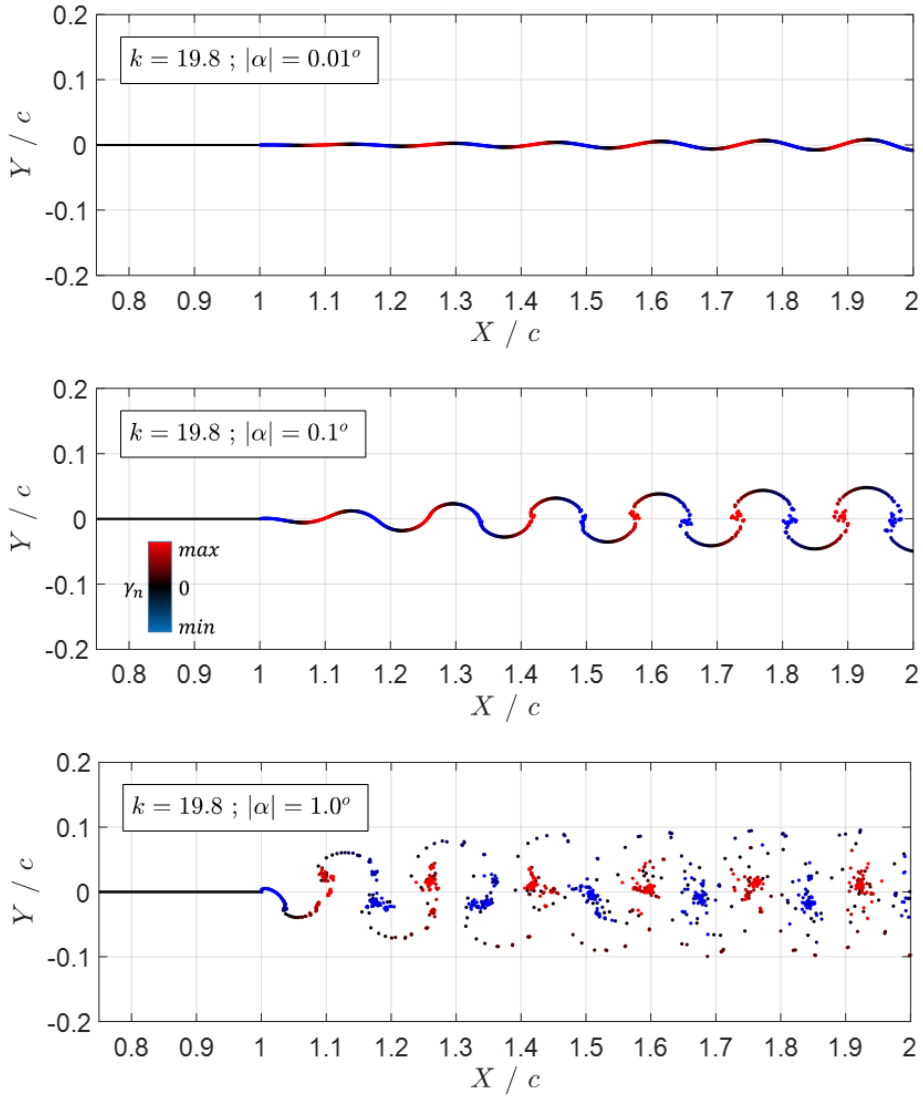

Figure 4.54. Visualization of the downstream wake of shed point vortices for multiple disturbance amplitudes

This wake behavior is responsible for the enhanced unsteady streamwise force response for the $|1.0^o|$ condition. As could be inferred, the flow potential terms dominate this high frequency response (as opposed to the contributions from velocity terms). By definition, the source flow potential contribution, $C_{D,4}$, is independent of the wake, therefore the wake flow potential contribution, $C_{D,5}$, must be the term altering the response (referring back to the decomposition development and discussion of Section 2.6 and Section 4.3). A sample of these normalized time series for these decomposed contributions at $k = 19.8$ is

provided in Figure 4.55 and Figure 4.56. As should be expected, the $C_{D,4}$ responses are all the same, as they are normalized. It is clearly seen that the wake contribution, $C_{D,5}$, to the response is elevated for the $|1.0^o|$ amplitude condition and exhibits added frequency content. Correspondingly, the decibel increase is in line with what is seen in the magnitude plots. Using approximate values for the ratio of large to small amplitude conditions for just the $C_{D,4}$ and $C_{D,5}$ contributions yields, $\left(C_{D,4}/|\alpha|^2 + C_{D,5}/|\alpha|^2\right)|_{|\alpha|=1.0^o}$ / $\left(C_{D,4}/|\alpha|^2 + C_{D,5}/|\alpha|^2\right)|_{|\alpha|=0.1^o} = 20\log_{10}((\sim 30 + \sim 30)/(\sim 30 + \sim 13)) \approx 2.9\, dB$, which agrees with the increase exhibited in Figure 4.53.

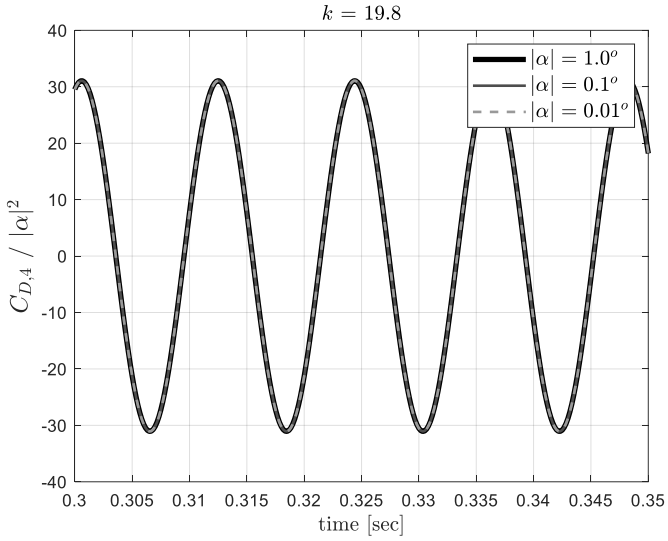

Figure 4.55. Decomposition of the source flow potential contributions to the unsteady streamwise force

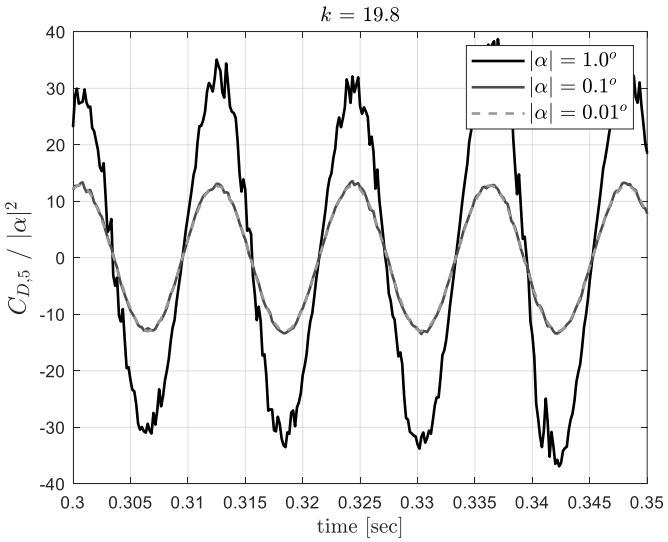

Figure 4.56. Decomposition of the wake flow potential contributions to the unsteady streamwise force

4.7.3 Brief Review of Selected Open Source References

The following is a quick review of the conditions and configurations from the references for which results are utilized to assess the unsteady streamwise force modeling expressions. The reference of Read et al. (2003) is a primarily experimental study concentrated on the propulsive and maneuvering forces generated from oscillating foils undergoing various heaving and pitching motions. A suite of primary operating parameters were varied for a NACA 0012 foil towed in a water tank. The foil chord and span are listed as 10 and 60 cm, respectively. The towing speed (i.e. freestream velocity) was held constant for all conditions at 0.40 m/s, which yields a chord-based Reynolds number of $4 * 10^4$. The motion of the foil is mechanically articulated and the unsteady forces are measured with force gauges.

Many of the results from this reference are presented as mean properties, for example mean thrust coefficients or propulsive efficiencies. However, there is a particular figure from this reference which provides time series of the unsteady lift and thrust coefficients for two separate operating conditions. This is Figure 15 of the reference document, and will be copied and represented in the subsequent analysis section below. Specifically, Figure 15a of their document presents these time series for combined sinusoidal heaving and pitching motions that have a 90^o phase shift between them. The operating conditions are defined by a Strouhal number, St, which links the frequency of oscillation and the heaving motion, as well as the mean offset and amplitude of the pitch angle. In this instance, $St = 0.40$, the mean pitch angle is 10^o, and the pitch amplitude is 25^o about this mean value. Further assessment of these conditions is provided in the subsequent analysis section below.

The reference of Young and Lai (2004) is primarily a numerical study for an oscillating NACA 0012 airfoil at a chord-based Reynolds number between $1 - 2 * 10^4$ and at elevated reduced frequencies, $k > 1$. The computational approach utilizes a two-dimensional, unsteady, compressible, Reynolds-Averaged Navier-Stokes solver, in addition to an unsteady panel method in the framework of potential flow. This work focuses primarily on the properties of the shed wake of vorticity which emanates from the foil trailing edge, though certainly also presents results for both the mean and unsteady properties of the lift and

thrust force responses. Very germane observations and discussion with regard to both the shed wake and the foil response behavior are presented; however, the result which is specifically concentrated on for the present purpose is a time series of unsteady thrust coefficient, C_T. This is presented within the reference in the context of a grid convergence study for their numerical results. The specific figure is copied and presented in the section below, and is presented as Figure 4 within the reference document.

The pertinent conditions which are listed are a NACA 0012 airfoil undergoing sinusoidal pitching about its quarter-chord, at $Re_c = 1.2 * 10^4$, $M_\infty = 0.05$, $k = 8.0$, and a pitching amplitude of $\alpha = \pm 2^o$. The variable definitions implemented in this reference are congruent with those presently implemented, and in the context of the Theodorsen model, the quarter-chord pitch axis corresponds to a pitch axis value of $a = -1/2$. Though not explicitly stated, it is inferred that the flow in these conditions remains attached across the foil and that vortex shedding from the foil leading edge is not occurring. As seen in their figure and variable definitions, the time axis of these time series results are normalized by a non-dimensional period. Again, while not explicitly stated, it is assumed and inferred from the results that the unsteady thrust is occurring at twice the frequency of the pitching motion. This reference provides additional details, observations, and results, which are certainly relevant.

The reference of Lu et al. (2013) is a numerical study which primarily is focused on the mean thrust performance of different foil profiles subjected to varying pitching conditions. Notably, these variations involve the pitching amplitude and the waveform of the pitching motion, which varies from a sawtooth, to a sinusoid, to a square wave. For the present analysis, a NACA 0012 foil will be concentrated on, where the chord-based Reynolds number is listed as $1.35 * 10^4$. The foil pitches about its quarter-chord location with an amplitude of 5^o and a sinusoidal waveform at a fixed reduced frequency of 4.5 (under their definition the reduced frequency is listed as 9, however, this is converted to the present definition).

The data utilized in the current analysis is presented as Figure 13 within the reference, which shows a time history of the unsteady thrust coefficient over one period of motion for four different foil profiles (the NACA 0012 being one of these). The amplitude of the unsteady thrust coefficient is visually assessed

for comparison. The numerical results are listed as being performed within CFX 11.0, for the unsteady, incompressible, viscous flow around the two-dimensional airfoil sections.

The reference of Hammer et al. (2019) is a mixed experimental and numerical study on the mean and unsteady responses of a pitching foil subjected to both a standard mean uniform inflow, as well as variable sheared inflow conditions. A NACA 0012 foil is also utilized in this work, where the chord-based Reynolds number is listed as approximately $1.2 * 10^4$, and the foil pitches with sinusoidal motion about its quarter-chord location with an amplitude of 2^o between reduced frequencies of 1 and 12. The data of this reference utilized in the present analysis is from their uniform inflow velocity condition (presented as Figure 11 within the reference), through results are available for multiple sheared inflow conditions. Care was take to digitize, extract, and analyze this data as reliably as possible from the reference document. This extracted data is utilized, and their figure is not copied and presented.

This reference concentrates on the properties of the foil wake, as well as the mean and unsteady characteristics of the C_L and C_T responses due to this pitching motion. While the motion of the foil is listed as sinusoidal, the unsteady response results are presented in terms of the root-mean-square (RMS) of these fluctuating signals. For the present analysis, it is assumed that the responses are at least predominantly sinusoidal, given the motion and amplitude of pitching. Additionally, within their presented data and discussion, there is no clear evidence of vortex shedding from the leading edge or regions of separated flow.

The experimental configuration consists of an instrumented foil with a 0.12 meter chord and aspect ratio of 5.14 placed in a water tunnel. The measurement of unsteady forces and the mechanical actuation of the foil are accomplished by force gauges and servo motors at one end of the foil span. The complementary numerical results are achieved by an unsteady, compressible, two-dimensional Navier-Stokes solver, specifically titled FDL3DI. Overset computational grids are utilized between the moving O-grid around the foil and the well-resolved background grid. As with the other references, the reference document contains numerous, additional pertinent details with regard to the experimental and numerical configurations, as well as additional results not concentrated on presently.

4.7.4 Analysis of Results from the Open Source References

The following subsections present the subsequent analysis of the results from the references of Read et al., Young and Lai, Lu et al., and Hammer et al. in the context of implementing the model expressions developed for the unsteady streamwise force response.

4.7.4.1 Analysis of Data from Read et al.

The reference of Read et al. is described earlier, and the specific aspect of this work to be analyzed is the unsteady time traces presented for the lift and thrust coefficients, C_L and C_T, as a result of combined sinusoidal heaving and pitching motions, To begin, the operating condition of the foil motion needs to be converted to reduced frequency from the reference definition of a Strouhal number, $St = 0.40$,

$$St = \frac{2\pi\omega A}{U_\infty} = 2\pi\frac{\omega b}{U_\infty}\frac{A}{b} = 2\pi k\frac{2h_o}{b} = 2\pi k\frac{2c}{b} = 8\pi k \tag{4.51}$$

where A is the wake width (and is approximated as $2h_o$ within the reference), and h_o is the amplitude of the heave motion which in this case is $h_o/c = 1.0$. This leads to the following reduced frequency operating condition,

$$k = \frac{St}{8\pi} = \frac{0.4}{8\pi} = 0.016 \tag{4.52}$$

which is in the lower range of typical reduced frequency values.

For the specific unsteady foil response results being analyzed from this reference, combined heaving and pitching motions are being performed, and therefore the effects of each will need to be assessed. Beginning with the unsteady lift, the transfer function expressions are,

$$\frac{C_L U_\infty}{\dot{h}} = 2\pi C + i\pi k \quad ; \quad \frac{C_L}{\alpha} = 2\pi C + i\pi\left[1 + 2C\left(\frac{1}{2} - a\right)\right]k + \pi a k^2 \tag{4.53}$$

where the pitch axis is listed as being at the $1/3$ chord location, which corresponds to $a = -1/6$. At this reduced frequency the Theodorsen function, $C(k)$, takes the following value, $C(k = 0.016) = 0.97 - i0.064$. Correspondingly, the magnitudes of these transfer functions are,

$$\left|\frac{C_L U_\infty}{\dot{h}}\right| = 6.11 \quad ; \quad \left|\frac{C_L}{\alpha}\right| = 6.11 \tag{4.54}$$

which are both dominated by the same low k contributions, $2\pi C$, and are therefore approximated by the same value moving forward.

The total lift response is the combined effect of these heaving and pitching contributions, along with the mean lift due to the mean angle of attack, $\bar{\alpha}$. As the heaving position and pitch angle motions are sinusoidal and listed as being 90 degrees phase shifted, this conveniently allows for the simple addition of the heave velocity, $\dot{h}$, and pitch angle, α, contributions,

$$C_{L,total} = 2\pi\bar{\alpha} + |C_L(k)| \quad ; \quad |C_L(k)| = \left|\frac{\dot{h}}{U_\infty}\right|(6.11) + |\alpha|(6.11) \tag{4.55}$$

however, the heaving term requires slight manipulation to be conducive to the definitions of this referenced work, as the heaving motion is listed as a normalized position amplitude, $h/c = 1.0$. Leveraging that the disturbance motion is harmonic,

$$\left|\frac{\dot{h}}{U_\infty}\right| = \left|\frac{i\omega h}{U_\infty}\right| = \left|\frac{\omega b}{U_\infty}\frac{h}{b}\frac{2b}{c}\right| = \left|2k\frac{h}{c}\right| = 2k \tag{4.56}$$

Now the amplitude of the predicted unsteady lift can be found as,

$$|C_L(k)| = (2k + |\alpha|)(6.11) \tag{4.57}$$

For the instance being analyzed, the angle of attack is swept through an amplitude variation of $|\alpha| = 25^o$, with a mean angle of attack (bias angle) of $\bar{\alpha} = 10^o$. Two points should now be directly apparent for the results of this reference: 1) these responses are predominantly influenced by the pitching motion, and 2) this pitching motion is not small. Despite the relatively large disturbance motion, which would seem

disqualifying for modeling founded in potential flow and utilizing the Theodorsen model, the analysis continues. This $C_{L,total}$ expression above yields positive and negative extrema for the unsteady lift of,

$$C_L^+ = 3.93 \quad ; \quad C_L^- = -1.40 \tag{4.58}$$

The specific plot of the results from this reference which are being assessed is recreated here as Figure 4.57.

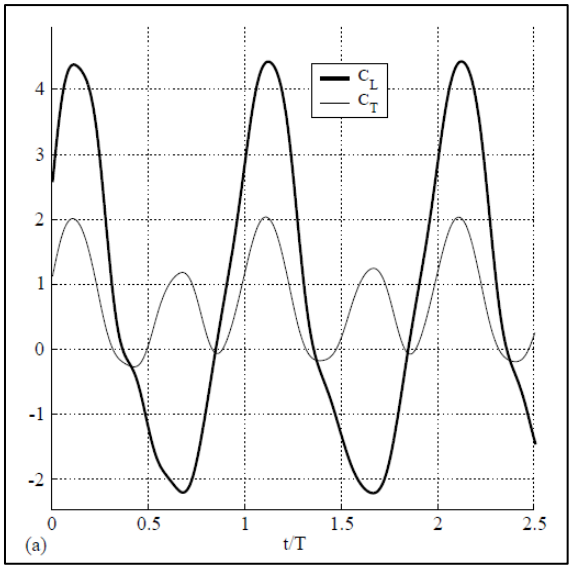

Figure 4.57. Example of the unsteady lift and streamwise force responses from Read et al. (copied from reference)

These predictions of the C_L extrema to this time series plot of this reference yield a satisfyingly positive comparison, given the attached, potential flow assumptions inherent to the predictions and the large angles of attack of the experimental results. These predicted values capture approximately 85% of the C_L amplitude of these unsteady results. Further quantitative comparison, however, seem unwarranted. This specific extracted result is only one of the various topics considered within the reference document, and therefore additional or supplemental information is not available. It is speculated (by the present author) that dynamic stall and leading edge vorticity shedding phenomena are very likely to have been occurring, and could account for the elevated levels and distortion of the sinusoidal response.

Turning now to the unsteady streamwise force, the expression to be populated is a slight variant of the prior amplitude expressions,

$$\left|\frac{C_T}{\alpha}\right| = \frac{1}{2}\left|\frac{C_L}{\alpha}\right| |\alpha| \rightarrow \ |C_T| = \frac{1}{2}|C_L|\left|\alpha_{eff}\right| \tag{4.59}$$

where α_{eff} is the effective angle of attack due to this combined motion; this is taken to be $\alpha_{eff} = 2k + |\alpha|$ which can be inferred from the development above. The predicted amplitude of the unsteady streamwise force, which should occur at twice the disturbance frequency, is therefore,

$$|C_T| = \frac{1}{2}(2k + |\alpha|)^2(6.11) = 0.67 \tag{4.60}$$

Again, comparing this predicted value to the associated time series plot yields a generally positive comparison, despite the operating conditions involved seeming to be well outside of the applicable range. The reference C_T experimental result exhibits the expected frequency doubling; however, has a variable amplitude bias between the positive and negative portions of the unsteady lift oscillations. This behavior is again speculated to be a result of the assumed complex unsteady flow field, though specific analysis of this is not available. Nonetheless, as a first-order prediction, this result is taken to be fairly acceptable on either a linear or decibel scale. Visual inference of the larger and small amplitude limits of this unsteady signal of C_T for these reference experimental results are approximately 1.1 and 0.6, respectively; this is in comparison to the predicted amplitude of 0.67.

Finally, a note on the ratio of the amplitudes of the lift and thrust responses. Employing the earlier expression, the unsteady C_L and C_T amplitudes are much closer to each other as a result of the exceedingly large effective angle of attack, $\frac{|C_L|}{|C_T|} = \frac{2}{|\alpha_{eff}|} = 4.27$. Taking the associated ratio of the amplitudes of these unsteady responses for the referenced experimental results agrees loosely with this ratio,

$$\frac{|C_L|}{|C_T|} = \frac{(\sim 4.2) + (\sim 2.1)}{(\sim 2.0) + (\sim 0.2)} = 2.9 \quad ; \quad \frac{|C_L|}{|C_T|} = \frac{(\sim 4.2) + (\sim 2.1)}{(\sim 1.1) + (\sim 0.0)} = 5.7 \tag{4.61}$$

though the large angle of attack condition is a significant stretch of the applicability of this expression.

4.7.4.2 Analysis of Data from Young and Lai

The reference of Young and Lai is described earlier, and in the context of the current motivations the specific aspect of this work to be analyzed is the unsteady time signal presented for the thrust coefficient, C_T, as a result of sinusoidal pitching motion. The starting point for this analysis therefore is the unsteady lift. Populating the unsteady lift transfer function expression for pitching motion yields,

$$\frac{C_L}{\alpha} = 2\pi(0.501 - i0.016) + i\pi\left[1 + 2(0.501 - i0.016)\left(\frac{1}{2} + \frac{1}{2}\right)\right](8.0) + \pi\left(-\frac{1}{2}\right)(8.0)^2 \qquad (4.62)$$

where the Theodorsen function is evaluated at a reduced frequency of $k = 8.0$, $C(k = 8.0)$, and the pitch axis is the foil quarter chord, $a = -1/2$. Sparing the algebraic simplification, the magnitude of the unsteady lift transfer function is ,

$$\left|\frac{C_L}{\alpha}\right| = 34.89\pi \qquad (4.63)$$

The specific result of Young and Lai that is to be compared to is again a visual of a time series plot; therefore the analysis is limited to assessing the magnitude of the unsteady streamwise force, as further quantitative analysis is not warranted (for example, the phase of the C_T response). The unsteady streamwise force transfer function developed earlier is slightly rewritten in order to be conducive to analysis of this time series plot,

$$|C_T| = \frac{1}{2}\left|\frac{C_L}{\alpha}\right||\alpha|^2 \qquad (4.64)$$

The magnitude of the unsteady lift transfer function is provided above, and the magnitude of the unsteady pitching motion in this specific instance is $|\alpha| = 2^o$. This yields a direct prediction of the magnitude of the unsteady streamwise force,

$$|C_T| = 0.0668 \qquad (4.65)$$

Direct assessment of this predicted amplitude is applicable to Figure 4 from this particular reference, which has been copied here for ease of comparison, and is presented as Figure 4.58. As can be

seen, the comparison between the calculated C_T results of Young and Lai and the predicted magnitude presented here for the streamwise force response is admirable, and deemed successful, given the flat foil assumption on which it is based. The calculated results of the reference are seen to fluctuate between the approximate limits of -0.07 and 0.08, therefore having an amplitude of approximately 0.075. Taking these approximate limits visually from the figure, the associated difference in the calculated and predicted magnitude of the response of the streamwise force can be assessed on a decibel scale as $20\log_{10}(0.075/0.0668) = 1.0\,dB$, or a linear scale as $(0.075 - 0.0668)/(0.075) = 11\%$. Correspondingly, there does not appear to be enough information available for the referenced results in order to make an assessment as to the associated phase of the calculated results, though it is understood that the expected frequency doubling of the response is occurring.

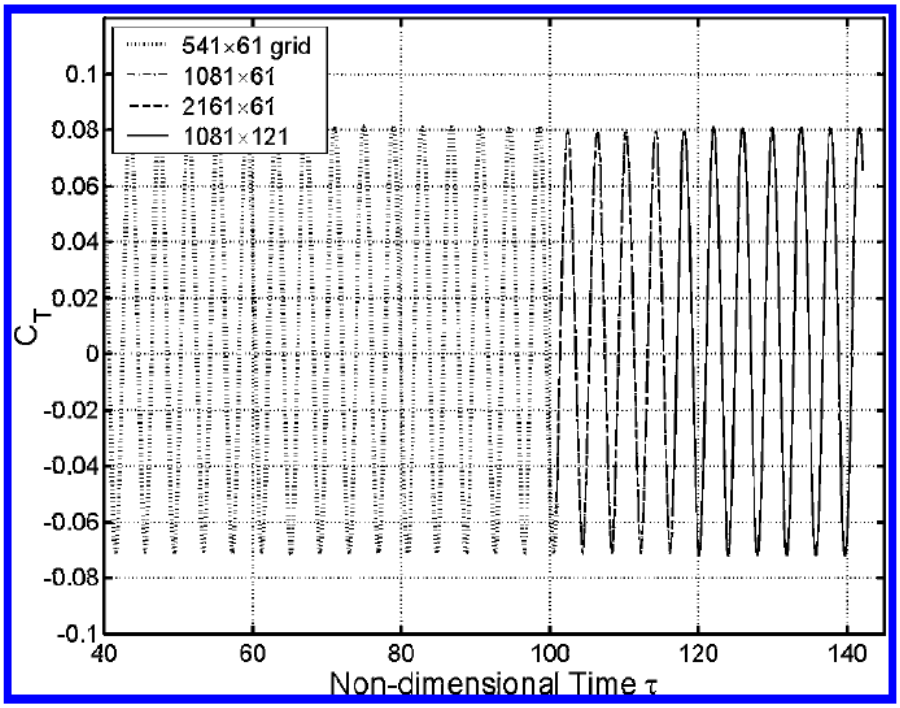

Fig. 4 Thrust coefficient time histories, NACA 0012 airfoil pitching about quarter-chord, $Re = 1.2 \times 10^4$, $M_\infty = 0.05$, $k = 8.0$, and $\alpha = \pm 2$ deg.

Figure 4.58. Example unsteady C_T response from Young and Lai (figure copied from reference)

The following discussion touches on some of the main aspects which are perceived to account for any differences between the calculated and predicted magnitudes of this response. The chord-based Reynolds number for these referenced results is not particularly high, being $Re_c = 1.2 * 10^4$. While not immediately quantifiable, the implication is that viscous effects are likely not negligible, as is the assumption within potential flow. Further, as this is an elevated reduced frequency condition, the wake of shed vorticity forms a non-planar distribution with distinct counter-rotating structures (which is extensively presented in the reference) that is a clear departure from the assumptions of the Theodorsen model (and the Garrick model, as well). As shown earlier in the UPF results, this can affect the amplitude of the unsteady streamwise force response, as well as the unsteady lift response. In Section 4.3.3, an approximate $2 - 3\ dB$ increase of the C_L response is seen at $k = 6.0$ and 19.8 conditions for $|\alpha| = 1.0^o$, and in Section 4.7.2 a similar increase of the C_D response is seen. It is presumed that the same interactions and alterations to the unsteady responses could be occurring within the results of this reference. Relation to the UPF results are understood to be representative, as further factors to consider are the differences in foil profile and pitch axis location.

4.7.4.3 Analysis of Data from Lu et al.

The reference of Lu et al. is described earlier, and for the current analysis the specific result which is focused on is the unsteady thrust coefficient of a NACA 0012 foil due to sinusoidal motion. Following the same progression as the prior analysis, the unsteady lift transfer function is,

$$\frac{C_L}{\alpha} = 2\pi(0.503 - i0.027) + i\pi\left[1 + 2(0.503 - i0.027)\left(\frac{1}{2} + \frac{1}{2}\right)\right](4.5) + \pi\left(-\frac{1}{2}\right)(4.5)^2 \qquad (4.66)$$

where $k = 4.5$ and $a = -1/2$. The magnitude of this transfer function is, $\left|\frac{C_L}{\alpha}\right| = 12.62\pi$. As the result from this reference is also assessed visually, analysis is limited to the magnitude of the unsteady streamwise force. This is expressed as, $|C_T| = \frac{1}{2}\left|\frac{C_L}{\alpha}\right||\alpha|^2$, where the magnitude of this specific pitching motion is listed as being 5^o. This yields a prediction of the magnitude of the unsteady streamwise force, $|C_T| = 0.151$.

Direct assessment of this predicted amplitude can be performed by visual inspection relative to Figure 4.59, which is a copied and cropped figure from the reference, where the comparison between this predicted value and the calculated result from Lu et al. is quite good. The calculated results of this reference for the NACA 0012 foil are seen to fluctuate between the approximate limits of -0.125 and 0.175, which yields an amplitude of approximately 0.15, and which compares very well to the predicted value above.

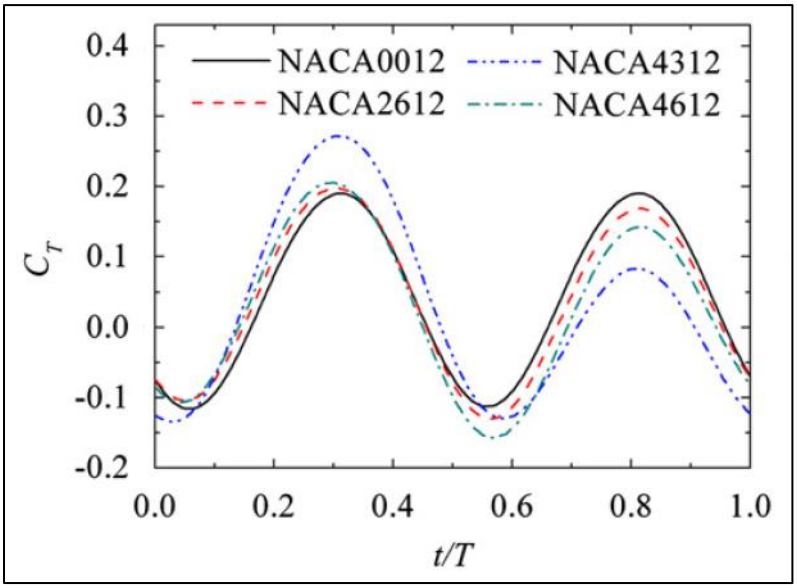

Figure 4.59. Example of the unsteady C_T responses from Lu et al. (figure copied from reference)

4.7.4.4 Analysis of Data from Hammer et al.

As with the others, the reference of Hammer et al. is also described earlier, and specific results from this reference are extracted and analyzed. These specific results are the magnitudes of the unsteady lift and thrust responses due to pitching motion. The analysis of this section compares this referenced data directly to the Theodorsen model for unsteady lift and the unsteady streamwise force magnitude expression to the corresponding data. This again begins with populating the unsteady lift transfer function expression,

$$\frac{C_L}{\alpha} = 2\pi C + i\pi[1 + 2C]k - \frac{\pi}{2}k^2 \tag{4.67}$$

where the pitching axis is the quarter-chord, and the disturbance motion amplitude is listed as $|\alpha| = 2^o$.

While the pitching motion is stated to be sinusoidal, the lift and thrust results are expressed as the *RMS* of these responses. Given the stated motion and the relatively small magnitude of the disturbance motion, it is assumed that these responses are also sinusoidal (or at least predominantly so), and therefore the *RMS* is taken to be a surrogate for the magnitude of these responses in the following way, $C_{L,RMS} = \frac{1}{\sqrt{2}}|C_L|$. The altered Theodorsen-based model expression for the magnitude of this C_L response is,

$$C_{L,RMS} = \frac{|\alpha|}{\sqrt{2}}\left|2\pi C + i\pi[1 + 2C]k - \frac{\pi}{2}k^2\right| \tag{4.68}$$

Correspondingly, the thrust response model expression is,

$$C_{T,RMS} = \frac{|\alpha|^2}{2\sqrt{2}}\left|2\pi C + i\pi[1 + 2C]k - \frac{\pi}{2}k^2\right| \tag{4.69}$$

These model expressions are compared directly to the C_L and C_T data extracted from this reference in Figure 4.60 and Figure 4.61 of the present document, where these responses are shown on both a linear scale (as presented in the reference) and a logarithmic scale. As seen in these figures, the Theodorsen model and the unsteady streamwise force model expressions both reliably capture the magnitudes of these unsteady lift and thrust responses across the reduced frequency range of these results.

The apparent degradation of the C_L results at the lowest reduced frequency when viewed as a transfer function in Figure 4.61 is a clear example of the difference between the linear and logarithmic scales. The results were extracted from plots within the reference document on a linear scale, and therefore small changes (or slight errors in the extraction) at the lowest values in this range of this plot are exacerbated on a logarithmic scale. The agreement between the model expressions and the referenced data, however, is taken to be quite acceptable.

Lastly, a comment is offered on the relative levels between the C_L and C_T magnitudes. In this instance the difference between the lift and thrust magnitudes is roughly $34\ dB$ or correspondingly an approximate factor of 50. This is in general agreement with the lift-to-thrust magnitude ratio expression,

$$\frac{|C_L|}{|C_T|} = \frac{2}{\left(2\frac{\pi}{180}\right)} = 57.3 \qquad or \qquad 20\log_{10}\left(\frac{|C_L|}{|C_T|}\right) = 35.2\ dB \tag{4.70}$$

Due to the different scaling between the C_L and C_T responses, $|\alpha|$ and $|\alpha|^2$ respectively, this difference either increases for small motion or decreases for larger motion.

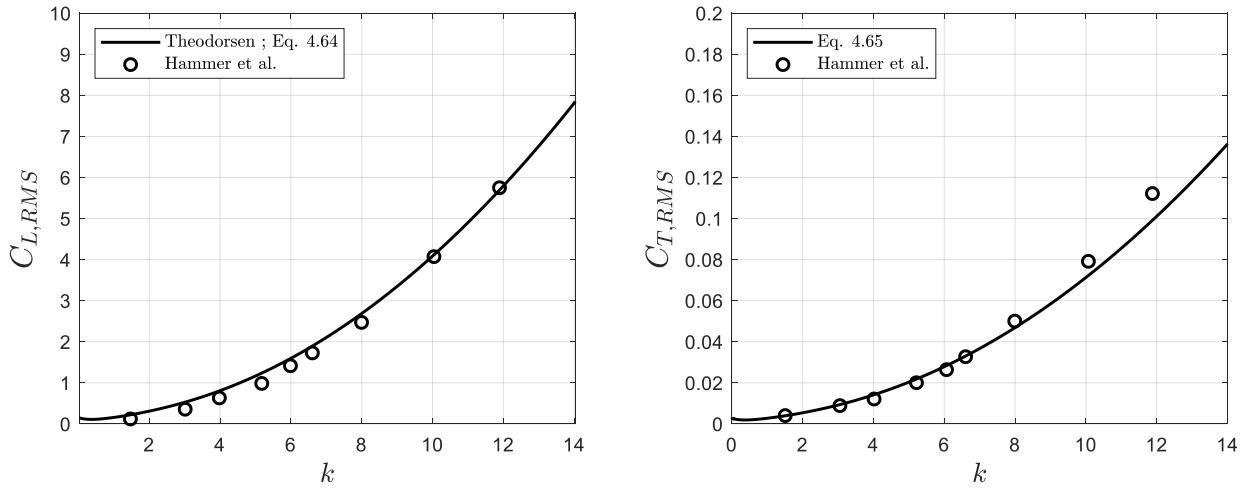

Figure 4.60. Extracted unsteady force responses from Hammer et al. viewed on a linear scale

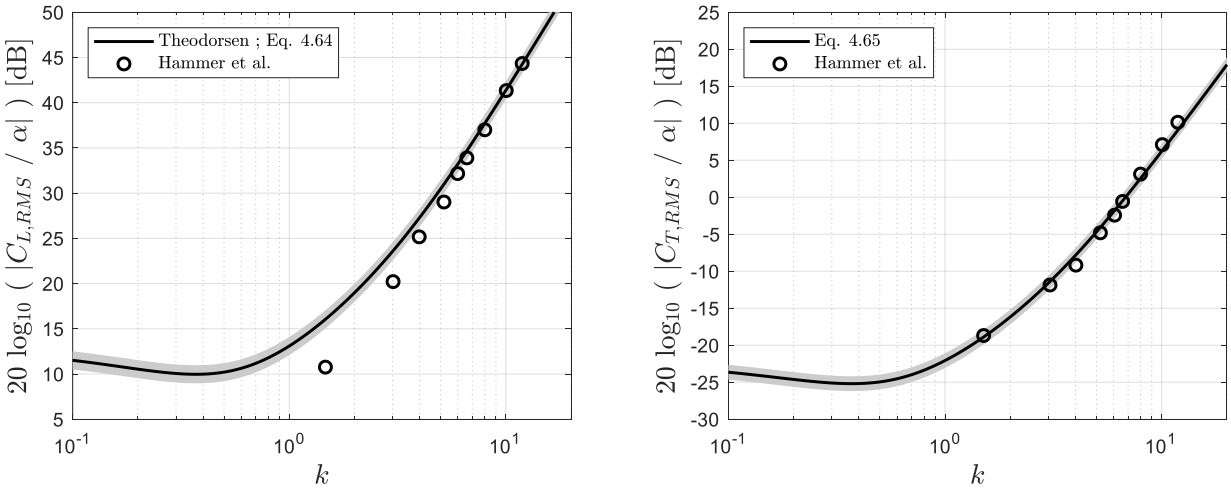

Figure 4.61. Extracted unsteady force responses from Hammer et al. viewed as transfer functions

4.7.5 Analysis of Heaving UPF Results for Variable Thickness Joukowski Foils

This section returns back to analysis of calculated UPF results for the same suite of Joukowski foils of $5, 10$, and 15% thickness-to-chord ratio for small-scale heaving motion. Under these conditions, there is now foil area which projects into the forward and aft streamwise directions and therefore an unsteady force is registered. A Bode plot of only the magnitude of these calculated results are presented in Figure 4.62, where the same disturbance heaving motion as has been utilized throughout is implemented; the heaving velocity amplitude and reduced frequencies are such that the maximum instantaneous angle of attack is 0.1 degrees. To be clear, these results are of the force response occurring at $2k$, normalized by the heave velocity which is occurring at k. Relative to the calculated results, two additional lines are present on this plot of the magnitude of the responses. The first is the magnitude of the unsteady lift transfer function for heaving motion, which is intended to provide reference for the relative magnitude between these streamwise force responses and the associated lift response. The second is the predictive expression for the magnitude of the unsteady streamwise force response, which has been slightly altered to attempt to account for a heaving configuration, as opposed to pitching motion; using α_{eff}.

As can be seen, these UPF results do not seem to exhibit any particularly strong behavior as a function of foil thickness in the magnitude of the responses. A notable feature is the much smaller magnitude of these streamwise responses relative to the lift, which is evident in the difference between the solid and dashed lines. The ratio expression presented earlier dictates this difference,

$$\frac{|C_L|}{|C_D|} = \frac{2}{\left(0.1\frac{\pi}{180}\right)} = 1{,}146 \quad or \quad 20\log_{10}\left(\frac{|C_L|}{|C_D|}\right) = 61.2\ dB \tag{4.71}$$

where the amplitude of the effective angle of attack, α_{eff}, is 0.1 degrees. This results in an approximate anticipated three orders of magnitude difference between the lift and streamwise force responses. This relation is followed fairly well for the lower reduced frequency conditions, up to an approximate threshold of $k \leq 1$. Above this value, the calculated UPF streamwise force response magnitudes continue to fall slowly and do not transition into a positive slope with increasing k.

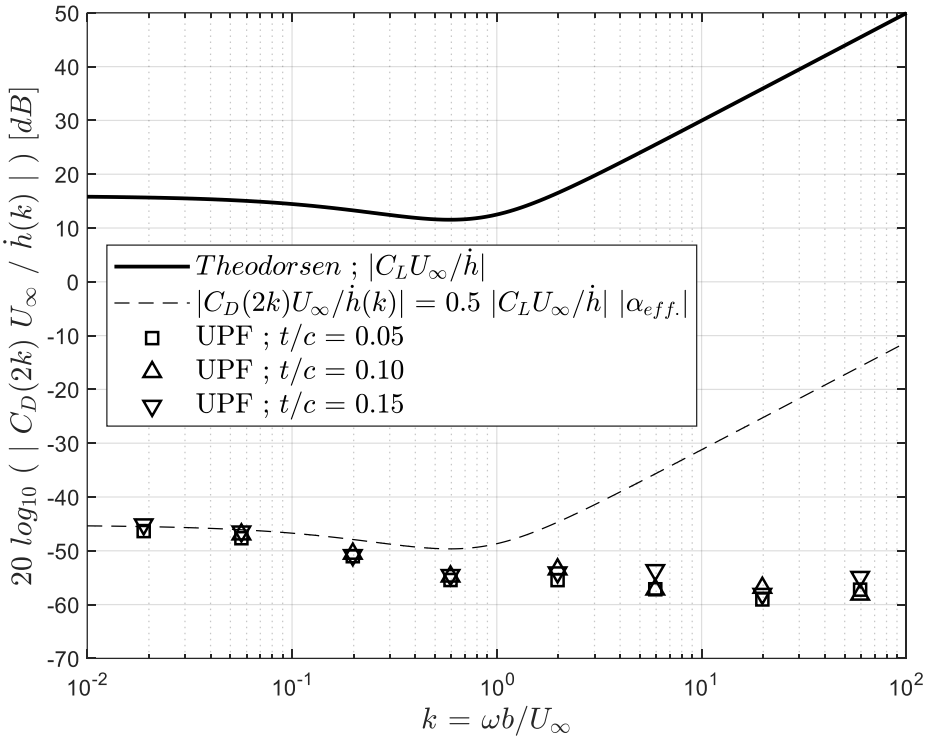

Figure 4.62. Predicted and calculated transfer functions of the unsteady streamwise force coefficient to sinusoidal heaving motion for variable thickness Joukowksi foils

This difference in the high frequency behavior of the magnitude of the response is understood by referring to the discussion of Section 4.2 and Section 4.5 for the high reduced frequency differential pressure distribution. This distribution at these conditions is mostly symmetric about the mid-chord, with an approximate half-period $\sin(\theta)$ distribution from the foil leading to trailing edge. Therefore the projections of these pressures into the streamwise direction for the forward and aft portions of the foil will mostly counteract and cancel. This is understood to be the reason for the flattening of this response, and not a transition into a region of k^1 growth.

Another view of these responses is provided in Figure 4.64, where the auto-spectral densities of these streamwise force responses (normalized by $\dot{h}/U_\infty$) are plotted for four distinct reduced frequencies. Each plot is annotated with the corresponding reduced frequency condition, which is defined by the disturbance motion, however it is seen that the principal response occurs at $2k$. For the lower reduced

frequency conditions, the tonal behavior of the responses at a single frequency is evident (the wide frequency spacing is a result of the characteristics of the signal). This changes for the higher reduced frequency conditions, where the response levels at the non-driven frequencies are much closer to the primary response frequency. It is inferred that the somewhat poor statistical quality (i.e. wide variation of levels between adjacent frequency bins) of these high frequency spectra are a result of the relatively short duration signals, and would improve with longer time series. Although these streamwise force responses are available within the UPF calculations, and are being presented, it is acknowledged that there are important limitations to potential flow. In the present focus of the unsteady streamwise force response, it is believed that similar detailed analysis from higher fidelity numerical or experimental results could easily show differences from those presented here. Potential flow only deals with pressure-based effects, and it is assumed that the role of viscosity in the shed wake, and details of the flow immediately at the foil trailing edge are important considerations which could yield differences relative to the current approach.

The remainder of this section provides reasoning for why these UPF streamwise force responses are seen to become increasingly broadband. Figure 4.65 and Figure 4.66 provide time series decomposition of these signals for reduced frequencies of 0.2 and 19.8, respectively. The total response is provided in each plot as the lighter trace, along with each subsequent component shown as the darker trace. Signals at $2k$ occur for the velocity terms, and the broadband character (appearing as a noisy time series) comes exclusively from the flow potential of the shed wake of vorticity. In corroboration with the prior figures showing the auto-spectra of the responses, this broadband behavior becomes increasingly dominant for progressively larger reduced frequencies.

Figure 4.67 provides quick visualizations of the associated wake of shed point vortices for the 15% thick foil for these same two reduced frequencies. These plots provide the same range of normalized spatial extent, and it can be seen that the higher reduced frequency condition produces a vorticity wake which is more displaced from the chordline-extended, showing undulations which eventually lead to rolled-up structures. Flow potential for point vortices takes the form, $i\log(z) = i\log(r) - \theta$, where the real

component (which contributes to the pressure) comes from the complex argument of $z = re^{i\theta}$. Evolution and progressive displacement of the wake leads to variation in this variable, which is believed to be the cause of the broadband character. Figure 4.63 provides an illustration of this concept, expressed in the circle plane. This appears to manifest as noise injected into the response signal, occurring across the range of frequencies, significantly altering the response of the non-disturbance frequencies. The non-preferential addition of this energy across frequencies is understood to be a result of the undulating nature of the entire vorticity distribution and the local rolling up of the shed vortices in the regions of local absolute maxima in the strength of the vortices.

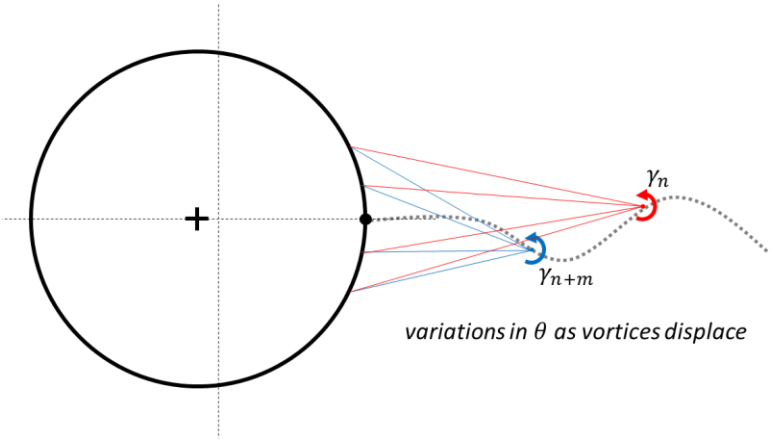

Figure 4.63. Illustration of the variation of shed vortices as they displace within the wake

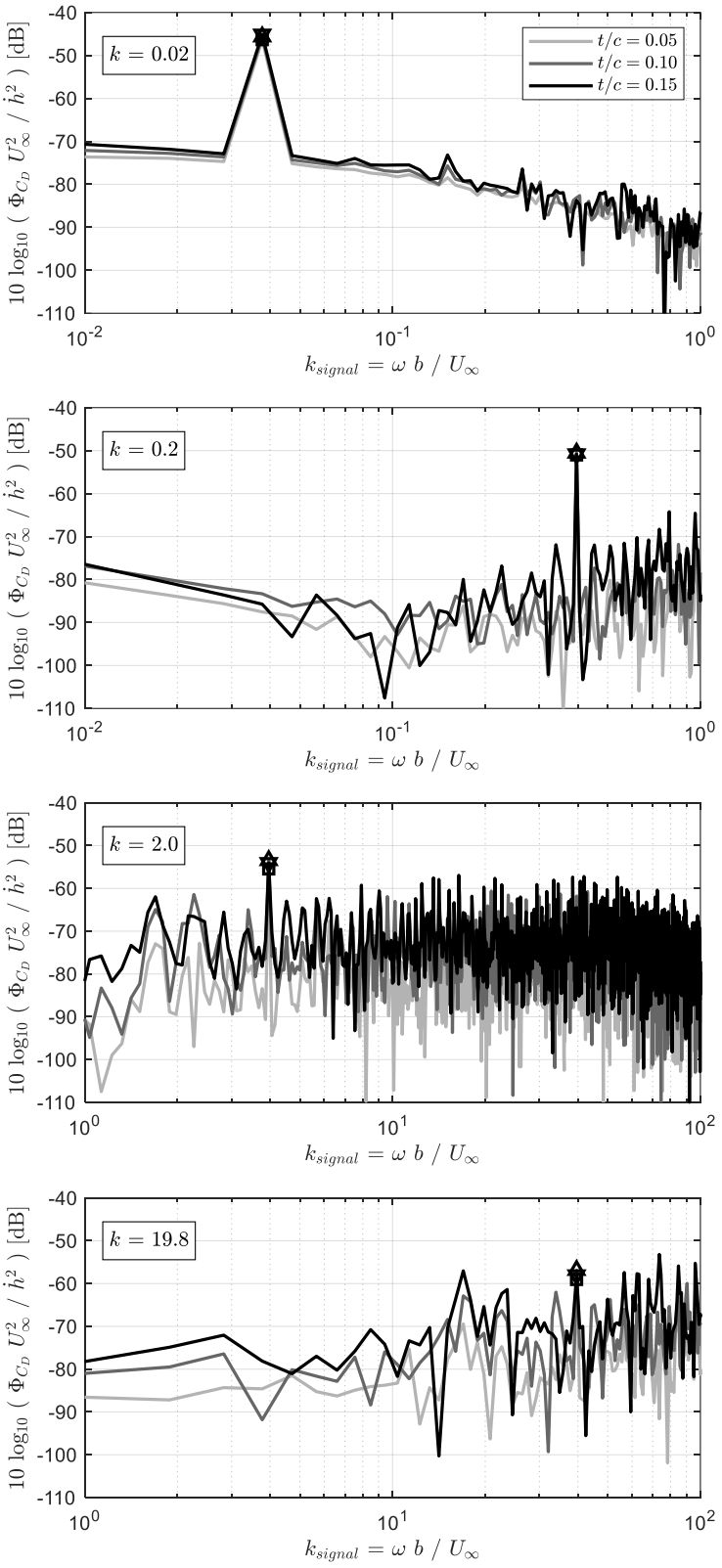

Figure 4.64. Auto-spectra of the unsteady streamwise force response for multiple reduced frequencies

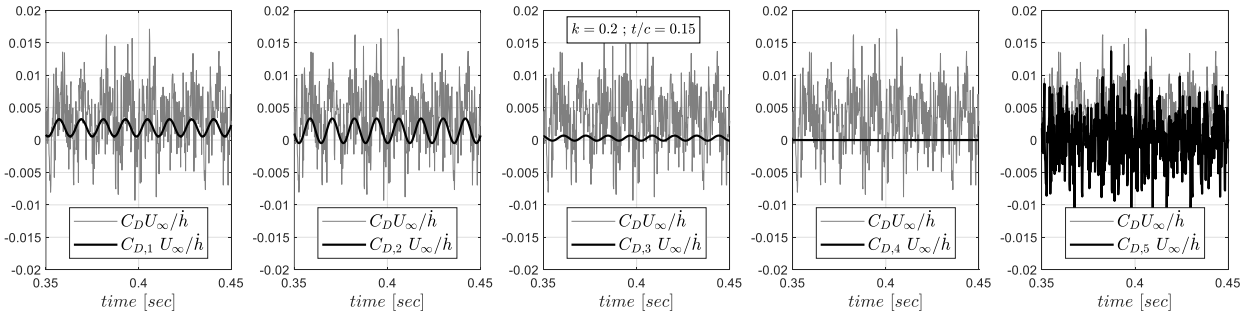

Figure 4.65. Decomposition of the streamwise force response at $k = 0.2$; see Eq. 2.39

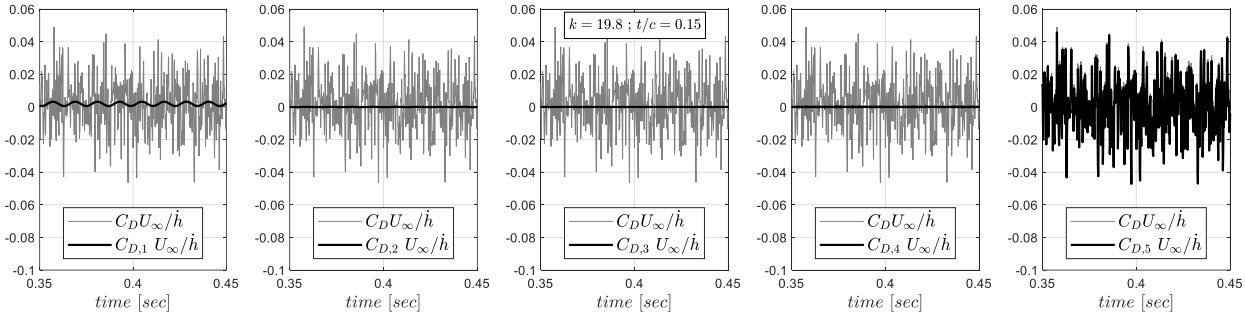

Figure 4.66. Decomposition of the streamwise force response at $k = 19.8$

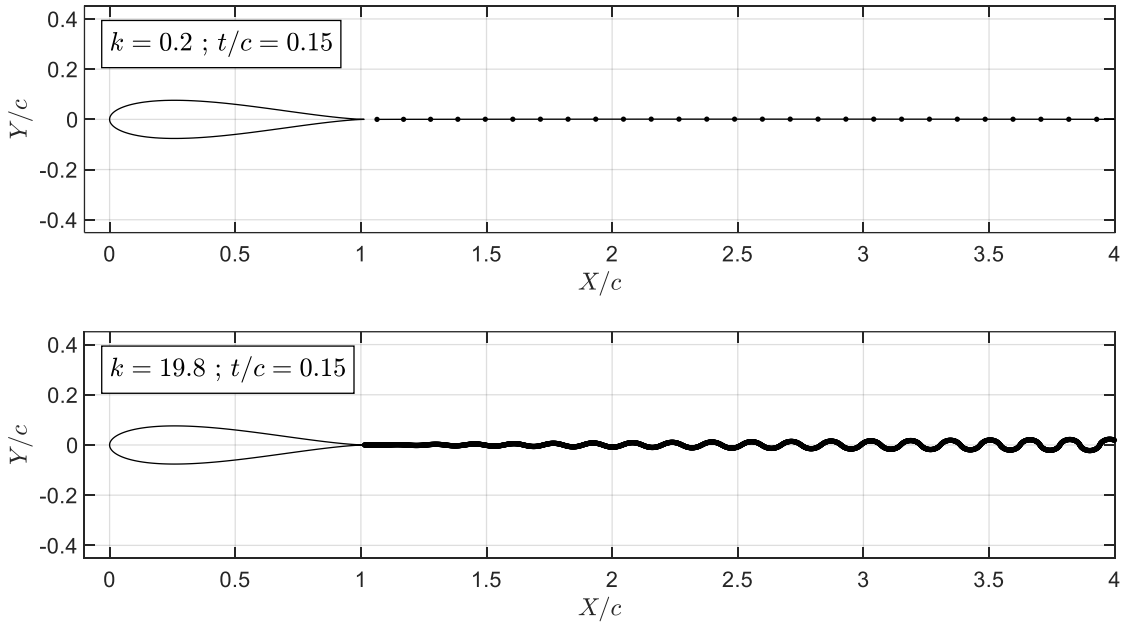

Figure 4.67. Visualization of the shed wakes at two separate reduced frequency conditions

4.7.6 Analysis of Mid-chord Pitching UPF Results for Variable Thickness Joukowski Foils

In a similar fashion as the previous section, this section presents the unsteady streamwise force responses for the same Joukowski foils of varied thickness due to mid-chord pitching disturbance motion of a maximum unsteady angle of attack of 0.1 degrees. These responses are also dominated by a response occurring at $2k$, though the disturbance motion is occurring, and is defined, at k. The magnitude of these streamwise force responses are presented in Figure 4.68, where the results from the numerically flat ($t/c = 0.00$) foil are also included. As the magnitude of the unsteady angle of attack is the same for these conditions as the heaving conditions, there is an anticipated nearly three orders of magnitude difference between the unsteady lift and streamwise force responses, $20\log_{10}\left(\frac{|C_L|}{|C_D|}\right) = \left(\frac{2}{\left(0.1\frac{\pi}{180}\right)}\right) = 61.2\ dB$. This difference is reflected in the difference between the solid and dashed lines of Figure 4.68, which correspond to the predictive expressions for unsteady lift from the Theodorsen model (again, for reference) and that for the magnitude of the streamwise force response. As can be seen, the calculated UPF results for these variable thickness foils do follow the predicted streamwise force expression fairly well over the entire reduced frequency range, however, there are also clear differences for the varied thickness conditions.

By definition these, streamwise force responses are a result of the projection of the pressure distribution relative to the normal vector along the foil surface. Referring back to Section 4.3 and Section 4.6 for discussion of these pressure distributions, they do notably change across the range of reduced frequencies under consideration. It is therefore somewhat anticipated that differences should occur given that the pressure distributions and normal projections of the foil surface both change as a result of foil thickness. Some of these differences are explored further.

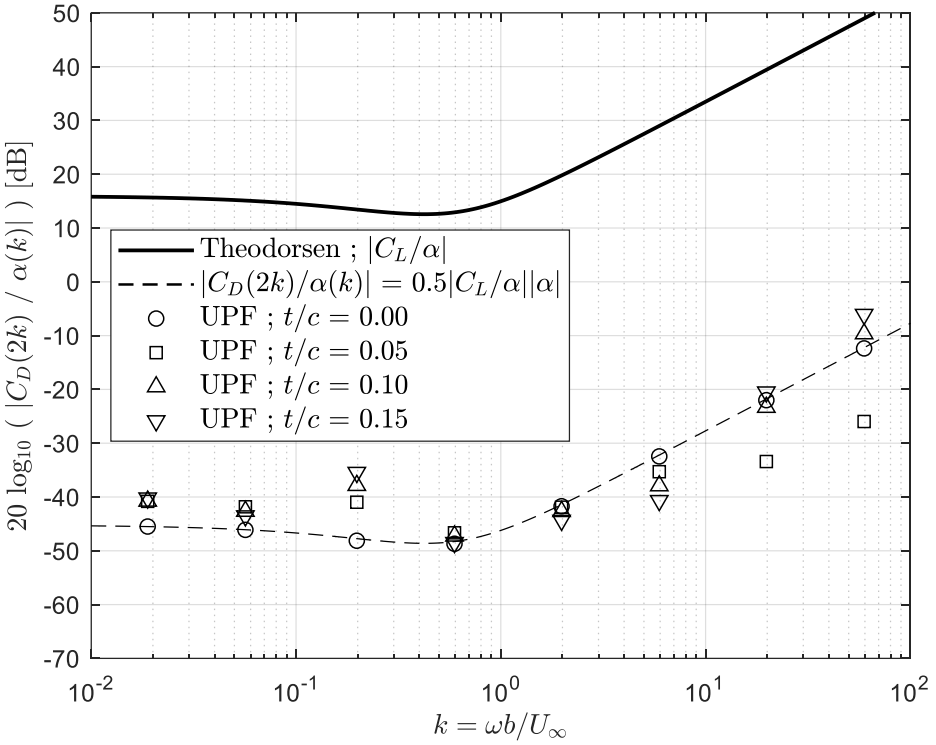

Figure 4.68. Predicted and calculated transfer functions of the unsteady streamwise force coefficient to sinusoidal, mid-chord pitching motion for variable thickness Joukowski foils

First, there are notable differences in the streamwise force responses at $2k$ for the variable foil thickness conditions at $k = 0.2$. Figure 4.69, however, provides a view of this response across the frequency spectrum. This view shows this difference at $2k$, but also the notably different responses across the range of non-disturbed reduced frequencies. These responses for the finite thickness foil conditions are particularly elevated relative to the flat foil condition, and manifest preferentially at various multiples of the disturbance motion reduced frequency: $3k, 4k, 5k$, etc. It remains an open topic as to the specific reason for this character, though additional analysis is provided by two decompositions of this response, which is presented in Figure 4.70. The plots in this figure correspond to either the flat foil or the 15% thick Joukowski foil conditions. For the flat foil condition, the response is controlled by the $C_{D,2}$ term which is occurring at $2k$. There is however an additional influence from $C_{D,5}$ (wake flow potential), which appears to be responsible for the contributions comprising the energy at all of the other frequencies. The exact same

type of plot is provided for the 15% foil, where it is seen that the $C_{D,5}$ is now exceedingly dominant and clearly comprised of contributions across the frequency spectrum. It is speculated that the rapid dominance of this term for a condition of finite foil thickness is a result of the non-zero exposure of the foil surface projected into the streamwise direction. It is however, not immediately clear why the response is manifesting so strongly at multiples of k, for frequencies greater than $2k$. Referring back to Section 2.5, the associated spatial wavelength of the vorticity distribution is given by, $\lambda = 2\pi b/k$, which corresponds to a normalized ratio of $\lambda/b = 10\pi$ for this condition. This implies that the wavelength of the vorticity distribution is a factor of 5π larger than the foil chord; continued and detailed analysis remains an open topic.

Lastly, a similar analysis is offered for the streamwise force response at $k = 2.0$. From Figure 4.68, little difference is found between the responses for the flat and finite thickness foil conditions as evaluated specifically at $2k$. Assessing the responses across the frequency spectrum however, as provided in Figure 4.69, clear differences as a result of finite foil thickness are seen. Not only do the responses exhibit elevated broadband energy at higher frequencies, but a notable response is registered at k as well. Similarly, Figure 4.71 provides the associated decomposition of the flat and 15% thick foil configuration responses. Again, it is the flow potential of the wake, $C_{D,5}$, which appears to be from where this character is emanating (zooming in on the axes for the other components shows sinusoidal, $2k$ response). The associated vorticity distribution is characterized by, $\lambda/b = \pi$, for this condition. This corresponds to a wavelength of the shed vorticity being very much on the order of the foil chord, which would seem plausible for inducing response at k.

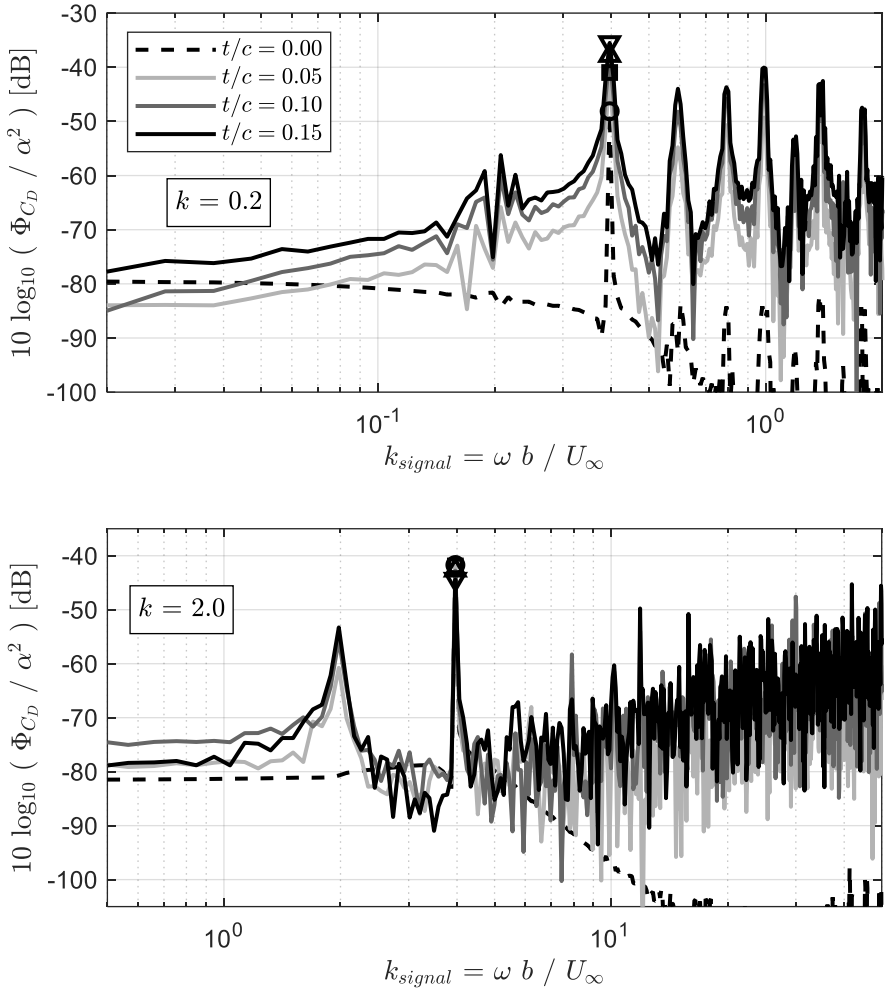

Figure 4.69. Auto-spectra of the unsteady streamwise force response for multiple reduced frequencies

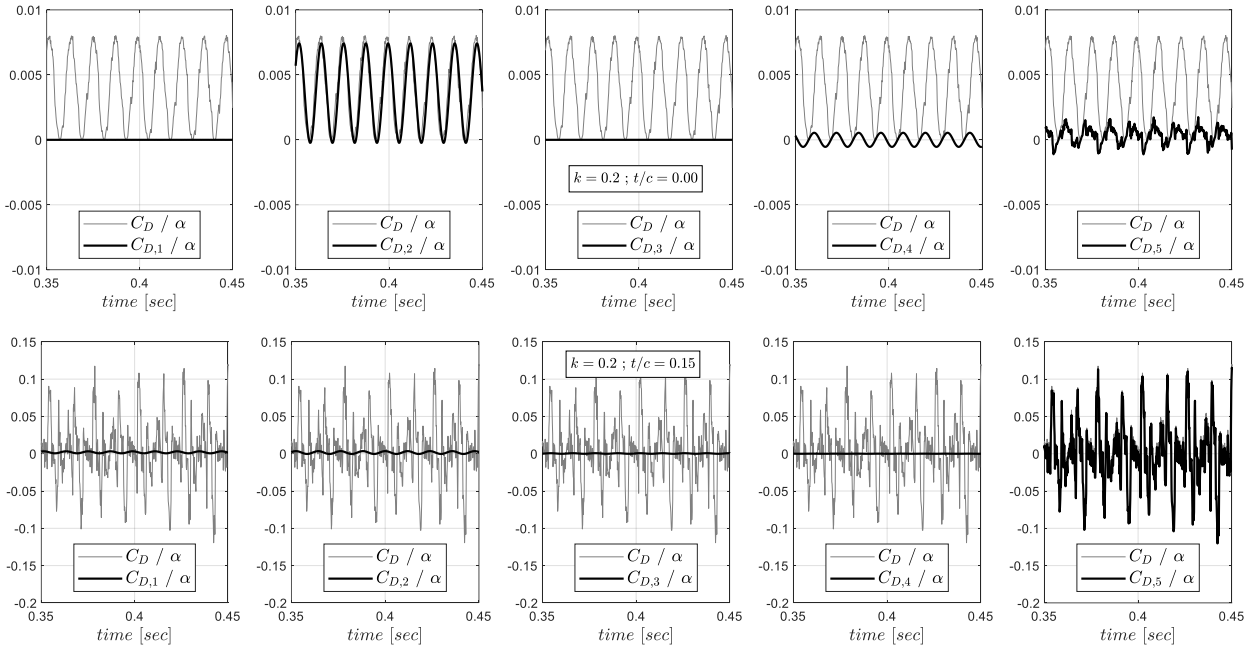

Figure 4.70. Decomposition of the streamwise force response at $k = 0.2$; see Eq. 2.39

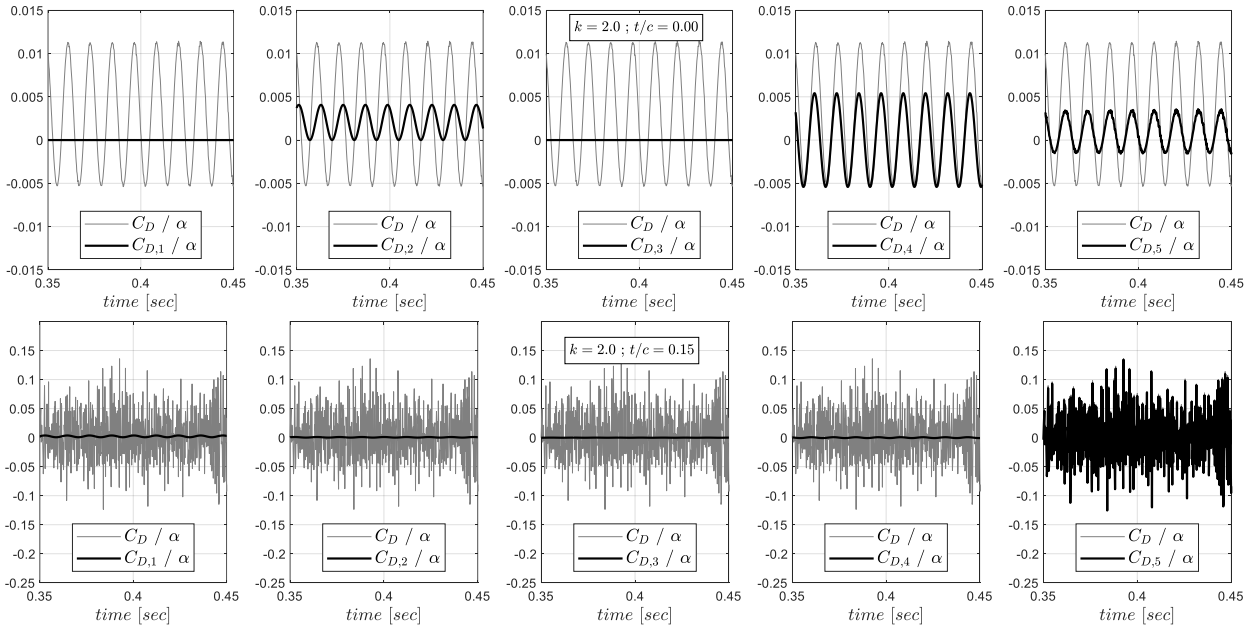

Figure 4.71. Decomposition of the streamwise force response at $k = 2.0$

5. Conclusions

5.1 Summary

This work studies the unsteady responses of foils subjected to small-scale, heaving and pitching motion over a wide range of reduced frequencies. A framework for unsteady potential flow calculations has been developed under the concept of a numerical implementation of the predictive approach posited by the Theodorsen model. The intent of the work has been to utilize these calculations to systematically explore the effects of the inherent assumptions of the Theodorsen model, and to identify conditions for when results vary from the Theodorsen model. The unsteady potential flow calculation approach has been developed such that numerical results can be assessed in conjunction with direct analysis of the explicit potential flow expressions which define the unsteady foil problem. A wide range of reduced frequencies are investigated in order to be as widely applicable as possible; and as a consequence of the large reduced frequencies which are considered, criteria are established based on the product of reduced frequency and freestream Mach number in order to justify the applicability of results based in potential flow.

The predictive expressions of the Theodorsen model are rearranged into normalized transfer functions for the unsteady responses of the various aerodynamic coefficients as a result of the disturbance motion. Calculated results for flat foil conditions compare very favorably to these Theodorsen expressions over the wide range of reduced frequencies considered. While the shed wake of vorticity from the foil trailing edge is seen to roll-up into counter-rotating vortical structures, and not retain a simplified, linear distribution for increasing disturbance motion amplitudes and reduced frequencies, this does not appear to induce a substantial difference in the unsteady foil responses at the disturbance reduced frequency. This wake behavior does however seem to induce coupling of unsteady response into reduced frequencies other than that of the disturbance motion.

The unsteady foil responses provided by the Theodorsen model expressions are found to be reliably robust in comparison to calculated results for symmetric Joukowski foil profiles of varying thickness-to-

chord ratio undergoing both heaving and mid-chord pitching disturbance motion for reduced frequencies that are nominally less than a value of one. However, for conditions which consider higher reduced frequencies, certain unsteady responses are seen to vary from the Theodorsen model. For heaving motion of Joukowski foils of varying thickness, the unsteady pitching moment is seen to vary in both its magnitude and phase properties. The reason for this augmented response is identified through analysis of the calculated results, and predictive expressions are generated for both the differential pressure and subsequent pitching moment responses as a result of finite foil thickness. In a similar, but distinctly different scenario, the high reduced frequency unsteady lift response is seen to be altered when symmetric Joukowski foils of varying finite thickness undergoing mid-chord pitching disturbance motion are considered. Again, augmenting expressions for the subsequent unsteady differential pressure and unsteady lift responses are generated based on the ability to leverage the explicitly known expressions which define the unsteady flow field.

The final concentration of the present results involves analysis and development on the unsteady streamwise force response as a result of these same small-scale, heaving and pitching disturbance motions. A predictive expression is developed for the magnitude of this unsteady response which occurs at twice the reduced frequency of the corresponding disturbance motion. Assessment of this expression relative to the unsteady potential flow calculation results is quite positive. Additionally, the corresponding results from four distinct references are analyzed with respect to this predictive expression, which also yields similarly positive comparisons.

5.2 Original Contributions

The present work addresses a topic which has received considerable attention for an extended amount of time. Despite this, several new contributions to the study of this problem have been made.

1) Through dimensional analysis of the governing equations, a broad set of quantitative criteria are established for the applicability of unsteady potential flow solutions for reduced frequency conditions which approach, surpass, and significantly exceed a value of unity.
2) The Theodorsen model expressions for unsteady lift, pitching moment, and differential pressure are recast into transfer functions of aerodynamic coefficients due to heaving or pitching motions, and the validity of analyzing the unsteady responses in this way was established for both a wide range of reduced frequencies and a wide range of small-scale disturbance motion amplitudes.
3) For sinusoidal disturbance motion of a flat foil at elevated reduced frequencies, it was identified that the wake of shed vorticity takes on non-linear behavior by forming counter-rotating vortical structures, as opposed to retaining an approximately linear downstream spatial distribution. This flow field observation is accompanied with corresponding unsteady foil responses. While this is a significant variation to the spatial distribution and convection behavior of the shed vorticity, it was found that this does not appear to significantly alter the unsteady lift and pitching moment responses at the reduced frequency of the disturbance motion.
4) For sinusoidal disturbance motion of a flat foil at a single frequency, it was identified that there is also an unsteady lift response over a non-trivial range of other non-driven frequencies. The responses at these frequencies which are different from that of the disturbance motion are lower in magnitude but not necessarily negligible. Varied behavior of these responses has been identified for different reduced frequency values across the range of reduced frequencies.
5) Calculated results were performed for flat foils undergoing broadband, small-scale pitching disturbance motion in order to confirm the validity of the Theodorsen model for these non-sinusoidal, but statistically stationary conditions. Ensemble-averaged, calculated results generally compare favorably

to the Theodorsen model across a wide range of reduced frequencies and for disturbance motion which spans a wide dynamic range. However, as the motion of the shed vorticity is not constrained, a high frequency threshold appears to be reached for which motion of this vorticity appears to alter the calculated high reduced frequency results.

6) For symmetric Joukowski foil profiles of varying finite thickness undergoing small-scale heaving motion, it has been found that for reduced frequencies above an approximate threshold of one that the unsteady pitching moment response, and not the unsteady lift, is significantly altered from that predicted by the Theodorsen model. The specific reason for this is identified as an alteration of the source flow potential contributions as a direct consequence of the finite size of the foil profile. Analysis of the controlling potential flow expressions was performed in order to achieve augmented expressions for the subsequent unsteady differential pressure distribution and unsteady pitching moment responses. These augmented expressions compare well to the associated UPF calculated results.
7) Similarly, for symmetric Joukowski foil profiles of varying finite thickness undergoing small-scale pitching motion about the foil mid-chord, it has been found that for reduced frequencies above an approximate threshold of one that the unsteady lift response, and not the pitching moment, is significantly altered from that predicted by the Theodorsen model. The specific reason for this has also been identified as an alteration of the source flow potential contributions as a direct consequence of the finite size of the foil profile. Analysis of the controlling potential flow expressions was performed in order to achieve augmented expressions for the subsequent unsteady differential pressure distribution and unsteady lift responses. These augmented expressions also compare well to the associated UPF calculated results.
8) New predictive expressions for the unsteady streamwise force response which occurs at twice the frequency of the disturbance motion have been developed. These expressions compare very favorably to the calculated UPF results of the present work. Additionally, the presented foil response results from four distinct technical references have been analyzed relative to these newly developed predictive expressions, for all of which positive comparisons are found.

The results within this document are intended to be presented in a cohesive, singular format. It is simply acknowledged however, that during the progression of these efforts that intermediary referenceable documents were generated. These are Catlett et al. (2018), Catlett et al. (2018 (2)), and Catlett et al. (2020).

5.3 Outlook for Future Work

This section offers various suggestions for future work based on the findings of the present work, and which maintain confined to the present motivations.

1) The robustness and general acceptability of the unsteady foil response expressions of the Theodorsen model are well established, though this has been predominantly based on results from aerodynamic conditions. In the context of the Theodorsen model, the primary ramification of considering hydrodynamic configurations is that they can easily involve higher reduced frequencies than are typically encountered. Further work at these elevated reduced frequencies, in either fluid media, would seem warranted given the witnessed changes to the vorticity distribution in the foil wake and the altered foil responses as a result of the finite foil size. It would seem that in this regime of attached flow, small-scale disturbance motion at high reduced frequencies that understanding of the roles and effects of compressibility (even for subsonic freestream conditions), viscosity, and the specifics of shed vorticity could be further advanced.
2) The shed wake of vorticity from the foil trailing edge is a critical component of this unsteady foil problem. Therefore, it seems plausible that for configurations that involve a mean angle of attack, though maintain attached flow across the foil, that there should be an effect due to the altered flow field and convection of vorticity. Historically, experimental and numerical results have shown there to be

little to no influence of implementing a mean angle of attack on the unsteady responses. However, these have typically not involved elevated reduced frequencies. Exploration of configurations with moderate mean angles of attack and small-scale, high reduced frequency disturbance motion conditions would seem warranted. An example question: Are there alterations to the foil responses from the tightly-spaced, consolidated vortex pairs which follow a displaced trajectory behind the foil?

3) For similar reasons as above, it seems plausible that varied foil profile shape could yield altered foil responses, especially at high reduced frequency conditions. While foil camber would result in flow field effects similar to a mean angle of attack, the altered orientation of the projection of the foil surface in the determination of the integrated responses could also yield differences. A simpler consideration would be varied symmetric foil profiles, where there could also be similar effects due to the foil surface orientation. Further investigation with either symmetric or cambered foil profiles would seem warranted.

4) The present efforts work to link the results achieved through potential flow to those of experimental and higher fidelity numerical results. The applicability of potential flow based results or predictive expressions is provided generally by the consideration of high Reynolds number, incompressible conditions. It is however, not always clear where these boundaries quantitatively are or what the ramifications are to the results of interest, even when staying within the confines of small-scale disturbance motion. It would seem a worthwhile effort to systematically study the effects of varying Reynolds number, Mach number, reduced frequency, and amplitude of disturbance motions at conditions that are perceived to push the boundaries of potential flow applicability. Though the considerations above could be pursued in numerous ways, the following are two example areas, where the topics are posed as questions: 1) For what conditions does the boundary layer which has developed along the foil surface affect the unsteady foil responses, and in what ways does this occur? 2) Are there effects of variable low Mach number freestream conditions on high reduced frequency disturbance motion conditions, and how do they manifest? The applicability criteria generated within this work provide guidance on reduced frequency and freestream Mach number conditions; can these

compressibility considerations be further refined, expanded upon, or targeted to specific aspects of the unsteady problem?

5) The streamwise force induced by unsteady foil motion is a main concern for flapping foil and wing configurations, as propulsive performance is often the primary motivation. Consideration of the unsteady streamwise force for configurations more aligned with vibratory-scale motion, and in line with the conditions of the Theodorsen model, however, appear to be less prevalent. It would seem that advancements could be made in understanding the roles which fluid viscosity and foil profile shape have on the unsteady streamwise force response of foils to this small-scale disturbance motion.
6) For most studies who either compare to or utilize the Theodorsen model, the disturbance motion involves a single-frequency sinusoid. However, broadband motion, or equally any statistically stationary signal defined in the frequency domain, can be utilized in the Theodorsen model. What does not appear to be fully explored however, is if there are any significant ramifications in terms of the foil responses at frequencies other than the disturbance motion; particularly if the disturbance motion is defined by multiple distinct frequencies. Whether there are or are not, this is not something that the expressions of the Theodorsen model provide. Further, and in a similar vein, for the streamwise force response which occurs at $2k$ from a disturbance motion defined at k, it is unclear precisely how this unsteady response would manifest for a disturbance motion which is defined by frequency content over a wide range of reduced frequencies.

Appendix A: Analysis of Joukowski Foil Profile Geometries

For the two-dimensional, unsteady potential flow configurations being investigated in this work, the orthogonal forces and pitching moment generated by the foil motion within the fluid stream are achieved by integrating the distributed pressures across the foil with respect to the projection of the surface normal into the desired direction. For forces this is summarized as,

$$F_n(Z,t) = \int_{foil} P(Z,t)\hat{n}(Z)\, dZ \qquad (A.1)$$

This appendix addresses details of the foil geometry, specifically Joukowski foil profiles, and the analytical development of the normal vector. The subsequent appendices address the analytic development of the pressure distributions. For the calculated UPF results presented throughout, the integral above is performed numerically; however, it is desired to evaluate these terms analytically such that direct expressions for the unsteady foil responses can be found for foils of finite profile. This begins with the definition of a symmetric foil according to the Joukowski mapping for a circle displaced from the origin along the negative real axis,

$$Z = z + \frac{a_c^2}{z} \quad ; \quad z = r_c e^{i\theta} + \delta_x \quad ; \quad a_c \neq r_c \qquad (A.2)$$

Substituting in z,

$$Z = r_c e^{i\theta} + \delta_x + \frac{a_c^2}{r_c e^{i\theta} + \delta_x} = r_c e^{i\theta} + \delta_x + \left(\frac{a_c^2}{r_c e^{i\theta}}\right)\left(\frac{1}{1 + \frac{\delta_x}{r_c e^{i\theta}}}\right) \qquad (A.3)$$

This can rewritten as an infinite summation series using, $\frac{1}{1+x} \approx 1 - x + x^2 - \cdots$, for $|x| < 1$,

$$Z = r_c e^{i\theta} + \delta_x + \left(\frac{a_c^2}{r_c e^{i\theta}}\right)\left(1 - \frac{\delta_x}{r_c} e^{-i\theta} + \frac{\delta_x^2}{r_c^2} e^{-i2\theta} - \cdots\right) \qquad (A.4)$$

$$Z = r_c e^{i\theta} + \delta_x - a_c^2 \sum_{n=1}^{\infty} (-1)^n\, r_c^{-n}\, e^{-in\theta}\, \delta_x^{n-1} \qquad (A.5)$$

Separating the real and imaginary components accordingly, $Z = X + iY$, and taking the derivative with respect to θ yields,

$$X = \delta_x + r_c \cos(\theta) - a_c^2 \sum_{n=1}^{\infty} (-1)^n \, r_c^{-n} \cos(n\theta) \; \delta_x^{n-1} \tag{A.6}$$

$$Y = r_c \sin(\theta) + a_c^2 \sum_{n=1}^{\infty} (-1)^n \, r_c^{-n} \sin(n\theta) \; \delta_x^{n-1} \tag{A.7}$$

$$\frac{\partial X}{\partial \theta} = -r_c \sin(\theta) + a_c^2 \sum_{n=1}^{\infty} (-1)^n \, r_c^{-n} \, n \sin(n\theta) \; \delta_x^{n-1} \tag{A.8}$$

$$\frac{\partial Y}{\partial \theta} = r_c \cos(\theta) + a_c^2 \sum_{n=1}^{\infty} (-1)^n \, r_c^{-n} \, n \cos(n\theta) \; \delta_x^{n-1} \tag{A.9}$$

Combining these expressions and canceling a common r_c term,

$$\frac{\partial Y / \partial \theta}{\partial X / \partial \theta} = \frac{\partial Y}{\partial X} = \frac{\cos(\theta) + a_c^2 \sum_{n=1}^{\infty} (-1)^n \, r_c^{-n-1} \, n \cos(n\theta) \; \delta_x^{n-1}}{-\sin(\theta) + a_c^2 \sum_{n=1}^{\infty} (-1)^n \, r_c^{-n-1} \, n \sin(n\theta) \; \delta_x^{n-1}} \tag{A.10}$$

This expression above defines the normal vector of the surface specifically for a Joukowski foil. For different foils, defined by different conformal mapping, an equivalent expression should be achievable (though may be more involved). Utilizing this expression, the normal projection of the foil surface can be defined as,

$$\xi = \tan^{-1}\left(-\frac{\partial Y}{\partial X}\right) \tag{A.11}$$

Now the unsteady lift force per unit span for an airfoil can now be defined as,

$$L(Z,t) = \int_{-b}^{b} P_U(Z,t) \cos(\xi) \, dX + \int_{-b}^{b} P_L(Z,t) \cos(\xi) \, dX \tag{A.12}$$

where P_U and P_L are pressure on the upper and lower sides of the symmetric foil, respectively. The influence of the projection of the normal vector within this expression, $\cos(\xi)$, is plotted in Figure A.1 specifically for the 15% thick Joukowski foil. The local surface orientation, $\partial Y / \partial X$, is defined as an infinite power

series, however the series converges quickly after only a few terms are included. The thinner lines in the figure correspond to the distributions for summation up to $n = 9$, while the thick line corresponds to the summation up to $n = 10$, which was deemed to be sufficiently converged. It should be noted that a negative sign is applied to this term between $0 < \theta < \pi$ as the pressure on the top side of the foil acts against the lift direction.

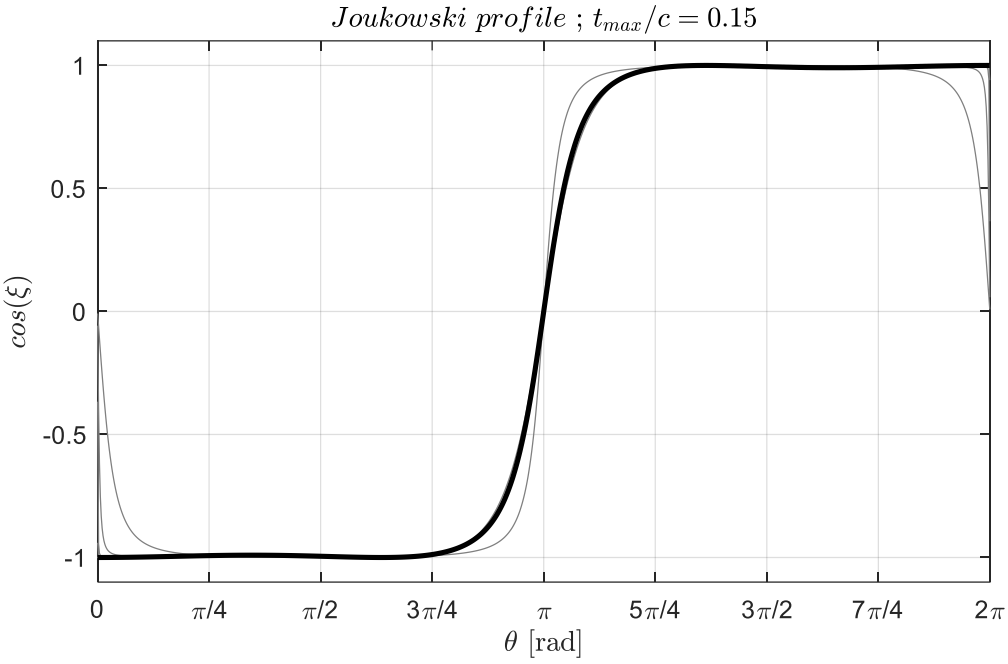

Figure A.1. Projection of the normal vector for a 15% thick Joukowski foil

Appendix B: Analysis of Heaving Contributions at High Reduced Frequency Conditions

In reference back to Section 4.5, the development of this section begins with the dominant flow potential source terms for a Joukowski foil of finite thickness undergoing sinusoidal heaving motion at high reduced frequencies, and carries through the analysis to the corresponding unsteady differential pressure distribution and pitching moment responses. This analysis yields direct expressions for these responses, which are correspondingly presented and discussed in the earlier results section. As identified for the high reduced frequency, thick foil, unsteady pitching moment response, the source flow potential term (the combination of the freestream and doublet) is the contribution which is predominantly altered. These can be written directly as,

$$f = U_o z e^{-i\,\alpha_o} + U_o \frac{a_c^2 e^{i\alpha_o}}{z - \delta_x} \qquad ; \qquad z = r_c e^{i\theta} + \delta_x \tag{B.1}$$

where the circle is displaced along the negative real axis. Substituting in this definition yields,

$$f = U_o\left(r_c e^{i\theta} + \delta_x\right) e^{-i\,\alpha_o} + U_o \frac{a_c^2 e^{i\alpha_o}}{r_c e^{i\theta}} \tag{B.2}$$

$$f = U_o r_c e^{i\theta} e^{-i\,\alpha_o} + U_o \delta_x e^{-i\,\alpha_o} + U_o \frac{a_c^2 e^{i\alpha_o}}{r_c e^{i\theta}} \tag{B.3}$$

$$f = U_o r_c e^{i(\theta - \alpha_o)} + U_o \delta_x e^{-i\,\alpha_o} + U_o \frac{a_c^2}{r_c} e^{i(\alpha_o - \theta)} \tag{B.4}$$

Expanding the exponentials,

$$f = U_o r_c[\cos(\theta - \alpha_o) + i\sin(\theta - \alpha_o)] + U_o \delta_x[\cos(\alpha_o) - i\sin(\alpha_o)] \ldots$$

$$+ U_o \frac{a_c^2}{r_c}[\cos(\alpha_o - \theta) + i\sin(\alpha_o - \theta)] \tag{B.5}$$

Retaining only the real components of $f = \phi + i\psi$, simplifies this expression to,

$$\phi = U_o r_c \cos(\theta - \alpha_o) + U_o \delta_x \cos(\alpha_o) + U_o \frac{a_c^2}{r_c} \cos(\alpha_o - \theta) \qquad (B.6)$$

The unsteady angle of attack, α_o, is due to small-scale heaving motion, h, and will be substituted for after the following angle summation identity is utilized, $cos(\alpha \pm \beta) = cos(\alpha)\, cos(\beta) \mp sin(\alpha)\, sin(\beta)$,

$$\phi = U_o r_c [\cos(\theta)\cos(\alpha_o) + \sin(\theta)\sin(\alpha_o)] + U_o \delta_x \cos(\alpha_o) \ldots$$

$$+ U_o \frac{a_c^2}{r_c} [\cos(\theta)\cos(\alpha_o) + \sin(\theta)\sin(\alpha_o)] \qquad (B.7)$$

Given that the disturbance motion is taken to be small, a small angle assumption for α_o is employed such that $\cos(\alpha_o) \approx 1$ and $\sin(\alpha_o) \approx \alpha_o$, which yields the following simplification,

$$\phi = U_o r_c [cos(\theta) + \alpha_o \sin(\theta)] + U_o \delta_x + U_o \frac{a_c^2}{r_c} [cos(\theta) + \alpha_o \sin(\theta)] \qquad (B.8)$$

$$\phi = U_o \left[r_c \cos(\theta) + \delta_x + \frac{a_c^2}{r_c} cos(\theta) \right] + U_o \alpha_o \left[r_c sin(\theta) + \frac{a_c^2}{r_c} sin(\theta) \right] \qquad (B.9)$$

The unsteady angle of attack and freestream are taken to have the following definitions,

$$\alpha_o = \tan^{-1}\left(\frac{\dot{h}}{U_\infty}\right) \approx \frac{\dot{h}}{U_\infty} \quad ; \quad U_o = \left(U_\infty^2 + \dot{h}^2\right)^{\frac{1}{2}} \qquad (B.10)$$

As the temporal derivative of the flow potential is to be taken in the determination of pressure, the corresponding derivatives for these terms are,

$$\dot{\alpha} \approx \frac{\ddot{h}}{U_\infty} \quad ; \quad \dot{U}_o = \frac{1}{2}\left(U_\infty^2 + \dot{h}^2\right)^{-\frac{1}{2}}\left(2\dot{h}\right)\left(\ddot{h}\right) = \frac{\dot{h}\ddot{h}}{U_o} = \frac{\dot{h}\ddot{h}}{U_\infty}\frac{U_\infty}{U_o} \approx \frac{\dot{h}}{U_\infty}\ddot{h} \qquad (B.11)$$

where a further implication of the small angle assumption is that $U_o \approx U_\infty$. Taking the time derivative of the flow potential term above yields,

$$\frac{\partial \phi}{\partial t} = \dot{U}_o \left[r_c \cos(\theta) + \delta_x + \frac{a_c^2}{r_c} cos(\theta) \right] + \left[\dot{U}_o \alpha_o + U_o \dot{\alpha}_o \right] \left[r_c sin(\theta) + \frac{a_c^2}{r_c} sin(\theta) \right] \qquad (B.12)$$

$$\frac{\partial \phi}{\partial t} = \left[\frac{\dot{h}}{U_\infty}\ddot{h}\right]\left[r_c \cos(\theta) + \delta_x + \frac{a_c^2}{r_c}cos(\theta)\right] + \left[\frac{\dot{h}}{U_\infty}\ddot{h}\frac{\dot{h}}{U_\infty} + U_o\frac{\ddot{h}}{U_\infty}\right]\left[r_c sin(\theta) + \frac{a_c^2}{r_c}sin(\theta)\right] \quad (B.13)$$

$$\frac{\partial \phi}{\partial t} = \left[\frac{\dot{h}}{U_\infty}\ddot{h}\right]\left[r_c \cos(\theta) + \delta_x + \frac{a_c^2}{r_c}cos(\theta)\right] + \left[\ddot{h}\left(\frac{\dot{h}}{U_\infty}\right)^2 + \ddot{h}\right]\left[r_c sin(\theta) + \frac{a_c^2}{r_c}sin(\theta)\right] \quad (B.14)$$

All of these terms have a common $\ddot{h}$ dependence, and therefore again under the premise of small disturbance motion, the terms with additional $\dot{h}/U_\infty$ dependence are dropped. This expression then simplifies to,

$$\frac{\partial \phi}{\partial t} = \ddot{h}\left[r_c sin(\theta) + \frac{a_c^2}{r_c}sin(\theta)\right] \quad (B.15)$$

Using the relevant portion of the unsteady Bernoulli equation, $P = -\rho\frac{\partial \phi}{\partial t}$, to express pressure,

$$P = -\rho\ddot{h}\left[r_c sin(\theta) + \frac{a_c^2}{r_c}sin(\theta)\right] \quad (B.16)$$

Expressing as an aerodynamic coefficient,

$$C_P = \frac{P}{0.5\rho U_\infty^2} = -2\frac{\ddot{h}}{U_\infty^2}\left[r_c sin(\theta) + \frac{a_c^2}{r_c}sin(\theta)\right] \quad (B.17)$$

Using an assumed harmonic relationship between the derivatives of the disturbance motion, $\ddot{h} = i\omega\dot{h}$,

$$C_P = -i2\frac{\omega}{U_\infty}\frac{\dot{h}}{U_\infty}\left[r_c sin(\theta) + \frac{a_c^2}{r_c}sin(\theta)\right] \quad (B.18)$$

Finally, the pressure coefficient expression is consolidated and written as a transfer function for normalized heaving motion,

$$\frac{C_P U_\infty}{\dot{h}} = -i2\frac{\omega r_c}{U_\infty}\left[sin(\theta) + \frac{a_c^2}{r_c^2}sin(\theta)\right] \quad (B.19)$$

$$\frac{C_P U_\infty}{\dot{h}} = -i2k\frac{r_c}{b}\left[1 + \frac{a_c^2}{r_c^2}\right]sin(\theta) \quad (B.20)$$

This transfer function represents an approximation for the pressure coefficient distribution for Joukowski foils of finite thickness at high reduced frequencies, such that the source flow potential terms dominate the response. While this expression does not rely on conformal mapping (flow potentials are unaltered between mapped planes) the analysis began because of behavior identified on Joukowski foil profiles. A quick check of this expression yields consistency with the corresponding portion of the Theodorsen expression for numerically flat foils, for which $\delta_x = 0$, $a_c = r_c$, $b = 2r_c$, and $C_{\Delta P} = 2C_P$,

$$\frac{C_{\Delta P} U_\infty}{\dot{h}} = 2\left\{-i2k\left(\frac{1}{2}\right)[2]sin(\theta)\right\} = -i4\ k\ sin(\theta)\ \checkmark \qquad (B.21)$$

Views of the calculated and modeled differential pressure distributions for thin and thick foils are available in the subsequent results section. Now, integration of the pressure distribution expression is needed for development of a pitching moment expression. As it will be illustrative for the finite thickness case, this development begins with the thin foil condition. For a thin foil, the expression for the pitching moment is determined by an integration of the pressure distribution,

$$M_y(Z,t) = \int_{-b}^{b} P_U(Z,t)\cos(\xi)\,X\,dX + \int_{-b}^{b} P_L(Z,t)\cos(\xi)\,X\,dX \qquad (B.22)$$

As the foil has no thickness, this is no contribution with a moment arm of Y, and the surface normal projection simplifies considerably to being either 1 or -1. Further, the chordwise distance, X, and differential element, dX, take simplified forms, $X = b\cos(\theta)$ and $dX = -b\sin(\theta)$. Inherent to how this is being expressed, the pitching moment is being determined about the foil mid-chord, which is congruent with the calculated UPF results to which this analysis is to be compared. Populating this expression,

$$M_y = \int_{\pi}^{0} P_U(b\cos(\theta))(-b\,sin(\theta))d\theta - \int_{\pi}^{2\pi} P_L(b\cos(\theta))(-b\sin(\theta))d\theta \qquad (B.23)$$

$$M_y = b^2\int_{0}^{\pi} P_U\,sin(\theta)\cos(\theta)\,d\theta + b^2\int_{\pi}^{2\pi} P_L\sin(\theta)\cos(\theta)\,d\theta \qquad (B.24)$$

Expressing the pitching moment and pressures as aerodynamic coefficients,

$$C_M\left(\frac{1}{2}\rho U_\infty^2(2b)^2\right) = b^2\int_0^\pi C_{P,U}\left(\frac{1}{2}\rho U_\infty^2\right) sin(\theta)\cos(\theta)\,d\theta + \cdots$$
$$b^2\int_\pi^{2\pi} C_{P,L}\left(\frac{1}{2}\rho U_\infty^2\right) sin(\theta)\cos(\theta)\,d\theta \qquad (B.25)$$

$$C_M = \frac{1}{4}\int_0^\pi C_P\, sin(\theta)\cos(\theta)\,d\theta + \frac{1}{4}\int_\pi^{2\pi} C_P\, sin(\theta)\cos(\theta)\,d\theta \qquad (B.26)$$

Expressing as transfer functions,

$$\frac{C_M\, U_\infty}{\dot{h}} = \frac{1}{4}\int_0^\pi \frac{C_P\, U_\infty}{\dot{h}} sin(\theta)\cos(\theta)\,d\theta + \frac{1}{4}\int_\pi^{2\pi} \frac{C_P\, U_\infty}{\dot{h}} sin(\theta)\cos(\theta)\,d\theta \qquad (B.27)$$

And finally, combining the integrals yields,

$$\frac{C_M\, U_\infty}{\dot{h}} = \frac{1}{4}\int_0^{2\pi} \frac{C_P\, U_\infty}{\dot{h}} sin(\theta)\cos(\theta)\,d\theta \qquad (B.28)$$

The integrand of this expression can easily be populated with the thin foil transfer function expression above for the pressure coefficient, $C_P U_\infty/\dot{h} = -i2k\sin(\theta)$. This yields,

$$\frac{C_M\, U_\infty}{\dot{h}} = \frac{1}{4}\int_0^{2\pi} [-i2k\, sin(\theta)]\, sin(\theta)\cos(\theta)\,d\theta \qquad (B.30)$$

where the integral falls to zero,

$$\frac{C_M\, U_\infty}{\dot{h}} = \frac{-ik}{2}\int_0^{2\pi} sin^2(\theta)\cos(\theta)\,d\theta = 0 \qquad (B.31)$$

This development shows that for a thin foil condition, the pitching moment that results from this high reduced frequency contribution drops out. This is completely consistent with the Theodorsen model, as these high reduced frequency contributions to the differential pressure cancel for the pitching moment calculated about the foil mid-chord (referring back to the earlier expressions). The purpose of showing this development is that this progression is essentially the same for the finite thickness foil condition, and the corresponding trigonometric terms that will vanish when executing the integral will be dropped for conciseness within the development.

Returning to analysis of the thick foil pressure distribution however, it is recognized that this expression also only has spatial variation due to $\sin(\theta)$, and therefore for the same reason as above would cancel when determining the pitching moment response. What is now different and which needs to be accounted for when considering a thick foil is that the moment arm, X, and the differential element, dX, will take altered definitions given the thick foil condition.

Referring to the previous appendix concentrated on expressions for Joukowski foil geometry and surface normal development, the full expression for the chordwise location, X, as a function of angle in the complex plane (due to conformal mapping between the circle and foil planes) is,

$$X = \delta_x + r_c \cos(\theta) - a_c^2 \sum_{n=1}^{\infty} (-1)^n r_c^{-n} \cos(n\theta)\, \delta_x^{n-1} \qquad (B.32)$$

Similarly, the expression for $dX/d\theta$ is,

$$\frac{dX}{d\theta} = -r_c \sin(\theta) + a_c^2 \sum_{n=1}^{\infty} (-1)^n r_c^{-n}\, n \sin(n\theta)\, \delta_x^{n-1} \qquad (B.33)$$

It can be seen that these expressions converge very quickly with only inclusion of a few of the terms of the corresponding summations. Figure B.1 and Figure B.2 plot these expression for X and $dX/d\theta$, respectively, for values of $n = 1,2$, and 10 for the 15% thick Joukowski foil condition. As just stated, the retention of only a very limited portion of the summations (in this case, two terms) provides very acceptable expressions for these variables.

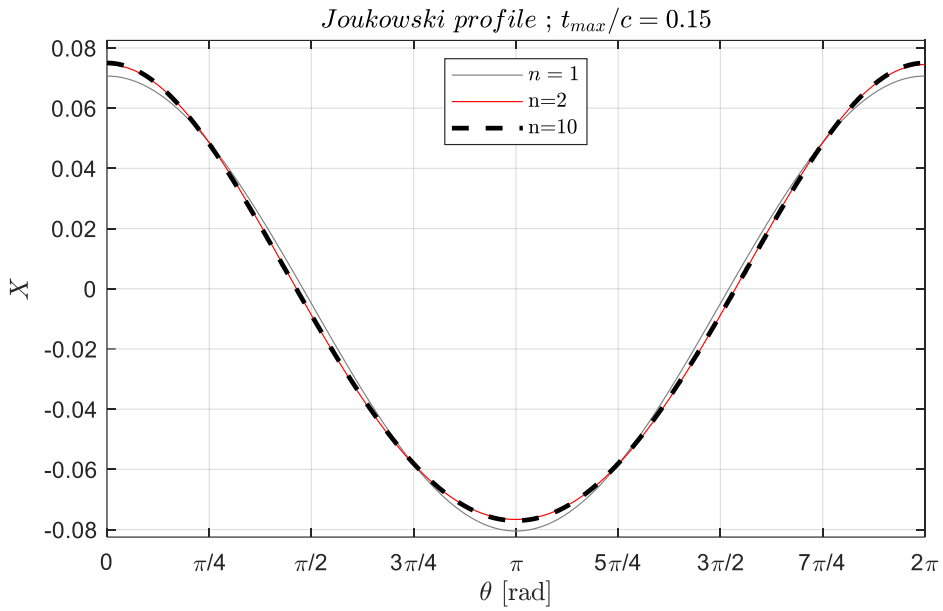

Figure B.1. Chordwise distance of a 15% Joukowski foil as a function of angle in the complex plane

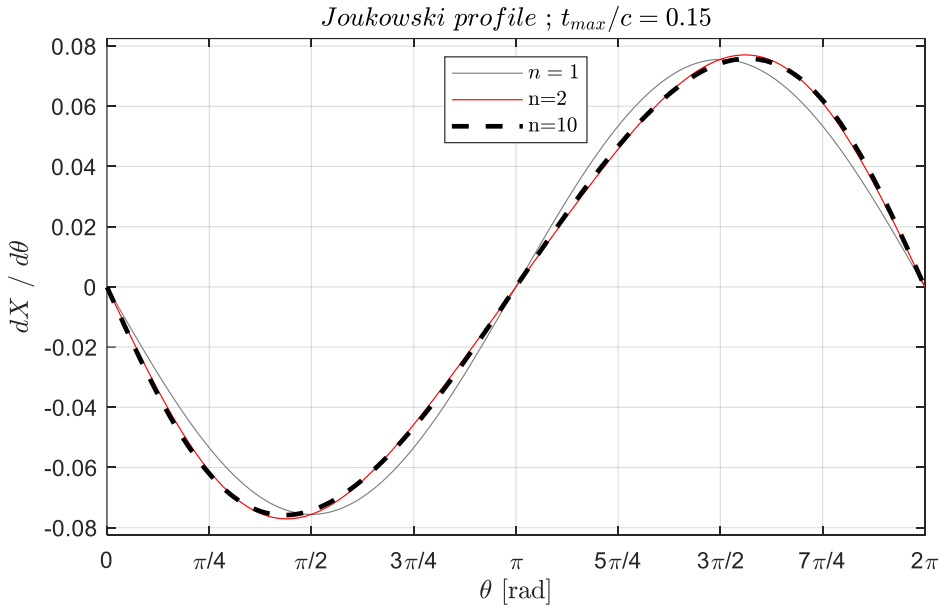

Figure B.2. Derivative of chordwise distance with respective to complex angle for a 15% Joukowski foil

Retaining only these initial portions of these terms up to $n = 2$ yields the following expressions,

$$X \approx \delta_x + r_c \cos(\theta) + \frac{a_c^2}{r_c}\cos(\theta) - \delta_x \frac{a_c^2}{r_c^2}\cos(2\theta) \qquad (B.34)$$

$$\frac{dX}{d\theta} \approx -r_c \sin(\theta) - \frac{a_c^2}{r_c}\sin(\theta) + 2\delta_x \frac{a_c^2}{r_c^2}\sin(2\theta) \qquad (B.35)$$

As a further simplifying assumption for the determination of the pitching moment, only contributions from the pressure distribution that are normal to the foil chord are utilized (pitching moment contributions that would have a moment arm along the chord-normal plane, Y, are neglected). Substituting these expressions above into the pitching moment integral expression that has been combined for the upper and lower pressure contributions (see earlier) yields,

$$M_y = -\int_0^{2\pi} P\left(\delta_x + r_c\cos(\theta) + \frac{a_c^2}{r_c}\cos(\theta) - \delta_x\frac{a_c^2}{r_c^2}\cos(2\theta)\right)\ldots$$

$$\left(-r_c\sin(\theta) - \frac{a_c^2}{r_c}\sin(\theta) + 2\delta_x\frac{a_c^2}{r_c^2}\sin(2\theta)\right)d\theta \qquad (B.36)$$

Expressing this with aerodynamic coefficients and then as transfer functions,

$$C_M\left(\frac{1}{2}\rho U_\infty^2(2b)^2\right) = -\int_0^{2\pi} C_P\left(\frac{1}{2}\rho U_\infty^2\right)\left(\delta_x + r_c\cos(\theta) + \frac{a_c^2}{r_c}\cos(\theta) - \delta_x\frac{a_c^2}{r_c^2}\cos(2\theta)\right)\ldots$$

$$\left(-r_c\sin(\theta) - \frac{a_c^2}{r_c}\sin(\theta) + 2\delta_x\frac{a_c^2}{r_c^2}\sin(2\theta)\right)d\theta \qquad (B.37)$$

$$C_M = -\frac{1}{4b^2}\int_0^{2\pi} C_P\left(\delta_x + r_c\cos(\theta) + \frac{a_c^2}{r_c}\cos(\theta) - \delta_x\frac{a_c^2}{r_c^2}\cos(2\theta)\right)\ldots$$

$$\left(-r_c\sin(\theta) - \frac{a_c^2}{r_c}\sin(\theta) + 2\delta_x\frac{a_c^2}{r_c^2}\sin(2\theta)\right)d\theta \qquad (B.38)$$

$$\frac{C_M\,U_\infty}{\dot{h}} = -\frac{1}{4b^2}\int_0^{2\pi}\frac{C_P\,U_\infty}{\dot{h}}\left(\delta_x + r_c\cos(\theta) + \frac{a_c^2}{r_c}\cos(\theta) - \delta_x\frac{a_c^2}{r_c^2}\cos(2\theta)\right)\ldots$$

$$\left(-r_c\sin(\theta) - \frac{a_c^2}{r_c}\sin(\theta) + 2\delta_x\frac{a_c^2}{r_c^2}\sin(2\theta)\right)d\theta \qquad (B.39)$$

Now the pressure distribution transfer function expression can be inserted, and the $\sin(\theta)$ is distributed,

$$\frac{C_M\, U_\infty}{\dot{h}} = -\frac{1}{4b^2}\int_0^{2\pi}\left(-i2k\frac{r_c}{b}\left[1+\frac{a_c^2}{r_c^2}\right]\right)\left(\delta_x + r_c\cos(\theta) + \frac{a_c^2}{r_c}\cos(\theta) - \delta_x\frac{a_c^2}{r_c^2}\cos(2\theta)\right)\ldots$$

$$\left(-r_c\sin^2(\theta) - \frac{a_c^2}{r_c}\sin^2(\theta) + 2\delta_x\frac{a_c^2}{r_c^2}\sin(\theta)\sin(2\theta)\right)d\theta \qquad (B.40)$$

Two steps are now taken. First, the constant terms with respect to the integral from the pressure term are pulled out. Second, the product of the middle and last terms of the integrand need to be expanded; while these are already simplified terms, this expansion would result in an excessive expression. It is therefore recognized that given the integration bounds and the trigonometric form of these terms, that significant cancellation will occur when the integral is executed. Terms similar in form to $\sin^2(\theta)$ will yield non-zero contributions, while terms similar to $\sin^2(\theta)\cos(\theta)$ will cancel, and the corresponding double angle identities for $\sin(2\theta)$ and $\cos(2\theta)$ are utilized to express all terms with the same argument. The full expansion of this expression is not listed, and only the terms which yield non-zero contributions are retained,

$$\frac{C_M\, U_\infty}{\dot{h}} = i\frac{1}{2}k\frac{r_c}{b^3}\left[1+\frac{a_c^2}{r_c^2}\right]\int_0^{2\pi} -\delta_x r_c\sin^2(\theta) - \delta_x\frac{a_c^2}{r_c}\sin^2(\theta) + 4\delta_x\left(\frac{a_c^2}{r_c}+\frac{a_c^4}{r_c^3}\right)\sin^2(\theta)\cos^2(\theta)\ldots$$

$$+\delta_x\left(\frac{a_c^2}{r_c}+\frac{a_c^4}{r_c^3}\right)(\sin^2(\theta) - 2\sin^4(\theta))\,d\theta \qquad (B.41)$$

Further simplification is provided by extracting a common $\delta_x r_c$ from the integrand,

$$\frac{C_M\, U_\infty}{\dot{h}} = i\frac{1}{2}k\frac{\delta_x r_c^2}{b^3}\left[1+\frac{a_c^2}{r_c^2}\right]\int_0^{2\pi} -\sin^2(\theta) - \frac{a_c^2}{r_c^2}\sin^2(\theta) + 4\left(\frac{a_c^2}{r_c^2}+\frac{a_c^4}{r_c^4}\right)\sin^2(\theta)\cos^2(\theta)\ldots$$

$$+\left(\frac{a_c^2}{r_c^2}+\frac{a_c^4}{r_c^4}\right)(\sin^2(\theta) - 2\sin^4(\theta))\,d\theta \qquad (B.42)$$

While this integral may appear unwieldy, it is recognized that each of these terms can be addressed individually and that integration of these trigonometric distributions over these limits are readily available. Executing this integral yields,

$$\frac{C_M\,U_\infty}{\dot{h}} = i\frac{1}{2}k\frac{\delta_x r_c^2}{b^3}\left[1+\frac{a_c^2}{r_c^2}\right]\left(-\pi-\frac{a_c^2}{r_c^2}\pi+4\left(\frac{a_c^2}{r_c^2}+\frac{a_c^4}{r_c^4}\right)\frac{\pi}{4}+\left(\frac{a_c^2}{r_c^2}+\frac{a_c^4}{r_c^4}\right)\left(\pi-2\left(\frac{3\pi}{4}\right)\right)\right) \quad (B.43)$$

Simplification yields,

$$\frac{C_M\,U_\infty}{\dot{h}} = i\frac{1}{2}k\frac{\delta_x r_c^2}{b^3}\left[1+\frac{a_c^2}{r_c^2}\right]\left(-\pi-\frac{a_c^2}{r_c^2}\pi+\left(\frac{a_c^2}{r_c^2}+\frac{a_c^4}{r_c^4}\right)\pi+\left(\frac{a_c^2}{r_c^2}+\frac{a_c^4}{r_c^4}\right)\pi-\left(\frac{a_c^2}{r_c^2}+\frac{a_c^4}{r_c^4}\right)\frac{3\pi}{2}\right) \quad (B.44)$$

$$\frac{C_M\,U_\infty}{\dot{h}} = i\frac{1}{2}k\frac{\delta_x r_c^2}{b^3}\left[1+\frac{a_c^2}{r_c^2}\right]\left(-\pi+\frac{a_c^2}{r_c^2}\left(-\pi+\pi+\pi-\frac{3\pi}{2}\right)+\frac{a_c^4}{r_c^4}\left(\pi+\pi-\frac{3\pi}{2}\right)\right) \quad (B.45)$$

$$\frac{C_M\,U_\infty}{\dot{h}} = i\frac{\pi}{2}k\frac{\delta_x r_c^2}{b^3}\left[1+\frac{a_c^2}{r_c^2}\right]\left(-1+\frac{a_c^2}{r_c^2}\left(-\frac{1}{2}\right)+\frac{a_c^4}{r_c^4}\left(\frac{1}{2}\right)\right) \quad (B.46)$$

$$\frac{C_M\,U_\infty}{\dot{h}} = -i\frac{\pi}{2}k\frac{\delta_x r_c^2}{b^3}\left[1+\frac{a_c^2}{r_c^2}\right]\left[1+\frac{a_c^2}{2r_c^2}-\frac{a_c^4}{2r_c^4}\right] \quad (B.47)$$

This expression represents the high reduced frequency contribution to the pitching moment determined about the mid-chord from only the source flow potential terms for Joukowski foil profiles of variable thickness. While the variables within this expression are mixed between the circle and foil planes, they are all completely defined by the desired or implemented foil geometry, and therefore are known variables. In a very similar manner as to the augmented expression for the unsteady lift due to mid-chord pitching motion, this term can be added to the corresponding Theodorsen model expression for the pitching moment about the mid-chord of a flat foil. Additionally, this term drops to zero for a flat foil condition, $\delta_x = 0$, which is consistent with the Theodorsen model.

Appendix C: Analysis of mid-chord Pitching Contributions at High Reduced Frequency Conditions

Similar to the development of the previous appendix, this section presents analysis of the dominant contributions to the unsteady pressure and lift responses for Joukowski foils of variable thickness that are undergoing pitching motion about the mid-chord at high reduced frequencies. This analysis culminates in direct expressions for the unsteady differential pressure distribution and lift responses. For a numerically flat foil, the flow potential terms attributed to the source (i.e. freestream, doublet, and rotation) are,

$$f = U_o z e^{-i\,\alpha} + U_o \frac{a_c^2 e^{i\alpha}}{z - \delta_x} + i\dot{\alpha}\left(\frac{1}{2}\left(z^2 - z^{*2}\right)\right) \tag{C.1}$$

where the third term in this expression (the flow potential due to rotational velocity of a flat foil) is developed in a succeeding appendix.

Subsequently, this term is more complicated for a foil of finite thickness, and the equivalent expression for a symmetric Joukowski foil of finite thickness is the following,

$$f = U_o z e^{-i\,\alpha} + U_o \frac{a_c^2 e^{i\alpha}}{z - \delta_x} \ldots$$

$$+ (i\dot{\alpha})\left(\frac{1}{2}\left(z^2 - z^{*2}\right) + \delta_x\left(2ze^{i\theta} - 2z^* e^{-i\theta} - 4r_c - i8\pi r_c\right) + \Delta_x(-z + z^*)\right) \tag{C.2}$$

where the constant terms will drop when assessing pressure differences. Now, two steps are taken. First, given that high frequency conditions are being considered, the freestream and doublet terms are dropped as they are of order α, while the rotation term is of order $\dot{\alpha}$ and is expected to dominate. Second, the following are utilized for the difference of complex conjugates, where the circle is defined as, $z = r_c e^{i\theta} + \delta_x$,

$$z^2 - z^{*2} = i2r_c^2 \sin(2\theta) + i4r_c\delta_x \sin(\theta) \tag{C.3}$$

$$2ze^{i\theta} - 2z^* e^{-i\theta} = i4r_c \sin(2\theta) + i4\delta_x \sin(\theta) \tag{C.4}$$

$$-z + z^* = -i2r_c \sin(\theta) \tag{C.5}$$

Utilizing this assumption and these expressions, the flow potential becomes,

$$f = i\dot{\alpha}(ir_c^2\sin(2\theta) + i2r_c\delta_x\sin(\theta) + \delta_x(i4r_c\sin(2\theta) + i4\delta_x\sin(\theta)) - i2\Delta_x r_c\sin(\theta)) \quad (C.6)$$

$$f = -\dot{\alpha}r_c^2\left(\sin(2\theta) + 4\frac{\delta_x}{r_c}\sin(2\theta) + 2\frac{\delta_x}{r_c}\sin(\theta) + 4\frac{\delta_x^2}{r_c^2}\sin(\theta) - 2\frac{\Delta_x}{r_c}\sin(\theta)\right) \quad (C.7)$$

Using $f = \phi + i\psi$,

$$\phi = -\dot{\alpha}r_c^2\left(\sin(2\theta) + 4\frac{\delta_x}{r_c}\sin(2\theta) + 2\frac{\delta_x}{r_c}\sin(\theta) + 4\frac{\delta_x^2}{r_c^2}\sin(\theta) - 2\frac{\Delta_x}{r_c}\sin(\theta)\right) \quad (C.8)$$

taking the time derivative of the flow potential,

$$\frac{\partial\phi}{\partial t} = -\ddot{\alpha}\, r_c^2\left(\sin(2\theta) + 4\frac{\delta_x}{r_c}\sin(2\theta) + 2\frac{\delta_x}{r_c}\sin(\theta) + 4\frac{\delta_x^2}{r_c^2}\sin(\theta) - 2\frac{\Delta_x}{r_c}\sin(\theta)\right) \quad (C.9)$$

and utilizing the associated portion of the unsteady Bernoulli equation, $P = -\rho\frac{\partial\phi}{\partial t}$,

$$C_P = \frac{P}{0.5\rho U_\infty^2} = 2\frac{\ddot{\alpha}}{U_\infty^2}r_c^2\left[\sin(2\theta) + 4\frac{\delta_x}{r_c}\sin(2\theta) + 2\frac{\delta_x}{r_c}\sin(\theta) + 4\frac{\delta_x^2}{r_c^2}\sin(\theta) - 2\frac{\Delta_x}{r_c}\sin(\theta)\right] \quad (C.10)$$

an expression for the distribution of coefficient of pressure is achieved. Utilizing an assumption of harmonic oscillations, $\ddot{\alpha} = -\omega^2\alpha$, allows for conversion from pitch acceleration to pitch position. Additionally, a sign change of α is implemented in order to address the frame of reference difference between the velocity of the foil and the velocity in the flow field. This sign change does not alter any of the functional characteristics of this rotational velocity term as detailed in Appendix D. Combining these yields,

$$C_P = \frac{\omega^2\alpha}{U_\infty^2}\, r_c^2\left[2\sin(2\theta) + 8\frac{\delta_x}{r_c}\sin(2\theta) + 4\frac{\delta_x}{r_c}\sin(\theta) + 8\frac{\delta_x^2}{r_c^2}\sin(\theta) - 4\frac{\Delta_x}{r_c}\sin(\theta)\right] \quad (C.11)$$

$$\frac{C_P}{\alpha} = \frac{\omega^2 b^2}{U_\infty^2}\,\frac{r_c^2}{b^2}\left[\left(2 + 8\frac{\delta_x}{r_c}\right)\sin(2\theta) + \left(4\frac{\delta_x}{r_c} + 8\frac{\delta_x^2}{r_c^2} - 4\frac{\Delta_x}{r_c}\right)\sin(\theta)\right] \quad (C.12)$$

$$\frac{C_P}{\alpha} = k^2\frac{r_c^2}{b^2}\left[\left(4 + 16\frac{\delta_x}{r_c}\right)\sin(\theta)\cos(\theta) + \left(4\frac{\delta_x}{r_c} + 8\frac{\delta_x^2}{r_c^2} - 4\frac{\Delta_x}{r_c}\right)\sin(\theta)\right] \quad (C.13)$$

a transfer function expression is arrived at for this response. A quick check shows that this expression reverts back to a consistent expression with the Theodorsen model, see Eq. 2.68, for a flat foil condition at a high reduced frequency limit; $\delta_x = \Delta_x = 0$, $r_c = b/2$, $\frac{C_{\Delta P}}{\alpha} = 2\frac{C_P}{\alpha}$.

For the utilization of this pressure expression in the determination of the unsteady lift a simplification is needed for the differential element in order to carry out the necessary integration. Utilizing the definition from Appendix A, the following simplifying assumption is made,

$$\frac{\partial X}{\partial \theta} \approx -2r_c \sin(\theta) \approx -b \sin(\theta) \qquad (C.14)$$

Distributions of this function are provided in Figure C.1 for two characteristic conditions which correspond to 5% and 15% thick Joukowski foils, as well as the approximation above. While the simplified term is only strictly valid for the flat foil condition, this approximation was deemed acceptable.

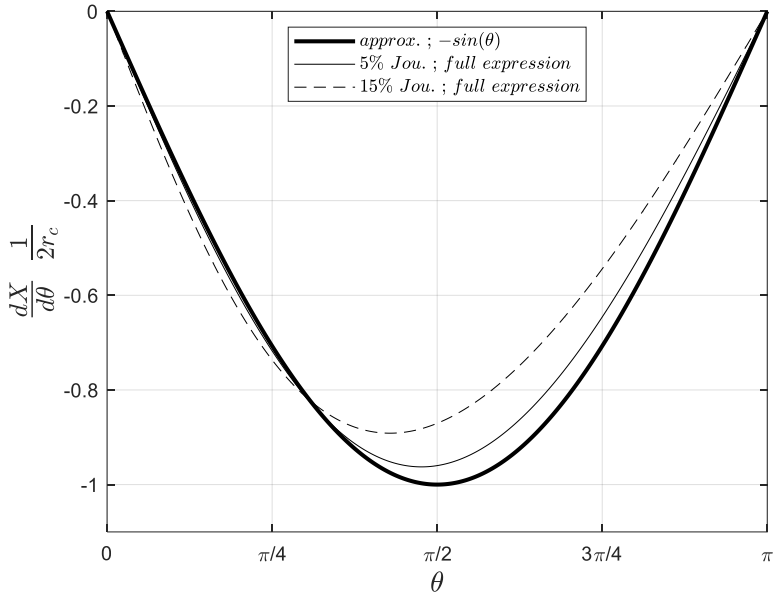

Figure C.1 Character of the differential element

Writing the lift expression of Appendix A with this approximation and updated integration limits,

$$L = \int_{\pi}^{0} P_U \cos(\xi)\,(-b)\sin(\theta)\,d\theta + \int_{\pi}^{2\pi} P_L \cos(\xi)\,(-b)\sin(\theta)\,d\theta \qquad (C.15)$$

$$L = b\int_{0}^{\pi} P_U \cos(\xi)\sin(\theta)\,d\theta - b\int_{\pi}^{2\pi} P_L \cos(\xi)\sin(\theta)\,d\theta \qquad (C.16)$$

Converting to lift and pressure coefficient transfer functions,

$$C_L\left(\frac{1}{2}\rho U_\infty^2(2b)\right) = b\int_{0}^{\pi} C_{P,U}\left(\frac{1}{2}\rho U_\infty^2\right) cos(\xi)\,sin(\theta)\,d\theta - b\int_{\pi}^{2\pi} C_{P,L}\left(\frac{1}{2}\rho U_\infty^2\right) cos(\xi)\,sin(\theta)\,d\theta \qquad (C.17)$$

$$\frac{C_L}{\alpha} = \frac{1}{2}\int_0^{\pi} \frac{C_{P,U}}{\alpha} cos(\xi)\, sin(\theta)\, d\theta - \frac{1}{2}\int_{\pi}^{2\pi} \frac{C_{P,L}}{\alpha} cos(\xi)\, sin(\theta)\, d\theta \qquad (C.18)$$

Dropping the C_P subscripts and substituting the C_P transfer function yields,

$$\frac{C_L}{\alpha} = \frac{1}{2}\int_0^{\pi} \left(k^2 \frac{r_c^2}{b^2} \left[\left(4 + 16\frac{\delta_x}{r_c}\right) sin^2(\theta)\, cos(\theta) + \left(4\frac{\delta_x}{r_c} + 8\frac{\delta_x^2}{r_c^2} - 4\frac{\Delta_x}{r_c}\right) sin^2(\theta) \right] \right) cos(\xi)\, d\theta \ \ldots$$

$$-\frac{1}{2}\int_{\pi}^{2\pi} \left(k^2 \frac{r_c^2}{b^2} \left[\left(4 + 16\frac{\delta_x}{r_c}\right) sin^2(\theta)\, cos(\theta) + \left(4\frac{\delta_x}{r_c} + 8\frac{\delta_x^2}{r_c^2} - 4\frac{\Delta_x}{r_c}\right) sin^2(\theta) \right] \right) cos(\xi)\, d\theta \qquad (C.19)$$

Recognizing the odd and even function characteristics of the trigonometric products across the integration limits and the symmetry of the distribution of the normal vector, these integrals reduce to the following,

$$\frac{C_L}{\alpha} = 2k^2 \frac{r_c^2}{b^2} \left(\frac{\delta_x}{r_c} + 2\frac{\delta_x^2}{r_c^2} - \frac{\Delta_x}{r_c} \right) \left[\int_0^{\pi} sin^2(\theta)\, cos(\xi)\, d\theta - \int_{\pi}^{2\pi} sin^2(\theta)\, cos(\xi)\, d\theta \right] \qquad (C.20)$$

The integral above can be evaluated, however the result is dependent upon the variable foil geometry, specifically the influence of $\cos(\xi)$. Therefore the integral is evaluated numerically for a range of offset values, δ_x, and the resulting distribution of the evaluated integrations is approximated by a polynomial which is found empirically. Figure C.2 presents these results as a function of δ_x/r_c (i.e. foil thicknesses) where the corresponding points for the 5, 10, and 15% thickness Joukowski foil conditions are plotted discretely as black dots. A second order polynomial expression is found to provide a very adequate approximation for this integral evaluation over the range of foil geometries considered.

Substituting this approximated polynomial expression for the integral expression,

$$\frac{C_L}{\alpha} \approx 2k^2 \frac{r_c^2}{b^2} \left(\frac{\delta_x}{r_c} + 2\frac{\delta_x^2}{r_c^2} - \frac{\Delta_x}{r_c} \right) \left[1.96\frac{\delta_x^2}{r_c^2} - 0.082\frac{\delta_x}{r_c} - \pi \right] \qquad (C.21)$$

While the higher order δ_x/r_c terms from this approximation are present, only the zeroth order term of the polynomial approximation is maintained as it dominates the value of the expression over this range of offset ratios; therefore,

$$\frac{C_L}{\alpha} \approx -2\pi k^2 \left(\frac{\delta_x r_c}{b^2} + 2\frac{\delta_x^2}{b^2} - \frac{\Delta_x r_c}{b^2} \right) \qquad (C.22)$$

Finally, a quick check shows that for a flat foil condition, $\delta_x = \Delta_x = 0$, these k^2 contributions vanish, which is consistent with the numerical results and the Theodorsen model.

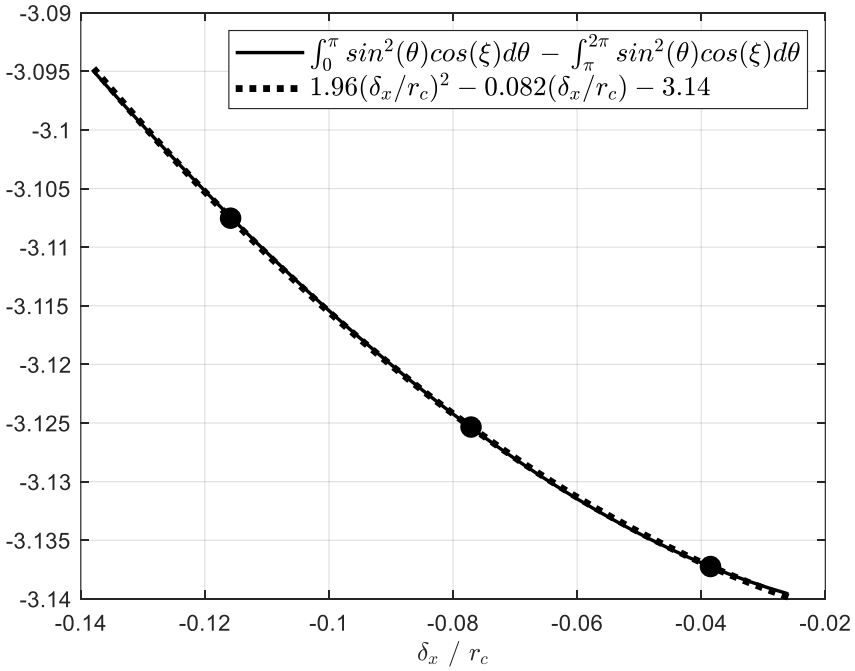

Figure C.2. Integral approximation for C_L/α expression

Appendix D: Development and Considerations for the Contributions of Rotational Velocity

It has been the intention to mirror and leverage the potential flow framework provided by the Theodorsen model as much as possible for the UPF calculations that were developed within this work. Because of the development and handling of the velocity and flow potential contributions from the rotational velocity in the foil plane as a result of foil pitching motion within the analysis of the Theodorsen model, a new term needed to be developed and implemented for the UPF calculations and analysis. This term represents the induced velocity on the foil surface due to the angular pitch rate, $\dot{\alpha}(t)$, which results from solid body rotation in the foil plane, $\dot{\alpha}r$, where r is the moment arm from the pitch axis in the foil plane. As illustrated in the foil plane in Figure D.1, this term is found to be,

$$W_{rot}(Z) = i\dot{\alpha}(Z - Z_o)^* \qquad (D.1)$$

where the pitch axis in the foil plane, Z_o, is known, and possibly offset from the origin so that a finite thickness Joukowski foil can pitch about its respective mid-chord (or a non-mid-chord location can be implemented, though this is not explored in the present UPF calculations or analysis). The complex conjugate, $[\quad]^*$, of the moment arm is taken in order to introduce the correct orientation of the unsteady velocity throughout the complex plane.

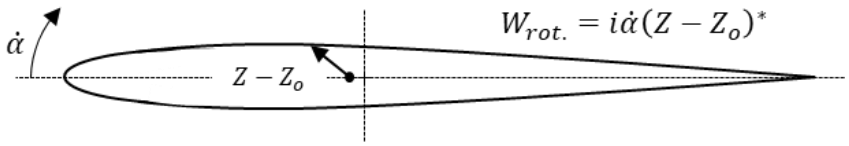

Figure D.1. Illustration of rotational velocity

The expression above pertains to the velocity in the foil plane, but the velocity in the circle plane is also needed (and is implemented). This is achieved by rearranging the velocity mapping,

$$w_{rot}(z) = i\dot{\alpha}\left(z^* + \frac{a_c^2}{z^*} - Z_o^*\right)\left(1 - \frac{a_c^2}{z^2}\right) \qquad (D.2)$$

where again, Z_o is a known value in the foil plane. There are several considerations in relation to this term which are presently addressed. To begin, it was not inherently assumed that this was an acceptable potential flow term for which a flow potential expression would be achievable. This will be addressed next, and afterwards it will also be confirmed that Laplace's equation is satisfied and that the circle is maintained as a streamline by this term.

Beginning with the rotational velocity term in the circle plane for a flat foil (i.e. circle located at the origin, and $r_c = a_c$),

$$w_{rot}(z) = i\dot{\alpha}\left(z^* + \frac{a_c^2}{z^*}\right)\left(1 - \frac{a_c^2}{z^2}\right) \tag{D.3}$$

$$w_{rot} = i\dot{\alpha}\left(r_c e^{-i\theta} + \frac{r_c}{e^{-i\theta}}\right)\left(1 - \frac{1}{e^{2i\theta}}\right) \tag{D.4}$$

$$w_{rot} = i\dot{\alpha}r_c\left(e^{-i\theta} + e^{i\theta}\right)\left(1 - e^{-2i\theta}\right) \tag{D.5}$$

$$w_{rot} = i\dot{\alpha}r_c\left(e^{-i\theta} + e^{i\theta} - e^{-3i\theta} - e^{-i\theta}\right) \tag{D.6}$$

$$w_{rot} = i\dot{\alpha}r_c\left(e^{i\theta} - e^{-3i\theta}\right) \tag{D.7}$$

$$w_{rot} = i\dot{\alpha}\left(r_c e^{i\theta} - \frac{r_c^4}{r_c^3 e^{3i\theta}}\right) \tag{D.8}$$

$$w_{rot} = i\dot{\alpha}\left(z - \frac{a_c^4}{z^3}\right) \tag{D.9}$$

The flow potential can be defined by the integration of the velocity; expressed in radial coordinates this is,

$$f_{rot} = \int w_{rot}\, dz = \int w_{rot}\, e^{i\theta} dr + \int w_{rot}\, ire^{i\theta} d\theta \tag{D.10}$$

where $dz = e^{i\theta}dr + rie^{i\theta}d\theta$. Utilizing Eq. D.7, the corresponding flow potential is found to be,

$$f_{rot} = \int i\dot{\alpha}r_c\left(e^{2i\theta} - e^{-2i\theta}\right)dr - \int \dot{\alpha}r_c^2\left(e^{2i\theta} - e^{-2i\theta}\right)d\theta \tag{D.11}$$

$$f_{rot} = i\frac{1}{2}\dot{\alpha}r_c^2\left(e^{2i\theta} - e^{-2i\theta}\right) \tag{D.12}$$

$$f_{rot} = i\frac{1}{2}\dot{\alpha}\left(r_c^2 e^{2i\theta} - r_c^2 e^{-2i\theta}\right) \tag{D.13}$$

$$f_{rot} = i\frac{1}{2}\dot{\alpha}(z^2 - (z^*)^2) \tag{D.14}$$

The term above corresponds for a flat foil. Using this development as a guideline, the subsequent velocity and flow potential terms for symmetric Joukowski foil profiles pitching about their respective mid-chords is developed.

Reengaging from Eq. D.2, the velocity expression for a non-flat foil is,

$$w_{rot} = i\dot{\alpha}\left(z^* + \frac{a_c^2}{z^*} - \Delta_x\right)\left(1 - \frac{a_c^2}{z^2}\right) \tag{D.15}$$

where Δ_x is the foil pitch axis offset from the origin. Utilizing $zz^* = r_c^2$ and acknowledging that $a_c \neq r_c$,

$$w_{rot} = i\dot{\alpha}\left(\frac{r_c^2}{z} + \frac{a_c^2 z}{r_c^2} - \Delta_x\right)\left(1 - \frac{a_c^2}{z^2}\right) \tag{D.16}$$

$$w_{rot} = i\dot{\alpha}\left(\frac{r_c^2}{z} + \frac{a_c^2 z}{r_c^2} - \Delta_x - \frac{r_c^2 a_c^2}{z^3} - \frac{a_c^4}{r_c^2 z} + \frac{\Delta_x a_c^2}{z^2}\right) \tag{D.17}$$

$$w_{rot} = i\dot{\alpha}\left(\frac{a_c^2}{r_c^2}z - \Delta_x + r_c^2 z^{-1} - \frac{a_c^4}{r_c^2}z^{-1} + \Delta_x a_c^2\, z^{-2} - r_c^2 a_c^2\, z^{-3}\right) \tag{D.18}$$

The following circle geometry expression is expanded and leveraged to continue the development,

$$a_c = r_c + \delta_x \;\; ; \;\; a_c^2 = r_c^2 + 2r_c\delta_x + \delta_x^2 \;\; ; \;\; a_c^4 = r_c^4 + 4r_c^2\delta_x^2 + \delta_x^4 + 4r_c^3\delta_x + 2r_c^2\delta_x^2 + 4r_c\delta_x^3 \tag{D.19}$$

Substituting these in,

$$w_{rot} = i\dot{\alpha}\left(\left(r_c + 2\delta_x + \frac{\delta_x^2}{r_c}\right)e^{i\theta} - \Delta_x + r_c e^{-i\theta} - \left(r_c + 4\frac{\delta_x^2}{r_c} + \frac{\delta_x^4}{r_c^3} + 4\delta_x + 2\frac{\delta_x^2}{r_c} + 4\frac{\delta_x^3}{r_c^2}\right)e^{-i\theta} \ldots\right.$$

$$\left. + \Delta_x\left(1 + 2\frac{\delta_x}{r_c} + \frac{\delta_x^2}{r_c^2}\right)e^{-2i\theta} - \left(r_c + 2\delta_x + \frac{\delta_x^2}{r_c}\right)e^{-3i\theta}\right) \tag{D.20}$$

All higher order terms based on δ_x are dropped, as δ_x is generally a small number, in order to yield the following approximated velocity term,

$$w_{rot} = i\dot{\alpha}\left((r_c + 2\delta_x)e^{i\theta} - \Delta_x + r_c e^{-i\theta} - (r_c + 4\delta_x)e^{-i\theta} + \Delta_x e^{-2i\theta} - (r_c + 2\delta_x)e^{-3i\theta}\right) \quad (D.21)$$

The flow potential is found through integration in the complex plane,

$$f_{rot} = i\dot{\alpha}\int\left((r_c + 2\delta_x)e^{i\theta} - \Delta_x + r_c e^{-i\theta} - (r_c + 4\delta_x)e^{-i\theta} + \Delta_x e^{-2i\theta} - (r_c + 2\delta_x)e^{-3i\theta}\right)\ldots$$

$$\left(e^{i\theta}dr + ire^{i\theta}d\theta\right) \quad (D.22)$$

$$f_{rot} = i\dot{\alpha}\int\left((r_c + 2\delta_x)e^{2i\theta} - \Delta_x e^{i\theta} + r_c - (r_c + 4\delta_x) + \Delta_x e^{-i\theta} - (r_c + 2\delta_x)e^{-2i\theta}\right)\ldots$$

$$(dr + ird\theta) \quad (D.23)$$

$$f_{rot} = i\dot{\alpha}\int\left((r_c + 2\delta_x)e^{2i\theta} - \Delta_x e^{i\theta} - 4\delta_x + \Delta_x e^{-i\theta} - (r_c + 2\delta_x)e^{-2i\theta}\right)dr \ldots$$

$$- \dot{\alpha}\int\left((r_c^2 + 2\delta_x r_c)e^{2i\theta} - \Delta_x r_c e^{i\theta} - 4\delta_x r_c + \Delta_x r_c e^{-i\theta} \ldots\right.$$

$$\left. - (r_c^2 + 2\delta_x r_c)e^{-2i\theta}\right)d\theta \quad (D.24)$$

$$f_{rot} = i\dot{\alpha}\left(\left(\frac{1}{2}r_c^2 + 2\delta_x r_c\right)e^{2i\theta} - \Delta_x r_c e^{i\theta} - 4\delta_x r_c + \Delta_x r_c e^{-i\theta} - \left(\frac{1}{2}r_c^2 + 2\delta_x r_c\right)e^{-2i\theta}\right)\ldots$$

$$+ \dot{\alpha}(8\pi\delta_x r_c) \quad (D.25)$$

$$f_{rot} = i\dot{\alpha}\left(\frac{1}{2}z^2 + 2\delta_x z e^{i\theta} - \Delta_x z - 4\delta_x r_c + \Delta_x z^* - \frac{1}{2}z^{*2} - 2\delta_x z^* e^{-i\theta}\right) + \dot{\alpha}(8\pi\delta_x r_c) \quad (D.26)$$

$$f_{rot} = i\dot{\alpha}\left(\frac{1}{2}\left(z^2 - z^{*2}\right) + \delta_x\left(2ze^{i\theta} - 2z^* e^{-i\theta} - 4r_c\right) + \Delta_x(-z + z^*)\right) - i\dot{\alpha}(i8\pi\delta_x r_c) \quad (D.27)$$

$$f_{rot} = i\dot{\alpha}\left(\frac{1}{2}\left(z^2 - z^{*2}\right) + \delta_x\left(2ze^{i\theta} - 2z^*e^{-i\theta} - 4r_c - i8\pi r_c\right) + \Delta_x(-z + z^*)\right) \qquad (D.28)$$

This expression is written such that the flat foil portion is clearly isolated at the beginning of the expression, and the contributions due to foil thickness are grouped according to δ_x and Δ_x, which are additive to the flat foil expression. These velocity and flow potential terms are what are implemented in the UPF calculations and utilized in the unsteady potential flow analysis.

Returning back to the ensuring the flow potential expression for the flat foil condition satisfies Laplace's equation,

$$\nabla^2 f_{rot} = 0 \quad ; \quad f_{rot} = i\dot{\alpha}\frac{1}{2}\left(z^2 - z^{*2}\right) \qquad (D.29)$$

$$\nabla^2\left(i\dot{\alpha}\frac{1}{2}((x+iy)^2 - (x-iy)^2)\right) \qquad (D.30)$$

$$\nabla^2\left(i\dot{\alpha}\frac{1}{2}\left(x^2 - y^2 + i2xy - (x^2 - y^2 - i2xy)\right)\right) \qquad (D.31)$$

$$\nabla^2\left(i\dot{\alpha}\frac{1}{2}(i4xy)\right) \qquad (D.32)$$

$$\nabla^2(-\dot{\alpha}2xy) \qquad (D.33)$$

$$\frac{\partial^2}{\partial x^2}(-\dot{\alpha}2xy) + \frac{\partial^2}{\partial y^2}(-\dot{\alpha}2xy) \quad = 0 \quad \checkmark \qquad (D.34)$$

As is shown above, the corresponding flow potential expression for finite thickness foils is additive to the flat foil expression and these additions are of sufficient order such that the condition on the Laplacian still holds.

Lastly, it is confirmed that this flow potential term maintains the circle (i.e. foil) as a streamline by checking that ψ is constant along z, where $f = \phi + i\psi$. Taking the flat foil expression above,

$$f_{rot} = i\dot{\alpha}\frac{1}{2}\left(z^2 - z^{*2}\right) \quad \rightarrow \quad f_{rot} = -\dot{\alpha}2xy \qquad (D.35)$$

it is acknowledged that this term yields only real values, and therefore satisfies this condition.

Correspondingly, Eq. D.28 is returned to and assessed for the condition of finite thickness foils,

$$f_{rot} = -\dot{\alpha}2xy + i\dot{\alpha}\left(\delta_x\left(2ze^{i\theta} - 2z^*e^{-i\theta} - 4r_c - i8\pi r_c\right) + \Delta_x(-z + z^*)\right) \qquad (D.36)$$

where Eqs. C.4 and C.5 are utilized for the difference of the complex conjugates.

$$f_{rot} = -\dot{\alpha}2xy + i\dot{\alpha}\left(\delta_x(i4r_c\sin(2\theta) + i4\delta_x\sin(\theta) - 4r_c - i8\pi r_c) + \Delta_x(-i2r_c\sin(\theta))\right) \qquad (D.37)$$

$$f_{rot} = -\dot{\alpha}2xy + \dot{\alpha}\left(\delta_x(-4r_c\sin(2\theta) - 4\delta_x\sin(\theta) - i4r_c + 8\pi r_c) + \Delta_x(2r_c\sin(\theta))\right) \qquad (D.38)$$

It is acknowledged that this expression can be further simplified, however, it should be clear that all of the functional contributions are real-valued, and the one imaginary term is a constant. It is therefore found that this rotational velocity expression maintains the impenetrability condition of the flow surface, as required.

Appendix E: Recasting the Non-Circulatory Term in the Kutta Condition

This material shows how the non-circulatory portion of the Kutta condition referenced in Section 2.4 is handled within these UPF calculations. First, the following manipulation is applied to simplify the integral expression,

$$\frac{2}{\pi}\int_0^{\pi}\frac{w_a\sin^2(\theta)}{\cos(\theta)-1}\,d\theta=\frac{2}{\pi}\int_0^{\pi}\frac{w_a(1-\cos^2(\theta))}{\cos(\theta)-1}\,d\theta=\cdots$$

$$\frac{2}{\pi}\int_0^{\pi}\frac{w_a(1-\cos(\theta))(1+\cos(\theta))}{\cos(\theta)-1}\,d\theta=-\frac{2}{\pi}\int_0^{\pi}w_a\,(1+\cos(\theta))\,d\theta \qquad (E.1)$$

Directly following the Theodorsen model development as presented by Bisplinghoff et al., the disturbance velocity is, $w_a=-\dot{h}-U_\infty\alpha-\dot{\alpha}(X-ba)$, where the pitching axis is defined as a. Plugging this in, splitting the integral, and evaluating yields,

$$-\frac{2}{\pi}\left(-\dot{h}-U_\infty\alpha+\dot{\alpha}ba\right)\int_0^{\pi}1+\cos(\theta)\;d\theta-\frac{2}{\pi}(-\dot{\alpha})\int_0^{\pi}X(1+\cos(\theta))\,d\theta \qquad (E.2)$$

where $X=b\cos(\theta)$, and b is the half chord of the foil.

$$\frac{2}{\pi}\left(\dot{h}+U_\infty\alpha-\dot{\alpha}ba\right)[\theta+\sin(\theta)]_0^{\pi}+\frac{2}{\pi}(\dot{\alpha})\int_0^{\pi}b\cos(\theta)\,(1+\cos(\theta))\,d\theta \qquad (E.3)$$

$$\frac{2}{\pi}\left(\dot{h}+U_\infty\alpha-\dot{\alpha}ba\right)[\pi]+\frac{2}{\pi}(\dot{\alpha}b)\int_0^{\pi}\cos(\theta)+\cos^2(\theta)\;d\theta \qquad (E.4)$$

$$\frac{2}{\pi}\left(\dot{h}+U_\infty\alpha-\dot{\alpha}ba\right)[\pi]+\frac{2}{\pi}(\dot{\alpha}b)\int_0^{\pi}\cos(\theta)+\frac{1}{2}+\frac{1}{2}\cos(2\theta)\;d\theta \qquad (E.5)$$

$$2\left(\dot{h}+U_\infty\alpha-\dot{\alpha}ba\right)+\frac{2}{\pi}(\dot{\alpha}b)\left[\left[\sin(\theta)+\frac{\theta}{2}\right]_0^{\pi}+\frac{1}{4}\int_0^{\pi}\cos\left(\tilde{\theta}\right)\,d\tilde{\theta}\right]\quad;\quad\tilde{\theta}=2\theta \qquad (E.6)$$

$$2\left(\dot{h}+U_\infty\alpha-\dot{\alpha}ba\right)+\frac{2}{\pi}(\dot{\alpha}b)\left[\frac{\pi}{2}+\frac{1}{4}\left[\sin\left(\tilde{\theta}\right)\right]_0^{\pi}\right] \qquad (E.7)$$

$$2\left(\dot{h}+U_\infty\alpha-\dot{\alpha}ba\right)+\frac{2}{\pi}(\dot{\alpha}b)\left[\frac{\pi}{2}+0\right] \qquad (E.8)$$

$$2\left(\dot{h} + U_\infty \alpha - \dot{\alpha} b a + \frac{1}{2}\dot{\alpha} b\right) \tag{E.9}$$

$$2\left(\dot{h} + U_\infty \alpha + \dot{\alpha} b\left(\frac{1}{2} - a\right)\right) \;=\; 2\,\widetilde{w}_a \tag{E.10}$$

Therefore the original non-circulatory contribution to the Kutta condition expression is,

$$\frac{2}{\pi}\int_0^\pi \frac{w_a \sin^2(\theta)}{\cos(\theta) - 1}\, d\theta \;\rightarrow\; 2\,\widetilde{w}_a \tag{E.11}$$

such that a separately defined disturbance velocity is utilized, $\widetilde{w}_a = \dot{h} + U_\infty \alpha + \dot{\alpha} b\left(\frac{1}{2} - a\right)$.

Appendix F: Considerations for the Shed and Image Vortices

The opening part of this appendix shows that the free field and image vortex pair retain the condition of impenetrability for the circle surface. Picking up from Section 2.1, the flow potential for a vortex in space and its image inside of a circle of r_c is given as,

$$f = i\frac{-\gamma}{2\pi}\log\left(z - z_\gamma\right) + i\frac{\gamma}{2\pi}\log\left(z - \frac{r_c^2}{z_\gamma^*}\right) \tag{F.1}$$

The evaluation of z is to occur on the circle surface, such that $z = r_c e^{i\theta}$ and the free field vortex can exist anywhere on $z_\gamma = a\, r_c e^{i\theta_\gamma}$ for $a > 1$. Substituting these in, and setting $\gamma = 2\pi$ as the vortex strength is simply a coefficient in this context and will not alter the spatial functionality,

$$f = -i\log\left(r_c e^{i\theta} - a r_c e^{i\theta_\gamma}\right) + i\log\left(r_c e^{i\theta} - \frac{r_c^2}{a r_c e^{-i\theta_\gamma}}\right) \tag{F.2}$$

Canceling a common r_c,

$$f = -i\log\left(e^{i\theta} - a e^{i\theta_\gamma}\right) + i\log\left(e^{i\theta} - \frac{1}{a}e^{i\theta_\gamma}\right) \tag{F.3}$$

$$f = i\log\left(\frac{e^{i\theta} - \frac{1}{a}e^{i\theta_\gamma}}{e^{i\theta} - a e^{i\theta_\gamma}}\right) \tag{F.4}$$

$$f = i\log\left(\frac{e^{i(\theta-\theta_\gamma)} - \frac{1}{a}}{e^{i(\theta-\theta_\gamma)} - a}\right) \tag{F.5}$$

Replacing $\theta - \theta_\gamma$ with θ, as θ_γ is a constant and this will equally cover the domain $[0,2\pi]$,

$$f = i\log\left(\frac{e^{i(\theta-\theta_\gamma)} - \frac{1}{a}}{e^{i(\theta-\theta_\gamma)} - a}\right) = i\log\left(\frac{e^{i\theta} - \frac{1}{a}}{e^{i\theta} - a}\right) \tag{F.6}$$

Isolating the streamfunction,

$$\psi = Im\left(i \log\left(\frac{e^{i\theta} - \frac{1}{a}}{e^{i\theta} - a} \right) \right) \tag{F.7}$$

Instead of pursuing a more rigorous proof and detailed analysis, this function is plotted for values of θ and a to exhibit that ψ is a constant function across θ for every a; this is presented in Figure F.1. There is also a plot of ψ across θ at two distinct values of a, further exhibiting the constant nature of this expression. Also present is a visual example of the circle and these two pairs of free field and image vortices. As should be clear, the superposition of any number of vortex pairs would not alter this characteristic behavior. Handling configurations where the circle is offset from the origin yields similarly constant functions.

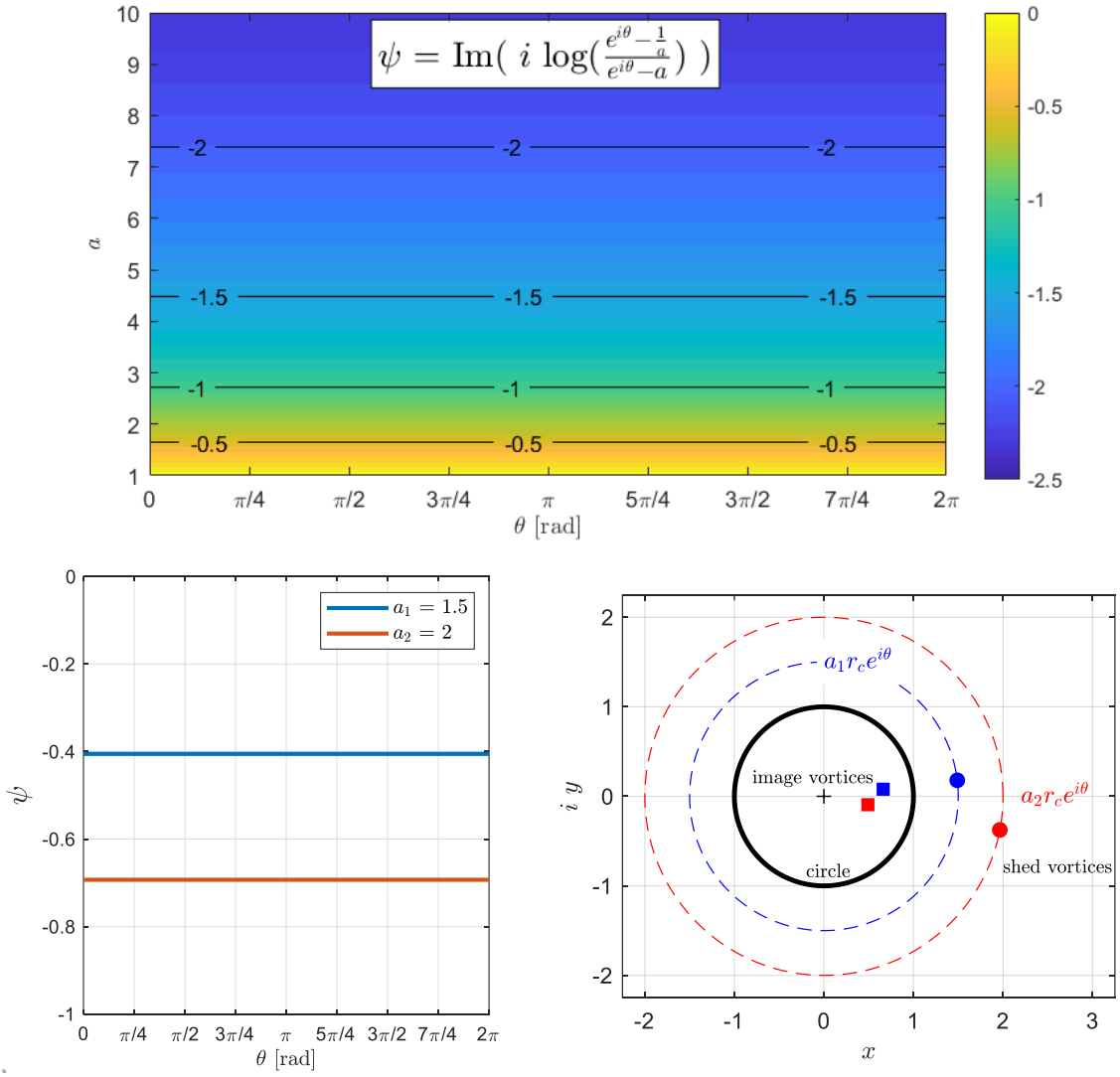

Figure F.1. Effect on the stream function for shed and image vortex pairs

The second part of this appendix addresses the weighting for the shed and image vortices in the application of the Kutta condition. Figure F.2 provides a visual for the configuration of a single free field and image vortex pair located at z_1 and z_2 relative to a circle offset by the origin along the negative real axis, δ_x.

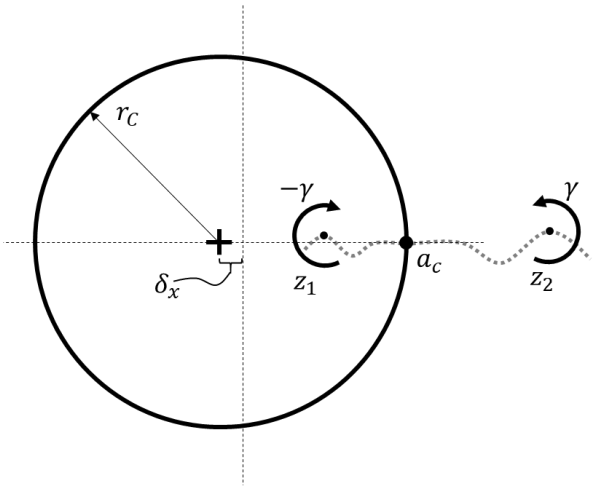

Figure F.2. Illustration of free field and image vortex pair

The velocity in the circle plane evaluated at a_c from this vortex pair is expressed as,

$$w(a_c) = -\frac{i\gamma}{2\pi\tilde{z}_2} + \frac{i\gamma}{2\pi\tilde{z}_1} \quad ; \quad \tilde{z}_2 = a_c - z_2 \quad ; \quad \tilde{z}_1 = a_c - \left(\frac{r_c^2}{z_2^* - \delta_x} + \delta_x\right) \qquad (F.8)$$

Substituting these locations in, generalizing the subscript on z_2 as z_γ, and then simplifying towards an expression for the vertical (i.e. tangential) velocity component yields,

$$w(a_c) = \frac{i\gamma}{2\pi}\left[-\frac{1}{a_c - z_\gamma} + \frac{1}{a_c - \frac{r_c^2}{z_\gamma^* - \delta_x} - \delta_x}\right] \qquad (F.9)$$

$$w(a_c) = \frac{i\gamma}{2\pi a_c}\left[\frac{a_c}{a_c - \frac{r_c^2}{z_\gamma^* - \delta_x} - \delta_x} - \frac{a_c}{a_c - z_\gamma}\right] \qquad (F.10)$$

$$w(a_c) = \frac{i\gamma}{2\pi a_c}\left[\frac{a_c(z_\gamma^* - \delta_x)}{a_c(z_\gamma^* - \delta_x) - r_c^2 - \delta_x(z_\gamma^* - \delta_x)} - \frac{a_c}{a_c - z_\gamma}\right] \qquad (F.11)$$

$$v(a_c) = -Im(\, w(a_c)\,) = \frac{\gamma}{2\pi a_c}\, Im\left(- i\left[\frac{a_c\left(z_\gamma^* - \delta_x\right)}{a_c\left(z_\gamma^* - \delta_x\right) - r_c^2 - \delta_x\left(z_\gamma^* - \delta_x\right)} - \frac{a_c}{a_c - z_\gamma}\right]\right) \qquad (F.12)$$

$$v(a_c) = \frac{\gamma}{2\pi a_c} G\left(z_\gamma\right) \qquad (F.13)$$

where the term comprised of $Im(...)$ in the expression above is written in consolidated form as $G\left(z_\gamma\right)$. For circles offset from the origin along the negative real axis (i.e. Joukowski foils of finite symmetric thickness), this is the term which is utilized to weight the distribution of point vortices in the application of the Kutta condition. The applicability of defining this function in the circle plane is shown with a check for the condition of a flat foil and planar vorticity sheet, $\delta_x = 0$, $a_c = r_c$, $z_\gamma = z_\gamma^* = x$; this yields,

$$\left[\frac{a_c x}{a_c x - a_c^2} - \frac{a_c}{a_c - x}\right] = \left[\frac{x}{x - a_c} - \frac{a_c}{a_c - x}\right] = \left[\frac{x}{x - a_c} + \frac{a_c}{x - a_c}\right] = \frac{x + a_c}{x - a_c}$$

Because of the implemented conformal mapping, $\frac{x+a_c}{x-a_c}$ is equivalent to $\sqrt{\frac{X+b}{X-b}}$. Consider $b = 2a_c$ and,

$$X = x + \frac{a_c^2}{x} \quad ; \quad X = x + \frac{a_c^2}{x} \qquad (F.14)$$

$$X + b = x + \frac{a_c^2}{x} + 2a_c \quad ; \quad X - b = x + \frac{a_c^2}{x} - 2a_c \qquad (F.15)$$

$$(X + b)x = x^2 + 2a_c x + a_c^2 \quad ; \quad (X - b)x = x^2 - 2a_c x + a_c^2 \qquad (F.16)$$

$$\frac{X + b}{X - b} = \frac{(x + a_c)^2}{(x - a_c)^2} \qquad \rightarrow \qquad \frac{x + a_c}{x - a_c} = \sqrt{\frac{X + b}{X - b}} \qquad (F.17)$$

Appendix G: The Mean Properties of the Streamwise Force Response

For the entirety of this document, the focus has been on the unsteady character of the various foil responses due to small-scale disturbance motion. Considering the force aligned in the streamwise direction though, there is also interest in the mean character of this response. At the onset, it must be acknowledged that the efforts and analysis of this appendix are not complete; however, the considerations and comparisons seem to warrant presentation (hence in an appendix). Additionally, it is further acknowledged that conducting analyses and drawing conclusions on the mean streamwise force solely within the framework of potential flow is precarious, given, as examples, D'Alembert's paradox and the overall lack of consideration for viscous effects. Lastly, it is also recognized that this work has not yet fully taken into consideration the predictive expressions from the Garrick model (which is a contemporary of the Theodorsen model and which concentrates specifically on the mean streamwise force). Despite these acknowledgements, the following analysis continues from Section 4.7, and looks to develop and assess predictive expressions for the mean streamwise force relative to the calculated UPF results.

The development for pitching disturbance motion picks up from Eq. 4.43,

$$\frac{C_D}{\alpha} = \frac{1}{2}\left|\frac{C_L}{\alpha}\right||\alpha|\left[-\cos(2\omega t+\phi)+\cos(\phi)\right] \quad ; \quad \phi = \angle\left(\frac{C_L}{\alpha}\right) \tag{G.1}$$

where ϕ is used to represent the phase angle of the unsteady lift transfer function. With regard to consideration of the mean properties of this response, this results in,

$$\overline{\frac{C_D}{\alpha^2}} = \frac{1}{2}\left|\frac{C_L}{\alpha}\right|\cos\left(\angle\left(\frac{C_L}{\alpha}\right)\right) \tag{G.2}$$

as the $\cos(2\omega t)$ term oscillates with an amplitude of unity with no implications on the mean (under assumptions of a sufficiently long signal and appropriately selected end points).

Figure G.1 provides the mean streamwise force determined from the UPF calculations for a numerically thin foil pitching about its mid-chord (note the plot of the response is on a linear scale). In

addition to the baseline condition of $|\alpha| = 0.1^o$, results are also shown for $|\alpha| = 0.01^o$ and 1.0^o at select reduced frequencies. For all but the highest reduced frequency range the predictive expression is seen to compare well to the calculated results. At the high reduced frequency conditions of $k = 19.8$ and 59.4 the results are seen to begin to diverge from the prediction.

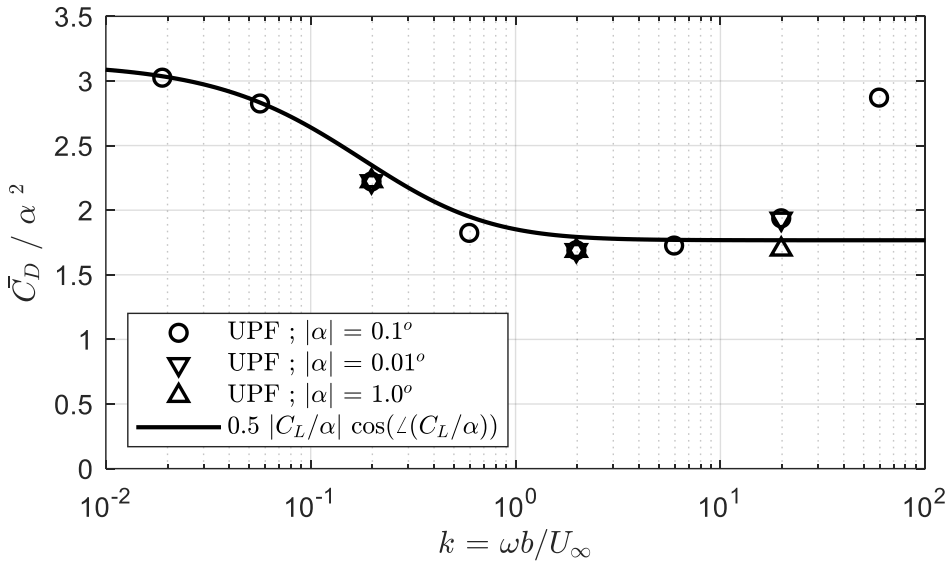

Figure G.1. Mean streamwise force for mid-chord pitching disturbance motion

The partial reasoning and implications for this deviation is understood to be the pronounced behavior of the shed vortices at these conditions. Figure G.2 presents views at distinct time steps of the flow field in the foil trailing edge and downstream region for progressively increasing reduced frequencies (in the same way as earlier in the document). Over this downstream spatial extent of a half-chord, it can be seen that the onset of pronounced wake motion corresponds with the deviation of the calculated results from the predictive expression shown in Figure G.1.

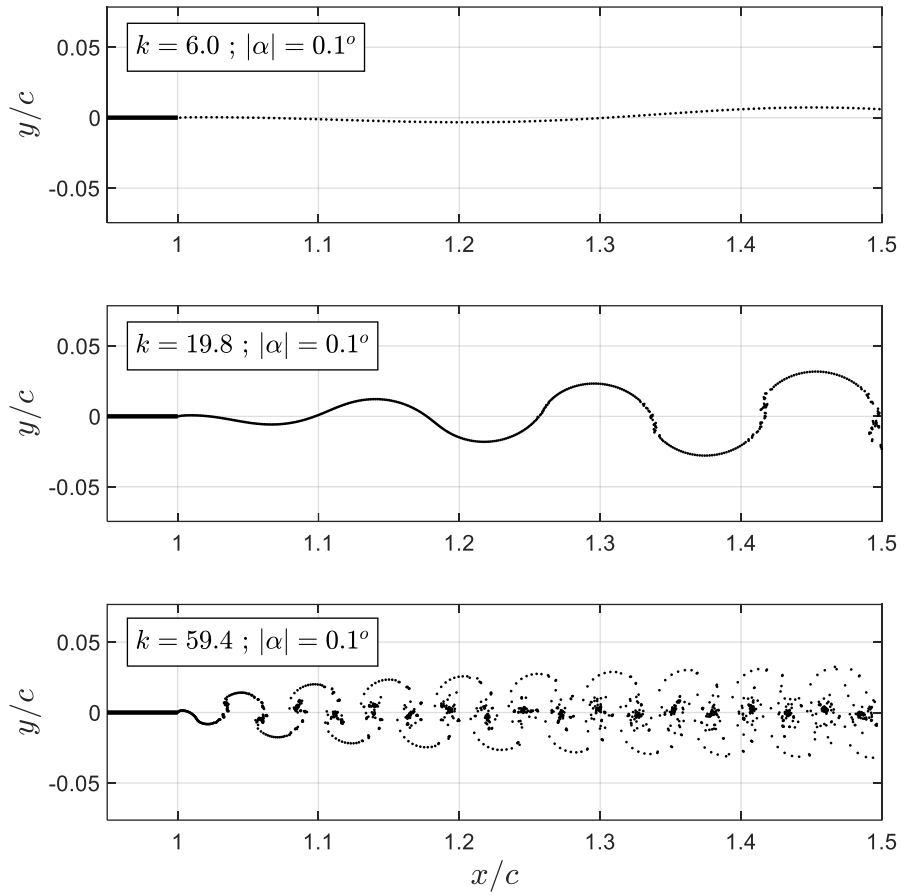

Figure G.2. View of shed point vortices over high reduced frequency conditions

For consideration of foils that are not numerically thin, then the chordwise force component should no longer be assumed to be zero, such that,

$$D = F_X + F_Y\,\alpha \tag{G.3}$$

which is rewritten as a transfer function,

$$\frac{C_D}{\alpha} = \frac{C_X}{\alpha} + \frac{C_L}{\alpha}\,\alpha \tag{G.4}$$

The implication on the mean properties of the streamwise force from the second term on the right hand side of the expression above is understood to be similar as earlier; however, the effect of the first term (or a corresponding expression) is unknown. Therefore, it is simply generalized in the following way,

$$\frac{\overline{C_D}}{\alpha^2} = \chi + \frac{1}{2}\left|\frac{C_L}{\alpha}\right| \cos\left(\angle\left(\frac{C_L}{\alpha}\right)\right) \qquad (G.5)$$

The calculated results for foils of $5, 10$, and 15% thickness-to-chord ratio are presented in Figure G.3, where there are several items to note in this figure. First, the results for the finite thickness foils are distinctly elevated from the thin foil results. Purely based on visual inspection and gross approximation, the dashed line provides a predictive expression which appears to nominally follow the trend of the results across the low and mid reduced frequency values. It is speculated that these differences relative to the thin foil results are attributed to the effects of the chordwise force component, summarized as χ above. Lastly, it is recognized that the calculated results over the higher reduced frequencies are considerably elevated (in fact they are outside of the limits of this figure, denoted by the arrows).

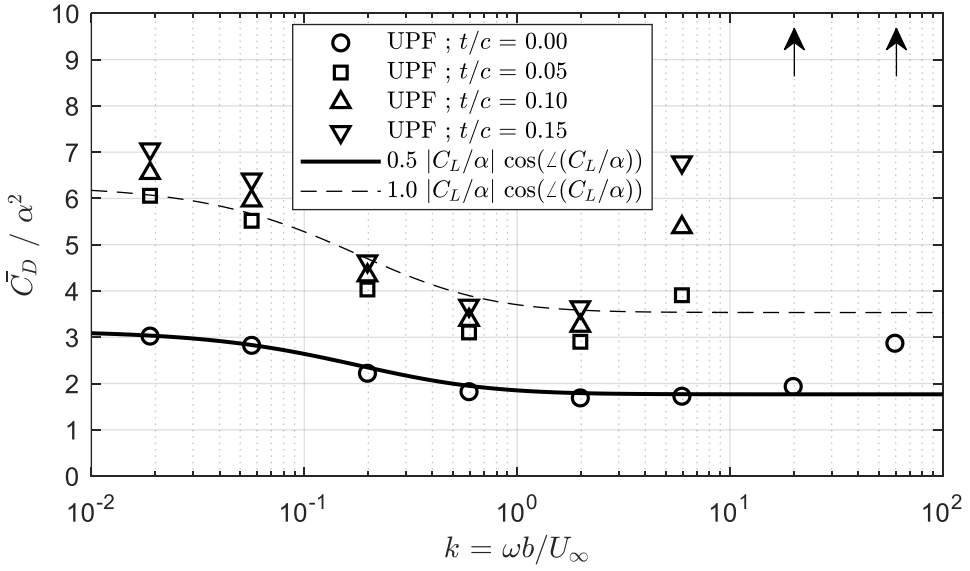

Figure G.3. Mean streamwise force for mid-chord pitching disturbance motion

Adjusting to a logarithmic scale, Figure G.4 provides the same results, though now the high frequency UPF results are within view. The two prior predictive expressions are also present, however, additional curves show the result of implementing the thick foil correction specified in Eq. 4.32. These are seen to capture this high reduced frequency behavior of the calculated results well. The significant alteration

to the results, and for which the predictive expressions are accounting for, is attributed to the altered phase of the unsteady lift response, as seen in Section 4.6.

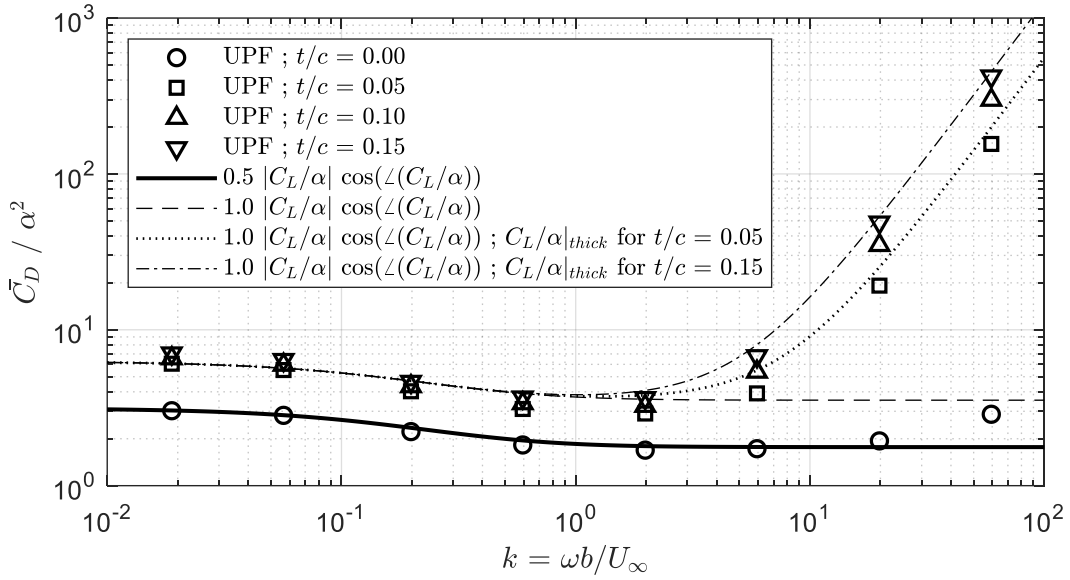

Figure G.4. Mean streamwise force for mid-chord pitching disturbance motion

Transitioning now to the consideration of heaving disturbance motion, which for the UPF results are for foils of finite thickness, similar expressions as above are not as readily available in the present development for the mean properties of the unsteady streamwise force response. Therefore the corresponding expression from the Garrick model is utilized, where it is rewritten here with the presently used nomenclature,

$$\overline{D} = \pi \rho b \omega^2 h^2 |C(k)|^2 \qquad (G.6)$$

Expressing this as a transfer function and simplifying yields the following,

$$\overline{C_D} = \frac{\overline{D}}{0.5\rho U_\infty^2 (2b)} = \pi \frac{\omega^2}{U_\infty^2} \left(\frac{\dot{h}}{i\omega} \right)^2 |C|^2 \qquad (G.7)$$

$$\frac{\overline{C_D}\, U_\infty^2}{\dot{h}^2} = -\pi |C|^2 \quad \rightarrow \quad \frac{\overline{C_T}\, U_\infty^2}{\dot{h}^2} = \pi |C|^2 \qquad (G.8)$$

where the negative sign is taken to denote the generation of thrust. This predictive expression is plotted alongside the corresponding UPF calculated results for the $5, 10,$ and 15% thickness-to-chord ratio Joukowski foils undergoing heaving motion in Figure G.5. The comparison between the calculated results and this predictive expression is seen to be quite positive over the entire range of reduced frequency, with the largest deviations occurring over the low reduced frequency range. As a final point, it is noted that the Garrick model was developed under the assumption of a numerically thin foil (as for the Theodorsen model); accordingly, the UPF results from the 5% thick foil are seen to compare best to this predictive expression.

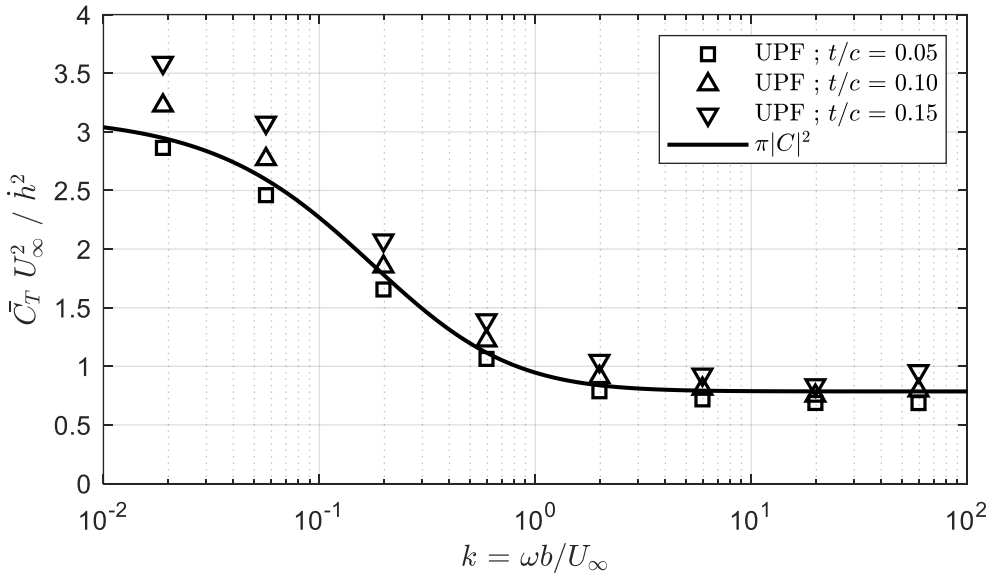

Figure G.5. Mean streamwise force for heaving disturbance motion

As acknowledged at the onset of this appendix, these efforts are not considered complete; however, are believed to comprise a useful footing for future considerations and efforts.

Bibliography

Anderson, J. M., Catlett, M. R., and Stewart, D. O., 2015, "Modeling Rotor Unsteady Forces and Sound Due to Homogeneous Turbulence Ingestion," *AIAA Journal*, vol. 53, no. 1, pp. 81-92.

Anderson, J. M. and DiPerna, D., 2017, "A Conformal Mapping Model for Force Response of Arbitrarily Shaped Thick Foils to Incident Turbulence," *AIAA AVIATION, 23rd AIAA/CEAS Aeroacoustics Conference*, AIAA-3532, Denver, CO, 5-9 June.

Ashraf, M. A., Young, J., and Lai, J. C. S., 2011, "Reynolds Number, Thickness and Camber Effects on Flapping Airfoil Propulsion," *Journal of Fluids and Structures*, Vol. 27, 145-160.

Basu, B. C., and Hancock, G. J., 1978, "The Unsteady Motion of a Two-Dimensional Airfoil in Incompressible Inviscid Flow," *Journal of Fluid Mechanics*, vol. 87, part 1, 159-178.

Bisplinghoff, R. L., Ashley, H., and Halfman, R. L., 1955, "Aeroelasticity," Addison-Wesley Publishing Company, Inc., Cambridge, MA.

Boutet, J., and Dimitriadis, G., 2018, "Unsteady Lifting Line Theory Using the Wagner Function for the Aerodynamic and Aeroelastic Modeling of 3D Wings," *Aerospace*, 5, 92.

Bratt, J. B., 1945, "The Effects of Mean Incidence, Amplitude of Oscillation, Profile and Aspect Ratio on Pitching Moment Derivatives," *Aeronautical Research Committee Reports and Memoranda*, No. 2064.

Bratt, J. B., 1953, "Flow Patterns in the Wake of an Oscillating Airfoil," *Aeronautical Research Council*, Reports and Memoranda No. 2773.

Catlett, M. R., and Anderson, J. M., 2016, "Modeling Unsteady Lift on a Hydrofoil due to the Ingestion of Turbulence and Hydro-elastic Motion," *AIAA AVIATION, 46th AIAA Fluid Dynamics Conference*, AIAA-3637, Washington, D.C., 13-17 June.

Catlett, M. R., Anderson, J. M., and Baeder, J. D., 2018, "Numerical Investigation of Aeroelastic Forces and Pressures on Joukowksi Foils of Variable Thickness due to Heaving Motion," *AIAA SciTech Forum*, AIAA-1073, Kissimmee, FL, 8-12 January.

Catlett, M. R., Anderson, J. M., Badrya, C., Govindarajan, B., and Baeder, J. D., 2018, "Numerical Investigation of Aeroelastic Forces and Pressures on Joukowski Foils of Variable Thickness due to Pitching Motion," *AIAA AVIATION, 2018 Fluid Dynamics Conference*, AIAA-2906, Atlanta, GA, 25-29 June.

Catlett, M. R., Anderson, J. M., Badrya, C., and Baeder, J. D., 2020, "Unsteady response of airfoils due to small-scale pitching motion with considerations for foil thickness and wake motion," *Journal of Fluids and Structures*, vol. 94, article 102889.

Chao, L. M, Pan, G., Zhang, D., and Yan, G. X., 2019, "Numerical investigations on the force generation and wake structures of a nonsinusoidal pitching foil," *Journal of Fluids and Structures*, vol. 85, pp. 27-39.

Cordes, U., Kampers, G., Meißner, T., Tropea, C., Peinke, J., and Hölling, M., 2017, "Note on the Limitations of the Theodorsen and Sears Functions," *Journal of Fluid Mechanics*, vol. 811, R1.

Crighton, D. G., 1985, "The Kutta Condition in Unsteady Flow," *Annual Review of Fluid Mechanics*, Vol. 17, 411-445.

Davis, S. S., and Malcolm, G. N., 1980, "Experimental Unsteady Aerodynamics of Conventional and Supercritical Airfoils," NASA TM 81221.

Garrick, I. E., 1936, "Propulsion of a Flapping and Oscillating Airfoil," NACA Report 567.

Giesing, J. P., 1968, "Nonlinear Two-Dimensional Unsteady Potential Flow with Lift," *Journal of Aircraft*, Vol. 5, No. 2, 135-143.

Glegg, S. A. L., and Devenport, W., 2009, "Unsteady loading on an airfoil of arbitrary thickness," *Journal of Sound and Vibration*, 319, pp. 1252-1270.

Halfman, R. L., 1952, "Experimental Aerodynamic Derivatives of a Sinusoidally Oscillating Airfoil in Two-dimensional Flow," NACA Report 1108.

Hammer, P. R., Olson, D. A., Visbal, M. R., Naguib, A. M., and Koochesfahani, M. M., 2019, "Joint Computational-Experimental Investigation of Harmonically Pitching Airfoil Aerodynamics in Uniform-Shear Approach Flow," *AIAA Journal*, Vol. 57, No. 8, 3290-3298.

Heathcote, S., and Gursul, I., 2007, "Flexible Flapping Airfoil Propulsion at Low Reynolds Numbers," *AIAA Journal*, vol. 45, no. 5, pp. 1066-1079.

Koochesfahani, M. M., 1989, "Vortical Patterns in the Wake of an Oscillating Airfoil," *AIAA Journal*, vol. 27, no. 9, pp. 1200-1205.

Küssner, H. G., 1929, "Schwingungen von Flugzeugflügeln," *Luftfahrtforschung*, vol. 4.

Leishman, J. G., 1993, "Indicial Lift Approximations for Two-Dimensional Subsonic Flow as Obtained from Oscillatory Measurements," *AIAA Journal of Aircraft*, Vol. 30, No. 3, 340-351.

Leishman, J. G., 2006, "Principles of Helicopter Aerodynamics," 2nd Edition, Cambridge University Press, Cambridge, England.

Liiva, J., Davenport, F. J., Grey, L., and Walton, I. C., 1968, "Two-Dimensional Tests of Airfoils Oscillating Near Stall," USAAVLABS TR 68-13.

Liu, X. L., Wo, A., and Covert, E., 1990, "Unsteady Streamlines near the Trailing Edge of NACA 0012 Airfoil at a Reynolds Number of 125,000," *AIAA Journal, Technical Notes*, vol. 28, no.1.

Lu, K., Xie, Y. H., and Zhang, D., 2013, "Numerical study of large amplitude, non-sinusoidal motion and camber effects on pitching airfoil propulsion," *Journal of Fluids and Structures*, 36, pp. 184-194.

McCroskey, W. J., 1982, "Unsteady Airfoils," *Annual Review of Fluid Mechanics*, Vol. 14, 285-311.

Medida, S., and Baeder, J. D., 2011, "Application of the Correlation-based $\gamma - Re\theta_t$ Transition Model to the Spalart-Allmaras Turbulence Model," *20th AIAA Computational Fluid Dynamics Conference*, Honolulu, HI, June 27-30.

Michelin, S. and Smith, S. G. L., 2009, "An unsteady point vortex method for coupled-fluid-solid problems," *Theoretical and Computational Fluid Dynamics*, Vol. 23, 127-153.

Münch, C., Ausoni, P., Braun, O., Farhat, M., and Avellan, F., 2010. "Fluid-Structure Coupling for an Oscillating Hydrofoil," *Journal of Fluids and Structures*, Vol. 26, 1018-1033.

Ohashi, H., and Ishikawa, N., 1972, "Visualization Study of Flow Near the Trailing Edge of an Oscillating Airfoil," *Bulletin of the JSME*, Vol. 15, 840-847.

Platzer, M. F., Jones, K. D., Young, J., and Lai, J. C. S., 2008, "Flapping-Wing Aerodynamics: Progress and Challenges," *AIAA Journal*, Vol. 46, No. 9, 2136-2149.

Poling, D. R., and Telionis, D. P., 1986, "The Response of Airfoils to Periodic Disturbances – The Unsteady Kutta Condition," *AIAA Journal*, vol. 24, p. 193.

Rainey, A. G., 1957, "Measurement of Aerodynamic Forces for Various Mean Angles of Attack on an Airfoil Oscillating in Pitch and on Two Finite-Span Wings Oscillating in Bending with Emphasis on Damping in the Stall," NACA report 1305.

Read, D. A., Hover, F. S., and Triantafyllou, M. S., 2003, "Forces on Oscillating Foils for Propulsion and Maneuvering," *Journal of Fluids and Structures*, Vol. 17, 163-183.

Rieper, F., 2011, "A Low-Mach Number Fix for Roe's Approximate Riemann Solver," *Journal of Computational Physics*, Vol. 230, 5263-5287

Satyanarayana, B., and Davis, S., 1978, "Experimental Studies of Unsteady Trailing-Edge Conditions," *AIAA Journal*, vol. 16, no. 2, p. 125-129.

Sears, W. R., 1941, “Some aspects of non-stationary airfoil theory and its practical application,” *Journal of the Aeronautical Sciences*, 8, 3.

Silverstein, A., and Joyner, U. T., 1939, “Experimental Verification of the Theory of Oscillating Airfoils,” NACA Report 673.

Srinivasan, G. R., and Baeder, J. D., 1992, “TURNS: A Free-Wake Euler/Navier-Stokes Numerical Method for Helicopter Rotors,” *AIAA Journal*, Vol. 31, No. 5, 959-962.

Strangfeld, C., Rumsey, C. L., Müller-Vahl, H., Greenblatt, D., Nayeri, C. N., and Paschereit, C. O., 2015, “Unsteady Thick Airfoil Aerodynamics: Experiments, Computation, and Theory,” *AIAA AVIATION Conference, 45th AIAA Fluid Dynamics Conference*, AIAA 2015-3071, Dallas, TX, 22-26 June 2015.

Taha, H. and Rezaei, A. S., 2019, “Viscous extension of potential-flow unsteady aerodynamics: the lift frequency response problem,” *Journal of Fluid Mechanics*, Vol. 868, 141-175.

Theodorsen, T., 1935, “General Theory of Aerodynamic Instability and the Mechanism of Flutter,” NACA Report 496.

Tijdeman, H., and Seebass, R., 1980, “Transonic Flow Past Oscillating Airfoils,” *Annual Review of Fluid Mechanics*, vol. 12, 181-222.

Wagner, H., 1925, “Über die entstehung des dynamischen auftriebes von tragflügeln,” *Z. agnew. Math. Mech.*, 5, 1.

Wang, C. and Eldredge, J. D., 2013, “Low-order phenomenological modeling of leading-edge vortex formation,” *Theoretical and Computational Fluid Dynamics*, Vol. 27, 577-598.

Wood, M. E., 1979, “Results of Oscillatory Pitch and Ramp Tests on the NACA0012 Blade Section,” Aircraft Research Association, Memo. 220, Bedford, England.

Xia, X. and Mohseni, K., 2017, “Unsteady aerodynamics and vortex-sheet formation of a two-dimensional airfoil,” *Journal of Fluid Mechanics*, Vol. 830, 439-478.

Yates, J. E., 1980, “Viscous Thin Airfoil Theory,” ARAP Report 413.

Young, J. and Lai, J. C. S., 2004, “Oscillation Frequency and Amplitude Effects on the Wake of a Plunging Airfoil,” *AIAA Journal*, Vol. 42, No. 10, 2042-2052.